PhD Thesis

Molecular Moiré Superlattices for Prospective Quantum Molecular Devices

Submitted by

Ujjala Dey

Roll No.- 196122043

Under the supervision of

Prof. Arun Chattopadhyay

01.05.2025

Dept of Chemistry

Indian Institute of Technology Guwahati

Guwahati – 781039, Assam, India

Molecular Moiré Superlattices for Prospective Quantum Molecular Devices

A Thesis Submitted by

Ujjala Dey

Roll No.- 196122043

To

Indian Institute of Technology Guwahati

For the award of the degree of

Doctor of Philosophy

01.05.2025

Dept of Chemistry

Indian Institute of Technology Guwahati

Guwahati – 781039, Assam, India

Statement

This thesis entitled "**Molecular Moiré Superlattices for Prospective Quantum Molecular Devices**" is a work of research and investigation carried by me under the supervision of Prof. Arun Chattopadhyay, Professor, Department of Chemistry, Indian Institute of Technology Guwahati. This thesis has been submitted by me to the Department of Chemistry, Indian Institute of Technology Guwahati for the award of Doctor of Philosophy. I further declare that this work has not been submitted anywhere else for the award of any degree in any institution or university to the best of my knowledge. The thesis does not contain any data or language produced with the help of any Artificial Intelligence (AI)-based software.

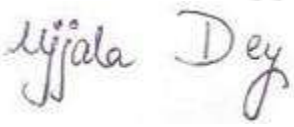

Ujjala Dey
Department of Chemistry, IIT Guwahati
Guwahati-781039, Assam, India
Date – 01.05.2025
Place – Guwahati, India

Certificate

It is certified that the thesis entitled "**Molecular Moiré Superlattices for Prospective Quantum Molecular Devices**" being submitted to the Indian Institute of Technology by Ujjala Dey (Roll No. 196122043) for the award of Doctor of Philosophy in Chemistry is a bonafide record of research work carried out by her. The information and data reported by her are solely the results of her original findings. She has meticulously carried out the investigations and followed the guidelines of the laboratory. This work has not been submitted elsewhere for any degree or diploma.

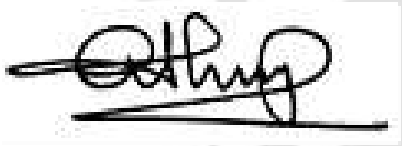

Prof. Arun Chattopadhyay
Thesis Supervisor
Professor,
Department of Chemistry, IIT Guwahati
Guwahati-781039, Assam, India
Date – 01.05.2025
Place – Guwahati, India

Dedicated to my parents

Maa

(Mrs. Ratna Dey)

and

Baba

(Mr. Pradyumna Kishore Dey)

Acknowledgements

My PhD journey has been a significant and eventful experience, filled with both challenges and achievements. Throughout this period, I have received invaluable support and guidance from numerous individuals, which helped me achieve my goals. I extend my heartfelt thanks to everyone who has been a part of this journey.

First and foremost, I would like to express my profound gratitude to my supervisor Prof. Arun Chattopadhyay for his constant support and guidance. His dedication and commitment toward contribution to science constantly motivated me to pursue high-quality research. I learned many valuable lessons from him, but most importantly, he instilled in me the importance of integrity and honesty in scientific research. He allowed me to take lead in projects as a scholar while always being there when assistance was needed. He constantly reminded us all that mental and physical health was equally important and should not be overlooked. He provided us with a supportive and healthy environment for research and ensured that we had all the facilities we needed to thrive. His continuous guidance, enthusiasm for science, honesty in research, and kindness not only helped me grow as a researcher but also as a human being.

I am grateful to my doctoral committee members, Prof. Chandan Mukherjee, Prof. Lal Mohan Kundu and Dr. Sunanda Chatterjee for their critical evaluation of my PhD thesis work and providing me with valuable suggestions and insights.

I express my sincere gratitude to all my lab mates, both past and present, for their invaluable help, advice and support. I especially thank my seniors for extending a warm welcome to me when I joined the lab and providing a positive work environment. I offer my best wishes to my juniors and present lab members and thank them for being a part of this journey. I am grateful for all their help and assistance, no matter how small or big. I am also thankful to all my collaborators for their contributions in my research endeavours.

I acknowledge Department of Chemistry, Center for Nanotechnology, Central Instrument Facility and IIT Guwahati for providing the requisite facilities for my research work.

Lastly, I want to express my heartful gratitude to my parents for their unwavering encouragement and unconditional love. Without their sacrifices, patience, and support, this journey would not have been possible. My PhD experience would have been incomplete without the love and support of my friends, who were there for me during both joyful and challenging times, making this journey enjoyable.

Ujjala Dey

Table of Contents

Abstract

The current thesis focuses on the assembly of small organic molecule to molecular moiré superlattices with application potential as quantum molecular devices. The initial work in this thesis focuses on the assembly of metal complexes to form 0-dimensional nanoparticles that display size-dependent luminescent and magnetic properties. These nanoparticles can further be assembled into 2D moiré superlattices. The chapters following this work discusses the self-assembly of simple organic molecules into 2D crystalline nanosheets that further forms multilayered moiré superlattices after twisted stacking. They display extraordinary tunable physical and chemical properties depending on the molecular interaction at the twisted interface compared to their 2D counterparts. Further the twist angles and moiré periodicities can be controlled by addition of Zn^{2+} ions to moiré superlattices. The Zn-complexed moiré superlattices of tryptophan further acted as spin filters.

The current thesis is divided into six chapters. The works reported in these chapters are briefly discussed below.

Chapter 1: The chapter includes a brief literature review on molecular organization to form hierarchical structures of 0, 1 and 2D crystalline assemblies and their properties based on their molecular interactions. It also includes a brief discussion of how molecules and their assemblies were proposed to be used as molecular machines and eventually became favorites in molecular electronics, spintronics and quantum molecular devices.

Chapter 2: The initial work for this dissertation focuses on the assembly of metal complexes to form 0-dimensional nanoparticles that display size-dependent luminescent and magnetic properties. These types of nanoparticles can also be further assembled into 2D moiré superlattices. This work inspired us to synthesize moiré superlattices that is assembled from simple organic molecules.

Chapter 3: The chapter introduces the concept of moiré superlattice formation from small organic molecules. In this chapter, the chemical synthesis of moiré superlattices of L or D tryptophan (trp) molecules are described that were formed by the twisted stacking of the self-

assembled crystalline 2D nanosheets in an aqueous medium that showcased new physical and chemical properties through interactions at the crystal interfaces.

Chapter 4: This chapter proposes the potential use of molecular moiré superlattices for building complex circuits, information storage, or sensing based on the principles of quantum mechanics at the molecular length scales. Further electrical properties of multilayered moiré superlattices of p-phenylenediamine were studied where it was dependent on the twist angle between two consecutive layers and pH of the medium.

Chapter 5: This chapter explores the concept of spin-polarized conductance through Zn-complexed moiré superlattices of D/L-trp and thus acted as spin filters. The twist angles and moiré periodicities were controlled by addition of Zn^{2+} ions to moiré superlattices of D/L-trp.

Chapter 6: This chapter includes the summarization and the future prospects for the work presented in this thesis.

Chapter 1: Introduction

Chapter 1

Introduction

Molecular assembly through supramolecular or covalent interactions into crystalline 0, 1, 2-dimensional superstructures are able to perform many well-orchestrated functions that can be tuned by their size, shape and chemical bonding within the assembly. Many naturally occurring molecular assemblies perform various designated functions, including cell division, energy production, and muscle locomotion, all of which are vital for the sustenance of life.[1-3] Taking inspiration from these processes, many artificial molecular machines[4] were designed that carried out specific functions.[3,5] For example, different molecular[6] and supramolecular[7] assemblies were explored for their usage as molecular wires or device components for fabrication of various device prototypes such as rectifiers[8], resistive switches[9] and transistors[10-11]. They are extensively studied in detail to explore their applications in molecule-based electronics[6,12], pharmaceuticals[13-14], photonics[15], and optoelectronics[16]. Therefore, it is desirable to engineer and design a suitable molecular assembly that can be manipulated based on their chemical bonding or constituent units to have specific functions and properties. Again, the assembled nanosized 0, 1, or 2-dimensional structures formed from covalent or/and non-covalent interactions between molecules has greatly impacted the field of materials chemistry and nanoscience.[17] They are widely used in many areas such as catalysis, as molecular wires, for sensing, and in optoelectronics, among other applications.[18-21] With the dawn of quantum computation era, an alternative to the demand for miniaturization of circuits has increased significantly while the size reduction of silicon-based semiconductors has almost reached its limit. Due to this demand, the focus has now shifted towards molecule-based assemblies where they are slowly becoming favorites as quantum molecular devices[22-24] though their integration into devices remains one of the major challenges faced due to their small size. Thus, different forms of assemblies are being explored that can be used for molecular electronics where they can be effectively incorporated in classical electronic circuits to reduce their physical dimension. As we move towards the future of artificial intelligence and quantum computing, there is an increasing exploration of bottom-up approaches for developing molecule-based electronics[6]. Having advantages such as suitable size for quantum mechanical effects, cheaper fabrication and better performance based on their tunable chemical properties, they are more suitable for quantum molecular[22] and molecular memory and processing devices[25].

Chapter 1

1.1 Synthesis of nanostructures based on principles of chemistry

Most of the work in the field of nanoscience was done using the top-down approach where the fabrication largely depended on the different lithography and etching methods. However, over the decades, significant advancements took place for the synthesis of nano-dimensional materials based on bottom up approaches. This section gives an overview for the various chemical methods used for the synthesis of different dimensioned nanostructures and their properties before we introduce and discuss the concept of molecular moiré superlattices and their potential use in molecular quantum devices[22]. The synthesis procedures largely relied on the principles of chemistry and biology and later developed into the field of molecular nanotechnology. Thus, following the visionary idea of molecular nanotechnology many bottom-up synthetic approaches were developed for the synthesis of zero-dimesional (0D), one-dimensional (1D) and two-dimensional (2D) materials.

1.1.1 Zero-dimensional nanostructures

The 0D structures[26] like metallic nanoparticles[27-28] or nanoclusters[27,29], quantum dots[30] or carbon dots[31] have their sizes constrained to nanometer scale in all the 3 dimensions and display size-dependent properties. Examples include surface plasmon resonance[32-33] in gold (Au) and silver (Ag) nanoparticles, excitonic emission in quantum dots[34], photoluminescence[35] (PL) in Au and Cu clusters, size-dependent PL with high quantum yield in carbon dots[31] and superparamagnetic iron oxide nanoparticles[36]. The bottom up synthesis methods of these 0D particles allowed a homogenous, well ordered product synthesis having less defects. Most of the synthesis processes involve colloidal synthesis[37], hydrothermal or solvothermal method,[38] wet-chemical[39] approach and metal reduction processes[40]. Examples include reduction of metallic salts in presence of stabilizers to form metal nanoparticles or nanoclusters,[40] colloidal synthesis involving injection of metal salts and stabilizers or organometallic compounds at high temperature for the synthesis of quantum dots[41] and carbonization of organic molecules using hydrothermal, microwave-assisted and template methods for the synthesis of carbon dots[31]. Synthesis of these 0D particles through chemical methods results in precise control over their size and composition where their further growth or aggregation is prevented by the surface-attached stabilizing ligands.

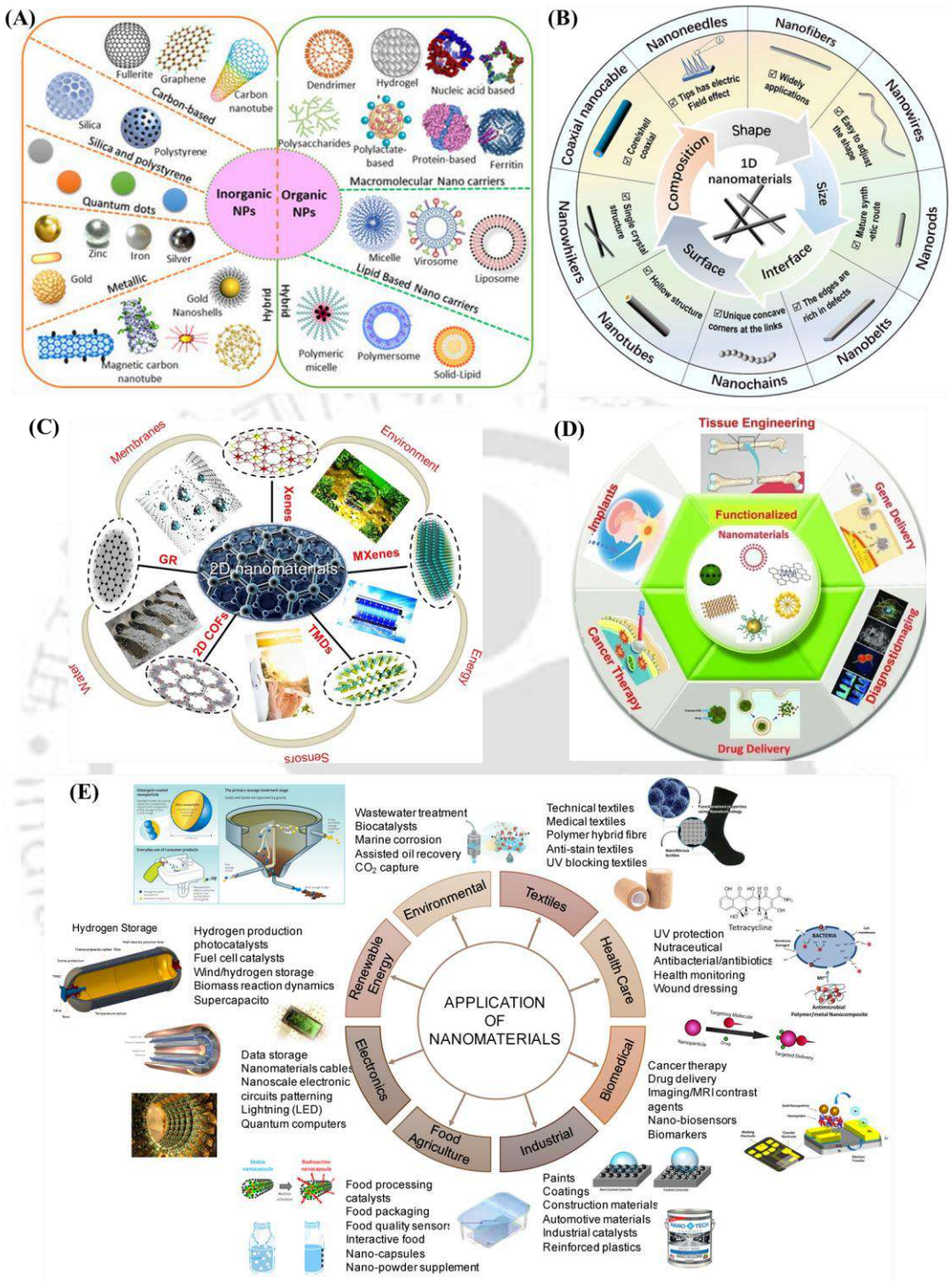

Figure 1. Illustration depicting different types of **(A)** 0D organic and inorganic nanoparticles (Image source: *Pharmaceutics* **2021**, *13*, 1829), **(B)** 1D nanomaterials (Image reprinted with permission from reference 45) and **(C)** 2D nanomaterials (Image reprinted with permission from reference 81). **(D)** and **(E)** Illustrations showing the various applications of these nanomaterials in various fields (Image in Figure 1D is reprinted from 14, Image source: *Materials* **2022**, *15*,

3251. Image in Figure 1E is reprinted from reference 21, Image source: *Nanomaterials* **2021**, *11*, 3324.).

Synthesis through chemical reactions has also enabled the development of nanoparticles based on polymers, organic molecules, metal complexes, metal-organic frameworks (MOFs), and covalent organic frameworks (COFs).[42-44] The organic nanoparticles[42] rely on molecular self-organization through supramolecular and covalent interactions whereas COF and MOF based nanoparticles are formed based on principles of reticular chemistry[44]. Their size, shape and also the composition and functionality can be tuned to atomic precision for desired applications such as drug loading and delivery, sensing, catalysis and other biomedical uses.

1.1.2 One-dimensional nanostructures

1D nanostructures are characterized by having two of their dimensions restricted to nanoscale range and examples include nanowires, nanoribbons, nanoneedles, nanorods, nanotubes and nanofibers.[45-47] Their synthesis procedures may involve the growth of molecules or nanoparticles into 1D structures via self-assembly and folding of flexible 2D nanofilms into 1D nanostructures.[46,48] Due to their unique electrical, optical and thermal properties they have gained significant recognition in the field of nanoelectronics[49-50], devices[49], solar cells[51] and biomedical applications[52]. The self-assembly of inorganic nanoparticles into 1D nanostructures involves further interaction with other nanoparticles or different moieties through surface stabilizing ligands. The forces for their interaction may be van der Waals (vdW), electrostatic and magnetic interactions depending on the type of nanoparticle.[53-55] Assembly into 1D nanostructures can be categorized into seed mediated growth where the nanoparticle itself serves as the seed from which the nanostructure grows. Another process uses template mediated synthesis processes where the precursor metal ions attach to the hard or soft template that direct its growth into 1D nanostructure.[49] Molecule based 1D nanostructures include conducting polymers where molecules are covalently bonded into a pi-conjugated long polymeric chain for example polyaniline (PANI) and polyacetylene (PA).[56] Another example includes self-assembly of peptides through non-covalent and covalent bonds to form nanofibers and nanoribbons that are used for drug delivery or bioimaging.[57-58] The spontaneous folding of 2D nanofilms can also lead to the formation of 1D nanostructure where new properties may arise along with the retention of 2D film's properties.[48]

1.1.3 Two-dimensional nanostructures

Similar to 1D nanostructures, many nanoparticles or nanocrystals can be assembled into a crystalline higher dimension nanostructure that can lead to enhancement of the existing properties of the 0D particles or demonstrate new properties after assembly.[53-54] Most of the approaches for the 2D assembly of nanoparticles are template based[54,60] but considerable studies have also been performed for their assembly through metal ion mediated complexation reactions. For example, zinc mediated complexation of Cu and Au clusters resulted in 2D crystalline nanosheets. The resulted assemblies had enhanced PL properties and were able to sense and store H_2, O_2 and CO_2,[63-65] enantiomerically separate amino acids[66] and delayed fluorescence properties[61-62]. For molecule-based 2D nanosheets, their synthesis involves self-assembly of the molecules through supramolecular interactions.[53-55] Their assembly can lead to formation of 2D crystalline functional materials with customized properties. Molecular 2D materials involves nanofilms based on organic molecules, COFs and MOFs having applications in catalysis, optoelectronics and sensing.[67-70] Again, many nanocrystals were assembled into hierarchical structures using metal chalcogenide complex ligands where strong coupling was achieved using these inorganic based surface ligands.[71] Also, many assemblies of nanocrystals were formed where they were organized into closed packed solids, ternary nanocrystal superlattices and quasicrystalline structures.[72-73] Another hierarchical arrangement of these nanoparticles or nanoclusters includes the formation of 2D moiré or quasiperiodic superlattices.[74-75] Here nanoclusters or complex based nanoparticles can result in the formation of moiré superlattices through their chemical bonding with metal ions or small molecules.

1.1.4 Involvement of supramolecular interactions for higher dimensional nanostructure assembly

The interactions that are involved for the hierarchical assembly of molecules, complexes or nanoparticles into 1D or 2D nanostructures are based on covalent and supramolecular interactions. Though covalent bonds were important for the formation of the higher dimensional structure, supramolecular interactions resulted in enhancing the properties, functionality and structural rigidity of the system. For example, in MOFs and COFs, where the functionality is enhanced by taking advantage of non-covalent host guest interactions[76], hydrophobic and hydrogen bonding (H-bonding) take part in the assembly of nanoparticles/peptides/organic

molecules into higher dimensional nanostructures[42,46,54,70] and sensing of molecules or ions through supramolecular interactions with the nanomaterials[77-78].

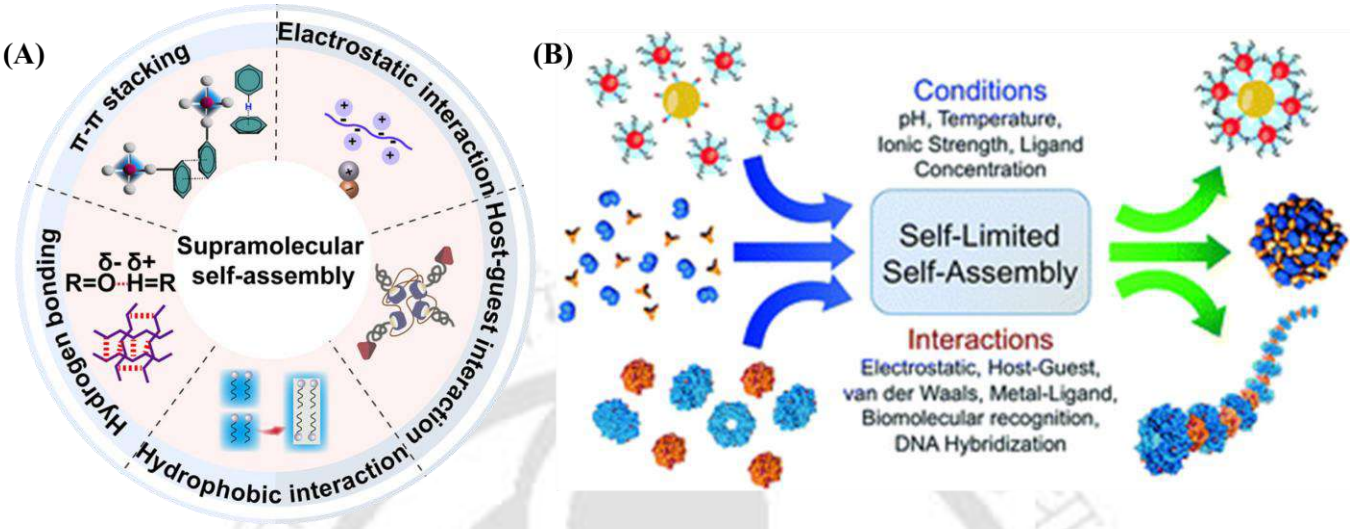

Figure 2. Different types of supramolecular interactions that are involved in nanoparticle and molecular assembly into higher dimensional structures (Image in Figure 2A is reprinted from reference 55, Image source: *iScience* **2023,** *26* (3), 106279. Image in Figure 2B is reprinted with permission from references 79).

Supramolecular interactions involve non-covalent bonds such as hydrogen bond (H-bond), π-π or anion/cation- π interaction, dipole-dipole or ion-dipole interaction, hydrophobic and electrostatic interactions.[80] As mentioned earlier, supramolecular chemistry can be exploited to design 1D, 2D and 3D crystals with the desired building block. These interactions enable the nanostructures to interact with molecules or ions that result in various applications, such as sensing, drug delivery, and surface functionalization. These non-covalent bonds facilitate self-interaction through stacking, pi-pi and hydrogen bonding, leading to formation of functional materials having novel properties.

1.2 2-D nanomaterials and their stacking

2D nanomaterials are more favorable over 0D and 1D materials due to their large surface area, flexibility, high mechanical strength and are easy to handle.[81] They are easier to assemble from molecules and nanoparticles as compared to 1D materials and the large surface area provides a greater number of active sites for sensing, catalysis and drug loading. Additionally, it was observed that stacking 2D materials with same or different nanosheet to form homo or hetero bi-

or multi-layers can result in new materials having additional properties.[82-83] Examples include multilayered materials involved for displaying giant magnetoresistance phenomenon, multilayered graphene or h-BN, metallic films or multilayered black phosphorus for the fabrication of robust, functional electronic devices.[84-91] Another method of stacking is through lattice misalignment where translational or rotational stacking of one layer with respect another takes place.[82,92-94] Both of these types of stacking may give rise lattice mismatch and thus produce moiré patterns through interference. As the current thesis work focuses on the chemical synthesis of moiré superlattices through twisted stacking of the 2D nanolattices of small organic molecules, a brief introduction on the 2D materials and their stacking is presented in the following section.

1.2.1 2D nanosheets based on molecular and vdW materials

2D nanomaterials based on organic compounds would include organic frameworks, polymers based 2D materials and 2D crystals where the constituent unit is the molecule.[68-70] The interaction involved in their assembly are covalent and non-covalent bonds (such as H-bonding, hydrophobic and electrostatic interactions). 2D vdW materials consists of atomically thin 2D films, which have covalently bonded network of atoms throughout the XY plane whereas vdW interactions hold the layers together along the perpendicular direction. Examples include graphene, hexagonal boron nitride (h-BN) and transition metal dichalcogenides (TMDs).[95-96] They have various potential applications in catalysis, electronics and sensing.

1.2.2 Twisted stacking of 2D nanosheets and their properties

Twisted layering of 2D materials has introduced twistronics as an important category in the field of quantum electronics.[97-99] Since then many unconventional properties[100-103] arising due to twisted stacking of these 2D systems were studied. Some of the examples include vdW materials such as twisted bilayer[104] and multilayered graphene[105], h-BN[106], TMDs[107], and perovskite oxide membranes[108]. The weak vdW forces hold the layers together and when twisted at an angle results in moiré patterns having higher periodicity. Conventionally, moiré superlattices of these vdW materials are fabricated through physical methods with careful stacking of a mechanically exfoliated monolayer over another at a desired angle.[82,93]

Twisted layering of a graphene monolayer sheet upon another at an angle of 1.1º results in strong interlayer coupling and correlation between the electrons. This leads to its transition from correlated insulator to superconductor having Tc (transition temperature) = 1.7 K upon doping with electrostatic charges.[100] Again, moiré excitons having much higher lifetime than excitons in monolayer was observed in $MoSe_2$–WSe_2 layered heterostructure.[101] Other examples include Mott-like insulator states due to localized electrons in the moiré superlattice[102] and ferromagnetism[103] resulting from anomalous Hall effect in tBLG.

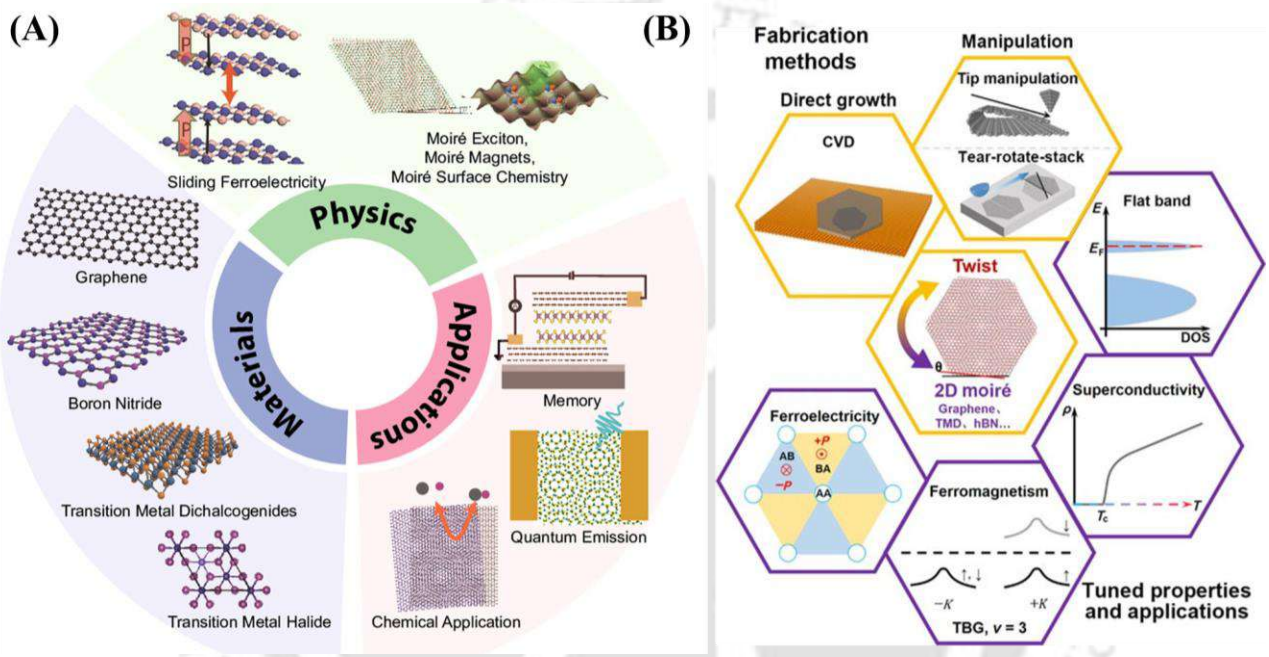

Figure 3. Illustrations depicting the properties and fabrication methods of moiré superlattices formed after translational and rotational stacking of 2D materials (Images in Figure 3A and 3B are reprinted with permission from references 82 and 93 respectively).

1.2.3 Chemical approach to moiré synthesis

As mentioned in the previous section, conventional synthesis procedures of moiré superlattices require extra care and time for twisted stacking after exfoliation. This restricts large-scale production of 2D moiré superlattices. Again, the synthesis for molecule-based moiré superlattices could be difficult using these physical approaches. Therefore, new methods are required for their synthesis. One possibility would be to rely on the bottom-up synthesis approaches where using the principles of chemistry one could synthesize the desired moiré

superlattices. There are a few examples where twisted stacking of 2D materials were achieved by chemical methods or in liquid medium, which are mentioned in the following sentences. Copper nanoclusters were at first organized into 2D nanosheets through complexation with Zn^{2+} ion that were further stacked at 30˚ by controlling the Zn^{2+} ion concentration to produce quasiperiodic 2D materials in the liquid medium.[74] Again, it was possible to organize these 2D nanosheets into multilayered moiré superlattices through chemical reaction with triphenyl phosphine.[110] Another example includes the chemical synthesis of spiral moiré nanosheets of bismuth oxychloride having superior photocatalytic activity.[111] Mn^{2+}-cysteine complex nanoparticles were assembled into 2D multilayered moiré superlattices through reaction of Zn^{2+} ions in liquid medium.[75]

Organization through chemical methods may result in tunable properties that would depend on the constituent particles and their chemical interactions. Chemical interactions within the moiré superlattice may provide extra stability and additional properties as observed for moiré superlattices of Zn complexed Cu nanoclusters, Mn^{2+}-cysteine complex nanoparticles and spiral moiré nanosheets of bismuth oxychloride.

1.3 Bridging the gap between molecular electronics and 2D material-based electronics

All the examples mentioned in the previous section include formation of moiré superlattices of vdW materials, nanocluster, nanoparticles and inorganic materials but there have rarely been any studies for the synthesis of 2D organic molecular crystals through chemical methods. The work reported in this thesis has tried to fill this void by chemically synthesizing and exploring the properties of molecular moiré superlattices. The crystalline molecular 2D nanosheets contains the molecule as the repetitive unit where it self assembles in an ordered manner through non-covalent such as hydrophobic, H-bonding and ionic interactions to form crystalline 2D nanosheet. Further twisted stacking of these 2D nanolattices in the liquid medium result in the formation of moiré superlattices where the surface interaction of the nanosheets at the interface determines its properties and twist angle.

2D materials are utilized for device fabrication due to their better electrical conductivity, mechanical strength and high surface area.[81-82] On the other hand, molecular assemblies are favored for fabrication of quantum molecular devices due to their smaller dimensions and tunable properties.[6-7] But their integration into circuits leading to fabrication of a working device is difficult. Thus, a new approach is required for their integration into devices. One possible way

could be the twisted layering of a 2D nanosheets of self-assembled molecules leading to the formation of moiré superlattices. The interfacial interactions would be different from the interactions within the lattice that could lead to extraordinary electrical and magnetic properties forming the basis of a functional device. Multilayered molecular moiré superlattices can provide tunable customized properties based on molecular interactions, large area for molecule-electrode contact and information processing based on the interfacial interactions.

1.4 From molecular machines to supramolecular devices

Soon after the proposal of atomic and molecular manipulation using molecular nanotechnology[112] to create nano-dimensional devices, miniaturization of machinery was achieved through the development of molecular machines[3-5]. The synthesis of the interlocked catenanes[113] and rotaxanes[114] paved the way for the development of probable molecular switches and devices.

1.4.1 The path towards world's smallest molecular machines

The first interlocked transition metal catenanes ([2] catenane) where two molecular rings were interlocked using a transition metal template showed the path for molecule manipulation.[113] The rings were free to move as they were interlocked by a mechanical bond. Later on [2] rotaxane was synthesized, which was formed by entangling a molecular ring to a molecular axle.[114] The rotaxane was termed as a 'molecular shuttle' in which a 'tetracationic' bead was able to move along a polyether axle from one hydroquinol ring to another and the movement at the end of the axle was terminated by bulky silyl group where the back and forth movement of the cationic bead was reported to be around 2000 times per second.[115] The synthesis procedure for the interlocked catenane and rotaxane, based on chemical bonding and ionic interactions, provided a clear template for the development of future molecular machines and eased the way for the production of probable molecular switches and devices.[116] This development opened up an entirely new realm for employing a bottom-up approach in the formation of nanoparticles, enabling the application of this concept for molecular-scale information.

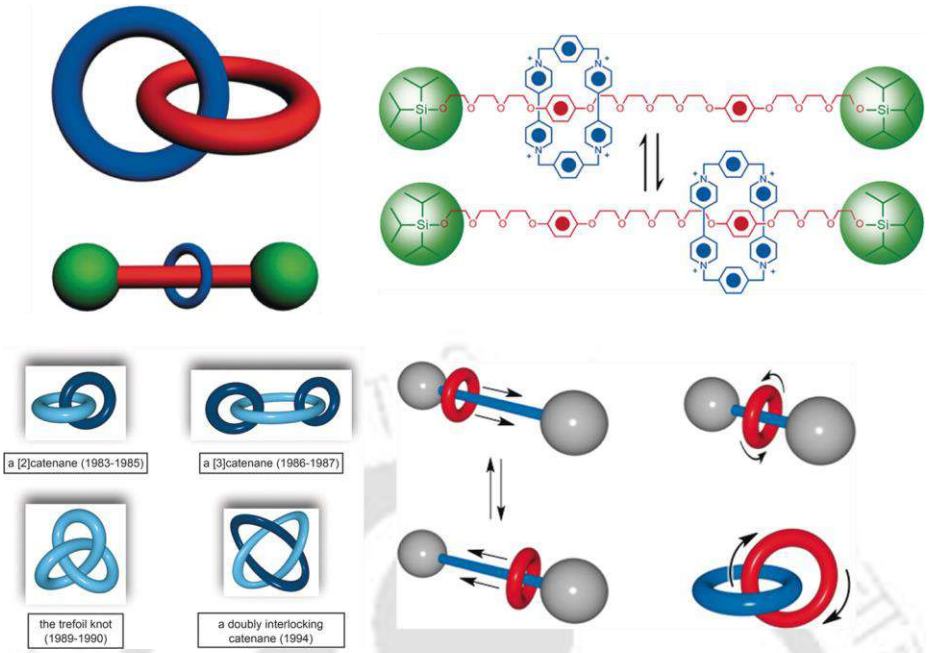

-

Figure 4. Illustration showing the motion in rotaxane and catenane. Images are reprinted with permission from references 116 and 121.

1.4.2 Molecular manipulations for the synthesis of molecular switches, motor and machines

For both catenane and rotaxane, chemical interaction between the constituents (interlocked rings by metal template in catenane and a ring and an axle in rotaxane) allowed free movement within the system. Further progress in the field of molecular machines was observed when the interactions were manipulated using external stimuli. For example, a molecular motor was designed using the molecule (3*R*,3′*R*)-(*P*,*P*)-*trans*-1,1′,2,2′,3,3′,4,4′-octahydro-3,3′-dimethyl-4,4′-biphenanthrylidene where the stereochemistry of the molecule plays an important role in its movement.[117] A 360º rotation was observed in one direction when subjected to alternative UV light irradiation and temperature change, thus acting as a molecular motor. Furthermore, a nanocar[118] was designed using molecules where molecular motors played the role of wheels.

Another example includes the swinging catenanes[119] where the motion of the interlocked rings was controlled electrochemically. Two rings – one containing two bidentate center and another containing a bidentate and a tridentate center- were interlocked using Cu ion. A reversible swinging movement was observed between the rings as electrochemical oxidation and reduction

of the Cu center occurred depending on the ion's coordination sphere. Next a molecular switch[120] was implemented consisting of a donor–acceptor [2] rotaxane, where the movement of the ring along the axle was induced by protonation of the benzidine recognition unit located on the axle. The switching can be reversed with addition of base.

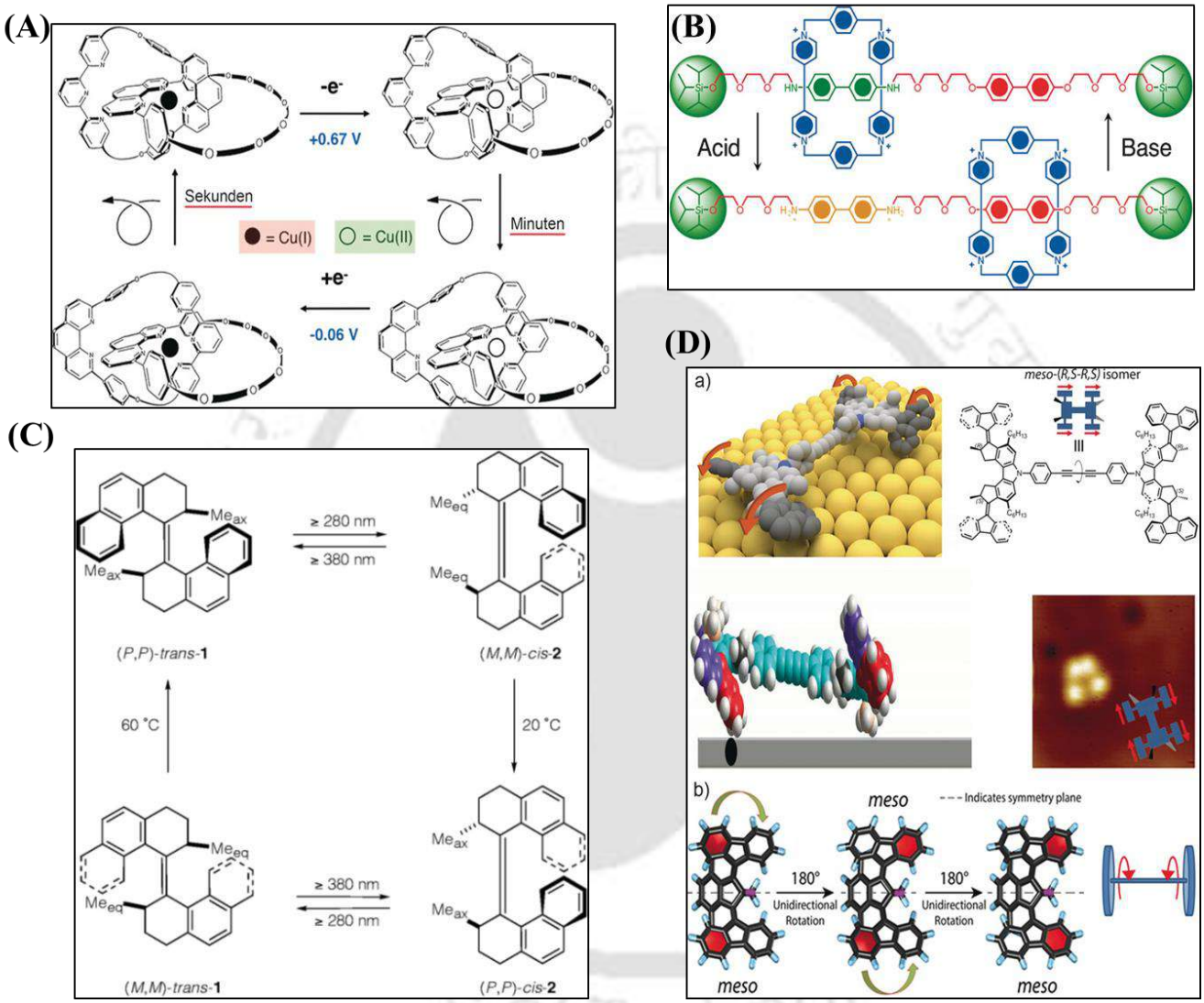

Figure 5. (A) Electrochemically driven swinging motion in catenanes (Image reprinted with permission from reference 121). **(B)** A switchable donor-acceptor [2]rotaxane where the motion could controlled by protonation and deprotonation of the axle (Image reprinted with permission from reference 116). **(C)** Light driven unidirectional rotational motion in molecule-based motor (Image reprinted with permission from reference 117). **(D)** Illustrations, STM image and

structure depicting a molecular car constructed using rotary molecular motors (Image reprinted with permission from reference 118).

1.4.3 Single molecular electronics to supramolecular electronics

With the advancement in technology, significant increase in demand has occurred for miniaturization of electronics and thus a rise in the studies for molecular electronics was noticed. The study of the charge transport at molecular junctions using break junction method, where the molecule is anchored between a metallic electrode (drain) and conductive atomic force microscopy (c-AFM) or scanning tunneling microscopy (STM) probe (source), is termed as molecular electronics or more specifically single molecular electronics.[6-7,12,122] Although many molecular devices such as molecular rectifiers[8], single molecule transistors[10-11], and single-molecule switches[9] have been devised, the focus is now shifting towards assembly of molecules or supramolecular electronic[12] devices for fabrication of practical electronic devices. Molecules or ensemble of molecules are studied for their development as electronics as they not only can lead to miniaturization of electronics but may also be developed into customized functional devices by exploiting the chemical properties and interactions at the molecular level. Though due to its low dimension and synthesis procedures, molecule-based electronics may provide low-cost and efficient solution to development of electronics having faster performance, but its fabrication into practical electronic devices is still being conceptualized due to difficulty in incorporation of the molecules between electrodes. To move towards integrating practical electronic circuits, molecular ensemble like self-assembled monolayer[123] (SAM) may prove advantageous over single molecule due to large area electrode contact. Again, the manipulation of the non-covalent bonds at supramolecular level could provide an opportunity for its fabrication as practical electronic devices, for example conductivity can be tuned according to polarity or interactions within the assembly.

1.5 From supramolecular electronics to quantum molecular devices

As previously discussed, due to their high scalability and ease of assembly into controlled arrays, many molecules[6,12] and supramolecular[7,122,124] assemblies have been employed and evaluated for applications in molecule-based electronics. Here, the charge transport occurs at a molecule level through a single molecule or assembly of molecule following the concepts of quantum tunneling.

These molecule-based devices have the potential to be used as quantum bits (or qubits) and quantum gates as manufacturers look for alternatives of silicon-based semiconductors.[22-25] Molecule-based devices may have the potential to revolutionize quantum information processing. But their fabrication into functional device still remains a challenge. Thus, there is a need for finding the best bottom-up synthesis procedure that can be useful for fabricating quantum molecular devices. Thus, the present work in this thesis tries to address this issue by introducing molecular moiré superlattices and proposing its use in fabrication of quantum molecular devices.

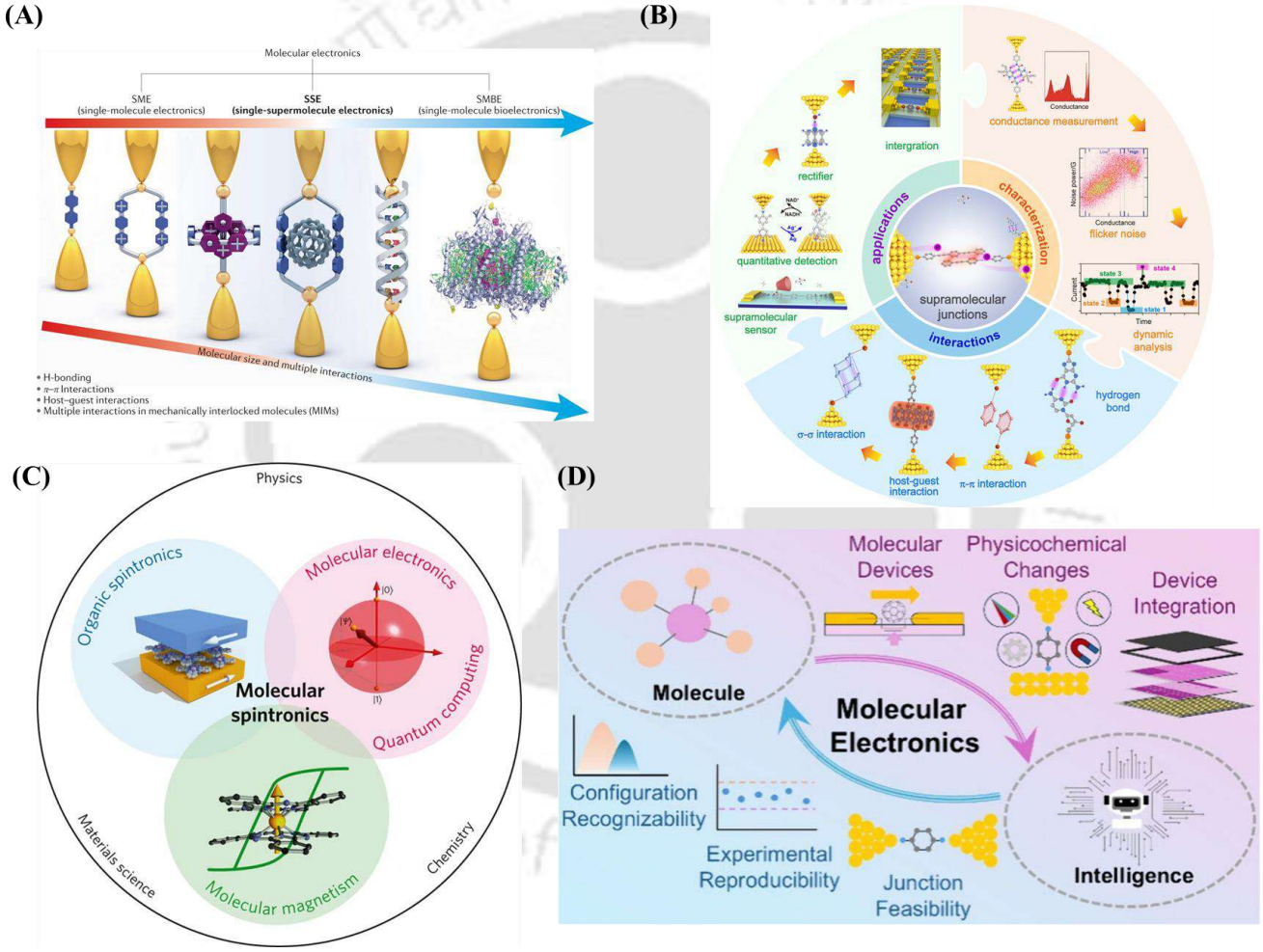

Figure 6. Illustration depicting the use of single molecules and supramolecular assemblies for electronics, spintronics and molecular memory and processing devices. Images in Figure 4A, 4B, 4C and 4D are reprinted with permission from references 122, 124, 23 and 25 respectively.

1.6 Objectives and Hypothesis

In today's rapidly evolving technological world, molecule-based electronics have attracted considerable scientific interest, particularly when quantum materials have become essential for the advancements in quantum information, artificial intelligence, and quantum phenomena. Single molecules, supramolecular and higher-dimensional molecular assemblies present promising avenues for significant advancements in spintronics, quantum sensing, and molecular switches. Integrating molecules into electronic circuits for functional molecular devices has been a longstanding goal. This holds importance as it might be able to address the rising demand for miniaturization electronic circuits as traditional semiconductor technology approaches its physical limitations. However, the challenge of positioning a single molecule between electrodes—and subsequently scaling this approach to millions of molecules for integrated circuit construction—remains a difficult task. Consequently, novel multifunctional molecular materials based on principles of chemistry and molecular engineering are needed to be designed which can replicate the functions of traditional transistors, diodes, and logic gates, thereby demonstrating potential applications in optoelectronics, quantum information, and advanced electronics. Further, the cooperativity arising from interactions within assemblies e.g., hydrogen bonds, enhances charge transport efficiency where the interactions and properties of these assemblies can be harnessed and manipulated at molecular level to convert the chemical information to electrical signals.

On the other hand, 2D moiré superlattices, which are formed by the lattice mismatch (either rotational or translational) of the layered crystalline 2D nanosheets, have shown unconventional properties that are not observed in their 2D counterparts. The twisted stacking of 2D materials such as of graphene, h-BN, metal dichalcogenides and vdW 2D materials have generated properties such as superconductivity, moiré excitons, Mott insulators. These materials have found applications in the field of electronics, quantum technologies, optoelectronics, sensing and hydrogen production. However molecular moiré superlattices have not yet been chemically synthesized or studied for applications in electronics, quantum information processing, sensing, or energy conversion. Molecular interactions such as non-covalent interactions can be utilized for their chemical synthesis in the liquid medium and can have application potential in the above-mentioned fields, especially considering that both 2D moiré superlattices and molecular

assemblies have already demonstrated great promise in these areas. The 2D nanocrystals can be generated in the liquid medium through supramolecular interactions and altering the environmental factors may lead to the twisted stacking of these 2D nanocrystals where the new interaction at twisted interface could lead to novel properties. Additionally, these properties could be manipulated using external stimuli by taking advantage of the molecular interactions.

Thus, this thesis aims to develop chemical synthesis methods for molecular moiré superlattices and utilize chemical reactions to control the twist angles and height of the multilayered moiré superlattices. It also seeks to understand the mechanism behind the formation of the moiré superlattices and study the novel properties that arises due to the twisted interfacial interactions using the necessary characterization techniques. Finally, we intend to explore their application potential as quantum materials in the field of molecular electronics, spintronics and sensing.

1.7 Overview of the thesis

The current thesis focuses on the synthesis of molecular moiré superlattices from a simple molecule having application potential as quantum molecular devices. The moiré superlattices are formed from twisted stacking of 2D nanolattices of self-assembled molecules. The interfacial chemical interactions resulted in properties not observed in the 2D nanosheet or in the single molecule. The thesis has also tried to address the issue of synthesis of precisely controlled twist angle in molecular moiré superlattices, which is difficult to achieve in liquid media through chemical reactions. The thesis consists 6 chapters:

Chapter 1: As discussed above, this chapter includes a brief literature review on molecular organization to form hierarchical structures of 0, 1 and 2D crystalline assemblies and their properties based on their molecular interactions. It also includes a brief discussion of how molecules and their assemblies were proposed to be used as molecular machines and eventually became favorites in molecular electronics, spintronics and quantum molecular devices.

Chapter 2: The initial work for this dissertation focuses on the assembly of metal complexes to form 0-dimensional nanoparticles that display size-dependent luminescent and magnetic properties. These types of nanoparticles can also be further assembled into 2D moiré superlattices. This work inspired us to synthesize moiré superlattices that is assembled from simple organic molecules.

Chapter 3: The chapter introduces the concept of moiré superlattice formation from small organic molecules. In this chapter, the chemical synthesis of moiré superlattices of L or D tryptophan (trp) molecules are described that were formed by the twisted stacking of the self-assembled crystalline 2D nanosheets in an aqueous medium that showcased new physical and chemical properties through interactions at the crystal interfaces.

Chapter 4: This chapter proposes the potential use of molecular moiré superlattices for building complex circuits, information storage, or sensing based on the principles of quantum mechanics at the molecular length scales. Further electrical properties of multilayered moiré superlattices of p-phenylenediamine were studied where it was dependent on the twist angle between two consecutive layers and pH of the medium.

Chapter 5: This chapter explores the concept of spin-polarized conductance through Zn-complexed moiré superlattices of D/L-trp and thus acted as spin filters. The twist angles and moiré periodicities were controlled by addition of Zn^{2+} ions to moiré superlattices of D/L-trp.

Chapter 6: This chapter includes the summarization and the future prospects for the work presented in this thesis.

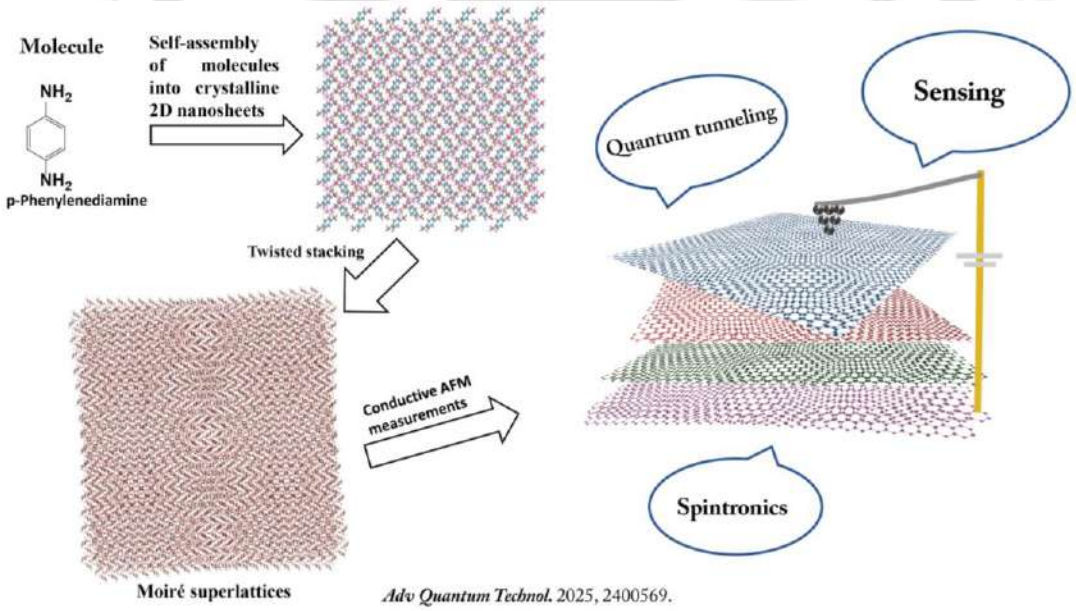

Figure 7. Illustration showing the formation of molecular moiré superlattices after twisted stacking of the 2D crystalline nanosheets and its possible applications.

References

1. Schliwa, M.; Woehlke, G., Molecular motors. *Nature* **2003,** *422* (6933), 759-765.
2. Piccolino, M., Biological machines: from mills to molecules. *Nat. Rev. Mol. Cell Biol.* **2000,** *1* (2), 149-152.
3. Kinbara, K.; Aida, T., Toward Intelligent Molecular Machines: Directed Motions of Biological and Artificial Molecules and Assemblies. *Chem. Rev.* **2005,** *105* (4), 1377-1400.
4. Erbas-Cakmak, S.; Leigh, D. A.; McTernan, C. T.; Nussbaumer, A. L., Artificial Molecular Machines. *Chem. Rev.* **2015,** *115* (18), 10081-10206.
5. Aprahamian, I., The Future of Molecular Machines. *ACS Cent. Sci.* **2020,** *6* (3), 347-358.
6. Li, T.; Bandari, V. K.; Schmidt, O. G., Molecular Electronics: Creating and Bridging Molecular Junctions and Promoting Its Commercialization. *Adv. Mater.* **2023,** *35* (22), 2209088.
7. Moulin, E.; Cid, J.-J.; Giuseppone, N., Advances in Supramolecular Electronics – From Randomly Self-assembled Nanostructures to Addressable Self-Organized Interconnects. *Adv. Mater.* **2013,** *25* (3), 477-487.
8. Aviram, A.; Ratner, M. A., Molecular rectifiers. *Chem. Phys. Lett.* **1974,** *29* (2), 277-283.
9. Kiguchi, M.; Ohto, T.; Fujii, S.; Sugiyasu, K.; Nakajima, S.; Takeuchi, M.; Nakamura, H., Single Molecular Resistive Switch Obtained via Sliding Multiple Anchoring Points and Varying Effective Wire Length. *J. Am. Chem. Soc.* **2014,** *136* (20), 7327-7332.
10. Song, H.; Kim, Y.; Jang, Y. H.; Jeong, H.; Reed, M. A.; Lee, T., Observation of molecular orbital gating. *Nature* **2009,** *462* (7276), 1039-1043.
11. Chen, S.; Chen, G.; Ratner, M. A. Designing Principles of Molecular Quantum Interference Effect Transistors. *J. Phys. Chem. Lett.* **2018**, *9*, 2843– 2847.
12. Yuan, M.; Qiu, Y.; Gao, H.; Feng, J.; Jiang, L.; Wu, Y., Molecular Electronics: From Nanostructure Assembly to Device Integration. *J. Am. Chem. Soc.* **2024,** *146* (12), 7885-7904.
13. Nisa, K.; Lone, I. A.; Arif, W.; Singh, P.; Rehmen, S. U.; Kumar, R., Applications of supramolecular assemblies in drug delivery and photodynamic therapy. *RSC Med. Chem.* **2023,** *14* (12), 2438-2458.
14. Díez-Pascual, A.M. Surface Engineering of Nanomaterials with Polymers, Biomolecules, and Small Ligands for Nanomedicine. *Materials* **2022**, *15*, 3251.

15. Zheng, H.; Ravaine, S. Bottom-Up Assembly and Applications of Photonic Materials. *Crystals* **2016**, *6*, 54.
16. Ma, J.; Gao, H.; Feng, J.; Zhang, S.-F.; Wang, L.; Zhao, D.; Wu, Y.; Jiang, L., Controlled Assembly of Conjugated Ladder Molecules with Different Bridging Structures toward Optoelectronic Application. *ACS Appl. Mater. Interfaces* **2021,** *13* (42), 50197-50205.
17. Whitesides, G. M.; Mathias, J. P.; Seto, C. T., Molecular Self-Assembly and Nanochemistry: a Chemical Strategy for the Synthesis of Nanostructures. *Science* **1991,** *254* (5036), 1312-1319.
18. Bai, C.; Wang, C., Molecular nanostructure and nanotechnology. *Philos Trans A Math Phys Eng Sci.* **2013,** *371* (2000), 20130263.
19. Pochan, D.; Scherman, O., Introduction: Molecular Self-Assembly. *Chem. Rev.* **2021,** *121* (22), 13699-13700.
20. Mekuye, B.; Abera, B., Nanomaterials: An overview of synthesis, classification, characterization, and applications. *Nano Select* **2023,** *4* (8), 486-501.
21. Nizam, N.U.M.; Hanafiah, M.M.; Woon, K.S. A Content Review of Life Cycle Assessment of Nanomaterials: Current Practices, Challenges, and Future Prospects. *Nanomaterials* **2021**, *11*, 3324.
22. Kosloff, R., Quantum Molecular Devices. *ACS Phys. Chem. Au* **2024,** *4* (3), 226-231.
23. Cornia, A.; Seneor, P., The molecular way. *Nat. Mater.* **2017,** *16* (5), 505-506.
24. Fursina, A. A.; Sinitskii, A., Toward Molecular Spin Qubit Devices: Integration of Magnetic Molecules into Solid-State Devices. *ACS Appl. Electron. Mater.* **2023,** *5* (7), 3531-3545.
25. Yan, C.; Fang, C.; Gan, J.; Wang, J.; Zhao, X.; Wang, X.; Li, J.; Zhang, Y.; Liu, H.; Li, X.; Bai, J.; Liu, J.; Hong, W., From Molecular Electronics to Molecular Intelligence. *ACS Nano* **2024,** *18* (42), 28531-28556.
26. Park, H.; Shin, D. J.; Yu, J., Categorization of Quantum Dots, Clusters, Nanoclusters, and Nanodots. *J. Chem. Educ.* **2021,** *98* (3), 703-709.
27. Jin, R.; Zeng, C.; Zhou, M.; Chen, Y., Atomically Precise Colloidal Metal Nanoclusters and Nanoparticles: Fundamentals and Opportunities. *Chem. Rev.* **2016,** *116* (18), 10346-10413.
28. Shahalaei, M.; Azad, A. K.; Sulaiman, W. M. A. W.; Derakhshani, A.; Mofakham, E. B.; Mallandrich, M.; Kumarasamy, V.; Subramaniyan, V., A review of metallic procles: present issues and prospects focused on the preparation methods, characterization techniques, and their theranostic applications. *Front. Chem.* **2024,** *12*, 2024.

29. Du, Y.; Sheng, H.; Astruc, D.; Zhu, M., Atomically Precise Noble Metal Nanoclusters as Efficient Catalysts: A Bridge between Structure and Properties. *Chem. Rev.* **2020,** *120* (2), 526-622.
30. García de Arquer, F. P.; Talapin, D. V.; Klimov, V. I.; Arakawa, Y.; Bayer, M.; Sargent, E. H., Semiconductor quantum dots: Technological progress and future challenges. *Science 373* (6555), eaaz8541.
31. Alafeef, M.; Srivastava, I.; Aditya, T.; Pan, D., Carbon Dots: From Synthesis to Unraveling the Fluorescence Mechanism. *Small* **2024,** *20* (4), 2303937.
32. Ringe, E.; Sharma, B.; Henry, A.-I.; Marks, L. D.; Van Duyne, R. P., Single nanoparticle plasmonics. *Phys. Chem. Chem. Phys.* **2013,** *15* (12), 4110-4129.
33. Hang, Y.; Wang, A.; Wu, N., Plasmonic silver and gold nanoparticles: shape- and structure-modulated plasmonic functionality for point-of-caring sensing, bio-imaging and medical therapy. *Chem. Soc. Rev.***2024,** *53* (6), 2932-2971.
34. Deng, Y.; Lin, X.; Fang, W.; Di, D.; Wang, L.; Friend, R. H.; Peng, X.; Jin, Y., Deciphering exciton-generation processes in quantum-dot electroluminescence. *Nat. Commun.* **2020,** *11* (1), 2309.
35. Lin, H.; Song, X.; Chai, O. J. H.; Yao, Q.; Yang, H.; Xie, J., Photoluminescent Characterization of Metal Nanoclusters: Basic Parameters, Methods, and Applications. *Adv. Mater.***2024,** *36* (25), 2401002.
36. Samrot, A. V.; Sahithya, C. S.; Selvarani A, J.; Purayil, S. K.; Ponnaiah, P., A review on synthesis, characterization and potential biological applications of superparamagnetic iron oxide nanoparticles. *Curr. Res. Green Sustain. Chem.* **2021,** *4*, 100042.
37. Personick, M. L. History and Fundamentals of the Colloidal Synthesis of Shaped Metal Nanoparticles. In *One Hundred Years of Colloid Symposia: Looking Back and Looking Forward*; ACS Symposium Series: 2023; Vol. 1457, pp 247-283.
38. Li, J.; Wu, Q.; Wu, J., Synthesis of Nanoparticles via Solvothermal and Hydrothermal Methods. In *Handbook of Nanoparticles*, Aliofkhazraei, M., Ed. Springer International Publishing: Cham, 2015; pp 1-28.
39. Bokov, D.; Turki Jalil, A.; Chupradit, S.; Suksatan, W.; Javed Ansari, M.; Shewael, I. H.; Valiev, G. H.; Kianfar, E., Nanomaterial by Sol-Gel Method: Synthesis and Application. *Adv. Mater. Sci. Eng.* **2021,** *2021* (1), 5102014.

40. Szczyglewska, P.; Feliczak-Guzik, A.; Nowak, I. Nanotechnology–General Aspects: A Chemical Reduction Approach to the Synthesis of Nanoparticles. *Molecules* **2023**, *28*, 4932.
41. Pu, Y.; Cai, F.; Wang, D.; Wang, J.-X.; Chen, J.-F., Colloidal Synthesis of Semiconductor Quantum Dots toward Large-Scale Production: A Review. *Ind. Eng. Chem. Res.* **2018,** *57* (6), 1790-1802.
42. Romero, G.; Moya, S. E., Chapter 4 - Synthesis of Organic Nanoparticles. In *Frontiers of Nanoscience*, de la Fuente, J. M.; Grazu, V., Eds. Elsevier: 2012; Vol. 4, pp 115-141.
43. Eker, F.; Duman, H.; Akdaşçi, E.; Bolat, E.; Sarıtaş, S.; Karav, S.; Witkowska, A.M. A Comprehensive Review of Nanoparticles: From Classification to Application and Toxicity. *Molecules* **2024**, *29*, 3482.
44. Wang, S.; McGuirk, C. M.; d'Aquino, A.; Mason, J. A.; Mirkin, C. A., Metal–Organic Framework Nanoparticles. *Adv. Mater.***2018,** *30* (37), 1800202.
45. Zeng, Q.; Deng, N.; Wang, S.; Luo, S.; Wang, G.; Gao, H.; Li, Y.; Wang, H.; Cheng, B.; Kang, W., A Review of One-Dimensional Nanomaterials as Electrode Materials for Oxygen Reduction Reaction Electrocatalysis. *ChemElectroChem* **2022,** *9* (21), e202200946.
46. Palmer, L. C.; Stupp, S. I., Molecular Self-Assembly into One-Dimensional Nanostructures. *Acc. Chem. Res.***2008,** *41* (12), 1674-1684.
47. Garnett, E.; Mai, L.; Yang, P., Introduction: 1D Nanomaterials/Nanowires. *Chem. Rev*. **2019,** *119* (15), 8955-8957.
48. Lai, Z.; Chen, Y.; Tan, C.; Zhang, X.; Zhang, H., Self-Assembly of Two-Dimensional Nanosheets into One-Dimensional Nanostructures. *Chem* **2016,** *1* (1), 59-77.
49. Samykano, M., Progress in one-dimensional nanostructures. *Mater. Charact.* **2021,** *179*, 111373.
50. Hochbaum, A. I.; Yang, P., Semiconductor Nanowires for Energy Conversion. *Chem. Rev.* **2010,** *110* (1), 527-546.
51. Ye, M.; Xin, X.; Lin, C.; Lin, Z., High Efficiency Dye-Sensitized Solar Cells Based on Hierarchically Structured Nanotubes. *Nano Lett.* **2011,** *11* (8), 3214-3220.
52. Song, S.; Kim, K. Y.; Lee, S. H.; Kim, K. K.; Lee, K.; Lee, W.; Jeon, H.; Ko, S. H., Recent Advances in 1D Nanomaterial-Based Bioelectronics for Healthcare Applications. *Adv NanoBiomed Res* **2022,** *2* (3), 2100111.
53. Akram, B.; Wang, X., Self-Assembly of Ultrathin Nanocrystals to Multidimensional Superstructures. *Langmuir* **2019,** *35* (32), 10246-10266.

54. Srivastava, S.; Kotov, N. A., Nanoparticle assembly for 1D and 2D ordered structures. *Soft Matter* **2009,** *5* (6), 1146-1156.
55. Liu, Y.; Wu, Y.; Luo, Z.; Li, M., Designing supramolecular self-assembly nanomaterials as stimuli-responsive drug delivery platforms for cancer therapy. *iScience* **2023,** *26* (3), 106279.
56. Kim, F. S.; Ren, G.; Jenekhe, S. A., One-Dimensional Nanostructures of π-Conjugated Molecular Systems: Assembly, Properties, and Applications from Photovoltaics, Sensors, and Nanophotonics to Nanoelectronics. *Chem. Mater.***2011,** *23* (3), 682-732.
57. Li, T.; Lu, X.-M.; Zhang, M.-R.; Hu, K.; Li, Z., Peptide-based nanomaterials: Self-assembly, properties and applications. *Bioact. Mater.* **2022,** *11*, 268-282.
58. Gao, Y.; Wang, L.; Zhang, X.; Zhou, Z.; Shen, X.; Hu, H.; Sun, R.; Tang, J. Advances in Self-Assembled Peptides as Drug Carriers. *Pharmaceutics* **2023**, *15*, 482.
59. Fang, Z.; Tang, S.; Wang, Z.; An, M.; Yu, G., General Synthesis of Large Inorganic Nanosheets via 2D Confined Assembly of Nanoparticles. *ACS Cent. Sci.* **2022,** *8* (5), 627-635.
60. Gangwar, N.; Gangwar, C.; Sarkar, J., A review on template-assisted approaches & self assembly of nanomaterials at liquid/liquid interface. *Heliyon* **2024,** *10* (17), e36810.
61. Das, P.; Chattopadhyay, A., Delayed Dual Emission of Two-Dimensional Copper Nanocluster Assembly. *J. Phys. Chem. C* **2022,** *126* (2), 997-1005.
62. Basu, S.; Chattopadhyay, A., Room-Temperature Delayed Fluorescence of Gold Nanoclusters in Zinc-Mediated Two-Dimensional Crystalline Assembly. *Langmuir* **2019,** *35* (15), 5264-5270.
63. Basu, S.; Paul, A.; Chattopadhyay, A., Zinc mediated crystalline assembly of gold nanoclusters for expedient hydrogen storage and sensing. *J. Mater. Chem. A* **2016,** *4* (4), 1218-1223.
64. Paul, M.; Basu, S.; Chattopadhyay, A., Complexation Reaction-Based Two-Dimensional Luminescent Crystalline Assembly of Atomic Clusters for Recyclable Storage of Oxygen. *Langmuir* **2020,** *36* (3), 754-759.
65. Basu, S.; Bhandari, S.; Pan, U. N.; Paul, A.; Chattopadhyay, A., Crystalline nanoscale assembly of gold clusters for reversible storage and sensing of CO2via modulation of photoluminescence intermittency. *J. Mater. Chem. C* **2018,** *6* (30), 8205-8211.

66. Basu, S.; Paul, A.; Chattopadhyay, A., Zinc-Coordinated Hierarchical Organization of Ligand-Stabilized Gold Nanoclusters for Chiral Recognition and Separation. *Chem. Eur. J.* **2017,** *23* (38), 9137-9143.
67. Zhang, J.; Qi, S.; Zhang, C.; Wang, W.; Ding, Q.; Zhang, H.; Dong, Z., Supramolecular 2D monolayered nanosheets constructed by using synergy of non-covalent interactions. *Chem. Commun.* **2021,** *57* (51), 6272-6275.
68. Ma, Y.; Wang, M.; Zhai, T., 2D Molecular Crystals for Electronic and Optoelectronic Devices: Status and Challenges. *Adv. Mater.***2025,** *37* (10), 2416160.
69. Han, W.; Huang, P.; Li, L.; Wang, F.; Luo, P.; Liu, K.; Zhou, X.; Li, H.; Zhang, X.; Cui, Y.; Zhai, T., Two-dimensional inorganic molecular crystals. *Nat. Commun.* **2019,** *10* (1), 4728.
70. Solomos, M. A.; Claire, F. J.; Kempa, T. J., 2D molecular crystal lattices: advances in their synthesis, characterization, and application. *J. Mater. Chem. A* **2019,** *7* (41), 23537-23562.
71. oropceanu, I.; Janke, E. M.; Portner, J.; Haubold, D.; Nguyen, T. D.; Das, A.; Tanner, C. P. N.; Utterback, J. K.; Teitelbaum, S. W.; Hudson, M. H.; Sarma, N. A.; Hinkle, A. M.; Tassone, C. J.; Eychmüller, A.; Limmer, D. T.; Olvera de la Cruz, M.; Ginsberg, N. S.; Talapin, D. V., Self-assembly of nanocrystals into strongly electronically coupled all-inorganic supercrystals. *Science* **2022,** *375* (6587), 1422-1426.
72. Dong, A.; Ye, X.; Chen, J.; Murray, C. B., Two-Dimensional Binary and Ternary Nanocrystal Superlattices: The Case of Monolayers and Bilayers. *Nano Lett.* **2011,** *11* (4), 1804-1809.
73. Boles, M. A.; Engel, M.; Talapin, D. V., Self-Assembly of Colloidal Nanocrystals: From Intricate Structures to Functional Materials. *Chem. Rev.* **2016,** *116* (18), 11220-11289.
74. Das, P.; Chattopadhyay, A., Enhanced Chemical Stability in the Twisted Dodecagonal Stacking of Two-Dimensional Copper Nanocluster Assemblies. *J. Phys. Chem. Lett.* **2022,** *13* (37), 8793-8800.
75. Hajra, A.; Chattopadhyay, A., Moiré Superlattices of Zn2+ Mediated 2D Assembly of Mn2+-Cysteine Complex Nanoparticles Alter Electron Spin Transitions in the X-Band. *Chem. Mater.***2024,** *36* (17), 8523-8533.
76. Ernst, M.; Gryn'ova, G., Engineering Host–Guest Interactions in Organic Framework Materials for Drug Delivery. *Helvetica Chimica Acta* **2023,** *106* (6), e202300013.
77. Samorì, P.; Biscarini, F., Nanomaterials properties tuned by their environment: integrating supramolecular concepts into sensing devices. *Chem. Soc. Rev.***2018,** *47* (13), 4675-4676.

78. Furlan de Oliveira, R.; Montes-García, V.; Ciesielski, A.; Samorì, P., Harnessing selectivity in chemical sensing via supramolecular interactions: from functionalization of nanomaterials to device applications. *Mater. Horiz.* **2021,** *8* (10), 2685-2708.
79. Piccinini, E.; Pallarola, D.; Battaglini, F.; Azzaroni, O., Self-limited self-assembly of nanoparticles into supraparticles: towards supramolecular colloidal materials by design. *Mol. Syst. Des. Eng.* **2016,** *1* (2), 155-162.
80. Lehn, J.-M., Supramolecular Chemistry—Scope and Perspectives Molecules, Supermolecules, and Molecular Devices (Nobel Lecture). *Angew. Chem. Int. Ed.* **1988,** *27* (1), 89-112.
81. Baig, N., Two-dimensional nanomaterials: A critical review of recent progress, properties, applications, and future directions. *Compos. - A: Appl. Sci. Manuf.* **2023,** *165*, 107362.
82. Fox, C.; Mao, Y.; Zhang, X.; Wang, Y.; Xiao, J., Stacking Order Engineering of Two-Dimensional Materials and Device Applications. *Chem. Rev.* **2024,** *124* (4), 1862-1898.
83. Guo, H.-W.; Hu, Z.; Liu, Z.-B.; Tian, J.-G., Stacking of 2D Materials. *Adv. Funct. Mater.* **2021,** *31* (4), 2007810.
84. Byrne, P. D.; Facchetti, A.; Marks, T. J., High-Performance Thin-Film Transistors from Solution-Processed Cadmium Selenide and a Self-Assembled Multilayer Gate Dielectric. *Adv. Mater.***2008,** *20* (12), 2319-2324.
85. Feng, M.; Feng, Y.; Zhang, T.; Li, J.; Chen, Q.; Chi, Q.; Lei, Q., Recent Advances in Multilayer-Structure Dielectrics for Energy Storage Application. *Adv. Sci.* **2021,** *8* (23), 2102221.
86. Richardson, J. J.; Björnmalm, M.; Caruso, F., Technology-driven layer-by-layer assembly of nanofilms. *Science* **2015,** *348* (6233), aaa2491.
87. Murata, H.; Nakajima, Y.; Saitoh, N.; Yoshizawa, N.; Suemasu, T.; Toko, K., High-Electrical-Conductivity Multilayer Graphene Formed by Layer Exchange with Controlled Thickness and Interlayer. *Sci. Rep.* **2019,** *9* (1), 4068.
88. Kim, S. M.; Hsu, A.; Park, M. H.; Chae, S. H.; Yun, S. J.; Lee, J. S.; Cho, D.-H.; Fang, W.; Lee, C.; Palacios, T.; Dresselhaus, M.; Kim, K. K.; Lee, Y. H.; Kong, J., Synthesis of large-area multilayer hexagonal boron nitride for high material performance. *Nat. Commun.* **2015,** *6* (1), 8662.

89. Nirmal, K. A.; Kumbhar, D. D.; Kesavan, A. V.; Dongale, T. D.; Kim, T. G., Advancements in 2D layered material memristors: unleashing their potential beyond memory. *npj 2D mater. appl.* **2024,** *8* (1), 83.
90. Koleśnik-Gray, M.; Meingast, L.; Siebert, M.; Unbehaun, T.; Huf, T.; Ellrott, G.; Abellán, G.; Wild, S.; Lloret, V.; Mundloch, U.; Schwarz, J.; Niebauer, M.; Szabo, M.; Rommel, M.; Hutzler, A.; Hauke, F.; Hirsch, A.; Krstić, V., Unconventional conductivity increase in multilayer black phosphorus. *npj 2D mater. appl.* **2023,** *7* (1), 21.
91. Yun, S. J.; Ko, H.; Park, S.; Lee, B. H.; Kim, N.; Duong, H. P.; Lee, Y.; Kim, S. M.; Kim, K. K., Van der Waals Multilayered Films: Wafer-Scale Synthesis and Applications in Electronics and Optoelectronics. *Adv. Funct. Mater.* **2024,** *34* (49), 2409458.
92. Zhang, X.; Long, Y.; Lu, N.; Jian, F.; Zhang, X.; Liang, Z.; He, L.; Tang, H., Moiré Superlattice in Two-Dimensional Materials: Fundamentals, Applications, and Recent Developments. *ACS Appl. Mater. Interfaces* **2024,** *16* (50), 68724-68748.
93. Yang, H.; Liu, L.; Yang, H.; Zhang, Y.; Wu, X.; Huang, Y.; Gao, H.-J.; Wang, Y., Advance in two-dimensional twisted moiré materials: Fabrication, properties, and applications. *Nano Res.* **2023,** *16* (2), 2579-2596.
94. Shi, B.; Qi, P.; Jiang, M.; Dai, Y.; Lin, F.; Zhang, H.; Fang, Z., Exotic physical properties of 2D materials modulated by moiré superlattices. *Mater. Adv.* **2021,** *2* (17), 5542-5559.
95. Lei, Y.; Zhang, T.; Lin, Y.-C.; Granzier-Nakajima, T.; Bepete, G.; Kowalczyk, D. A.; Lin, Z.; Zhou, D.; Schranghamer, T. F.; Dodda, A.; Sebastian, A.; Chen, Y.; Liu, Y.; Pourtois, G.; Kempa, T. J.; Schuler, B.; Edmonds, M. T.; Quek, S. Y.; Wurstbauer, U.; Wu, S. M.; Glavin, N. R.; Das, S.; Dash, S. P.; Redwing, J. M.; Robinson, J. A.; Terrones, M., Graphene and Beyond: Recent Advances in Two-Dimensional Materials Synthesis, Properties, and Devices. *ACS Nanosci. Au* **2022,** *2* (6), 450-485.
96. Xu, M.; Liang, T.; Shi, M.; Chen, H., Graphene-Like Two-Dimensional Materials. *Chem. Rev.* **2013,** *113* (5), 3766-3798.
97. Huang, Z.-C.; Liew, K. M., Strain Engineering towards Enriched Surface Patterns in Graphene Twistronics. *ACS Appl. Mater. Interfaces* **2025,** *17* (11), 17622-17635.
98. Liu, M.; Wang, L.; Yu, G., Developing Graphene-Based Moiré Heterostructures for Twistronics. *Adv. Sci.* **2022,** *9* (1), 2103170.

99. Carr, S.; Massatt, D.; Fang, S.; Cazeaux, P.; Luskin, M.; Kaxiras, E., Twistronics: Manipulating the electronic properties of two-dimensional layered structures through their twist angle. *Phys. Rev. B* **2017,** *95* (7), 075420.

100. Cao, Y.; Fatemi, V.; Fang, S.; Watanabe, K.; Taniguchi, T.; Kaxiras, E.; Jarillo-Herrero, P., Unconventional superconductivity in magic-angle graphene superlattices. *Nature* **2018,** *556* (7699), 43-50.

101. Alexeev, E. M.; Ruiz-Tijerina, D. A.; Danovich, M.; Hamer, M. J.; Terry, D. J.; Nayak, P. K.; Ahn, S.; Pak, S.; Lee, J.; Sohn, J. I.; Molas, M. R.; Koperski, M.; Watanabe, K.; Taniguchi, T.; Novoselov, K. S.; Gorbachev, R. V.; Shin, H. S.; Fal'ko, V. I.; Tartakovskii, A. I., Resonantly hybridized excitons in moiré superlattices in van der Waals heterostructures. *Nature* **2019,** *567* (7746), 81-86.

102. Cao, Y.; Fatemi, V.; Demir, A.; Fang, S.; Tomarken, S. L.; Luo, J. Y.; Sanchez-Yamagishi, J. D.; Watanabe, K.; Taniguchi, T.; Kaxiras, E.; Ashoori, R. C.; Jarillo-Herrero, P., Correlated insulator behaviour at half-filling in magic-angle graphene superlattices. *Nature* **2018,** *556* (7699), 80-84.

103. Pixley, J. H.; Andrei, E. Y., Ferromagnetism in magic-angle graphene. *Science* **2019,** *365* (6453), 543-543100.

104. Andrei, E. Y.; MacDonald, A. H., Graphene bilayers with a twist. *Nat. Mater.* **2020,** *19* (12), 1265-1275.

105. Brzhezinskaya, M.; Kononenko, O.; Matveev, V.; Zotov, A.; Khodos, I. I.; Levashov, V.; Volkov, V.; Bozhko, S. I.; Chekmazov, S. V.; Roshchupkin, D., Engineering of Numerous Moiré Superlattices in Twisted Multilayer Graphene for Twistronics and Straintronics Applications. *ACS Nano* **2021**, 15 (7), 12358-12366.

106. Yao, K.; Finney, N. R.; Zhang, J.; Moore, S. L.; Xian, L.; Tancogne-Dejean, N.; Liu, F.; Ardelean, J.; Xu, X.; Halbertal, D.; Watanabe, K.; Taniguchi, T.; Ochoa, H.; Asenjo-Garcia, A.; Zhu, X.; Basov, D. N.; Rubio, A.; Dean, C. R.; Hone, J.; Schuck, P. J., Enhanced tunable second harmonic generation from twistable interfaces and vertical superlattices in boron nitride homostructures. *Sci. Adv.* **2021**, 7 (10), eabe8691.

107. Devakul, T.; Crépel, V.; Zhang, Y.; Fu, L., Magic in twisted transition metal dichalcogenide bilayers. *Nat. Commun.* **2021,** *12* (1), 6730.

108. Shen, J.; Dong, Z.; Qi, M.; Zhang, Y.; Zhu, C.; Wu, Z.; Li, D., Observation of Moiré Patterns in Twisted Stacks of Bilayer Perovskite Oxide Nanomembranes with Various Lattice Symmetries. *ACS Appl. Mater. Interfaces* **2022,** *14* (44), 50386-50392.

109. Hejazi, K.; Luo, Z. X.; Balents, L. Heterobilayer Moiré Magnets: Moiré Skyrmions and Commensurate-Incommensurate Transitions. *Phys. Rev. B* **2021**, *104*, L100406.

110. Das, P.; Chattopadhyay, A., Moiré superlattices of two-dimensional copper nanocluster assemblies with tuneable twin emissions from hierarchical components leading to white light emission. *J. Mater. Chem. C* **2023,** *11* (35), 12029-12036.

111. Liu, L.; Sun, Y.; Cui, X.; Qi, K.; He, X.; Bao, Q.; Ma, W.; Lu, J.; Fang, H.; Zhang, P.; Zheng, L.; Yu, L.; Singh, D. J.; Xiong, Q.; Zhang, L.; Zheng, W., Bottom-up growth of homogeneous Moiré superlattices in bismuth oxychloride spiral nanosheets. *Nat. Commun.* **2019,** *10* (1), 4472.

112. Drexler E.K. Molecular engineering: An approach to the development of general capabilities for molecular manipulation. *Proc. Natl. Acad. Sci. USA.* **1981**, 78, 5275–5278.

113. Dietrich-Buchecker, C.O.; Sauvage, J.-P.; Kern, J.-M. Templated synthesis of interlocked macrocyclic ligands: ¬the catenands, *J. Am. Chem. Soc*, 1984, 106, 3043–3045.

114. Schill, G., *Catenanes, rotaxanes, and knots*. Elsevier: 2013; Vol. 22.

115. Anelli, P. L.; Spencer, N.; Stoddart, J. F. A molecular shuttle, *J. Am. Chem. Soc*., **1991**, 113, 5131–5133.

116. Stoddart, J. F., Mechanically Interlocked Molecules (MIMs)—Molecular Shuttles, Switches, and Machines (Nobel Lecture). *Angew. Chem. Int. Ed.* **2017,** *56* (37), 11094-11125.

117. Koumura, N.; Zijlstra, R. W.; van Delden, R. A.; Harada, N.; Feringa, B. L. Light-driven monodirectional molecular rotor, *Nature*, **1999**, 401, 152–155.

118. Feringa, B. L., The Art of Building Small: From Molecular Switches to Motors (Nobel Lecture). *Angew. Chem. Int. Ed.* **2017,** *56* (37), 11060-11078.

119. Livoreil, A.; Dietrich-Buchecker, C. O.; Sauvage, J.-P., Electrochemically Triggered Swinging of a [2]-Catenate. *J. Am. Chem. Soc.* **1994,** *116* (20), 9399-9400.

120. Bissell, R. A.; Córdova, E.; Kaifer, A. E.; Stoddart, J. F., A chemically and electrochemically switchable molecular shuttle. *Nature* **1994,** *369* (6476), 133-137.

121. Sauvage, J.-P., From Chemical Topology to Molecular Machines (Nobel Lecture). *Angew. Chem. Int. Ed.* **2017,** *56* (37), 11080-11093.

122. Chen, H.; Fraser Stoddart, J., From molecular to supramolecular electronics. *Nat. Rev. Mater.* **2021,** *6* (9), 804-828.

123. Kong, G. D.; Song, H.; Yoon, S.; Kang, H.; Chang, R.; Yoon, H. J., Interstitially mixed self-assembled monolayers enhance electrical stability of molecular junctions. *Nano Lett.* **2021,** *21* (7), 3162-3169.

124. Li, X.; Ge, W.; Guo, S.; Bai, J.; Hong, W., Characterization and Application of Supramolecular Junctions. *Angew. Chem. Int. Ed.* **2023,** *62* (13), e202216819.

Chapter 2: The Potential of Gadolinium Ascorbate Nanoparticles as Safer Contrast Agent

J. Phys. Chem. B **2023**, 127(1) 346–358

(https://pubs.acs.org/doi/full/10.1021/acs.jpcb.2c05831)

Chapter 2

The Potential of Gadolinium Ascorbate Nanoparticles as Safer Contrast Agent

Abstract: There has been health concerned raised against the use of Gadolinium (Gd)-based magnetic resonance imaging contrast agents. The primary observation is that Gd-ions are prone to leaking into the blood stream causing nephrogenic systemic fibrosis as one of the side effects. In addition, such leakage of the ions inhibits easy clearance from the body. Herein we propose that Gd-ascorbate nanoparticles could be one of the safer choices as they are rather stable in aqueous dispersion and they do not get affected by Zn or Fe ions in the medium. The magnetic properties of the ions are preserved in the nanoparticles and particles when sufficiently small may be amenable to renal clearance from the human body. Thus, when an aqueous solution of Gd-acetate and ascorbic acid were left to evolve with time, Gd-ascorbate complex was formed that led to the formation of nanoparticles with time. The sizes of the nanoparticles increased with time and when the particles were sufficiently large they precipitated out of the medium. In addition, smaller nanoparticles were consistently present at all times of observations. UV-vis, photoluminescence and FTIR spectroscopy, mass spectrometry and transmission electron microscopy analyses confirmed the formation of nanoparticles of Gd-ascorbate complex. In addition, magnetic measurements confirmed high relaxivity of the nanoparticles as compared to the parent salt, indicating the effectiveness of the nanoparticles as contrast agents. Density functional theory-based calculations of the molecular complex-based nanoparticles accounted for the experimental observations.

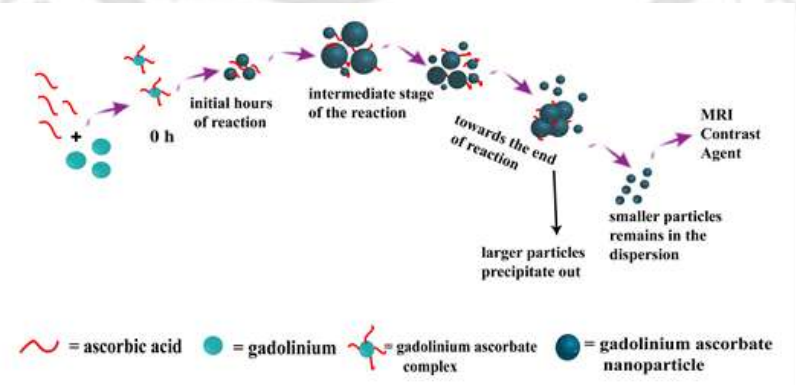

Scheme 1. Graphical representation showing the assembly of Gd-ascorbate complex into nanoparticles and evolution of its size with time.

Chapter 2

Introduction

Contrast agents play a vital role in improving the quality of MRI images thus helping the radiologists in the diagnosis of the diseased as well as healthy tissues. The significant developments that have arisen in this regard consist of molecular materials such as inorganic complexes, nanoscale magnetic particles and typically, manganese or gadolinium (Gd) ion - loaded nanoparticles. However, the key issues such as toxicity, lack of clearance from the body due to their chemical reactivity and size still limit their usage. Thus, the field is still open to new and significant discoveries.

A popular choice in this regard is based on Gd chelates.[1-5] However, there are several shortcomings that still need to be addressed for betterment of the application potential. For example, clinically administered gadolinium dodecane tetraacetic acid (Gd-DOTA) or gadolinium-diethylenetriamine-pentaacetic acid (Gd-DTPA) has moderate relaxivity at high magnetic field. Thus, a high amount of the contrast agent is required to be administered to the patient for better quality imaging of the cells, which in turn raises the chance of Gd accumulation in the body. Hence, a contrast agent that offers high relaxivity at relatively small doses and gets cleared from the body more easily would be preferred. In the last few decades, contrast agents based on dendrimers,[6-8] gadofullerenes[9-12] and nanoparticles loaded[8,13-20] with Gd chelates or complexes have been reported. Further, Gd oxide nanoparticles encapsulated in polymer[21-23] or multinuclear Gd clusters[24-25] have shown better prospects as contrast agents. Metal organic frameworks (MOFs) based on Gd and other metals such as manganese are also known to have high relaxivity and thus have significant potential as MRI constrast agents.[26] It has also been shown that by controlling the size of the MOF nanoparticle, the relaxivity could be further tuned.[27]

Recent developments in high nuclearity lanthanide clusters such as polyoxometalates and metal chalcogenides or oxoclusters of transition or lanthanide metals with their remarkable structures,[28-30] bonding and physical properties - may bring new avenues in MRI imaging.[24-25] These clusters, in which the metals are connected through metallic bonding or bridging ligands, can behave as single molecule exhibiting optical,[32-37] magnetic[31,33,38,39] and catalytic properties.[40-41] Among different lanthanides, Gd-based clusters are promising as single molecular magnets,[29] MRI contrast agents[24-25] or as industrial coolants with high magnetocaloric effect.[30,31,41-43]

Chapter 2

Synthesis of multi-nuclear Gd clusters requires skilful selection and manipulation of, coordinating ligands, bridging ligands and the solvent. Although the synthesis poses a challenge, however, the very nature of the complexity provides great opportunities for the investigation of structure-function relationship especially magnetism and its potential applications. The clusters largely consist of organic ligand-stabilized Gd ions connected by bridging groups. Due to the presence of closely connected Gd ions that form the cluster, it has the potential to offer many applications in magnetism. This would be based on magnetic coupling involving interatomic interactions.[44-47] Considering the stability under physiological conditions, toxicity, clearance from the body and coercivity and magnetization, it may be pertinent to use nanoscale assemblies of Gd-based inorganic complex. This may prove to be useful if the ligand used is biofriendly and the complex easily forms assembly in the aqueous medium. Such an approach may lead to tuneability of magnetic property and can bring out other physical or chemical properties useful for theranostics. For example, suppose a molecular complex is allowed to aggregate in a dispersion medium. Thus, depending on the average dimensions of the aggregates, the magnetic property and stability of the aggregates in the medium may evolve. That may provide one with an option to choose the best nanoscale particles for practical applications such as in MRI imaging.

It is important to emphasize here that health concerns have been raised recently regarding the usage of Gd-based contrast agents (GBCAs). In this regard, the retention of Gd in the body and the consequent risk of the patients developing nephrogenic systemic fibrosis[48-49] has led to the development of contrast agents based on different paramagnetic metal ions such as manganese[50-51,54] (Mn) or iron[52-53] (Fe). However, the paramagnetic transition metals are prone to getting oxidized following administration and thus, leading to loss of their paramagnetism. Further, although Mn is an essential trace element for normal cellular functioning, high quantity of it is also considered neurotoxic.[55-56] A large amount of free Mn ion exposure may lead to neurological disorder called ‘manganism’,[57] having symptoms similar to parkinson’s disease. Thus, the paramagnetic based contrast agents are administered as metal chelates to avoid potential risk of release of free metal ions in vivo.

The better-quality image contrast and the crucial information that could be obtained using GBCAs are yet to be offered by other contrast agents. As the debate for the risk to benefit ratio

for using GBCAs continues, search for alternatives as safer agents also continues. A practical option in the regard could be based on GBCAs that would be stable under physiological conditions and the agent should come out of the body in its intact form without affecting the internal biological processes. One way out could be to use Gd-based nanoparticles - instead of complexes – with ease of clearance from the body. They could be formed based on aggregation of the complexes that are likely to be thermodynamically and kinetically stable under physiological conditions. We propose that with suitable choice of ligand, the metal complex itself can assemble into nanoparticles in water such that the relaxivity and the stability increase with their formation. The ligand ought to be biofriendly and the nanoparticles need to support facile renal clearance.

Herein we report that nanoscale particles of Gd-ascorbate - resulting from aggregation of the parent complex in water - with substantive magnetic properties, may serve as a viable contrast agent for MRI. Thus, an aqueous mixture of Gd acetate and ascorbic acid - when left to have evolved with time under ambient conditions- led to the formation of nanoscale particles consisting of Gd-ascorbate complex. The dimensions of the particles evolved with time; small spherical particles of diameter on the order of 2-4 nm were formed initially. Formation of a mixture of small and large particles were observed in the intermediate times. At longer times, even larger particles were observed to have precipitated out and small particles again populated the dispersion medium. Electrospray ionization mass spectrometry (ESI-MS) revealed the formation of tetra-nuclear Gd-ascorbate cluster as the basic unit of the nanoscale particles. Computational analyses supported the formation of the unit consisting of four Gd-ascorbate moieties. A peak around 373 nm was obtained when the UV-vis spectrum of the basic unit was simulated using Gaussian 16 and was close to the experimental peak at 380 nm. The luminescent dispersion emitted in the range 450-470 nm with a maximum quantum yield of ~2 % at 48 h when the population was dominated by the larger particles. The magnetisation of Gd-ascorbate nanoparticles, following separation through centrifugation, was found to be around 1 emu/g at room temperature. As mentioned before, the magnetisation value didn't vary significantly with average particle size. The longitudinal and transverse relaxation times of the dispersion was found to change with time owing to the changes in the average dimensions of the nanoparticles present in the medium. At later stages of the reaction, the relaxation times decreased as reaction

progressed, thus resulting in higher relaxivity as the concentration of the Gd remained same throughout the reaction. This was probably due to the formation of smaller nanoparticles in the medium (in addition to the larger particles that precipitated out of the medium).

Result and Discussion

Solid ascorbic acid (24 mM) was added sequentially to an aqueous solution of gadolinium (Gd) acetate hydrate (9 mM) under ambient conditions. The mixture was then stirred for 60 h (or longer) that resulted in the formation of a colloidal dispersion. UV-Vis absorption spectrum of the mixture was recorded at different time intervals (Figure 1A). A peak centered at 380 nm gradually developed after a few hours (typically 24 h) of the reaction. The absorbance increased as the reaction progressed, indicating the possible formation and growth of a new species in the reaction medium. However, at 60 h or so, precipitates started to appear from the reaction medium and the absorbance did not increase significantly after that time.

Transmission electron microscopic (TEM) images were recorded for samples collected at different time intervals (Figure 1) as the reaction advanced. The images obtained for the sample at 30 min contained amorphous particulates having no distinct features (Figure 1B, Figure S1). At 10 h, nanoparticles having size in the range 2-10 nm were present and particles in the range of 2-4 nm populated the dispersion. The average size of the nanoparticles at this time was 3.99 ± 1.35 nm. (Figure 1C, Figure S2). At 24 h, the particle size increased and was found to be in the range of 10 nm to 60 nm (Figure 1D, Figure S3). Upon focusing on the larger particles, it was revealed that smaller particles having size in the range 1-3 nm were present in aggregated form, which formed the larger particle (Figure S3D, Figure S3E). Thus, the system at this time was polydisperse and the average size was calculated to be 30.17 ± 16.46 nm. Again at 48 h, larger nanoparticles with size in the range 20-50 nm were also present (Figure 1E) having average size of 17.47 ± 6.09 nm (Figure S4). At 58 h (Figure 1F), TEM images contained discrete smaller sized particles along with larger particles of size 20 nm and having maximum population in the range 1-5 nm and the average particle size was of 9.96 ± 6.91 nm (Figure S5). The TEM image containing particles at 58 h and in the range of 1-5 nm is presented in Figure S5B. As is clear from the image, the particles were present in an assembled form. Again at 72 h, the larger particles started to precipitate out and the majority of the nanoparticles were in the range of 4-10 nm (Figure 1G, Figure S6) and particles with size up to 18 nm were also present in the reaction

mixture. At 72 h, the system consisted of a large number of smaller sized particles with an average particle size of 4.81 ± 2.81 nm. The selected area electron diffraction (SAED) of the crystalline nanoparticle were acquired at different time. The lattice parameters obtained from the SAED pattern are represented in Table S1. The high resolution TEM (HRTEM) images (Figure 1H) were taken at 10 h and the analysis of the images resulted in the lattice spacing value equal to 0.35 nm.

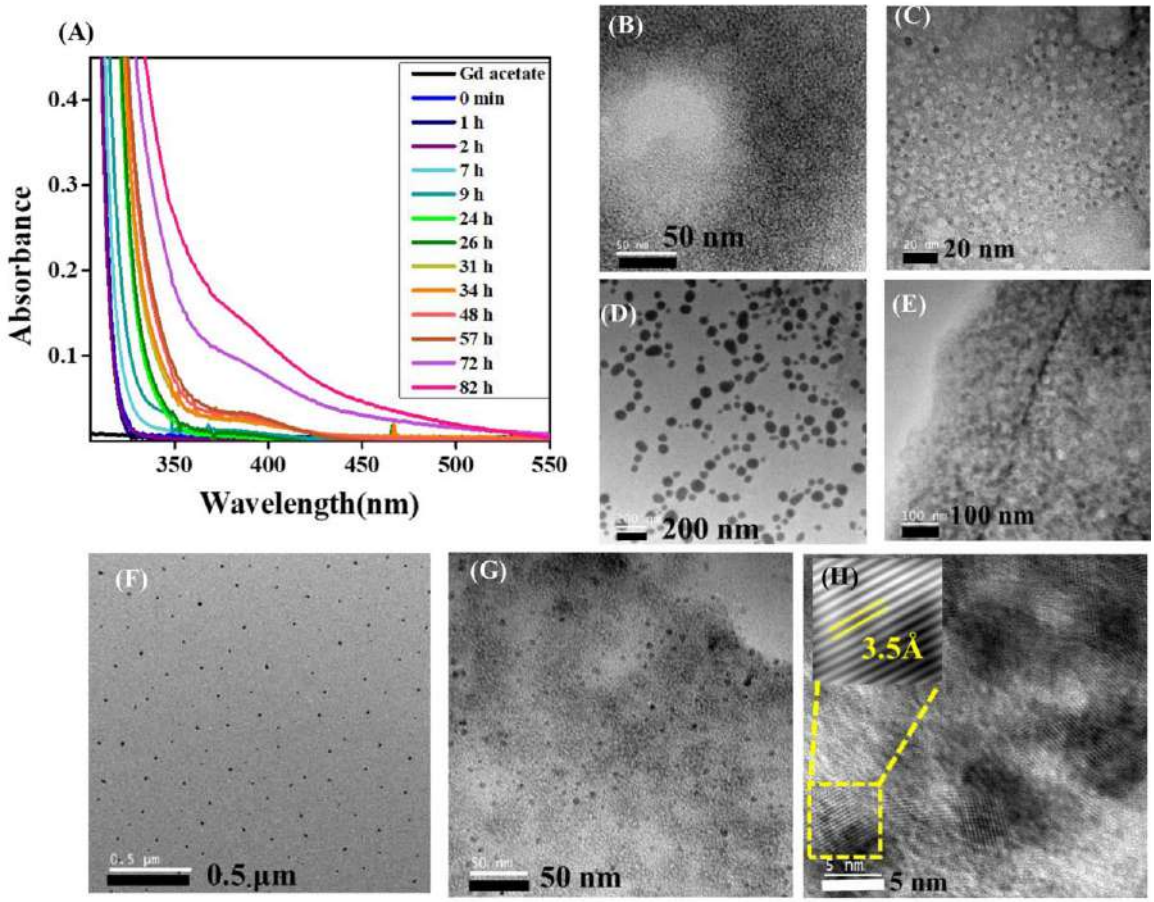

Figure 1. (**A**) UV-Vis absorbance spectrum of Gd acetate and of the reaction mixture containing Gd acetate and ascorbic acid at different time. (**B**)-(**G**). TEM images of the reaction mixture at 30 min, 10 h, 25 h, 48 h, 58 h and 72 h, respectively. (**H**) HRTEM image of the reaction mixture taken at 10 h.

Electron-spray ionization mass-spectrometry (ESI-MS) analysis of the dispersion provided the chemical structure of the unit of the nanoparticle as well as of its fragments. The full ESI-MS spectrum is presented in Figure S7. The m/z value with highest intensity peak corresponds to

684.0083 having metal complex formula as [Gd($C_6H_7O_6$)($C_6H_6O_6$)($C_6H_8O_6$)] (Figure S9D). The next intense m/z peak corresponding to 860.0367 is assigned to the Gd ascorbate complex having molecular formula [Gd($C_6H_7O_6$)($C_6H_6O_6$)($C_6H_8O_6$)$_2$] (Figure 2A) where four ascorbic acid (AA) ligands are coordinated to the metal centre (Figure 2D). Gd complexes where only AA or where both acetate and AA were coordinated to the central metal ion were present in the dispersion as evaluated from the spectrum (Figure S8- Figure S13). These might have been formed during the initial stages of complexation. Complexes with two, three and four Gd ions connected by ligand ascorbic acid with molecular formula [Gd_2($C_6H_6O_6$)($C_6H_7O_6$)$_4$($C_6H_8O_6$)$_2$] (Figure S10D), [Gd_3($C_6H_6O_6$)$_3$($C_6H_7O_6$)$_3$($C_6H_8O_6$)] (Figure S11D), [Gd_3($C_6H_6O_6$)$_3$($C_6H_7O_6$)$_3$($C_6H_8O_6$)$_2$] (Figure S12D), [Gd_4($C_6H_6O_6$)$_5$($C_6H_7O_6$)$_2$($C_6H_8O_6$)$_2$] (Figure S13D), [Gd_4($C_6H_6O_6$)$_5$($C_6H_7O_6$)$_2$($C_6H_8O_6$)$_3$] (Figure 2H) respectively, were also assigned to be present in the samples for which mass spectra were recorded. The structural optimization and time-dependent density functional theory (TD-DFT) calculations using Gaussian 16 were performed for [Gd($C_6H_7O_6$)($C_6H_6O_6$)($C_6H_8O_6$)$_2$], [Gd_2($C_6H_6O_6$)($C_6H_7O_6$)$_4$($C_6H_8O_6$)$_2$], [Gd_3($C_6H_6O_6$)$_3$($C_6H_7O_6$)$_3$($C_6H_8O_6$)$_2$] and [Gd_4($C_6H_6O_6$)$_5$($C_6H_7O_6$)$_2$($C_6H_8O_6$)$_3$] and are presented in the computation section. [Gd_4($C_6H_6O_6$)$_5$($C_6H_7O_6$)$_2$($C_6H_8O_6$)$_3$] is considered to be the constituent unit of the nanoparticle (Figure 2H). This was further supported by the simulated UV-Vis spectrum of the unit, which matched well with the experimental observations (Figure 3).

The synthesis was also pursued in ambient conditions with 5.7 mM of ascorbic acid while the concentration (9 mM) of Gd acetate hydrate had been kept the same. The molar ratio was 5.7:9 for ascorbic acid and Gd acetate, respectively and the PL quantum yield of the resultant mixture was low. Moreover, the ESI-MS spectra didn't provide us with molecular mass of the nanoparticles formed. At the 24:9 ratio of ascorbic acid to Gd acetate, the molecular structure and formula of the nanoparticles were obtained. Further experiments were pursued using this concentration of ascorbic acid.

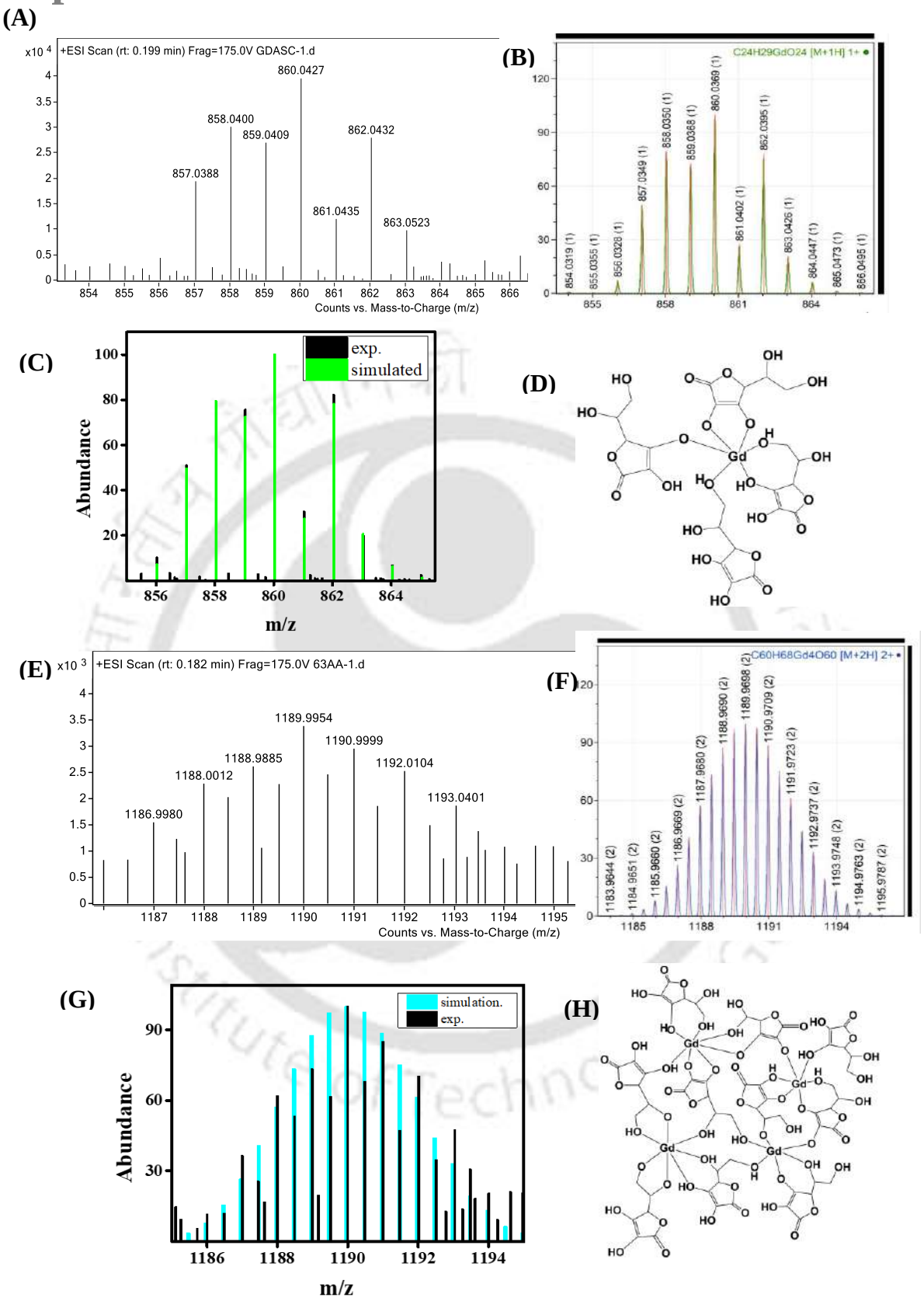

Figure 2. (A) Experimental mass spectrum representing $[Gd(C_6H_7O_6)(C_6H_6O_6)(C_6H_8O_6)_2]$ with mass 860.0427, (**B**) simulated mass spectrum of $[Gd(C_6H_7O_6)(C_6H_6O_6)(C_6H_8O_6)_2]$ and (**C**) plot

representing overlaid experimental and simulated data. (**D**) Proposed structure of $[Gd(C_6H_7O_6)(C_6H_6O_6)(C_6H_8O_6)_2]$. (**E**) Experimental mass spectrum of $[Gd_4(C_6H_6O_6)_5(C_6H_7O_6)_2(C_6H_8O_6)_3]$ with mass 1189.9954, (**F**) simulated mass spectrum of $[Gd_4(C_6H_6O_6)_5(C_6H_7O_6)_2(C_6H_8O_6)_3]$ and (**G**) plot representing overlaid experimental and simulated data. (**H**) Proposed structure of $[Gd_4(C_6H_6O_6)_5(C_6H_7O_6)_2(C_6H_8O_6)_3]$.

The FTIR spectral data (Figure S14) further supported the complex formation and coordination via the oxygen atoms of the ascorbic acid. The discrete OH stretching frequencies (3523 cm^{-1} and 3311 cm^{-1} for the ring O-H groups and 3406 cm^{-1} and 3209 cm^{-1} for the side chain O-H groups) of the ascorbic acid were replaced by a very strong and broad O-H stretching frequency at 3203 cm^{-1} of the Gd ascorbate. The broad peak can be attributed to the complex formation via coordination with OH group of the ascorbic acid. The C-H stretching frequency peak was present in the complex at 2659 cm^{-1}. The –C=O stretching frequency was absent in the spectrum, which may be due to its plausible participation in complex formation. A strong peak positioned at 1583 cm^{-1} is assigned to the –C=C- bond stretching and was shifted by 71 cm^{-1} when compared with that of pure L-ascrobic acid (1654 cm^{-1}). The C-O-C and O-C stretching frequencies were also shifted and were present in the range 1000 cm^{-1} to 1200 cm^{-1}. The C-H bending of the Gd ascorbate originated at 1421 cm^{-1} while for ascorbic acid it was at 1449 cm^{-1}. The shift in these stretching and bending frequencies implied the effective participation of the O-H groups for coordination with the Gd ion. The asymmetric (1534 cm^{-1}) and symmetric (1449 cm^{-1}) stretching frequency peaks due to the carboxylate group ($-COO^-$) of acetate were not present in the complex, indicating the absence of acetate coordination with Gd and absence of acetate in the centrifuged product.

Computational studies

The ground state structure of Gd ascorbate complex and that of its clusters having molecular formulas, $[Gd(C_6H_7O_6)(C_6H_6O_6)(C_6H_8O_6)_2]$, $[Gd_2(C_6H_6O_6)(C_6H_7O_6)_4(C_6H_8O_6)_2]$, $[Gd_3(C_6H_6O_6)_3(C_6H_7O_6)_3(C_6H_8O_6)_2]$ and $[Gd_4(C_6H_6O_6)_5(C_6H_7O_6)_2(C_6H_8O_6)_3]$ respectively, were optimized in the vapor phase, based on density functional theory (DFT) calculations with M06-2X[59] functional using GAUSSIAN 16 software package.[58] The calculations were performed under *gen* basis set by utilizing the concept of split basis set for H,C,O (6-31G(d)) and Gd (mwb53).

Chapter 2

The optimization required large-core relativistic effective core potential mwb53 for modelling of Gd using corresponding basis set. Time-dependent DFT (TD-DFT) calculations were pursued in both gas and solvent phases to obtain the UV-Vis spectra (Figure 3) of the optimized structures $[Gd(C_6H_7O_6)(C_6H_6O_6)(C_6H_8O_6)_2]$ (Figure 3A(i)), $[Gd_2(C_6H_6O_6)(C_6H_7O_6)_4(C_6H_8O_6)_2]$ (Figure 3B(i)), $[Gd_3(C_6H_6O_6)_3(C_6H_7O_6)_3(C_6H_8O_6)_2]$ (Figure 3C(i)) and $[Gd_4(C_6H_6O_6)_5(C_6H_7O_6)_2(C_6H_8O_6)_3]$ (Figure 3D(i)). Water was considered as the solvent as it was the reaction medium and the calculations were performed using polarizable continuum model (PCM).

Optimised structure	Vapour phase	Water solvent
A(i) 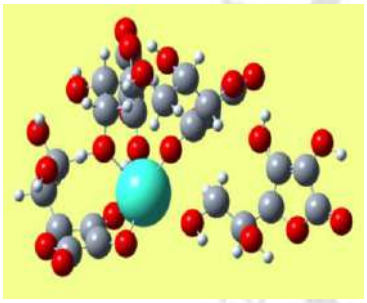	A(ii) 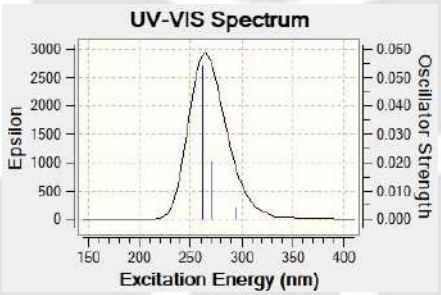	A(iii) 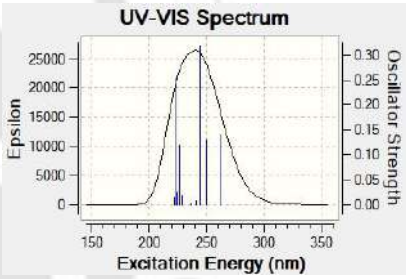
B(i) 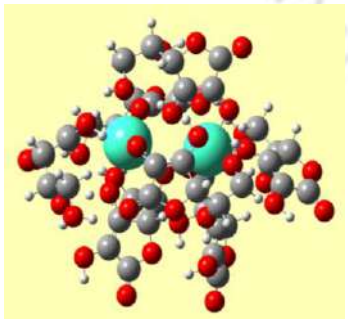	B(ii) 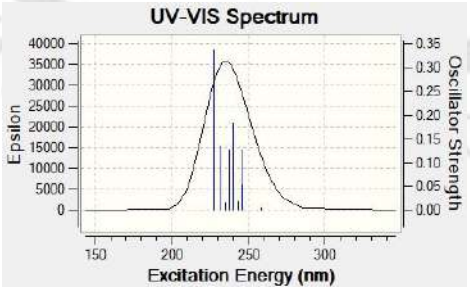	B(iii) 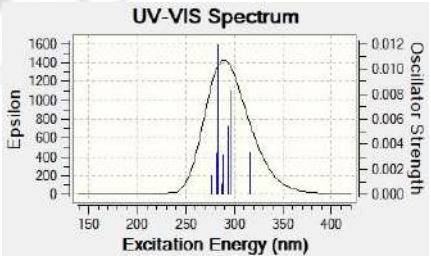

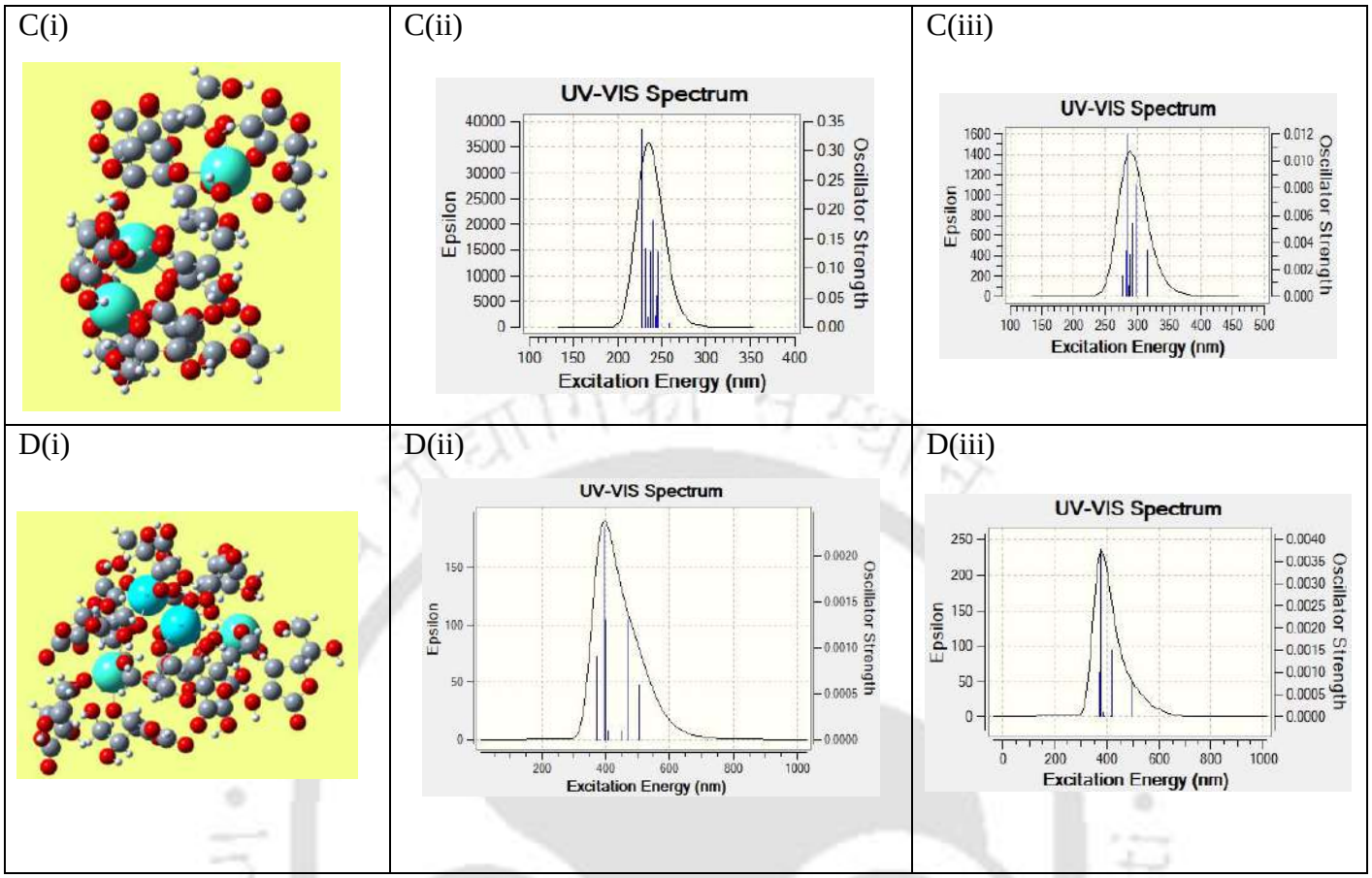

Figure 3. (A(i)-D(i)) Computationally optimized structures of the Gd ascorbate complexes $[Gd(C_6H_7O_6)(C_6H_6O_6)(C_6H_8O_6)_2]$, $[Gd_2(C_6H_6O_6)(C_6H_7O_6)_4(C_6H_8O_6)_2]$, $[Gd_3(C_6H_6O_6)_3(C_6H_7O_6)_3(C_6H_8O_6)_2]$ and $[Gd_4(C_6H_6O_6)_5(C_6H_7O_6)_2(C_6H_8O_6)_3]$ respectively. (A(ii)-D(ii)) Corresponding UV-vis spectra of the structures in vapor phase and (A(iii)-D(iii)) of those in the aqueous medium, as obtained from TD-DFT calculations. The cyan colored atom represents the Gd ion whereas red and grey colored atoms represents oxygen and carbon respectively. The hydrogen atoms are represented in white.

The Gd and O bond distance obtained from the optimized structure was in the range of 2.2 -2.4 Å in all of the optimized structures. The smallest Gd – Gd distance obtained from the optimized structure of $[Gd_4(C_6H_6O_6)_5(C_6H_7O_6)_2(C_6H_8O_6)_3]$ was 3.58 Å, which was close to the distance obtained from HRTEM - that is 3.5 Å (Figure 1H). The UV – Vis spectrum was simulated for $[Gd(C_6H_7O_6)(C_6H_6O_6)(C_6H_8O_6)_2]$, $[Gd_2(C_6H_6O_6)(C_6H_7O_6)_4(C_6H_8O_6)_2]$, $[Gd_3(C_6H_6O_6)_3(C_6H_7O_6)_3(C_6H_8O_6)_2]$ and $[Gd_4(C_6H_6O_6)_5(C_6H_7O_6)_2(C_6H_8O_6)_3]$ following TD-DFT

calculation using Gaussian 16. The calculated UV-Vis spectrum for Gd complex $[Gd(C_6H_7O_6)(C_6H_6O_6)(C_6H_8O_6)_2]$ was at 250 nm in vapor phase as well as solvent phase. For the di-nuclear complex $[Gd_2(C_6H_6O_6)(C_6H_7O_6)_4(C_6H_8O_6)_2]$, the calculated UV-Vis spectrum had a peak positioned at 250 nm in vapor phase and 280 nm in solvent phase. The tri-nuclear complex $[Gd_3(C_6H_6O_6)_3(C_6H_7O_6)_3(C_6H_8O_6)_2]$ had a peak at 250 nm in vapor as well as and solvent phase in the simulated UV-Vis spectrum. These results were similar to the experimental UV-Vis spectrum obtained at early hours (before 24 h) of the reaction, which appeared within 280 nm and where the peaks were possibly due to complexes and the precursors and no distinguishable peak was present at 380 nm. For $[Gd_4(C_6H_6O_6)_5(C_6H_7O_6)_2(C_6H_8O_6)_3]$ the simulated UV-vis spectra consisted of a major peak at 400 nm in vapor phase and 373 nm in solvent (water) phase close to the value of 380 nm for the experimental UV-Vis spectrum obtained for the dispersion. This further supported the formation of nanoparticle or molecular clusters from the complexes of Gd and ascorbic acid. The complexes initially formed possibly with the structures presented above further reacted with precursors or other complexes and grew to form the nanocrystals that showed unique properties at the nanoscale level. With further growth, even larger particles were formed that precipitated out of the medium. However, both experimental evidences and computational studies suggested that the basic unit of the nanoparticle were as described above.

PHOTOLUMINESCENCE PROPERTIES

The photoluminescence (PL) properties of the dispersion were measured by acquiring the PL emission (Figure 4A), excitation (Figure 4B) and time resolved PL (Figure 4D) data at different intervals of time. The dispersion was excited at λ_{ex}=362 nm, which resulted in PL emission in the range of 445 – 470 nm at different times similar to the observed PL spectrum for zinc ascorbate acetate nanoparticles.[60] As time advanced, there was a hypsochromic shift of about 20 nm (Figure 4C) with simultaneous intensity enhancement. Parallel measurement of the excitation spectrum (Figure 4B) of the reaction mixture with progression of time resulted in the observation of a bathochromic shift of around 12 nm as the peak shifted from 362 nm and developed into an intense peak at 375 nm at later stages. Initially the vague PL observed might have been emerging from the smaller nanoparticles present in the dispersion. With time, the population of the nanoparticles increased along with their size with the emission peak appearing at 467 nm by 24 h. As reaction progressed, the larger particles precipitated out but smaller nanoparticles

populated the dispersion again, with the emission peak appearing at 450 nm by 60 h. The blue shift of about 20 nm at 60 h as compared to that at 24 h was retained in the supernatant when the larger particles were removed by centrifugation. No further change in the peak position was observed for samples of period of standing beyond 60 h. The dispersion at 60 h was centrifuged at 26000 rpm for 10 min and PL properties along with UV-Vis spectrum of the redispersed pellet and that of the supernatant were recorded (Figure S15). The emission maximum for the supernatant was found to be at 452 nm and the redispersed pellet showed emission maximum at 450 nm. It could be possible that only smaller particles coming out of the precipitate were present in the redispersion and thus the PL spectrum was nearly the same as that of the supernatant.

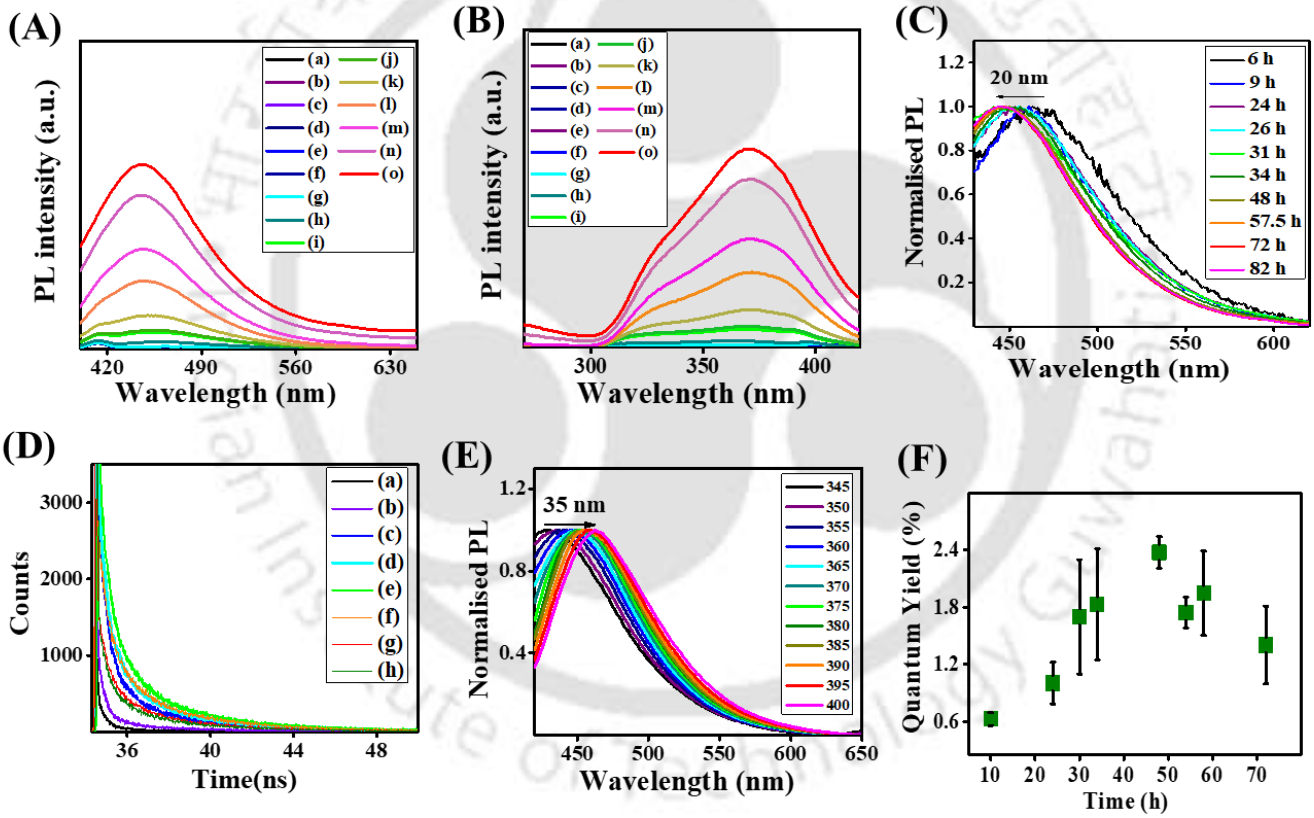

Figure 4. (**A**) Luminescence emission spectrum (λ_{ex} = 362 nm) of (a) Gd acetate and of reaction mixture at (b) 0 h, (c) 0.5 h, (d) 1 h, (e) 1.5 h, (f) 2 h, (g) 6 h, (h) 9 h, (i) 24 h, (j) 26 h, (k) 34 h, (l) 48 h, (m) 57.5 h, (n) 72 h and (o) 82 h. (**B**) Corresponding excitation spectrum of (a) Gd acetate and of reaction mixture at (b) 0 h, (c) 0.5 h, (d) 1 h, (e) 1.5 h, (f) 2 h, (g) 6 h, (h) 9 h, (i) 24 h, (j) 26 h, (k) 34 h, (l) 48 h, (m) 57.5, h (n) 72 h and (o) 82 h. (**C**) Normalized emission spectra of the reaction mixture at different time when excited at 362 nm showing 20 nm blue

shift. (**D**) Time-resolved photoluminescence spectra of the reaction mixture (a) 7 h, (b) 9 h, (c) 25 h, (d) 33 h, (e) 48 h, (f) 57 h, (g) 72 h and (h) 82 h. (**E**) Normalized emission spectra of the reaction mixture at 57 h with varying excitation wavelengths. (**F**) Quantum yield of the dispersion at different intervals of time.

Further, the PL lifetime (Figure 4D) was measured for samples at different time by exciting the dispersion using a 375 nm laser source. The lifetime values at different time of the reaction are tabulated in Table S2. The average lifetime at 9 h was 4.4 ± 0.1 ns, which decreased to 2.7 ± 1.0 ns at 48 h. At 57 h, when smaller sized particles populated the medium, the average lifetime further decreased to 1.9 ± 0.1 ns, which eventually increased to 2.6 ± 0.9 ns at 72 h. The lifetimes of supernatant and that of the redispersed pellet centrifuged at 72 h were 2.7 ± 1.1 ns and 2.8 ± 1.1 ns, respectively. The lifetimes of the redispersed pellet and supernatant were close to the average lifetimes observed at 57 h, which again confirms the presence of smaller sized particles in the supernatant and redispersed pellet obtained after centrifugation at 60 h (as mentioned before).

Further, it was observed that the dispersion exhibited excitation wavelength dependent emission. A maximum bathochromic shift of 35 nm was observed when the dispersion was excited from 345 nm to 400 nm with 5 nm increment of excitation wavelength (Figure 4E). Calculation of quantum yield (done using equation S1 in SI) for the dispersion at different time (Table S3) and its plot against time (Figure 4F) clearly showed the variation with time, which can be attributed to the variable sizes of nanoparticles. Importantly, there was a monotonic increase in quantum yield with time having maximum yield at 48 h with a value of 2.4 ± 0.2 %. This was consistent in the increase in the average particle size in the medium till that time. After that, there was a monotonic decrease in the quantum yield with time (Figure 4F.). The sharp decrease in its value at 58 h indicated the presence of a large number of smaller sized distinct nanoparticles, which again decreased the quantum yield. The average particle size continued to grow with time till 48 h, thus, increasing the PL quantum yield monotonically. Further, following precipitation out of the medium of the larger particles after 48 h, the smaller particles populated the same and thus the PL quantum yield decreased gradually with time.

Two control experiments were performed to understand the origin of optical properties. Aqueous solutions of ascorbic acid and Gd acetate (at the same concentrations used in the mixture) were

stirred in two separate vials for a few days. Time-dependent PL and UV-Vis spectra were recorded for both of the dispersions (Figure S16). With time, no discernible emission peak appeared for the Gd acetate solution (Figure S16D), however after a few days (3 days) of stirring a low intensity broad emission peak was observed for ascorbic acid unlike the intense peak observed for nanoparticles (Figure S16B). The peak maximum was at 450 nm and is probably due to the agglomeration of the ascorbic acid molecules. Further, the time-dependent UV-Vis spectrum of ascorbic acid did not give rise to (Figure S16A) any distinguishable peak in the range 250 – 450, indicating the absence of significant population of nanoparticles in the dispersion as similar to those formed in the mixture. These luminescent nanoparticles, having a maximum PL quantum yield of 2.4 ± 0.2%, in addition of their use as a MRI contrast agent could be of vital use as a fluorescent imaging probes.

MAGNETIC PROPERTIES

The samples from the reaction mixture collected at different times were centrifuged at 26000 rpm and the electron paramagnetic resonance (EPR) spectra of the solids collected were recorded (Figure 5A). The typical spectrum observed was broad with g value being around 2.1 as expected for cluster of Gd ions present together in solid form (Figure 5A).[52,61] The EPR spectra (Figure 5A) recorded for the dispersion at different times in the liquid phase gave sharp peak with g ≈ 2.1 for the hydrated Gd ions.[61,62] In addition to the EPR measurements, MH curves of the centrifuged nanoparticles were acquired (Figure 5B). There was slight change in the magnetisation value but that remained nearly the same with time (Table S4). The magnetisation values of the centrifuged product were recorded at 61 h, 66 h, 72 h and 100 h. The values at 61 h and 66 h were 0.9 emu/g and 0.8 emu/g respectively and for 72 h and 100 h were 0.9 emu/g and 0.8 emu/g, respectively. Thus, the values did not change much with time or more precisely with particle size and remained close to ~1 emu/g.

Time-dependent measurements of longitudinal (T1) and transverse (T2) relaxation times were pursued at 1.41 T and 37 °C and are tabulated in Table S5 and Table S6. Two separate solutions – one containing the reaction mixture of Gd acetate and ascorbic acid (Figure 5C) and another containing only Gd acetate (Figure S17) were stirred continuously and relaxation times at different times were measured. Initially, the reaction mixture containing Gd acetate and ascorbic acid showed an enhancement in both T1 and T2 relaxation times as mentioned in the subsequent

section but after 48 h (when the dispersion became colloidal) both T1 and T2 gradually decreased. The solution containing only Gd acetate did not show any change in its relaxation times with respect to reaction time and T1 and T2 values remained near 14.5 ms and 12.7 ms respectively till 114 h. Similarly, T1/T2 ratio (Figure 5D) showed a consistent change with time. The ratio was around 1.15 ± 0.01 at 30 min of reaction that remained at 1.15 ± 0.01 till 58 h and as the time progressed further, there was an increase in its value with 1.21 ± 0.01 at 72 h and 1.29 ± 0.01 at 105 h.

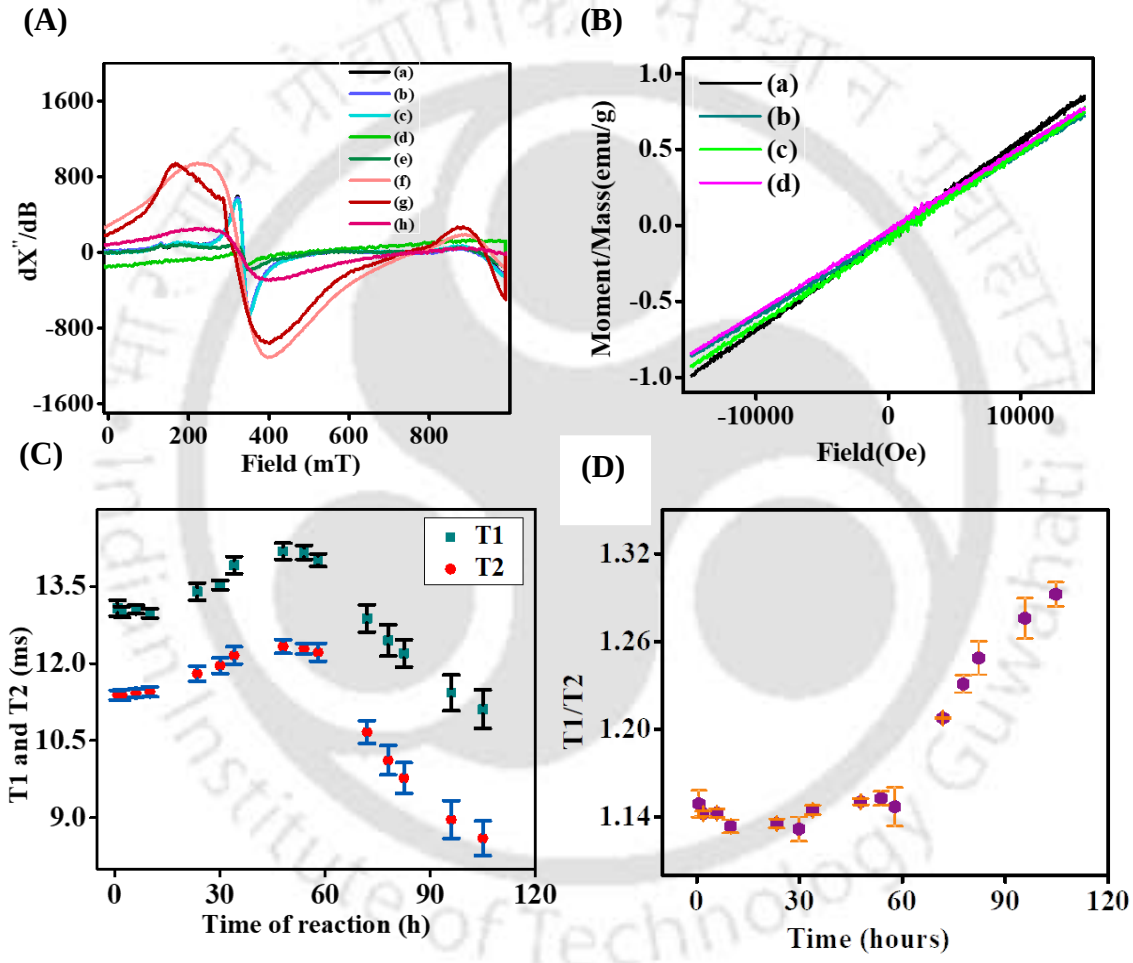

Figure 5. (**A**) EPR spectra of the dispersion at (a) 5 min, (b) 14 h, (c) 24 h, (d) 48 h and (e) 72 h and that of the centrifuged product at (f) 62 h, (g) 71 h and (h) 95 h. (**B**) MH curves of the product obtained after centrifugation at (a) 61 h, (b) 66 h, (c) 72 h and (d) 100 h. (**C**) T1 and T2 relaxation time at different time interval. (**D**) Ratio of T1 and T2 at different time of the reaction progression.

At 30 min, relaxation times measured at 37 °C for the reaction mixture were lower than the values obtained for only Gd acetate. At this time, Gd ions interacted with ascorbic acid to have possibly formed multi-nuclear complexes of Gd ascorbate along with small nanoparticles Thus, at 30 min of standing, the mixture resulted in T1 = 13.1 ± 0.2 ms and T2 = 11.4 ± 0.1 ms. The values were slightly less when compared with T1 = 14.5 ms and T2 = 12.7 ms for only Gd acetate solution at 30 min of standing. At 10 h, the nanoparticles of sizes 2-4 nm populated the dispersion (Figure S2F). At this time, T1 and T2 values were 13.0 ± 0.1 ms and 11.4 ± 0.1 ms respectively. These 2-4 nm particles were assembled at 24 h to form the larger particles having size in the range 20 – 60 nm size that resulted in solvent exclusion. The relaxation times at this time were T1 = 13.4 ± 0.2 ms and T2 = 11.8 ± 0.1 ms and were again less but close to the T1 and T2 values of Gd acetate. Again at 48 h, the values for the dispersion were T1 = 14.2 ± 0.2 ms and T2 = 12.3 ± 0.1 ms and they were similar to the relaxation time values obtained for Gd acetate (T1 = 14.2 ms and T2 = 12.4 ms). In other words, larger nanoscale particles would have the properties of metal ions in the nanoparticles with ascorbate as the neighboring ions. The maximum values of relaxation times were found to be at 48 h after which both the relaxation times slowly decreased. The trend was similar to that of quantum yield as depicted in Figure 4F. Both relaxation time and quantum yield versus time plots suggested that agglomeration leading to larger nanoparticles peaked at 48 h. This was also evident from TEM images recorded for the samples at different times (Figure 1). The larger particles started precipitating out of the medium typically at 60 h and the medium was again populated with smaller nanoparticles that continued to grow with time (Figure 1F). At 58 h, the measured T1 and T2 values were 14.0 ± 0.1 ms and 12.2 ± 0.2 ms, respectively. Those continued to decrease to values of 11.1 ± 0.4 ms and 8.6 ± 0.4 ms, respectively, at 105 h. The concentration of Gd ions in the medium till the dispersion did not start precipitating out was constant. Thus, the change in relaxation time suggested that the effective concentration of the solvated Gd ions decreased continuously with the formation of the nanoparticles in the dispersion medium. The observation of significant relaxation times at 105 h, notwithstanding the precipitation of significant amount of Gd ions through the formation of complex nanoparticles, indicated the importance of nanoscale particles of the salt – as opposed to the solvated ions – in providing option of superior contrast agent for MRI. The relaxivity values (r1 and r2) were calculated using equation S2 in SI and the calculated values are given in Table S5 and Table S6. The reported relaxivity value (r1) of clinically approved Gd DOTA and Gd

DTPA and most of the other Gd complex based contrast agents are in the range 2.8 – 4.9 $mM^{-1}s^{-1}$ (Table S7).[63] The calculated r1 value for the dispersion at 10 h was 8.5 ± 0.1 $mM^{-1}s^{-1}$ which decreased to 7.8 ± 0.1 $mM^{-1}s^{-1}$ at 48 h and then started to increase after 48 h and was maximum at 105 h (9.95 ± 0.3 $mM^{-1}s^{-1}$). Although the change in relaxation time was ±2 ms, they were indications of small change in the properties with the particle sizes.

We further pursued the effects of Fe and Zn ions on the stability of the nanoparticles in the dispersion medium. The amount of free Zn (typically 70-150 µg/dL)[65,67] and Fe (typically 60 to 150 µg/dL)[66,67] in human serum can interfere with the stability of the Gd ascorbate nanoparticles and transmetallation may occur.[64] In order to test the stability of the dispersions in the presence of the above mentioned ions, Fe(III) (0.5 mM and 24.4 µM) and Zn(II) (2.1 mM) salts were added separately to the dispersion at 48 h and the stability of the same was checked. There was no immediate precipitation of the nanoparticles out of the medium following the addition of the salts. However, addition of 0.5 mM Fe salt seemed to have hastened the precipitation and Zn did not seem to have affected the rate of precipitation. For example, after addition of Zn(II) salt, the medium became colloidal at 60 h (that is 12 h after addition), which was the same as that without adding the salt. But the precipitation started to occur in 5 h following addition of 0.5 mM Fe(III) salt. Further, the photoluminescence of the medium did not change immediately after addition of the salts. However, the photoluminescence started to decrease at 24 h following the addition of 0.5 mM Fe(III) salt (Figure S18A), thus, supporting the loss of the nanoparticles through precipitation out of the medium. The intensity of emission of the dispersion was not affected when Zn was added to the medium (Figure S18B). The experiment was repeated with 24.4 µM $FeCl_3.6H_2O$. At 48 h, Fe(III) salt (40 µL of 9.25 mM $FeCl_3.6H_2O$ solution) was added to the dispersion and the PL spectrum was recorded with time to check the stability of the nanoparticles. The observed PL spectrum (Figure S18C) was similar to the PL spectrum of the dispersion in absence of iron (Figure 4A). High concentration of iron (0.5 mM) might have affected the PL spectrum (Figure S18A) of the nanoparticles after 24 h of addition of Fe ions due to high ionic strength, which could have also hastened the precipitation process. As human serum typically contains 60 to 150 µg/dL of free iron, it is less likely to interfere with the nanoparticles. It was further investigated through X-ray photoelectron (XPS) spectroscopy study whether Fe ions had indeed interacted with the nanoparticles (Figure S18). Thus, the dispersion was

centrifuged following addition of iron salt (0.5 mM) and XPS analysis of the precipitate was pursued. The atomic percentages of Gd (Figure S18G) and Fe (Figure S18H) were 4.16% and 1.39% respectively, and those of C (Figure S18E) and O (Figure S18F) were 46.87% and 47.58%, respectively (Table S8). This was compared with the percentage of Gd in the nanoparticle unit of formula $Gd_4(C_6H_6O_6)_5(C_6H_7O_6)_2(C_6H_8O_6)_3$, which was calculated to be 3.22% (while not taking the H-atoms into consideration; by taking H-atoms of the ascorbic acid into consideration - the percentage was calculate to be 2.08 %). The C and O atomic percentages were calculated to be 48.38 % and 48.38 % when H atoms were not considered. The presence of Gd ions in the precipitated dispersion discounted the transmetallation; however, Fe might have been bonded to the free surface OH groups of the ascorbates present in the nanoparticles.

The effect of buffer on the relaxivity of the reaction mixture was observed. To check the stability of nanoparticles at pH = 7.4, 1mL of reaction mixture at 48 h was added to 3 mL of 4-(2-hydroxyethyl)-1-piperazineethanesulfonic acid (HEPES) buffer solution (pH =7.4) resulting in Gd concentration of 2.25 mM. The relaxation times of the resulting dispersion was checked. The relaxation times obtained at 37°C at 1.41T were T1 = 80.0 ± 0.8 ms and T2 = 58.2 ± 2.2 ms. These results were compared with same amount of reaction mixture diluted with an equal amount of deionized water in place of buffer solution (1 mL of reaction mixture added to 3 mL of deionized water) resulting in Gd concentration of 2.25 mM. The relaxation times obtained were T1 = 60.5 ± 1.1 ms and T2 = 52.9 ± 0.8 ms. The T1 and T2 values were higher as in case of buffer due to interaction of surface Gd of the nanoparticles with the ions present in the buffer and thus resulting in decrease of relaxivity (Table S9). Also, the unreacted Gd ions present in the reaction mixture precipitates out after being added to HEPES buffer solution and in turn affects the relaxivity of the reaction mixture. Thus, a moderate change in relaxation times of the reaction mixture in buffer solution was observed when compared to the reaction mixture in water considering the effect on surface Gd ions and unreacted Gd ions in the reaction mixture.

It may be mentioned here that the dispersion could be centrifuged at 72 h at low speed (14000 rpm) to separate out the larger particles, keeping the smaller nanoparticles in the medium. Following centrifugation, the TEM images of the supernatant were acquired and the smaller nanoparticles having typical sizes in the range 1-3 nm were present in the aggregated structure forming a branched network of particles (Figure S19). It has been reported that nanoscale

particles of diameters less than 10 nm undergo facile renal clearance.[68,69] The smaller nanoparticles still provided significant relaxivity as was observed at 105 h. The photoluminescent dispersion of Gd ascorbate nanoparticles with sizes less than 10 nm may provide a superior option as MRI contrast agent.

Conclusion

To summarize, we have shown that an aqueous mixture of Gd-acetate and ascorbic acid – under ambient conditions - led to the formation of nanocrystals of Gd ascorbate complex, the sizes of which evolved with time. The nanocrystals showed unique luminescent and magnetic properties at different time, owing to the different size of the particles that populated the medium. The presence of different sized particles in the medium was confirmed by TEM images and the chemical nature of nanoparticle was evaluated through ESI-MS. The dispersion was luminescent, emitting in the blue region and the magnetization of the material after centrifugation was found to be ~1emu/g. The value did not change significantly with the sizes of the particles present in the medium. The quantum yield vs time plot and the relaxation times (T1 and T2) vs reaction time showed a similar trend where both increased with time at first and then decreased continuously after 48 h. This change was explained by the formation of different sized particles in the dispersion at different times. The dispersion after 48 h showed better relaxation as the larger particles precipitated out and a greater number of smaller sized particles in the range 2-10 nm were formed in the medium. The results reported herein suggest that the idea of synthesis of nanoscale Gd-ascorbate particles and their potential use as a safer MRI contrast agent could potentially be tested for practical use.

Experimental Section:

Materials: Gadolinium acetate hydrate (Sigma Aldrich), ascorbic acid (Sigma Aldrich), HEPES solution (Sigma Aldrich) and acetonitrile (HPLC grade) were used as procured without any further purification. Milli-Q grade water (resistivity 18.2 MΩ cm-1 at 25˚C) was used for all experiments.

Instruments:

Fluorescence emission and excitation spectra of all samples were acquired using HORIBA Fluoromax 4 spectrophotometer. UV-Vis spectra were recorded using Agilent Cary Series UV-

vis spectrophotometer. Fluorescence lifetime was measured using a time-correlated single-photon counting (TCSPC) set up from Horiba instruments that uses a 375 nm laser diode. Transmission electron microscopy (TEM) images and high resolution TEM (HRTEM) images were acquired using JEOL-JEM 2100 transmission electron microscope. Electrospray ionization (ESI) mass spectrometric analyses were performed using Agilent Accurate Mass (Q-TOF 6520) spectrometer in ESI positive mode. Fourier transform infrared spectroscopy (FTIR) analyses were performed using the Perkin Elmer (Spectrum Two) FTIR spectrometer in ATR mode (Perkin Elmer UATR spectrum Two). Vibrating sample magnetometer (VSM) analysis were carried out to record the MH curve using with Lakeshore Vibrating sample magnetometer (Model:7410 series). A PHI 5000 Versa Probe II, FEI Inc. instrument was used for X-ray photoelectron spectroscopy (XPS) analyses. X-band EPR measurement was performed using a JEOL (Model: JES-FA200) spectrometer. The longitudinal relaxation (T1) and transverse (T2) times at 1.41 T were measured using BRUKER minispec mq60 NMR Analyzer.

Synthesis of Gd ascorbate nanoparticles:

Gadolinium acetate hydrate (50.0 mg) was dissolved in 15.0 mL of Milli-Q water in a clean vial. To the above-mentioned solution, 63 mg of ascorbic acid was added and the resultant mixture was stirred at room temperature (~25 ˚C) for up to 60 h.

Photoluminescence and UV-vis absorbance study:

3.0 mL of aliquot of the resultant dispersion containing mixture of gadolinium acetate hydrate and ascorbic acid was taken in a quartz fluorescence cuvette. The photoluminescence and UV-vis absorption spectra were acquired at different interval of time.

TEM sample preparation:

40.0 µL of the dispersion containing the mixture of gadolinium acetate hydrate and ascorbic acid was diluted with 1 mL Milli-Q water. 7.0 µL of the resultant dispersion was drop-cast on carbon coated copper TEM grid and was allowed to dry overnight.

Purification of the luminescent product of reaction between ascorbic acid and gadolinium acetate hydrate:

The luminescent dispersion of the product of reaction between ascorbic acid and gadolinium acetate hydrate was centrifuged at 26000 rpm at 10 °C for 12 min. The so-obtained pellet was redispersed in water and was used for further experiments.

Measurement of T1 and T2 relaxation time:

220 µL of the aliquot was taken from the reaction mixture and was used for recording the relaxation times.

EPR and VSM sample preparation:

The product obtained after centrifugation was dried and was then wrapped in teflon tape for the VSM analysis. The EPR spectrum of the reaction mixture was recorded by taking small amount of aliquot in capillary tube using a syringe.

Sample preparation for ESI- Mass spectrometric analysis:

600 µL aliquot was taken from the reaction mixture and was dissolved in acetonitrile-water (60:40 V/V) mixture and mass spectra of the samples were acquired in ESI positive mode.

Simulation of mass spectra:

Mass spectra simulation was pursued using mMass software.

Computational studies:

All the optimization of the structures and time-dependent density functional theory (TD-DFT) calculations were done using GAUSSIAN 16 software package.[58] Optimization was carried out using density functional theory (DFT) calculations in M06-2X[59] functional in Gen basis set. Gd was modelled using mwb53 pseudopotential with corresponding basis set and 6-31G(d) basis set was used for all other atoms. TD-DFT calculations were performed in both vapor and solvent phases.

References

1. Caravan, P.; Ellison, J. J.; McMurry, T. J.; Lauffer, R. B. Gadolinium(III) Chelates as MRI Contrast Agents: Structure, Dynamics, and Applications. *Chem. Rev.* **1999**, *99*, 2293– 2352.

2. Xu, K.; Xu, N.; Zhang, B.; Tang, W.; Ding, Y.; Hu, A. Gadolinium complexes of macrocyclic diethylenetriamine-*N*-oxide pentaacetic acid-bisamide as highly stable MRI contrast agents with high relaxivity. *Dalton Trans.*, **2020**, *49*, 8927-8932.

3. Li, Y.; Beija, M.; Laurent, S.; Elst, LV.; Muller, RN.; Duong, HT.; Lowe, AB.; Davis, TP.; Boyer, C. Macromolecular ligands for gadolinium MRI contrast agents. *Macromolecules*. **2012**, *45*, 4196–204.

4. Zairov, R.; Pizzanelli, S.; Dovzhenko, A. P.; Nizameev, I.; Orekhov, A.; Arkharova, N.; Podyachev, S. N.; Sudakova, S.; Mustafina, A. R.; Calucci, L. Paramagnetic Relaxation Enhancement in Hydrophilic Colloids Based on Gd(III) Complexes with Tetrathia- and Calix[4]arenes. *The Journal of Physical Chemistry C* **2020,** *124* (7), 4320-4329.

5. Bonnet, C. S.; Fries, P. H.; Crouzy, S.; Delangle, P. Outer-Sphere Investigation of MRI Relaxation Contrast Agents. Example of a Cyclodecapeptide Gadolinium Complex with Second-Sphere Water. *J. Phys. Chem. B* **2010**, *114* (26), 8770– 8781.

6. Pinto, L. F.; Lloveras, V.; Zhang, S.; Liko, F.; Veciana, J.; Muñoz-Gómez, J. L.; Vidal-Gancedo, J. Fully Water-Soluble Polyphosphorhydrazone-Based Radical Dendrimers Functionalized with Tyr-PROXYL Radicals as Metal-Free MRI T1 Contrast Agents. *ACS Appl. Bio Mater.* **2020**, *3*, 369– 376.

7. Zhang, S.; Lloveras, V.; Lope-Piedrafita, S.; Calero-Pérez, P.; Wu, S.; Candiota, A. P.; Vidal-Gancedo, J. Metal-Free Radical Dendrimers as MRI Contrast Agents for Glioblastoma Diagnosis: Ex Vivo and In Vivo Approaches. *Biomacromolecules* **2022**, *23* (7), 2767-2777.

8. Villaraza, A. J. L.; Bumb, A.; Brechbiel, M. W. Macromolecules, dendrimers, and nanomaterials in magnetic resonance imaging: the interplay between size, function, and pharmacokinetics. *Chem. Rev.* **2010**, *110*, 2921– 2959.

9. Zhao, Z.; Zhen, M.; Zhou, C.; Li, L.; Jia, W.; Liu, S.; Li, X.; Liao, X.; Wang, C. A gadofullerene based liver-specific MRI contrast agent for an early diagnosis of orthotopic hepatocellular carcinoma. *J. Mater. Chem. B* **2021**, *9*, 5722-5728.

10. Wang, S.; Zhou, Z.; Wang, Z.; Liu, Y.; Jacobson, O.; Shen, Z.; Fu, X.; Chen, Z.-Y.; Chen, X. Gadolinium Metallofullerene-Based Activatable Contrast Agent for Tumor Signal Amplification and Monitoring of Drug Release. *Small* **2019**, *15*, 1900691.

11. Shu, C.-Y.; Zhang, E.-Y.; Xiang, J.-F.; Zhu, C.-F.; Wang, C.-R.; Pei, X.-L.; Han, H.-B. Aggregation studies of the water-soluble gadofullerene magnetic resonance imaging contrast agent: $[Gd@C_{82}O_6(OH)_{16}(NHCH_2CH_2COOH)_8]_x$. *J. Phys. Chem. B* **2006**, *110*, 15597– 15601.

12. Shu, C.; Corwin, F. D.; Zhang, J.; Chen, Z.; Reid, J. E.; Sun, M.; Xu, W.; Sim, J. H.; Wang, C.; Fatouros, P. P., et al. Facile preparation of a new gadofullerene-based magnetic resonance imaging contrast agent with high 1H relaxivity. *Bioconjugate Chem.* **2009**, *20*, 1186– 1193.

13. Song, Y.; Xu, X.; MacRenaris, K.; Zhang, X.-Q.; Mirkin, C.; Meade, T. Multimodal gadolinium-enriched DNA–gold nanoparticle conjugates for cellular imaging. *Angew Chem Int Ed.* **2009,** *48*, 9143–9147.

14. Reynolds, C. H.; Annan, N.; Beshah, K.; Huber, J. H.; Shaber, S. H.; Lenkinski, R. E.; Wortman, J. A. Gadolinium-Loaded Nanoparticles: New Contrast Agents for Magnetic Resonance Imaging. *J. Am. Chem. Soc.* **2000**, *122*, 8940– 8945.

15. Sun, S.-K.; Dong, L.-X.; Cao, Y.; Sun, H.-R.; Yan, X.-P. Fabrication of Multifunctional Gd_2O_3/Au Hybrid Nanoprobe via a One-Step Approach for Near-Infrared Fluorescence and Magnetic Resonance Multimodal Imaging In Vivo. *Anal. Chem.* **2013**, *85* (17*)*, 8436– 8441.

16. Shao, Y.-Z.; Liu, L.-Z.; Song, S.-q.; Cao, R.-h.; Liu, H.; Cui, C.-y.; Li, X.; Bie, M.-J.; Li, L. A Novel One-Step Synthesis of Gd3+-Incorporated Mesoporous SiO2 Nanoparticles for Use as an Efficient MRI Contrast Agent Contrast Media. *Mol. Imaging* **2011**, *6* (2), 110– 118.

17. Tian, X.; Shao, Y.; He, H.; Liu, H.; Shen, Y.; Huang, W.; Li, L. Nanoamplifiers Synthesized from Gadolinium and Gold Nanocomposites for Magnetic Resonance Imaging. *Nanoscale* **2013**, *5* (8), 3322– 3329.

18. Lin, Y.-S.; Hung, Y.; Su, J.-K.; Lee, R.; Chang, C.; Lin, M.-L.; Mou, C.-Y. Gadolinium(III)-Incorporated Nanosized Mesoporous Silica as Potential Magnetic Resonance Imaging Contrast Agents. *J. Phys. Chem. B* **2004**, *108*, 15608– 15611.

19. Pan, Y.; Chen, W.; Yang, J.; Zheng, J.; Yang, M.; Yi, C. Facile Synthesis of Gadolinium Chelate-Conjugated Polymer Nanoparticles for Fluorescence/Magnetic Resonance Dual-Modal Imaging. *Analytical Chemistry* **2018,** *90* (3), 1992-2000.

20. Briley-Saebo, K. C.; Geninatti-Crich, S.; Cormode, D. P.; Barazza, A.; Mulder, W. J.; Chen, W.; Giovenzana, G. B.; Fisher, E. A.; Aime, S.; Fayad, Z. A. High-Relaxivity Gadolinium-Modified High-Density Lipoproteins as Magnetic Resonance Imaging Contrast Agents. *J. Phys. Chem. B* **2009**, *113*, 6283– 6289.

21. Bridot, J.-L.; Faure, A.-C.; Laurent, S.; Rivière, C.; Billotey, C.; Hiba, B.; Janier, M.; Josserand, V.; Coll, J.-L.; Vander Elst, L., et al. Hybrid Gadolinium Oxide Nanoparticles: Multimodal Contrast Agents for in Vivo Imaging. *J. Am. Chem. Soc.* **2007**, *129* (16), 5076– 5084.

22. Viger, M. L.; Sankaranarayanan, J.; de Gracia Lux, C.; Chan, M.; Almutairi, A. Collective Activation of MRI Agents via Encapsulation and Disease-Triggered Release. *J. Am. Chem. Soc.* **2013**, *135*, 7847– 7850.

23. Mekuria, S. L.; Debele, T. A.; Tsai, H.-C. Encapsulation of Gadolinium Oxide Nanoparticle (Gd2O3) Contrasting Agents in PAMAM Dendrimer Templates for Enhanced Magnetic Resonance Imaging in Vivo. *ACS Appl. Mater. Interfaces* **2017**, *9*, 6782– 6795.

24. Lin, X.; Zhang, Q.; Chen, J.; Kong, X.; Long, L.S.; Wang, C.; Lin, W. Gadolinium nicotinate clusters as potential MRI contrast agents. *RSC Adv.* **2015**, *5*, 2914.

25. He, C.; Wu, X.; Kong, J.; Liu, T.; Zhang, X.; Duan, C. A Hexanuclear Gadolinium-Organic Octahedron as a Sensitive MRI Contrast Agent for Selectively Imaging Glucosamine in Aqueous Media. *Chem. Commun.* **2012**, *48*, 9290– 9292.

26. Peller, M.; Böll, K.; Zimpel, A.; Wuttke, S. Metal–organic framework nanoparticles for magnetic resonance imaging. *Inorg. Chem. Front.* **2018**, *5*, 1760– 1779.

27. Hatakeyama, W.; Sanchez, T. J.; Rowe, M. D.; Serkova, N. J.; Liberatore, M. W.; Boyes, S. G. Synthesis of Gadolinium Nanoscale Metal-Organic Framework with Hydrotropes: Manipulation of Particle Size and Magnetic Resonance Imaging Capability. *ACS Appl. Mater. Interfaces* **2011**, *3*, 1502– 1510.

28. Liu, J.-L.; Chen, Y.-C.; Guo, F.-S.; Tong, M.-L. Recent advances in the design of magnetic molecules for use as cryogenic magnetic coolants. *Coord. Chem. Rev.* **2014**, *281*, 26– 49.

29. Li, J.; Gómez-Coca, S.; Dolinar, B. S.; Yang, L.; Yu, F.; Kong, M.; Zhang, Y. Q.; Song, Y.; Dunbar, K. R. Hexagonal Bipyramidal Dy(III) Complexes as a Structural Archetype for Single-Molecule Magnets. *Inorg. Chem.* **2019**, *58*, 2610– 2617.

30. Zheng, X.-Y.; Xie, J.; Kong, X.-J.; Long, L.-S.; Zheng, L.-S. Recent advances in the assembly of high-nuclearity lanthanide clusters. *Coord. Chem. Rev.* **2019**, *378*, 222– 236.

31. Li, Y.-L.; Wang, H.-L.; Zhu, Z.-H.; Li, J.; Zou, H.-H.; Liang, F.-P. A Series of High-Nuclear Gadolinium Cluster Aggregates with a Magnetocaloric Effect Constructed through Two-Component Manipulation. *Inorg. Chem.* **2021**, *60*, 16794– 16802.

32. Gálico, D. A.; Kitos, A. A.; Ovens, J. S.; Sigoli, F. A.; Murugesu, M. Lanthanide-Based Molecular Cluster-Aggregates: Optical Barcoding and White-Light Emission with Nanosized $\{Ln_{20}\}$ Compounds. *Angew. Chem., Int. Ed.* **2021**, *60*, 6130– 6136.

33. Zhang, Y.-X.; Zhang, Y.-H.; Liu, B.-Y.; Wang, W.-M.; Tang, G.-P.; Wei, H.-Y.; Wu, Z.-L.. Synthesis, luminescence and magnetic properties of tetranuclear lanthanide-based (Eu4, Gd4 and Dy4) clusters. *New J. Chem*. **2018**, *42*, 18305-18311.

34. Gálico, D. A.; Ovens, J. S.; Murugesu, M. NIR-to-NIR Emission on a Water-Soluble $\{Er_6\}$ and $\{Er_3Yb_3\}$ Nanosized Molecular Wheel. *Nanoscale* **2020**, *12*, 11435– 11439

35. Shi, D.; Yang, X.; Chen, H.; Ma, Y.; Schipper, D.; Jones, R. A. Self-assembly of luminescent 42-metal lanthanide nanowheels with sensing properties towards metal ions and nitro explosives. *J. Mater. Chem. C* **2019**, *7*, 13425– 13431.

36. Shi, D.; Yang, X.; Xiao, Z.; Liu, X.; Chen, H.; Ma, Y.; Schipper, D.; Jones, R. A. A 42-metal Yb(III) nanowheel with NIR luminescent response to anions. *Nanoscale* **2020**, *12*, 1384– 1388.

37. Thielemann, D. T.; Wagner, A. T.; Rosch, E.; Kolmel, D. K.; Heck, J. G.; Rudat, B.; Neumaier, M.; Feldmann, C.; Schepers, U.; Brase, S., et al. Luminescent cell-penetrating pentadecanuclear lanthanide clusters. *J. Am. Chem. Soc*. **2013**, *135*, 7454– 7457.

38. Woodruff, D. N.; Winpenny, R. E. P.; Layfield, R. A. Lanthanide Single-Molecule Magnets. *Chem. Rev*. **2013**, *113*, 5110– 5148.

39. Nehrkorn, J.; Greer, S. M.; Malbrecht, B. J.; Anderton, K. J.; Aliabadi, A.; Krzystek, J.; Schnegg, A.; Holldack, K.; Herrmann, C.; Betley, T. A., et al. Spectroscopic Investigation of a Metal-Metal-Bonded Fe_6 Single-Molecule Magnet with an Isolated S = 19/2 Giant-Spin Ground State. *Inorg. Chem.* **2021**, *60*, 4610– 4622.

40. Wu, J.; Li, X.-L.; Zhao, L.; Guo, M.; Tang, J. Enhancement of Magnetocaloric Effect through Fixation of Carbon Dioxide: Molecular Assembly from Ln_4 to Ln_4 Cluster Pairs. *Inorg. Chem*. **2017**, *56*, 4104– 4111.

41. Sarkar, A.; Gómez-García, C. J.; Benmansour, S.; Nayek, H. P. Trinuclear Lanthanide Coordination Clusters: Single-Molecule-Magnet Behavior and Catalytic Activity in the Friedel-Crafts Alkylation Reaction. *ChemPlusChem* **2019**, *84*, 974.

42. Chen, Y.-C.; Guo, F.-S.; Zheng, Y.-Z.; Liu, J.-L.; Leng, J.-D.; Tarasenko, R.; Orendáč, M.; Prokleška, J.; Sechovský, V.; Tong, M.-L. Gadolinium(III)-Hydroxy Ladders Trapped in Succinate Frameworks with Optimized Magnetocaloric Effect. *Chem. - Eur. J.* **2013**, *19*, 13504– 13510.

43. Luo, X.-M.; Hu, Z.-B.; Lin, Q.-F.; Cheng, W.-W.; Cao, J.-P.; Cui, C.-H.; Mei, H.; Song, Y.; Xu, Y. Exploring the Performance Improvement of Magnetocaloric Effect Based Gd-Exclusive Cluster Gd_{60}. *J. Am. Chem. Soc.* **2018**, *140*, 11219– 11222.

44. Chakarawet, K.; Atanasov, M.; Marbey, J.; Bunting, P. C.; Neese, F.; Hill, S.; Long, J. R. Strong Electronic and Magnetic Coupling in M_4 (M = Ni, Cu) Clusters via Direct Orbital Interactions between Low-Coordinate Metal Centers. *J. Am. Chem. Soc.* **2020**, *142*, 19161– 19169.

45. Noodleman, L.; Case, D. A. Density-Functional Theory of Spin Polarization and Spin Coupling in Iron–Sulfur Clusters. *Adv. Inorg. Chem.* **1992**, *38*, 423– 470.

46. Sweet, L. E.; Roy, L. E.; Meng, F.; Hughbanks, T. Ferromagnetic Coupling in Hexanuclear Gadolinium Clusters. *J. Am. Chem. Soc.* **2006**, *128*, 10193– 10201.

47. Bencini, A.; Ghilardi, C. A.; Midollini, S.; Orlandini, A.; Russo, U.; Uytterhoeven, M. G.; Zanchini, C. Crystal and Molecular Structure, Magnetic Properties and Scattered-Wave Description of the Electronic Structure of the Hexanuclear Octahedral Clusters $[Fe_6(\mu_3\text{-}S)_8(PEt_3)_6][PF_6]_n$ (n = 1 or 2). *J. Chem. Soc., Dalton Trans.* **1995**, *963* (6), 963– 974.

48. Prince, M. R.; Zhang, H. L.; Zou, Z. T.; Staron, R. B.; Brill, P. W. Incidence of Immediate Gadolinium Contrast Media Reactions. *AJR, Am. J. Roentgenol.* **2011**, *196*, W138– W143.

49. Grobner, T. Gadolinium—a specific trigger for the development of nephrogenic fibrosing dermopathy and nephrogenic systemic fibrosis? *Nephrol. Dial. Transpl.* **2006,** *21*, 1104–1108.

50. Gale, E.M.; Atanasova, I.P.; Blasi, F.; Ay, I.; Caravan, P. A manganese alternative to gadolinium for MRI contrast. *J. Am. Chem Soc.* **2015**, *137*, 15548–15557

51. Li, H.; Meade, T. J. Molecular Magnetic Resonance Imaging with Gd(III)-Based Contrast Agents: Challenges and Key Advances. *J. Am. Chem. Soc.* **2019**, *141*, 17025– 17041.

52. Wahsner, J.; Gale, E. M.; Rodriguez-Rodriguez, A.; Caravan, P. Chemistry of MRI Contrast Agents: Current Challenges and New Frontiers. *Chem. Rev.* **2019**, *119*, 957– 1057.

53. Wang, H.; Jordan, V. C.; Ramsay, I. A.; Sojoodi, M.; Fuchs, B. C.; Tanabe, K. K.; Caravan, P.; Gale, E. M. Molecular Magnetic Resonance Imaging Using a Redox-Active Iron Complex. *J. Am. Chem. Soc.* **2019**, *141*, 5916– 5925.

54. Pan, D.; Schmieder, A. H.; Wickline, S. A.; Lanza, G. M. Manganese-based MRI contrast agents: past, present, and future. *Tetrahedron* **2011**, *67*, 8431– 8444.

55. Bertin, A.; Michou-Gallani, A. I.; Gallani, J. L.; Felder-Flesch, D. In vitro neurotoxicity of magnetic resonance imaging (MRI) contrast agents: influence of the molecular structure and paramagnetic ion. *Toxicol. In Vitro* **2010**, *24*, 1386– 1394.

56. Bouabid, S.; Tinakoua, A.; Lakhdar-Ghazal, N.; Benazzouz, A. Manganese neurotoxicity: behavioral disorders associated with dysfunctions in the basal ganglia and neurochemical transmission. *J. Neurochem*. **2016**, *136*, 677-691.

57. B.S. Levy, W.J. Nassetta, Neurologic effects of manganese in humans: a review. *Int. J. Occup. Environ. Health* **2003,** *9*, 153-163.

58. Frisch, M. J.; Trucks, G. W.; Schlegel, H. B.; Scuseria, G. E.; Robb, M. A.; Cheeseman, J. R.; Scalmani, G.; Barone, V.; Mennucci, B.; Petersson, G. A., et al. *Gaussian 16*, Revision C.01; Gaussian Inc.: Wallingford CT, 2016.

59. Zhao, Y.; Truhlar, D. G. The M06 suite of density functionals for main group thermochemistry, thermochemical kinetics, noncovalent interactions, excited states, and transition elements: two new functionals and systematic testing of four M06-class functionals and 12 other functionals. *Theor. Chem. Acc.* **2008**, *120*, 215– 241.

60. Basu, S.; Hajra, A.; Chattopadhyay, A. An ambient complexation reaction of zinc acetate and ascorbic acid leads to a new form of nanoscale particles with emergent optical properties. *Nanoscale Adv.* **2021**, *3*, 3298–3305.

61. Rast, S.; Borel, A.; Helm, L.; Belorizky, E.; Fries, P. H.; Merbach, A. E. EPR Spectroscopy of MRI-Related Gd(III) Complexes: Simultaneous Analysis of Multiple Frequency and Temperature Spectra, Including Static and Transient Crystal Field Effects. *J. Am. Chem. Soc.* **2001**, *123* (11), 2637– 2644.

62. Leniec, G.; Kaczmarek, S. M.; Typek, J.; Kołodziej, B.; Grech, E.; Schilf, W. Spectroscopic and Magnetic Properties of a Gadolinium Macrobicyclic Complex. *J. Phys.: Condens. Matter* **2006**, *18*, 9871.

63. Rohrer, M.; Bauer, H.; Mintorovitch, J.; Requardt, M.; Weinmann, H. J. Comparison of magnetic properties of MRI contrast media solutions at different magnetic field strengths. *Invest. Radiol.* **2005**, *40*, 715– 724.

64. Sherry, A.D.; Caravan, P.; Lenkinski, R.E. Primer on gadolinium chemistry. *J. Magn. Reson. Imaging*, **2009**, *30*, 1240-1248.

65. Oldewage-Theron, W.H.; Samuel, F.O.; Venter, C.S. Zinc deficiency among the elderly attending a care centre in Sharpeville, South Africa. *Journal of Human Nutrition and Dietetics* **2008**, *21*, 566-574.

66. Burns, E. R.; Goldberg, S. N.; Lawrence, C.; Wenz, B. Clinical Utility of Serum Tests for Iron Deficiency in Hospitalized Patients, *American Journal of Clinical Pathology* **1990**, *93*, 240–245.

67. Buxaderas, S. C.; Farre-Rovira, R. Whole blood and serum zinc levels in relation to sex and age. *Rev Esp Fisiol* **1985,** *41*, 463–470.

68. Li, X.; Sun, Y.; Ma, L.; Liu, G.; Wang, Z. The Renal Clearable Magnetic Resonance Imaging Contrast Agents: State of the Art and Recent Advances. *Molecules* **2020**, *25*, 5072.

69. Choi, C. H. J.; Zuckerman, J. E.; Webster, P.; Davis, M. E. Targeting Kidney Mesangium by Nanoparticles of Defined Size. *Proc. Natl. Acad. Sci. U. S. A.* **2011**, *108*, 6656– 6661.

Supporting Information

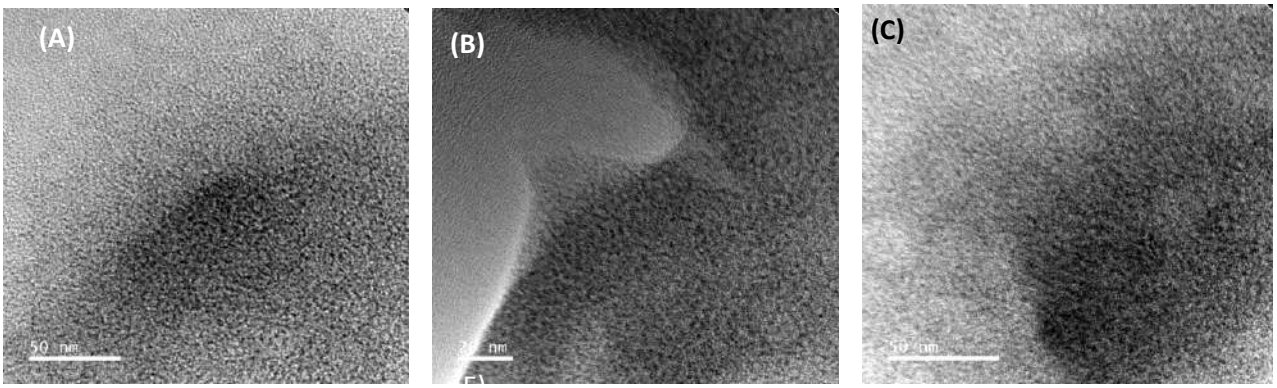

Figure S1. (**A-C**) TEM images of the dispersion containing a mixture of gadolinium acetate and ascorbic acid at 0.5 h. (p.34)

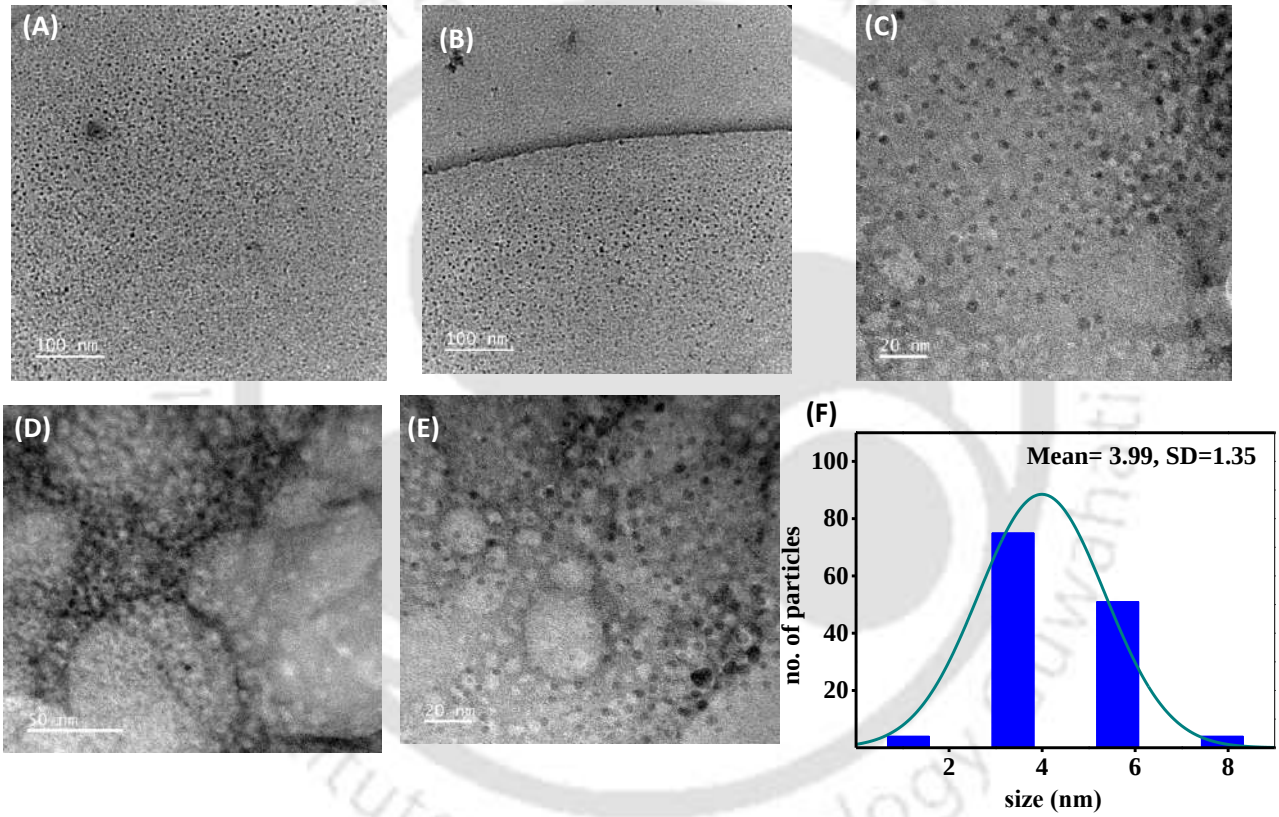

Figure S2. (**A-E**) TEM images of the dispersion containing a mixture of gadolinium acetate and ascorbic acid at 10 h. (**F**) Size distribution of nanoparticles calculated from several TEM images with a total of 100 particles with average particle size 3.99 ± 1.35 nm. (p.34, p.46)

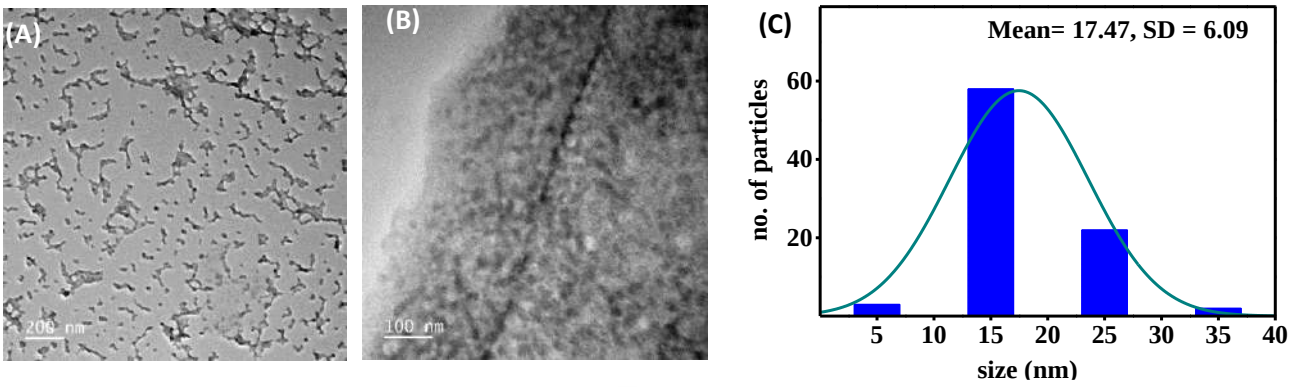

Figure S3. (**A-E**) TEM images of the dispersion containing a mixture of gadolinium acetate and ascorbic acid at 24 h. (**F**) Size distribution of nanoparticles calculated from several TEM images with a total of 300 particles with average particle size 30.17 ± 16.46 nm. (p.34)

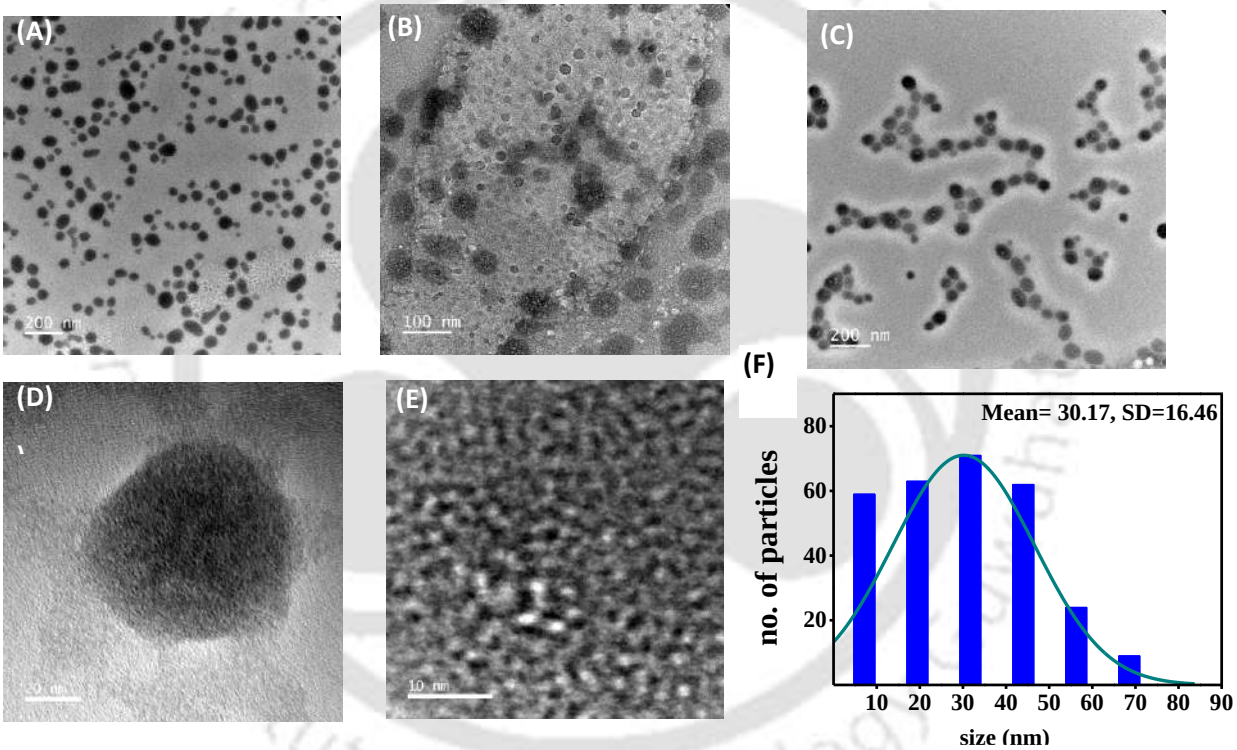

Figure S4. (**A-B**) TEM images of the dispersion containing a mixture of gadolinium acetate and ascorbic acid at 48 h. (**C**) Size distribution of nanoparticles calculated from several TEM images with a total of 100 particles with average particle size 17.47 ± 6.09 nm. (p.34)

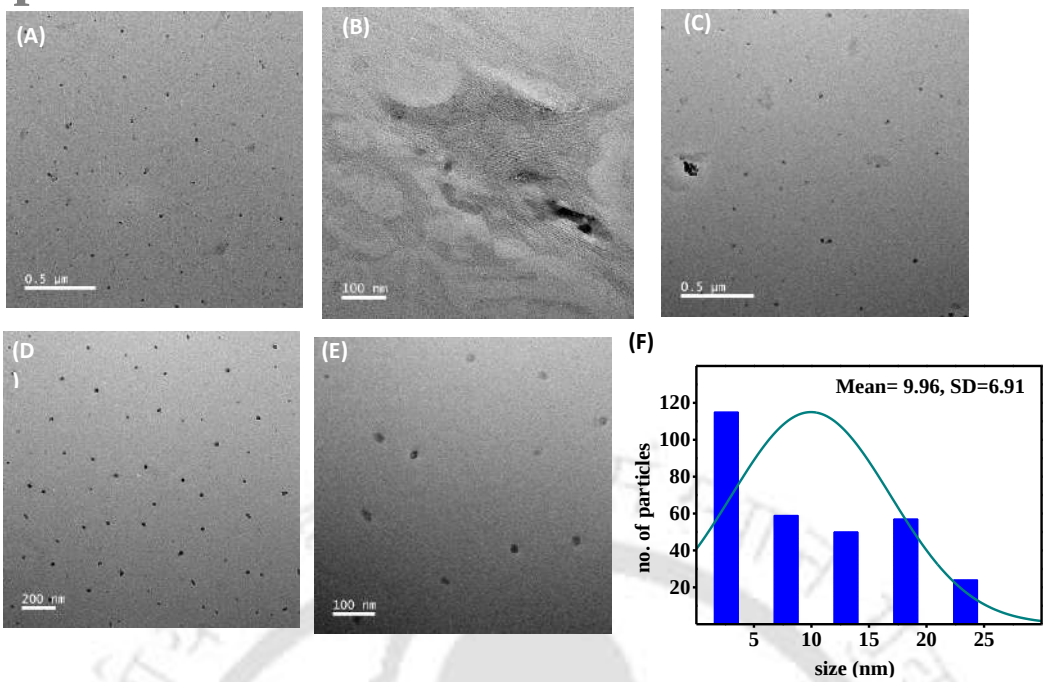

Figure S5. (**A-E**) TEM images of the dispersion containing a mixture of gadolinium acetate and ascorbic acid at 58 h. (**F**) Size distribution of nanoparticles calculated from several TEM images with a total of 300 particles with average particle size 9.96 ± 6.91 nm. (p.34)

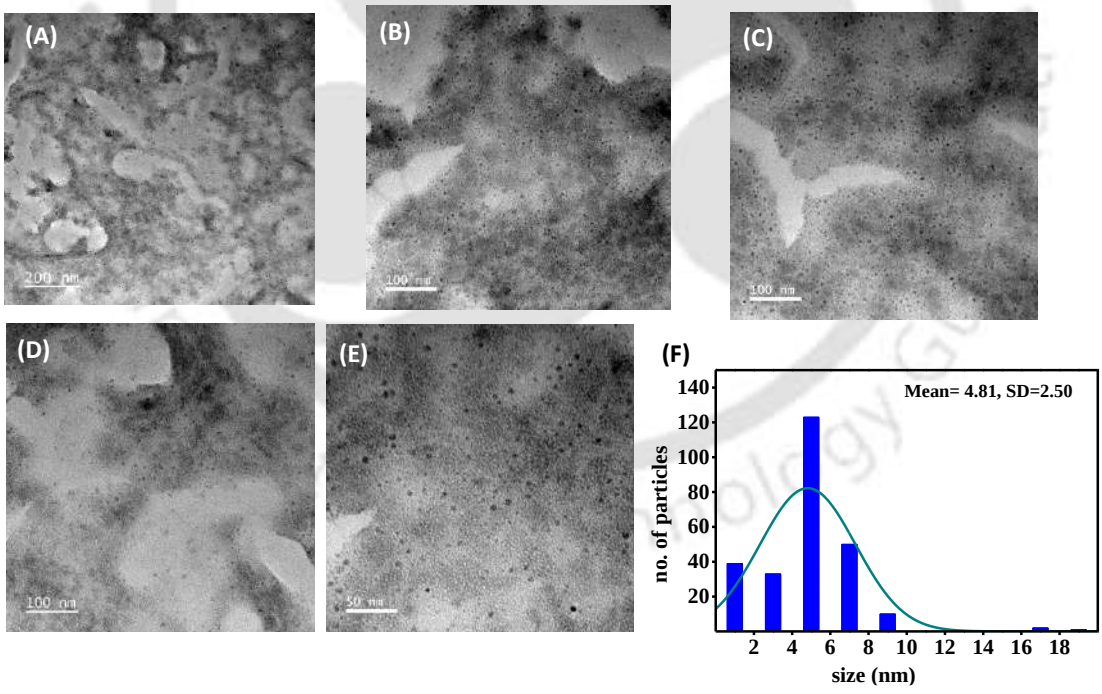

Figure S6. (**A-E**) TEM images of the dispersion containing a mixture of gadolinium acetate and ascorbic acid at 72 h. (**F**) Size distribution of nanoparticles calculated from several TEM images with 300 particles with average particle size 4.81 ± 2.50 nm. (p.34)

Table S1. Crystal parameters obtained after analyzing the SAED pattern of nanoparticles at different intervals of time. (p.34)

Time at which SAED pattern was acquired	TEM image of the sample for which the SAED pattern was obtained	SAED pattern obtained for gadolinium ascorbate nanoparticle	d-spacing (nm) from centre (000)
0.5 h	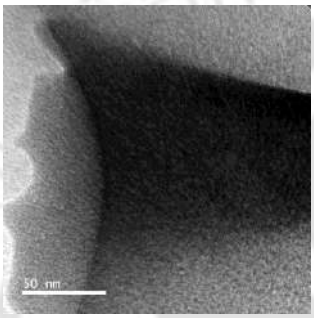	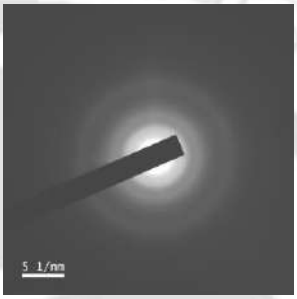	1st ring = 0.2562 2nd ring = 0.1947 3rd ring = 0.1121
10 h	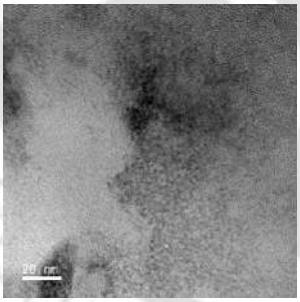	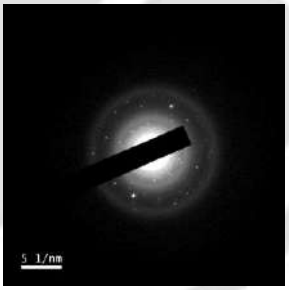	1st ring = 0.3039 2nd ring = 0.2273 3rd ring = 0.1456
24 h	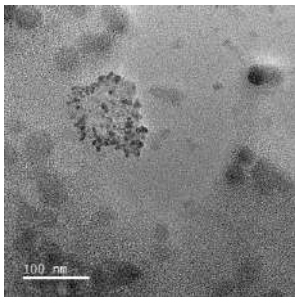	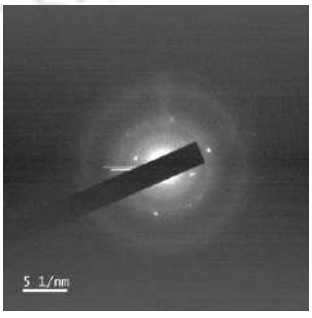	1st ring point = 0.3210 2nd ring point = 0.1962 3rd ring = 0.1140

32 h	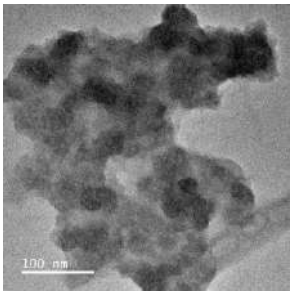	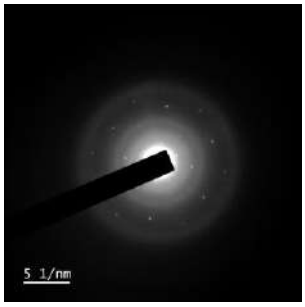	1st ring point = 0.4583 2nd ring point = 0.2946 3rd ring point = 0.1656
48 h	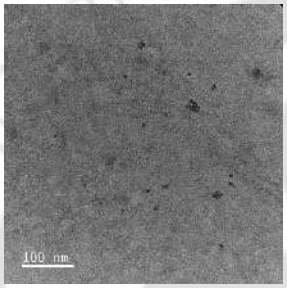	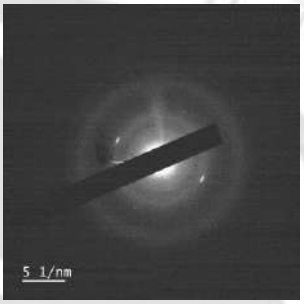	1st ring = 0.2767 2nd ring = 01832 3rd ring = 0.1085
72 h	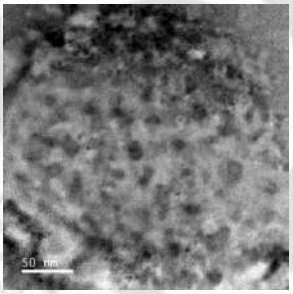	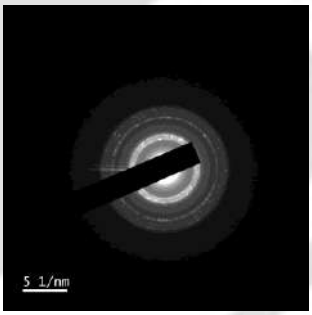	1st ring = 0.2962 2nd ring = 0.2631 3rd ring = 0.1727 4th ring = 0.1109

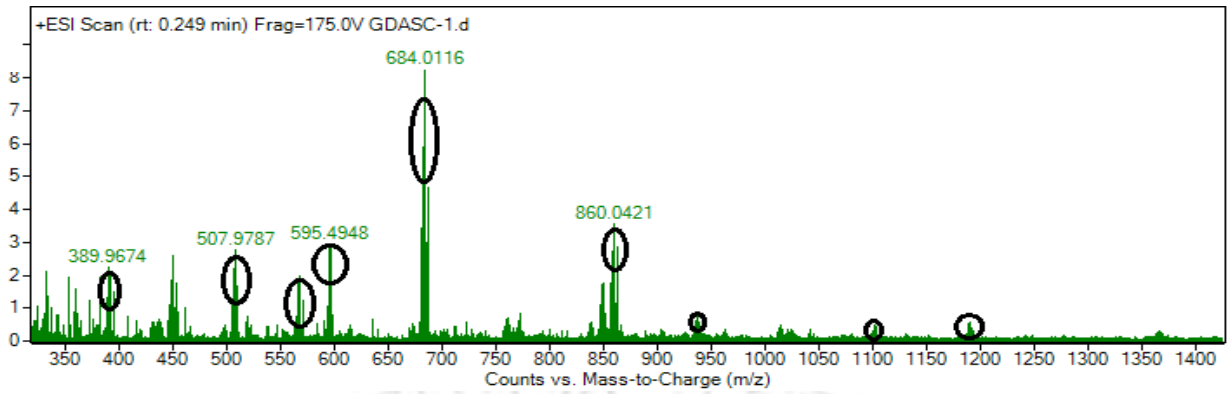

Figure S7. Electrospray ionization mass spectrum of dispersion at time 48 h. (p.35)

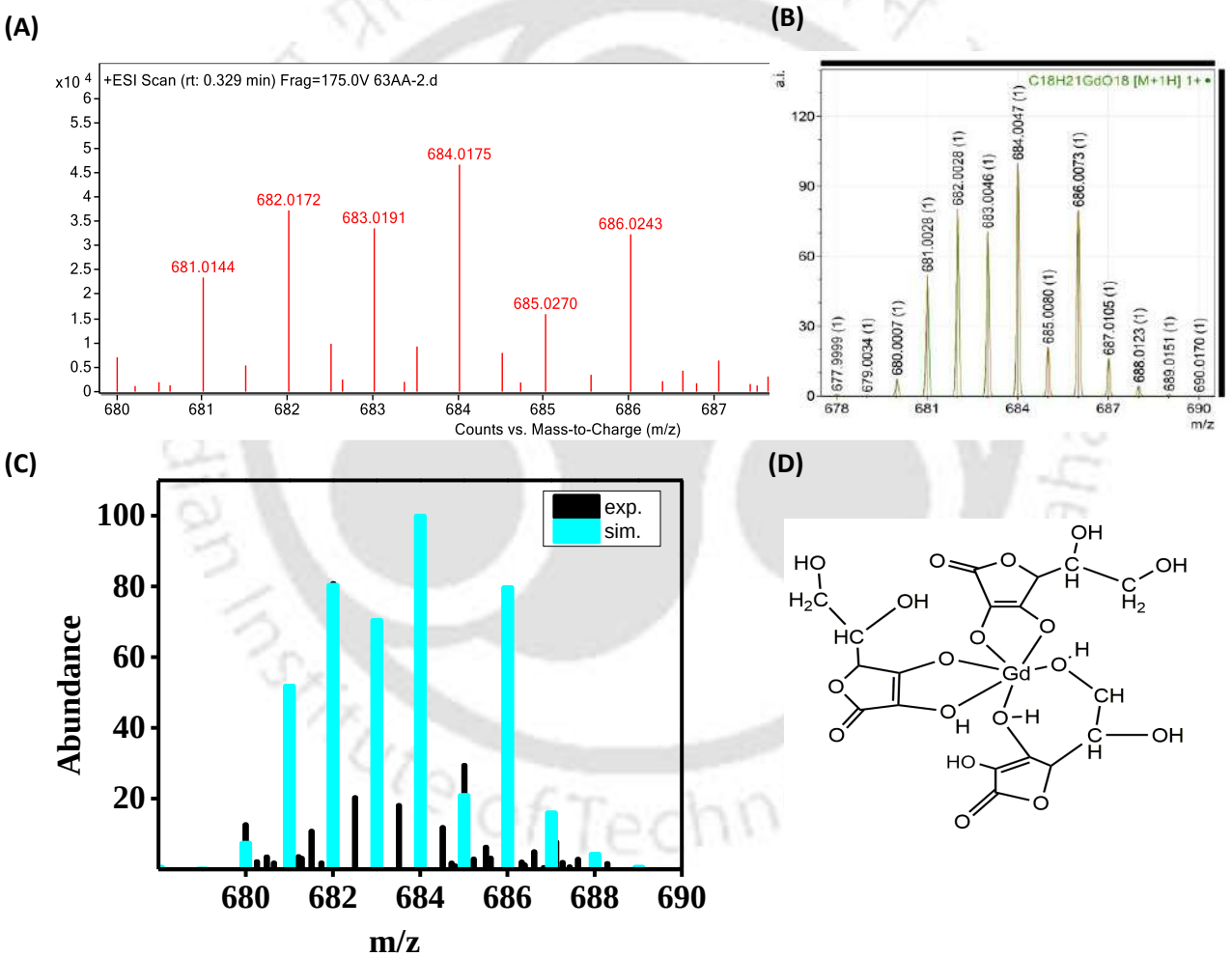

Figure S8. (**A**) Experimental mass spectrum representing [Gd($C_6H_6O_6$)$C_2H_3O_2$] with mass 391.9707, (**B**) simulated mass spectrum of [Gd($C_6H_6O_6$)$C_2H_3O_2$], (**C**) plot representing overlaid experimental and simulated data. (**D**) Proposed structure of [Gd($C_6H_6O_6$)$C_2H_3O_2$]. (p.36)

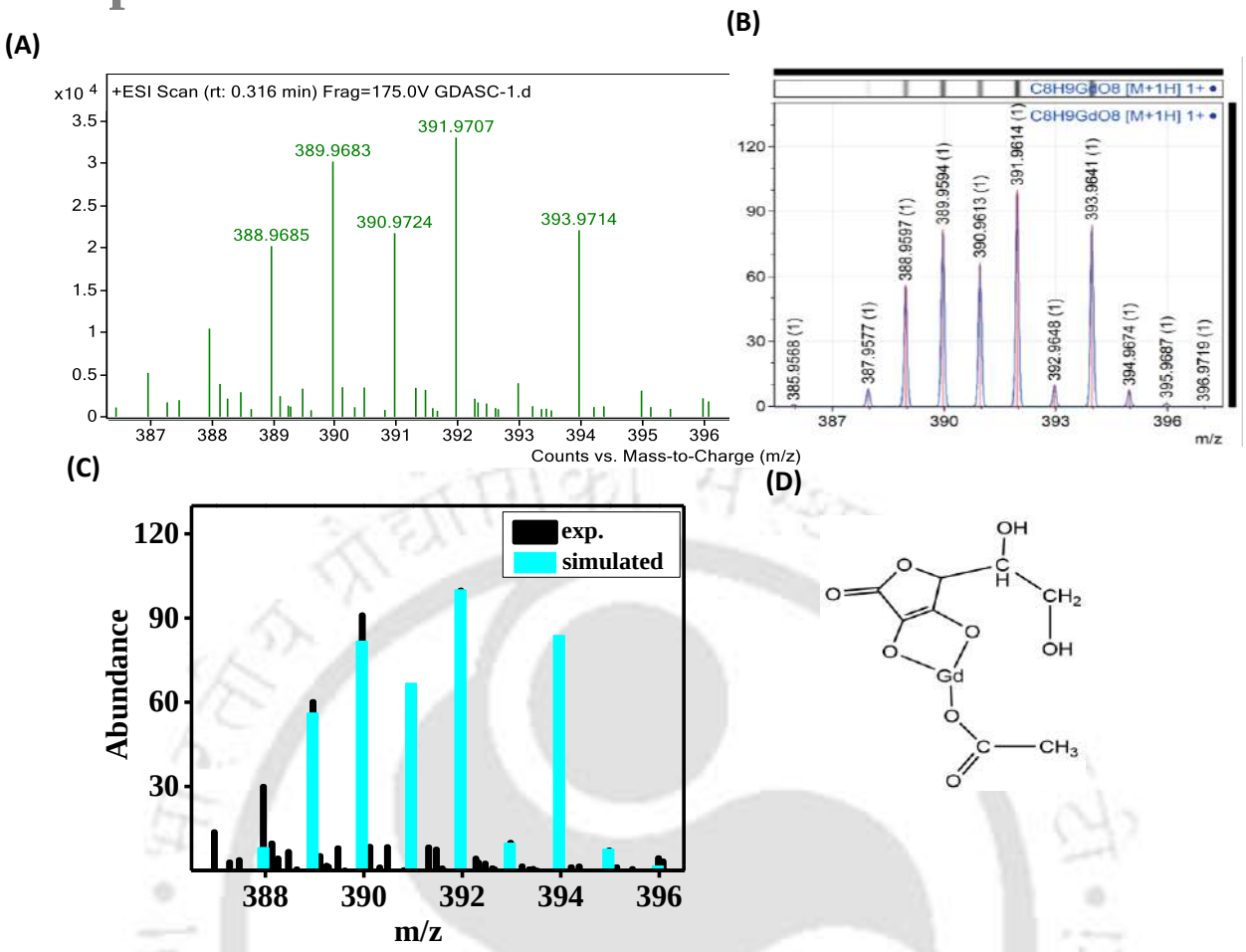

Figure S9. (**A**) Experimental mass spectrum representing [Gd($C_6H_7O_6$)($C_6H_6O_6$)($C_6H_8O_6$)] with mass 684.0175, (**B**) simulated mass spectrum of [Gd($C_6H_7O_6$)($C_6H_6O_6$)($C_6H_8O_6$)] and (**C**) plot representing overlaid experimental and simulated data. (**D**) Proposed structure of [Gd($C_6H_7O_6$)($C_6H_6O_6$)($C_6H_8O_6$)]. (p.36)

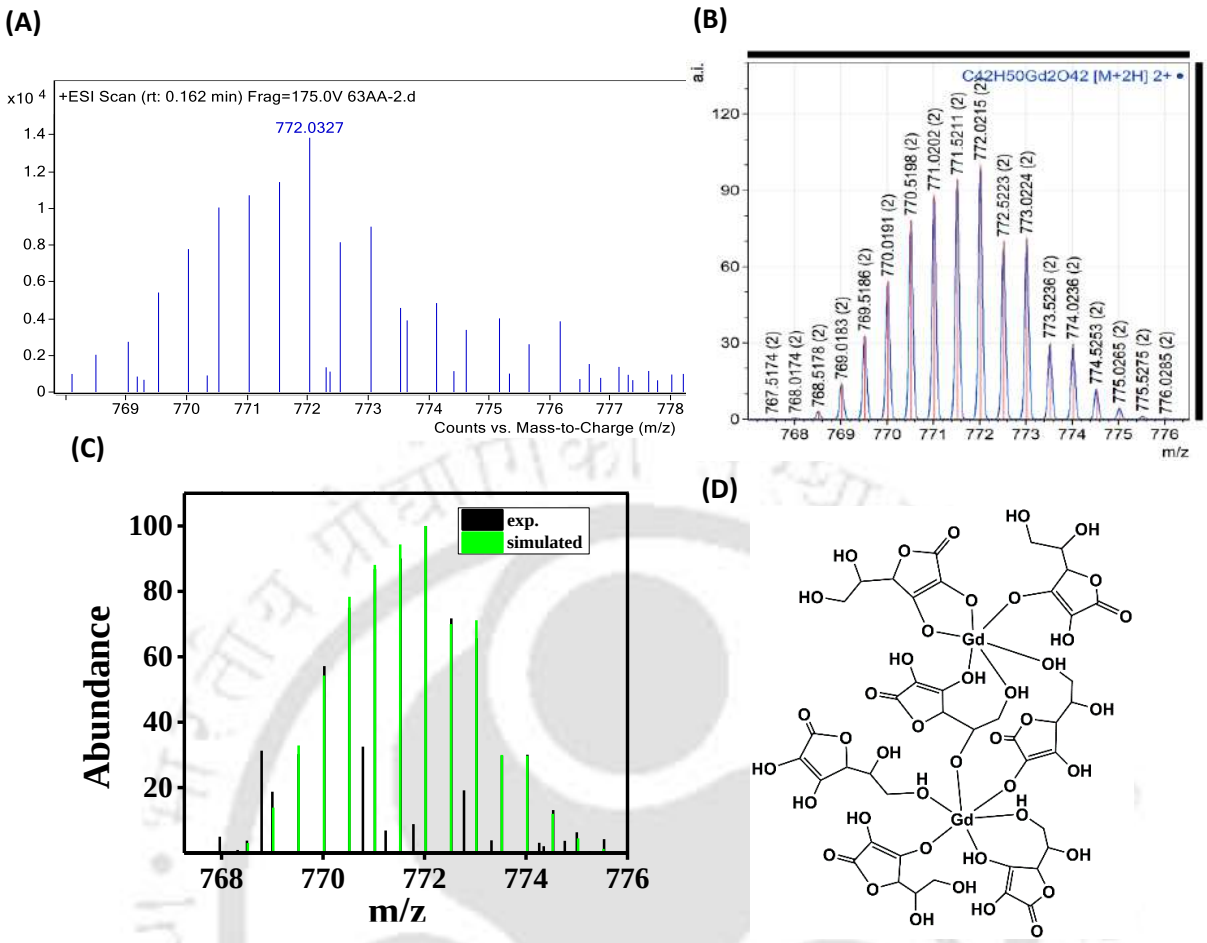

Figure S10. (**A**) Experimental mass spectrum of $[Gd_2(C_6H_6O_6)(C_6H_7O_6)_4(C_6H_8O_6)_2]$ with mass 772.0327, (**B**) simulated mass spectrum of $[Gd_2(C_6H_6O_6)(C_6H_7O_6)_4(C_6H_8O_6)_2]$and (**C**) plot representing overlaid experimental and simulated data. (**D**) Proposed structure of $[Gd_2(C_6H_6O_6)(C_6H_7O_6)_4(C_6H_8O_6)_2]$. (p.36)

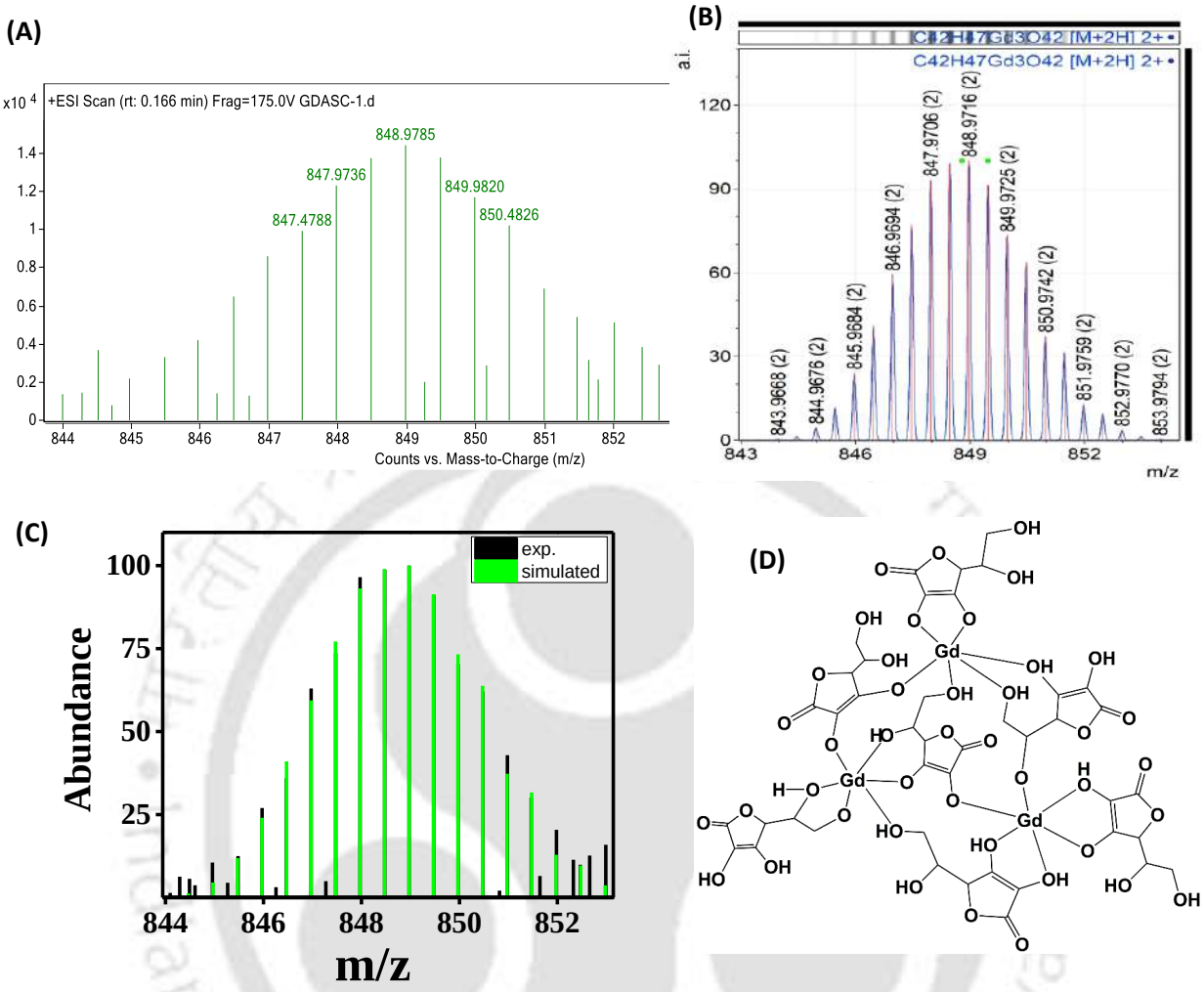

Figure S11. (**A**) Experimental mass spectrum of $[Gd_3(C_6H_6O_6)_3(C_6H_7O_6)_3(C_6H_8O_6)]$ with mass 848.9785, (**B**) simulated mass spectrum of $[Gd_3(C_6H_6O_6)_3(C_6H_7O_6)_3(C_6H_8O_6)]$ and (**C**) plot representing overlaid experimental and simulated data. (**D**) Proposed structure of $[Gd_3(C_6H_6O_6)_3(C_6H_7O_6)_3(C_6H_8O_6)]$. (p.36)

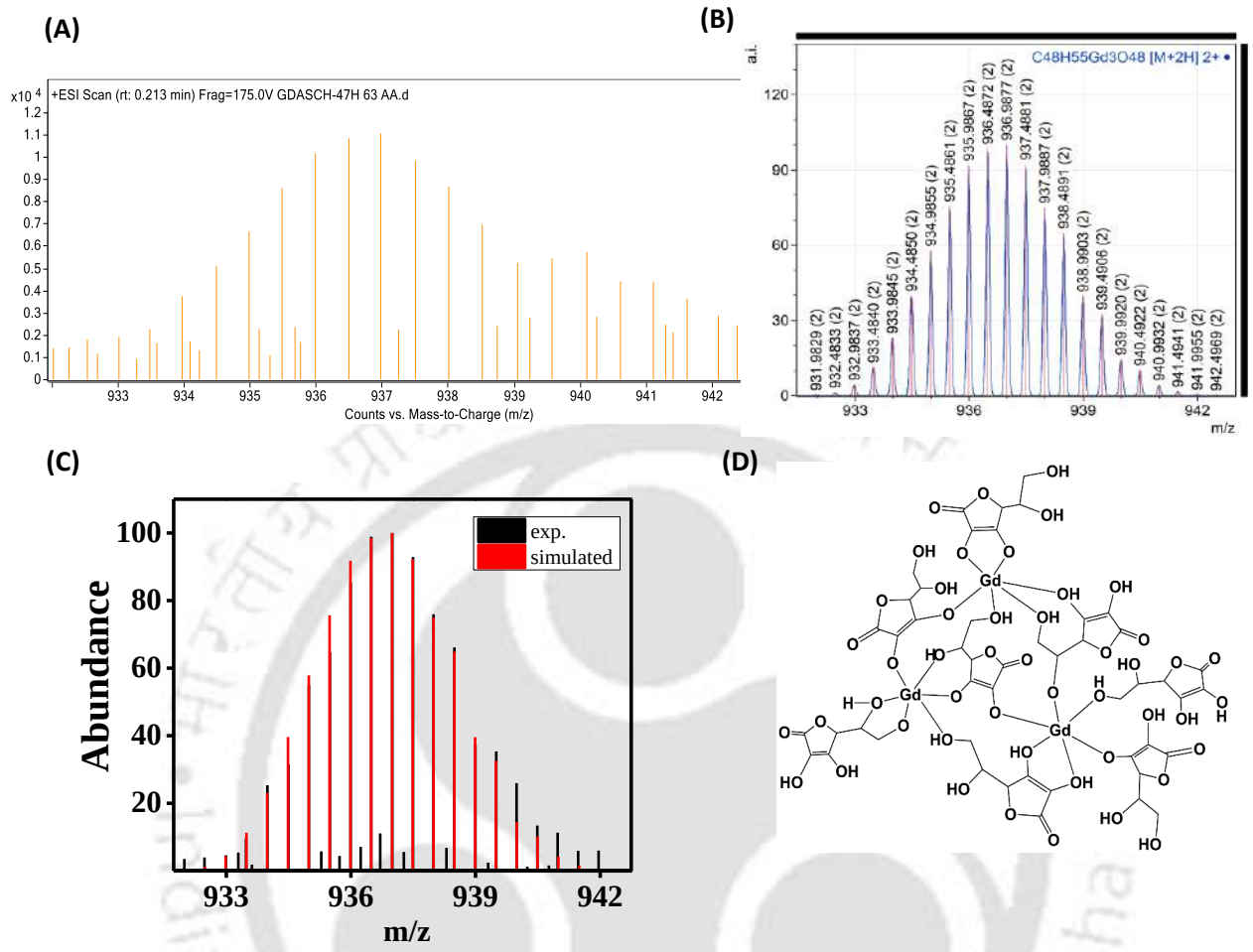

Figure S12. (**A**) Experimental mass spectrum of $[Gd_3(C_6H_6O_6)_3(C_6H_7O_6)_3(C_6H_8O_6)_2]$ with mass 936.9944, (**B**) simulated mass spectrum of $[Gd_3(C_6H_6O_6)_3(C_6H_7O_6)_3(C_6H_8O_6)_2]$ and (**C**) plot representing overlaid experimental and simulated data. (**D**) Proposed structure of $[Gd_3(C_6H_6O_6)_3(C_6H_7O_6)_3(C_6H_8O_6)_2]$. (p.36)

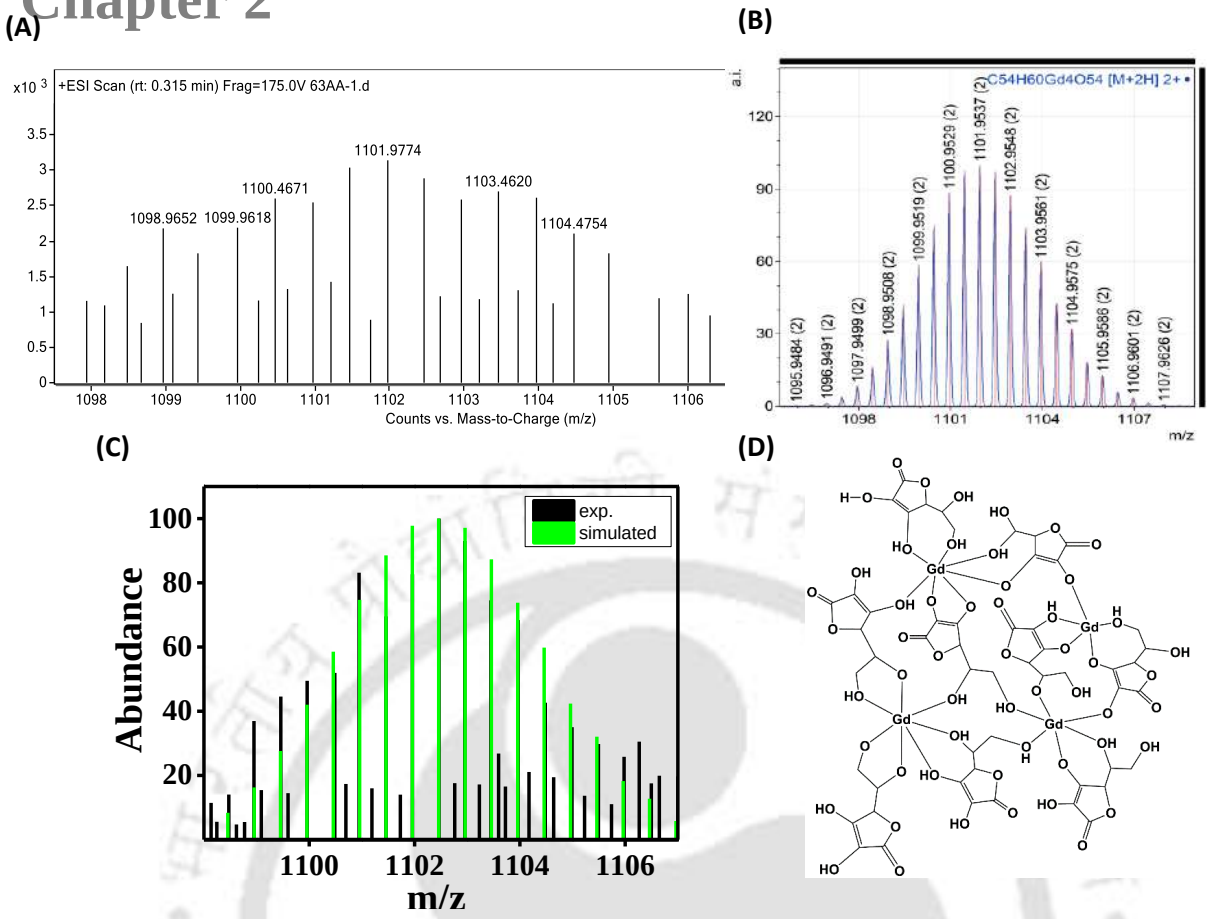

Figure S13. (**A**) Experimental mass spectrum of $[Gd_4(C_6H_6O_6)_5(C_6H_7O_6)_2(C_6H_8O_6)_2]$ with mass 1101.9774, (**B**) simulated mass spectrum of $[Gd_4(C_6H_6O_6)_5(C_6H_7O_6)_2(C_6H_8O_6)_2]$and (**C**) plot representing overlaid experimental and simulated data. (**D**) Proposed structure of $[Gd_4(C_6H_6O_6)_5(C_6H_7O_6)_2(C_6H_8O_6)_2]$. (p.36)

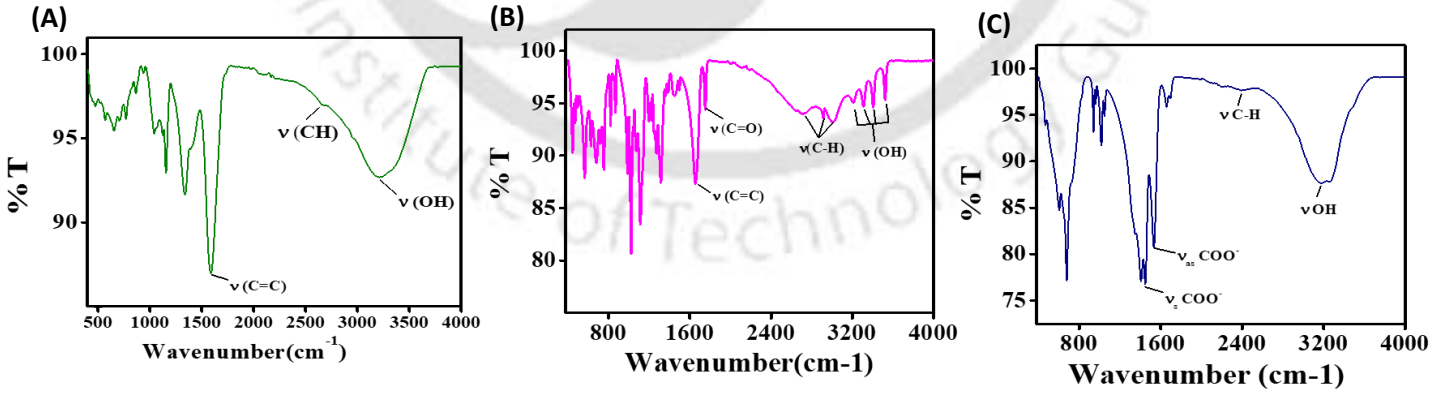

Figure S14. FTIR spectra of (**A**) gadolinium ascorbate nanoparticle as obtained after centrifugation of the dispersion at 60 h, (**B**) ascorbic acid and (**C**) gadolinium acetate hydrate. (p.38)

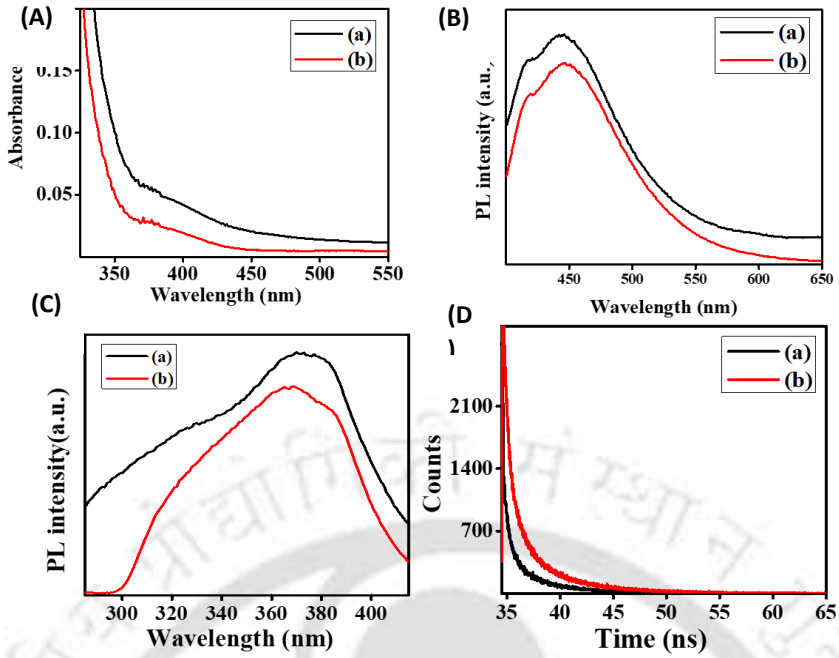

Figure S15. (A) Absorption spectra of (a) the redispersion of the pellet obtained after the centrifugation of the dispersion at 72 h and (b) of the supernatant. (B) PL emission (λ_{ex} = 362 nm) of (a) redispersed pellet and (b) supernatant. (C) corresponding excitation spectrum of (a) redispersed pellet and (b) supernatant. (D) fluorescence lifetime of (a) redispersed pellet and (b) supernatant. Here supernatant refers to the remaining dispersion obtained after centrifugation of the dispersion at 72 h. (p.42)

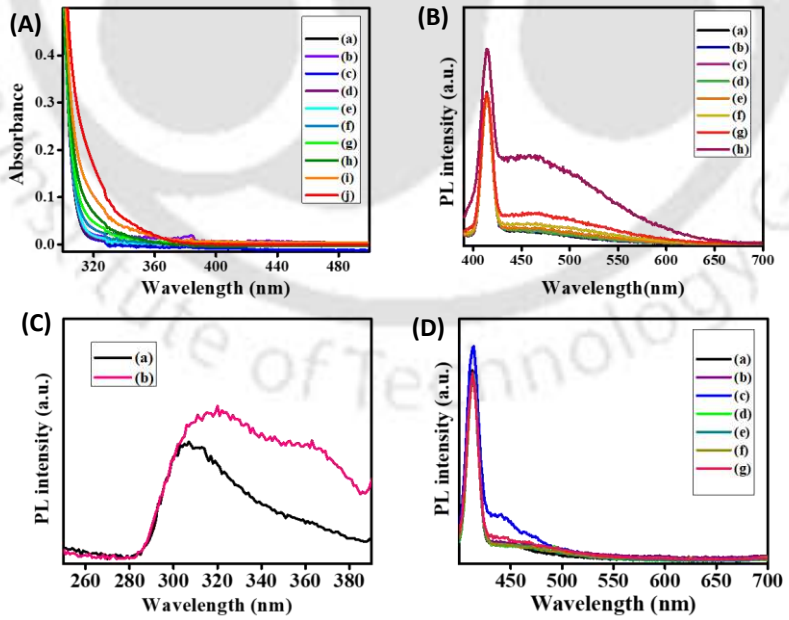

Figure S16. (A) UV-Vis absorbance spectra of dispersion containing only gadolinium acetate (a) 0 h, (b) 2 h, (c) 9 h, (d) 24 h, (e) 34 h, (f) 48 h, (g) 58 h, (h) 72 h, (i) 81 h and (j) 106 h. (B)

Photoluminescence emission spectra dispersion containing only ascorbic acid (λ_{ex} = 362 nm) at (a) 2 h, (b) 15.5h, (c) 22.5 h, (d) 26 h, (e) 40 h, (f) 50 h, (g) 64 h and (h) 97 h and (C) corresponding excitation spectra at (a) 64 h and (b) 97 h. (D) Photo Luminescence emission spectra (λ_{ex} = 362 nm) of Gadolinium acetate at (a) 1 h, (b) 21.5h, (c) 25 h, (d) 38.5 h, (e) 49 h, (f) 63 h and (g) 96 h. (p.44)

Table S2. Average Photoluminescence lifetime of the reaction mixture containing gadolinium acetate and ascorbic acid at different interval of time. (p.43)

reaction time (h)	average lifetime (τ_{av} (ns)) values with corresponding χ^2 value of experiment number			average lifetime (τ_{av} (ns)) with standard error bar
	1	2	3	
9	4.4 χ^2 = 1.00	4.5 χ^2 = 1.00	4.4 χ^2 = 1.00	4.4 ± 0.1
25	4.0 χ^2 = 1.01	2.0 χ^2 = 1.01	2.1 χ^2 = 1.00	2.7 ± 1.0
33	4.1 χ^2 = 1.00	3.9 χ^2 = 1.01	4.0 χ^2 = 1.00	4.0 ± 0.1
48	4.1 χ^2 = 1.01	1.9 χ^2 = 1.01	2.0 χ^2 = 1.01	2.7 ± 1.0
57	2.1 χ^2 = 1.00	1.8 χ^2 = 1.02	2.0 χ^2 = 1.01	1.9 ± 0.1
72	4.0 χ^2 = 1.00	2.0 χ^2 = 1.00	1.9 χ^2 = 1.01	2.6 ± 0.9
82 h	4.0 χ^2 = 1.00	1.8 χ^2 = 1.00	1.9 χ^2 = 1.00	2.6 ± 1.0

Quantum Yield Measurement

Photoluminescence quantum yield of the reaction mixture at different interval of time was measured with respect to quinine sulfate dissolved in 0.1 mM H_2SO_4 with reported quantum yield (QY) of 54.6 % using the following equation-

$$\Phi_S = \Phi_R \times \frac{I_s}{I_R} \times \frac{A_R}{A_s} \times \frac{\eta_S^2}{\eta_R^2} \quad \text{..... Equation S1}$$

Here, Φ_R = quantum yield of the reference; Φ_S = quantum yield of the sample; I_S = area under the emission spectrum of the sample; I_R = area under the emission spectrum of reference; A_R = absorbance of reference; A_S = absorbance of the sample; η_S = refractive index of the sample solution; η_R = refractive index of reference and refractive index of water = 1.33. The absorbance of the reference and reaction mixture were kept below 0.2 at the excitation wavelength of 375 nm.

Table S3. Quantum yield of the reaction mixture at different interval of time. (p.43)

Time (h)	9 h	24 h	29 h	33 h	48 h	53 h	57 h	72 h
Quantum yield (%)	0.6	1.0	1.7	1.8	2.4	1.7	1.9	1.4
±Error(%)	0.1	0.2	0.6	0.6	0.2	0.2	0.4	0.4

Table S4. The magnetisation value of the nanoparticle centrifuged at different time of reaction and obtained after MH curve analysis. (p.44)

Time (h)	Magnetisation (emu/g)
61	**0.9**
66	**0.8**
72	**0.9**
100	**0.8**

Calculation of relaxivity

The relaxivity values can be calculated using the equation

$$relaxivity = \frac{\left(\frac{1}{T_i} - \frac{1}{T_{id}}\right)}{[Gd]}$$ equation S2

where T_i is the longitudinal relaxation time and T_{id} is the intrinsic diamagnetic solvent relaxation time (T_{1d} = 2986 ms for water). [Gd] is the concentration of gadolinium present in the medium, which was taken as 9 mM.

Table S5. Longitudinal relaxation time (T1) and relaxivity (r1) of the reaction mixture at different interval of time. (p.44, p.46)

Reaction time (h)	T1 values for the experiment number and (resulting r1 values calculated from equation S2)			average T1 (ms) with standard error bar (and average r1 value with error bar in $mM^{-1}s^{-1}$)
	1	2	3	
0.5	13.1 ms (r1= 8.4$mM^{-1}s^{-1}$)	12.9 ms (8.6 $mM^{-1}s^{-1}$)	13.3 ms (8.3 $mM^{-1}s^{-1}$)	13.1 ± 0.2 (8.4 ± 0.1)
2	12.9 ms (8.6 $mM^{-1}s^{-1}$)	12.9 ms (8.6 $mM^{-1}s^{-1}$)	13.2 ms (8.5 $mM^{-1}s^{-1}$)	13.0 ± 0.1 (8.5 ± 0.1)
6	13.0 ms (8.5 $mM^{-1}s^{-1}$)	13.0 ms (8.5 $mM^{-1}s^{-1}$)	13.2 ms (8.4 $mM^{-1}s^{-1}$)	13.0 ± 0.1 (8.5 ± 0.1)
10	12.9 ms (8.6 $mM^{-1}s^{-1}$)	12.9 ms (8.6 $mM^{-1}s^{-1}$)	13.1 ms (8.4 $mM^{-1}s^{-1}$)	13.0 ± 0.1 (8.5 ± 0.1)
23.5	13.2 ms (8.4 $mM^{-1}s^{-1}$)	13.4 ms (8.3 $mM^{-1}s^{-1}$)	13.6 ms (8.1 $mM^{-1}s^{-1}$)	13.4 ± 0.2 (8.2 ± 0.1)
30	13.4 ms (8.3 $mM^{-1}s^{-1}$)	13.6 ms (8.1 $mM^{-1}s^{-1}$)	13.6 ms (8.1 $mM^{-1}s^{-1}$)	13.5 ± 0.1 (8.2 ± 0.1)
34	13.7 ms (8.1 $mM^{-1}s^{-1}$)	13.9 ms (7.9 $mM^{-1}s^{-1}$)	14.1 ms (7.8 $mM^{-1}s^{-1}$)	13.9 ± 0.2 (7.9 ± 0.1)
48	14.0 ms (7.9 $mM^{-1}s^{-1}$)	14.2 ms (7.8 $mM^{-1}s^{-1}$)	14.4 ms (7.7 $mM^{-1}s^{-1}$)	14.2 ± 0.2 (7.8 ± 0.1)
54	14.2 ms (7.8 $mM^{-1}s^{-1}$)	14.0 ms (7.9 $mM^{-1}s^{-1}$)	14.3 ms (7.7 $mM^{-1}s^{-1}$)	14.2 ± 0.1 (7.8 ± 0.1)
58	14.0 ms (7.9 $mM^{-1}s^{-1}$)	13.8 ms (8.0 $mM^{-1}s^{-1}$)	14.2 ms (7.8 $mM^{-1}s^{-1}$)	14.0 ± 0.1 (7.9 ± 0.1)

72	12.5 ms (8.8 $mM^{-1}s^{-1}$)	12.9 ms (8.6 $mM^{-1}s^{-1}$)	13.2 ms (8.4 $mM^{-1}s^{-1}$)	12.9 ± 0.3 (8.6 ± 0.2)
78	12.1 ms (9.1 $mM^{-1}s^{-1}$)	12.5 ms (8.8 $mM^{-1}s^{-1}$)	12.8 ms (8.6 $mM^{-1}s^{-1}$)	12.5 ± 0.3 (8.8 ± 0.2)
82.5	11.9 ms (9.3 $mM^{-1}s^{-1}$)	12.2 ms (9.1 $mM^{-1}s^{-1}$)	12.5 ms (8.8 $mM^{-1}s^{-1}$)	12.2 ± 0.3 (9.1 ± 0.2)
96	11.0 ms (10.1 $mM^{-1}s^{-1}$)	11.5 ms (9.9 $mM^{-1}s^{-1}$)	11.8 ms (9.5 $mM^{-1}s^{-1}$)	11.4 ± 0.3(9.7 ± 0.3)
105	10.7 ms (10.3 $mM^{-1}s^{-1}$)	11.1 ms (9.9 $mM^{-1}s^{-1}$)	11.6 ms (9.5 $mM^{-1}s^{-1}$)	11.1 ± 0.4(9.95 ± 0.3)

Table S6. Transverse relaxation time (T2) and relaxivity (r2) of the reaction mixture at different interval of time ((p.44, p.46)

Reaction time (h)	T2 (ms) values for the experiment number (resulting r2 values calculated from equation S2)			average T2 (ms) with standard error bar(and average r1 value with error bar in $mM^{-1}s^{-1}$)
	1	2	3	
0.5	11.3 ms (9.8 $mM^{-1}s^{-1}$)	11.4 ms (9.7 $mM^{-1}s^{-1}$)	11.5 ms (9.6 $mM^{-1}s^{-1}$)	11.4 ± 0.1 (9.7 ± 0.1)
2	11.3 ms (9.8 $mM^{-1}s^{-1}$)	11.3 ms (9.8 $mM^{-1}s^{-1}$)	11.5 ms (9.6 $mM^{-1}s^{-1}$)	11.4 ± 0.1 (9.7 ± 0.1)
6	11.3 ms (9.8 $mM^{-1}s^{-1}$)	11.4 ms (9.7 $mM^{-1}s^{-1}$)	11.5 ms (9.6 $mM^{-1}s^{-1}$)	11.4 ± 0.1 (9.7 ± 0.1)
10	11.3 ms (9.8 $mM^{-1}s^{-1}$)	11.4 ms (9.7 $mM^{-1}s^{-1}$)	11.6 ms (9.5 $mM^{-1}s^{-1}$)	11.4 ± 0.1 (9.4 ± 0.1)
23.5	11.6 ms (9.5 $mM^{-1}s^{-1}$)	11.8 ms (9.4 $mM^{-1}s^{-1}$)	11.9 ms (9.3 $mM^{-1}s^{-1}$)	11.8 ± 0.1 (9.4 ± 0.1)
30	11.8 ms (9.4 $mM^{-1}s^{-1}$)	12.0 ms (9.2 $mM^{-1}s^{-1}$)	12.1 ms (9.1 $mM^{-1}s^{-1}$)	12.0 ± 0.1 (9.2 ± 0.1)
34	11.9 ms (9.3 $mM^{-1}s^{-1}$)	12.2 ms (9.1 $mM^{-1}s^{-1}$)	12.3 ms (9.0 $mM^{-1}s^{-1}$)	12.2 ± 0.2 (9.1 ± 0.1)
48	12.2 ms (9.1 $mM^{-1}s^{-1}$)	12.3 ms (9.0 $mM^{-1}s^{-1}$)	12.5 ms (8.8 $mM^{-1}s^{-1}$)	12.3 ± 0.1 (8.9 ± 0.1)
54	12.2 ms (9.1 $mM^{-1}s^{-1}$)	12.2 ms (9.1 $mM^{-1}s^{-1}$)	12.4 ms (8.9 $mM^{-1}s^{-1}$)	12.3 ± 0.1 (9.0 ± 0.1)
58	12.4 ms (8.9 $mM^{-1}s^{-1}$)	12.0 ms (9.2 $mM^{-1}s^{-1}$)	12.2 ms (9.1 $mM^{-1}s^{-1}$)	12.2 ± 0.2 (9.1 ± 0.1)
72	10.4 ms (10.6 $mM^{-1}s^{-1}$)	10.5 ms (10.5 $mM^{-1}s^{-1}$)	10.9 ms (10.2 $mM^{-1}s^{-1}$)	10.6 ± 0.2 (10.4 ± 0.2)
78	9.7 ms (11.4 $mM^{-1}s^{-1}$)	10.2 ms (10.8 $mM^{-1}s^{-1}$)	10.4 ms (10.6 $mM^{-1}s^{-1}$)	10.1 ± 0.3 (10.9 ± 0.3)
82.5	9.4 ms (11.8 $mM^{-1}s^{-1}$)	9.8 ms (11.3 $mM^{-1}s^{-1}$)	10.1 ms (10.9 $mM^{-1}s^{-1}$)	9.8 ± 0.3 (11.3 ± 0.3)
96	8.5 ms (13.0 $mM^{-1}s^{-1}$)	9.0 ms (12.3 $mM^{-1}s^{-1}$)	9.4 ms (11.8 $mM^{-1}s^{-1}$)	9.0 ± 0.4 (12.4 ± 0.5)
105	8.2 ms (13.5 $mM^{-1}s^{-1}$)	8.6 ms (12.9 $mM^{-1}s^{-1}$)	9.0 ms (12.3 $mM^{-1}s^{-1}$)	8.6 ± 0.4 (12.9 ± 0.5)

Table S7. Relaxivity values of different Gd based MRI contrast agents at 37°C in water[1] at 1.5 T magnetic field and of the current dispersion containing Gd acetate and ascorbic acid at 105 h. (p.47)

Different Gd based MRI contrast agents	r1 ($mM^{-1}s^{-1}$)	r2 ($mM^{-1}s^{-1}$)
MAGNEVIST	3.3 (3.1–3.5)	3.9 (2.8–5.0)
GADOVIST	3.3 (3.1–3.5)	3.9 (3.1–4.7)
PROHANCE	2.9 (2.7–3.1)	3.2 (2.5–3.9)
MULTIHANCE	4.0 (3.8–4.2)	4.3 (3.8–4.8)
DOTAREM	2.9 (2.7–3.1)	3.2 (2.5–3.9)
OMNISCAN	3.3 (3.1–3.5)	3.6 (3.0–4.2)
OPTIMARK	3.8 (3.6–4.0)	4.2 (3.5–4.9)
PRIMOVIST	4.7 (4.5–4.9)	5.1 (4.5–5.7)
Reaction mixture containing Gd acetate and ascorbic acid at 105 h	9.95 ± 0.3	12.9 ± 0.5

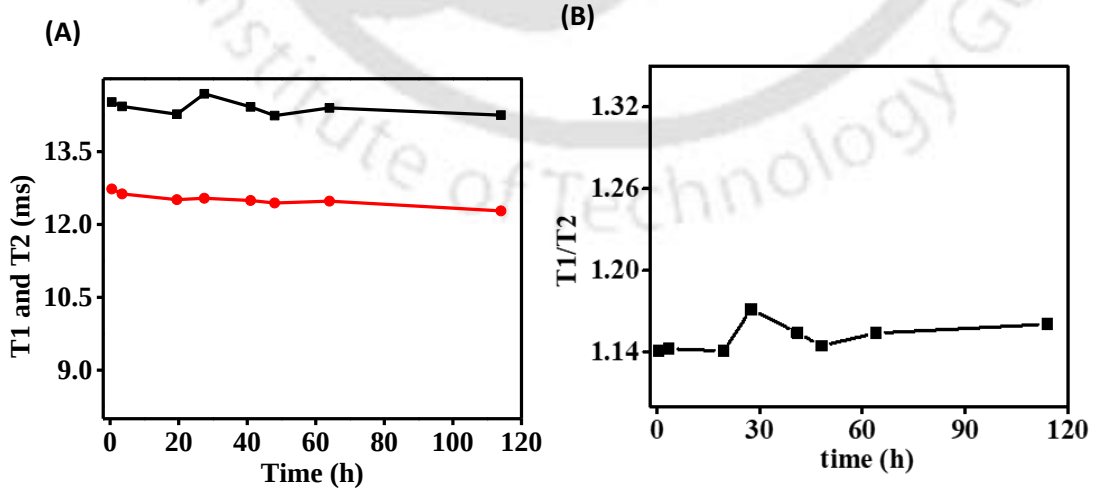

Figure S17. (**A**) T1 and T2 relaxation times of dispersion containing gadolinium acetate hydrate

recorded at different time intervals. (**B**) Ratio of T1 and T2 of the dispersion containing gadolinium acetate hydrate recorded at different time interval. ((p.44)

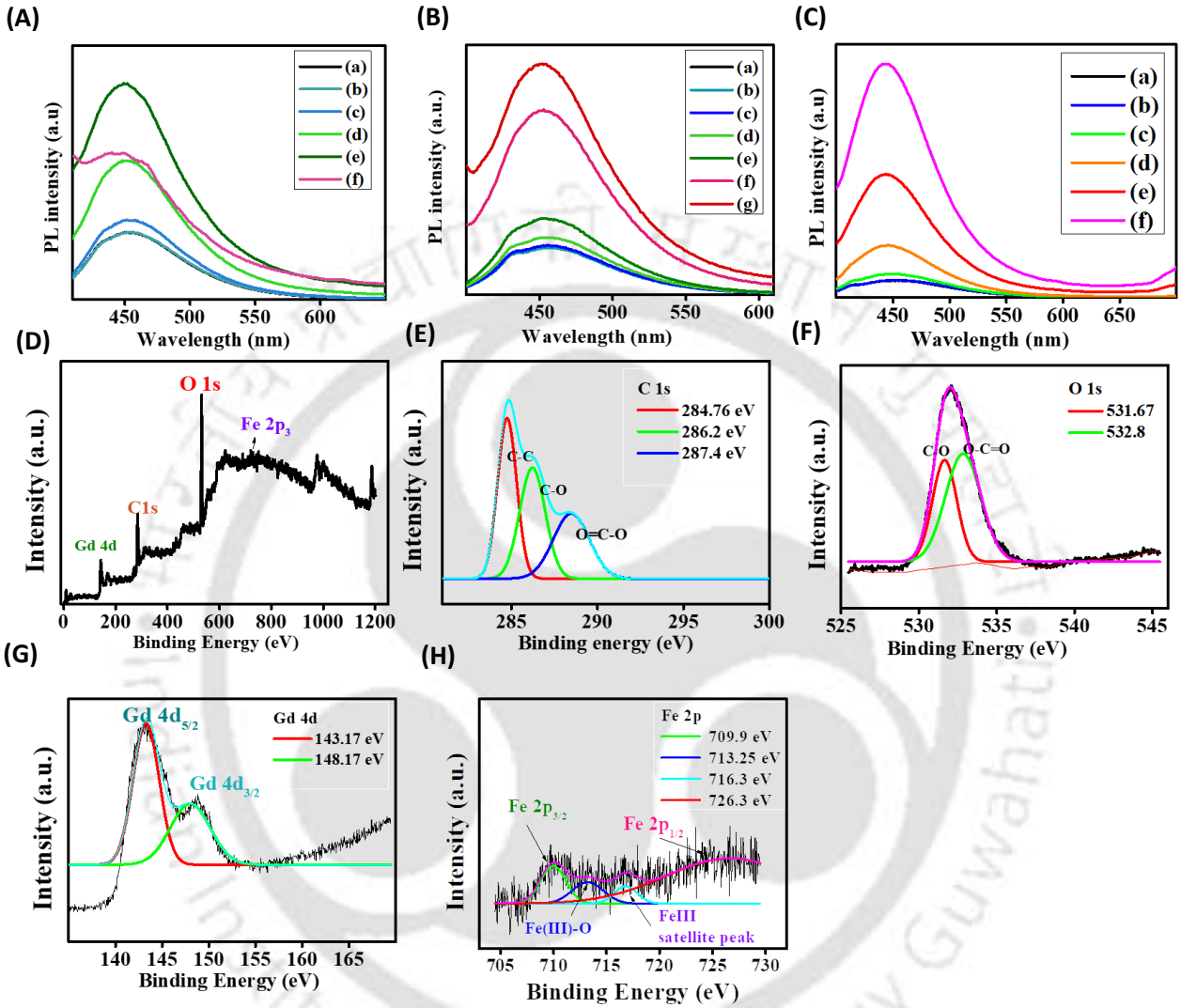

Figure S18. (**A**) Photo Luminescence emission spectra (λ_{ex} = 375 nm) of (a) Gd ascorbate reaction mixture at 48 h and of reaction mixture after addition of Fe(III) (0.5 mM) at (b) 0 min (c) 1 h, (d) 4 h, (e) 8 h and (f) 24 h. (**B**) Photo Luminescence emission spectra (λ_{ex} = 375 nm) of (a) Gd ascorbate reaction mixture at 48 h, and of reaction mixture after addition of Zn(II) salt (2 mM) at (b) 0 min, (c) 1 h, (d) 4 h, (e) 8 h, (f) 24 h and (g) 29 h. (**C**) Photo Luminescence emission spectra (λ_{ex} = 375 nm) of (a) Gd ascorbate reaction mixture at 48 h and of reaction mixture after addition of Fe(III) (24.4 µM) at (b) 0 min (c) 2 h, (d) 8 h, (e) 24 h and (f) 48 h. (**D**)

X-ray photoelectron (XPS) survey spectrum for the centrifuged product of the reaction mixture (containing Gd acetate and ascorbic acid) at 24 h after addition of Fe(III). (**E**) Deconvulated xps peaks for C_{1s} obtained at 284.76, 286.2 and 287.4 eV for C-C, C-O and O-C=O binding energies respectively. (**F**) Deconvulated xps peaks for O_{1s} obtained at 531.67 eV and 532.8 eV for C-C and O-C=O binding energies respectively. (**G**) Deconvulated xps peaks for Gd_{4d} obtained at 143.17 eV and 148.17 eV for Gd $4d_{5/2}$ and Gd $4d_{3/2}$ respectively.[2] (**H**) Deconvulated xps peaks Fe_{2p} obtained at 709.9 eV, 713.25 eV, 716.3 eV and 726.3 eV for Fe $2p_{3/2}$, Fe (III)-O binding energy, Fe (III) satellite peak and Fe $2p_{1/2}$ respectively.[3] (p.47, p.48)

Table S8. Atomic percentages of elements present in the centrifuged product obtained from the dispersion being kept standing at 48 h following which Fe (III) was added. The centrifugation was carried out at 24 h after addition of iron. (p.48)

Elements present	Carbon	Oxygen	Gadolinium	Iron
Atomic percentage (%)	46.87	47.58	4.16	1.39

Table S9. Relaxation times (T1 and T2) and relaxivity values of reaction mixture (1 mL) at 48 h (and measured at 37°C and 1.41 T magnetic field) and recorded after addition to HEPES buffer solution (3 mL) and water (3 mL) respectively. (p.48)

		Number of sets of reaction from which relaxation times are measured			Average relaxation times (and calculated relaxivity) with standard error bar
		1	2	3	
Reaction mixture (1 mL) at 48 h added to 3 mL of hepes buffer	T1 (and r1)	81.0 ms ($5.3\ mM^{-1}s^{-1}$)	80.0 ms ($5.4\ mM^{-1}s^{-1}$) **80**	79.0 ms ($5.5\ mM^{-1}s^{-1}$)	80.0 ± 0.8 ms ($5.4 \pm 0.1\ mM^{-1}s^{-1}$)

	T2 (and r2)	61.1 ms ($7.1\ mM^{-1}s^{-1}$)	57.9 ms ($7.5\ mM^{-1}s^{-1}$)	55.8 ms ($7.8\ mM^{-1}s^{-1}$)	58.2 ± 2.2 ms ($7.5 \pm 0.3\ mM^{-1}s^{-1}$)
Reaction mixture (1 mL) at 48 h added to 3 mL of water	T1 (and r1)	60.98 ms ($7.1\ mM^{-1}s^{-1}$)	59.0 ms ($7.4\ mM^{-1}s^{-1}$)	61.5 ms ($7.1\ mM^{-1}s^{-1}$)	60.5 ± 1.1 ms ($7.2 \pm 0.1\ mM^{-1}s^{-1}$)
	T2 (and r2)	53.0 ms ($8.2\ mM^{-1}s^{-1}$)	51.9 ms ($8.4\ mM^{-1}s^{-1}$)	53.8 ms ($8.1\ mM^{-1}s^{-1}$)	52.9 ± 0.8 ms ($8.3 \pm 0.1\ mM^{-1}s^{-1}$)

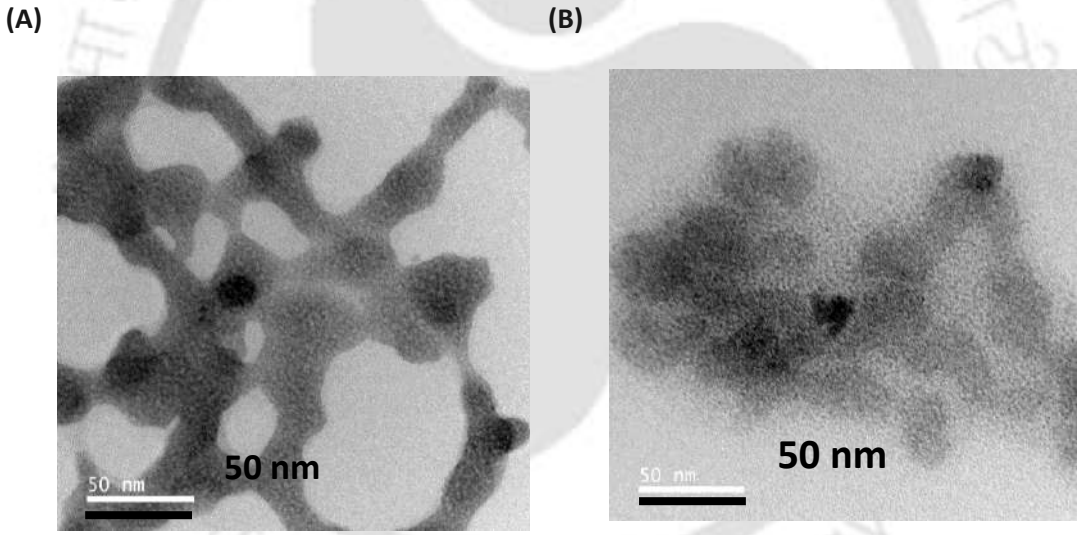

Figure S19. TEM images of the supernatant obtained after centrifuging the reaction mixture at 72 h that contains particles in the range 2-8 nm present in a branched network. (p.48)

References

1. Rohrer, M.; Bauer, H.; Mintorovitch, J.; Requardt, M.; Weinmann, H. J. Comparison of magnetic properties of MRI contrast media solutions at different magnetic field strengths. *Invest. Radiol.* **2005**, *40*, 715– 724.

2. Ullah, N.; Imran, M.; Liang, K.; Yuan, C.-Z.; Zeb, A.; Jiang, N.; Qazi, U. Y.; Sahar, S.; Xu, A.-W. Highly dispersed ultra-small Pd nanoparticles on gadolinium hydroxide nanorods for efficient hydrogenation reactions. *Nanoscale* **2017**, *9*, 13800– 13807.

3. Yang, S.; Song, X.; Zhang, P.; Sun, J.; Gao, L. Self-Assembled α-Fe_2O_3 Mesocrystals/Graphene Nanohybrid for Enhanced Electrochemical Capacitors. *Small* **2014**, *10*, 2270– 2279.

Chapter 3: Two-Dimensional Molecular Moiré Superlattices of Tryptophan with Visible Photoluminescence for Photo-activatable CO_2 Sensing and Storage

J. Mater. Chem. C, **2024,**12, 5506-5516

(https://pubs.rsc.org/en/content/articlelanding/2024/tc/d4tc00050a)

Chapter 3

ABSTRACT

Moiré superlattices of simple molecules portends to bring about new physical and chemical properties through the interactions at the crystal interfaces, which could be termed as hypermolecular interactions. We report the formation of moiré superlattices of L or D tryptophan (trp) molecules in the aqueous medium. A strong photoluminescence peak at 452 nm and an additional peak at 500 nm were observed. Transmission emission microscopy investigations revealed the formation of moiré superlattices with low-angle twisted hexagonal crystalline nanosheets of trp as the units. The atomic force microscopy measurements of the force-distance curves indicated van der Waals interactions typical of soft matter. The results could be accounted for by 25-30° helical stacking of 2D molecular crystals of trp, where a new interfacial interaction provided extraordinary stability to the superlattices. The superlattices were also found to have superior chemical stability under alkaline conditions as compared to the crystalline films. These molecular superlattices were useful for CO_2 sensing as well as storage that was more efficient following exposure to UV light (Scheme 1).

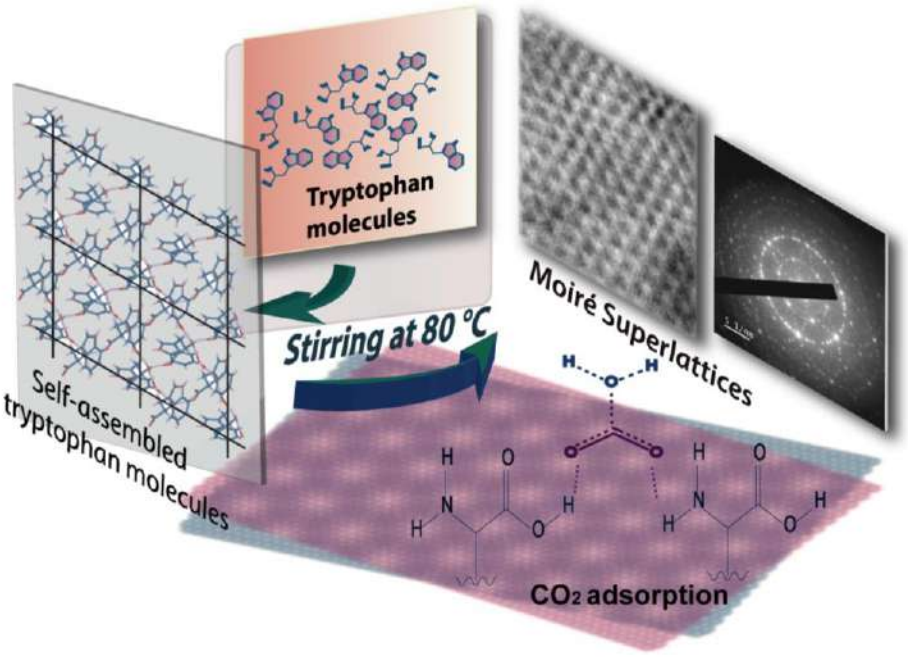

Scheme 1. Graphical representation showing assembly of trp molecules into 2D nanosheets that form moiré superlattices after twisted stacking. These superlattices were further used for CO_2 sensing.

Chapter 3

Introduction

Engineering macroscopic matter based on the principles of inter-molecular interactions has led to the development of programmed assemblies of molecules for wide applications such as in pharmaceuticals, chemical catalysis, sensing and separation, optoelectronics and photonics.[1,2] Of particular importance is the design of molecules and development of principles for the growth of crystals with emergent properties such as self-healing[3] or ferroelectricity[4] in molecular crystals. In addition, mechanical responsivity of the molecular crystals under external stimuli has led to their use in optoelectronics, sensors, pharmaceuticals or as biomimetics.[5-9] Thus, the repertoire of chemistry has been greatly utilized in order to develop a plethora of crystals with supramolecular synthons as structural motifs.[10,11] The vast progress also leads to an enticing possibility of 'chemical reaction' of such crystals in the liquid medium with distinct structures and properties arising out of the molecular interactions at the interfaces of the two intervening crystals. It may also be plausible that the interfacial interactions give rise to additional properties such as chemical stability to the constituent crystals. Thus, interactions involving the molecular moieties at the interfaces of the crystals, that could be defined as hypermolecular interactions, might bring novel chemistry of molecular superlattices especially when stacked twisted against each other. To begin with, it would be interesting to have such chemically superstack two-dimensional (2D) molecular crystals in the liquid medium under ordinary reaction conditions.

Evidences suggest that layered moiré 2D materials such as twisted bilayer[12] or multi-layered graphene[13], metal dichalcogenides[14], hexagonal boron nitride[15], black phosphorus[16] and perovskite oxide membranes[17] exhibit physical properties that are fundamentally different from regular crystalline stacking. For example, strong inter-layer electron coupling through van der Waals (vdW) interactions in 1.1º twisted bilayer graphene leads to superconductivity at 1.7 K.[18] Other examples include observation of moiré excitons in vdW heterostructures[19], Mott-like insulator states due to localized electrons in the moiré superlattices[20] and ferromagnetism resulting from anomalous Hall effect[21] in twisted bilayer graphene.

In physical methods, moiré superlattices are fabricated by mechanical exfoliation followed by careful stacking of twisted 2D monolayers. While the methods produce twisted layers with precise angular placements, scalability for industrial productions could be a major challenge. Recent results suggest that stacking of 2D materials can also be achieved by chemical methods in the liquid medium.[22,23,24] For example, gold[25] or copper nanoclusters[26] can be organized into 2D

nanosheets through complexation with zinc (Zn^{2+}) ions. Further twisted stacking of the 2D copper nanocrystal sheets, at 30° angles of each other, have been achieved by controlling the Zn^{2+} ion concentration in the liquid medium.[22] Further, chemically synthesised moiré superlattices of bismuth oxychloride spiral nanosheets are known to have superior photocatalytic activity.[24] Also, organization through chemical processes would make it possible to tune the properties of the assembly according to the chemical interaction of the constituents. Chemical methods of forming superlattices may also lead to additional stability of the 2D super-structure and offer properties arising out of interlayer interactions such as delayed fluorescence[22] or fluorescence with high quantum yield[23]. Although, moiré superlattices have been achieved for the above-mentioned materials, such an arrangement is yet to be reported for organic molecules. Fabrication of molecular superlattices through chemical method in a liquid medium and the resultant properties are yet to be reported.

A molecule of choice could be an amino acid that forms higher order structures through supramolecular interactions.[27] Amino acids self-assemble into structures such as nanoscale rods, ribbons, fibrils and sheets in a liquid medium with emergent physico-chemical properties.[28] For example, β-glycine crystalline needles and γ-glycine crystals show high shear piezoelectricity constant[29,30] close to variety of inorganic materials such as $BaTiO_3$, AlN or lead zirconate titanate while centrosymmetric α-glycine crystals display anomalous surface polarity[31]. Further, crystals of L-tyrosine[32] and racemic amino acids such as DL phenylalanine[33] are found to be mechanically robust having high young's moduli. The DL racemic mixture of trp can self-assemble to form bulk crystal and unlike the pure enantiomer, which grow into 1D fibril, it can grow to form stable 2D or 3D structures.[33] However, 2D assemblies of amino acid into well-aligned superlattices are yet to be reported.

Herein, we report that when an aqueous solution of (L or D) tryptophan (trp) was heated to 80 °C under stirring condition, formation of crystalline nanosheets of moiré superlattices of the molecule was observed. Transmission emission microscopy (TEM) experiments confirmed the presence of single crystalline nanosheets and moiré superlattices that resulted from the twisted stacking of the nanosheets. The superlattices showed strong photoluminescence at 452 nm when excited by 362 nm light. In addition, a peak at 500 nm that could be discerned upon deconvolution of the spectrum was observed. Treatment with a base led to quenching of the peak at 452 nm; however, the peak at the higher wavelength was persistent. TEM studies indicated the

extraordinary stability of the moiré films under basic conditions, while the crystalline nanosheets vanished giving rise to folded 1D structures. Atomic force microscopy (AFM) measurements, in both phase and amplitude modes, supported the formation of moiré superstructures with force-distance curves indicating the van der Waals interactions between the crystalline films at the interfaces of the superlattices. The results suggested the formation of molecular moiré superlattices that was consistent with the crystal structures of the molecule. The current nanosheets possibly indicated a new form of interactions that could be called hypermolecular interactions between the moieties at the interfaces of the crystalline sheets leading to the formation of such assemblies and the observed properties therein. Additionally, the molecular superlattices formed through such interactions showed good efficiency in sensing and storage of CO_2 especially upon prior exposure to UV light.

Results and Discussion

Optical properties

An aqueous solution of trp (288 μM) was stirred vigorously under a constant temperature of 80 °C for 24 h and UV-vis and photoluminescence (PL) spectra at different times were recorded for 3 mL aliquots. In addition to the native peaks due to trp (250-310 nm), a peak at 362 nm appeared in the UV-vis spectrum (Figure 1a) as the reaction progressed. Initially, at 0 h when the solution was excited by 300 nm light (Figure 1b), the intrinsic fluorescence of trp molecule[34] with peak maximum at 360 nm was observed. An additional prominent peak at around 452 nm was observed by 6 h. Amino acids such as trp in their aggregated forms are known to emit in the blue region.[35,36] Trp molecules can self-assemble through van der Waals (vdW) interactions, which primarily include hydrophobic interaction and hydrogen bonding (H-bonding) between the carboxylate and amine groups to form supramolecular structures[27,33,36] like fibrils and β sheets that result in blue emission. Similarly, here the emission peak observed at 452 nm could have resulted from an assembly of trp. When excitation spectrum for the emission at 452 nm was recorded, an additional peak at 362 nm emerged with time and a simultaneous increase in the intensity at 300 nm was observed (Figure 1c). Thus, the assembly so formed absorbed simultaneously at 300 nm and 362 nm, resulting in an emission peak at 452 nm (Figure 1b and 1d).

With time, the intensity of the emission peak at 360 nm decreased while that at 452 nm increased, indicating continuing assembly formation of the molecules. As the absorption at 300 nm gave rise to both the emissions, the decrease in the intensity of emission at 360 nm could be due to inner filter effect arising from the self-assembled structure. The asymmetric emission peak at 452 nm (λ_{ex} = 362 nm) was deconvulated into two components – one at 450 nm and another at 500 nm (Figure 1e). The presence of a new emission peak at 500 nm was an indication of another type of interaction between the trp molecules possibly with the formation of a new kind of assembly. Further, the rate constant of the reaction to form the assembly was determined by plotting PL intensity at 360 nm against time (Figure 1f) as detailed in the SI. The plot of 1/(intensity) vs time indicated that the reaction followed second order kinetics and the rate constant was calculated to be $(1.55 \pm 0.68) \times 10^{-3}\ \mu M^{-1}\ h^{-1}$.

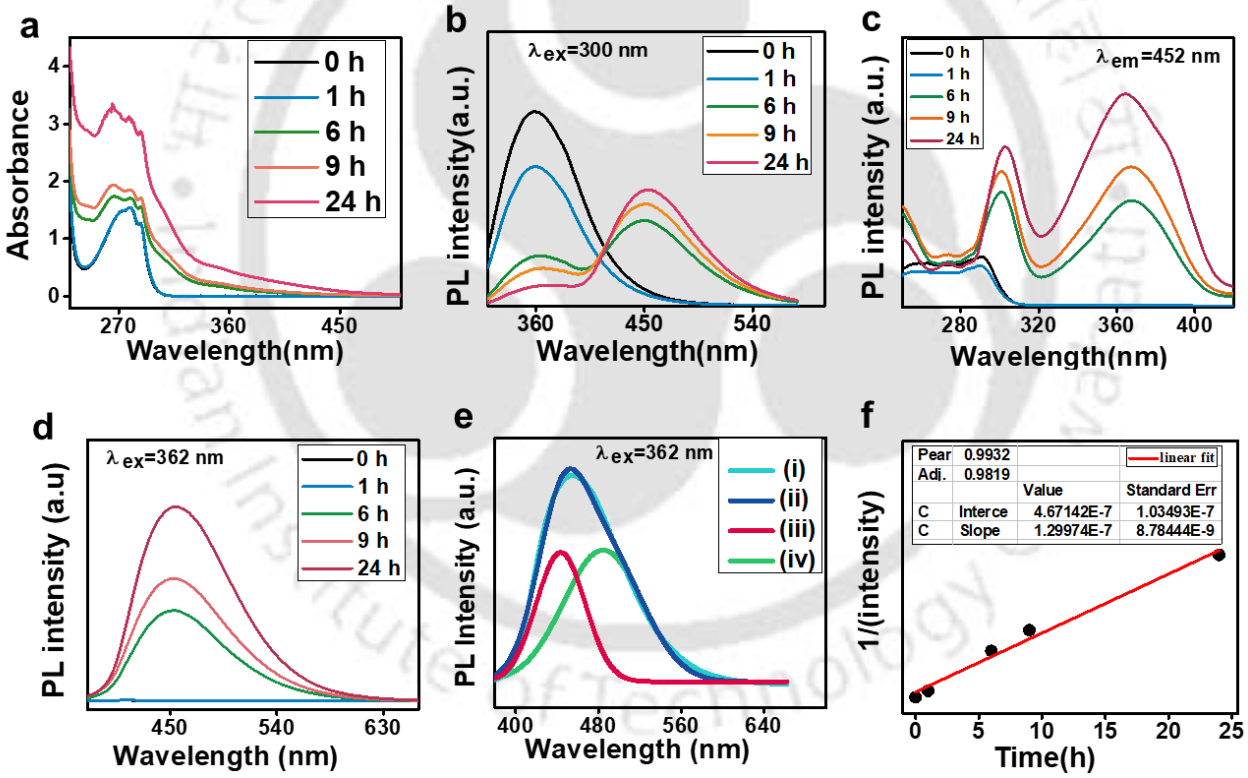

Figure 1. (a) UV-vis spectra recorded at different time intervals of tryptophan (trp) solution, which was continuously stirred and heated at 80 °C. Inset: enlarged view of the normalised UV-vis spectra identifying the peak around 360 nm. Photoluminescence (PL) **(b)** spectra (λ_{ex} = 300 nm), **(c)** excitation spectra (λ_{em} = 452 nm) and **(d)** spectra (λ_{ex} = 362 nm) of the dispersion taken at different times. **(e)** (**i**) PL spectrum of trp solution at 24 h and its deconvoluted components

having peak maxima at (**ii)** 450 nm and (**iii)** 500 nm and (**iv)** is fitted curve for the two components. **(f)** 1/(intensity) vs time plot for the 360 nm peak in (**b)**.

Transmission emission microscopy (TEM) was pursued for the dispersion at different times. The images (Figure S2) indicated the presence of 2D multi-layered nanosheets in the dispersion at any given time. However, the dispersion at 24 h consisted of crystalline nanosheets of high population. Thus, further experiments and analyses were pursued using the dispersion at 24 h. Interestingly, there was a mixture of two types of sheets at 24 h – nanosheets with single crystalline diffraction pattern and multi-layered sheets displaying moiré patterns (Figure S3).

Single crystalline 2D nanosheet

The crystalline 2D nanosheets presented in Figure 2a and the corresponding selected area electron diffraction (SAED) pattern in Figure 2b revealed a hexagonal pattern with d-spacing 0.47 nm. The planes correspondent diffraction spots in Figure 2b are identified and indicated through circles in Figure S4. L-trp crystallises in triclinic unit cell with space group P1 where the crystal follows a pseudo-hexagonal arrangement and the asymmetric unit contains 16 trp molecules.[37] The diffraction spots that are observed for the crystal follows- the given set of rules: h + k = even and k = even.[37] The SAED pattern for the crystal was simulated from the crystallographic information file (cif) of L-trp using ReciPro software[38] and is presented in Figure 2c. The allowed diffraction spots following the above rule are encircled in yellow in Figure 2c and is compared with experimental SAED in Figure 2b and in Figure S4 where the spots are designated with respective hkl planes. The d spacing obtained after simulation are listed in Table S1 and are compared with the calculated d spacing from the SAED pattern of the crystalline nanosheets.

The unit cell of L-trp is recreated here along the c axis using the cif data of L-trp and the mentioned planes in Figure 2d are redrawn using the software vesta. Considering the centre of the unit cell as origin (000), the diffraction spots that would have been observed for the set of planes in the inverse space are marked as circles. L or D-tryptophan can form 2D crystalline nanosheet through H-bonding and hydrophobic interaction if the crystal growth along one direction is terminated. The single crystalline nanosheet that is presented in Figure 2a have formed due to the termination of crystal growth along c axis. The growth along a and b axes are

shown in Figure 2e where the first layer of the trp crystal is represented for clarity. The diagram representing the subsequent layers is presented in Figure S5. Here, the molecular units are organized in hexagonal order in the supercell with each molecule facing the adjacent unit at ±60º angle.

Figure 2. (a) TEM image of the 2-dimensional nanosheet formed through the assemblies of trp molecules. **(b)** Corresponding hexagonal selected area diffraction pattern (SAED) pattern. **(c)** Simulated SAED pattern obtained from the crystallographic information file (cif) of trp crystal,

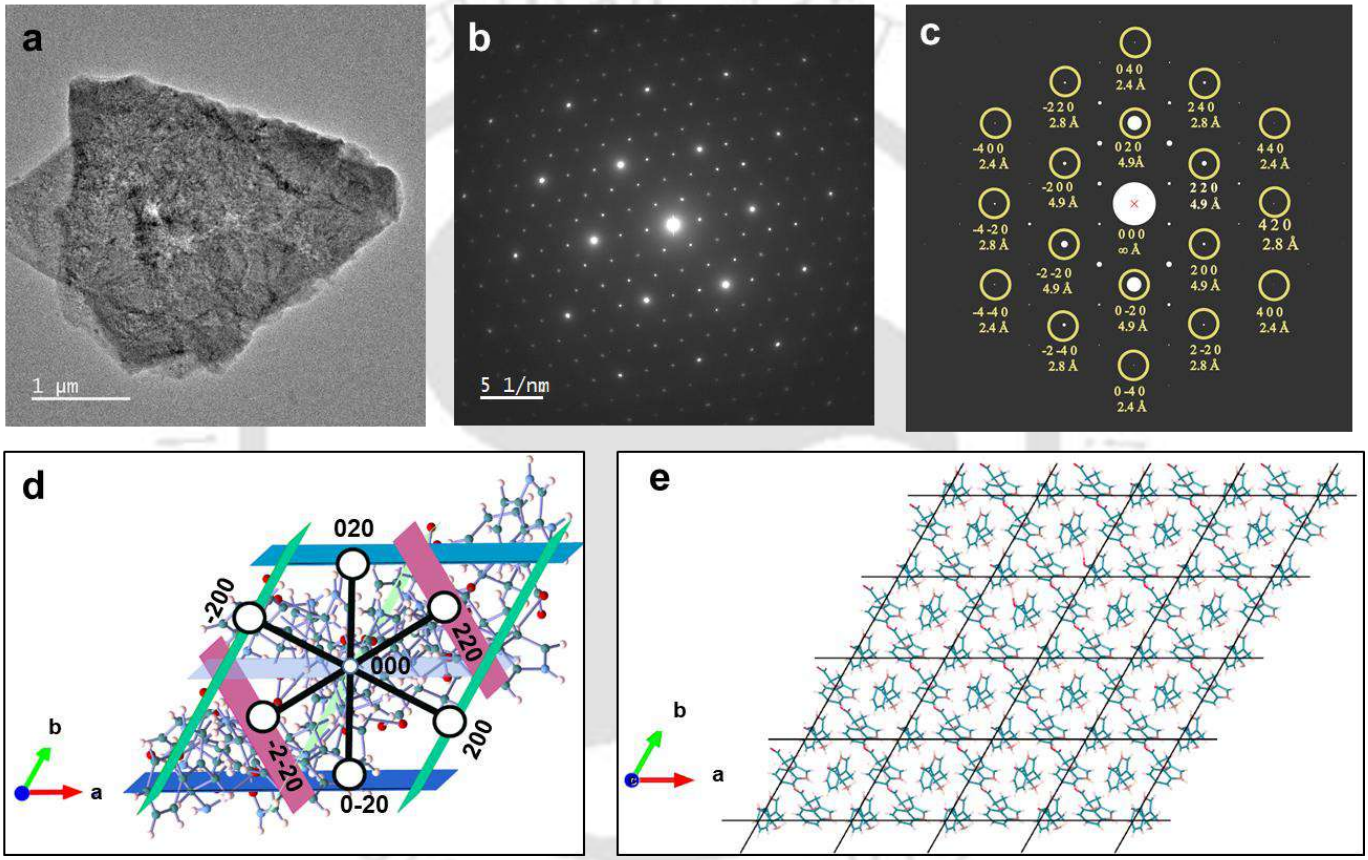

and drawn using Recipro software where the allowed diffraction spots are encircled in yellow. **(d)** Unit cell representation of the asymmetric unit of the trp crystal viewed along the c axis showing the lattice planes 200, 020, 220, -200, 0-20, -2-20. **(e)** First layer of the supercell viewed along the c axis.

Moiré Superlattices

The dispersion after 24 h of reaction largely contained multi-layered crystalline nanosheets exhibiting moiré patterns (Figure 3). It was evident from that TEM images that both the mixture

of moiré and non-moiré nanosheets or most of the time only moiré sheets were observed. Moiré fringes were formed by the twisted stacking of the single crystalline nanosheets. Multi-layered stacking of the nanosheets resulted in hexagonal (Figure 3a-b) or parallel line moiré patterns. At a small twisted angle moiré patterns of much higher periodicity are formed whereas a higher twist angle between the sheets offers smaller moiré periodicity. The corresponding SAED pattern obtained at the hexagonal moiré superlattice in Figure 3b shows multi-diffraction pattern (Figure 3c). Figure 3d-e show parallel moiré pattern and the corresponding SAED pattern of Figure 3e is presented in Figure 3f. The d spacing corresponding to the first circle of SAED pattern in Figure 3c and Figure 3f is 0.21 nm.

Moiré patterns in Figure 3 are formed after twisted layering of the trp 2D nanosheets at particular angles. Since hexagonal SAED pattern is obtained along the c axis, the diffraction pattern obtained from twisted layered trp nanosheets should resemble a set of hexagonal spots, which are rotated at an angle. Here, the SAED pattern in Figure 3c contains seven set of hexagonal patterns rotated at different angles obtained from seven twisted layered sheets (Figure 4). The d spacing obtained from the SAED pattern of moiré sheets was 0.21 nm while the d spacing obtained for the spots in first circle of SAED pattern in single crystal nanosheet of trp was 0.47 nm. Ideally, the first ring of the SAED of the layered sheets should provide with d spacing equal to 0.47 nm same as the parameter of the single crystal. However, the spots in the 3rd circle with d spacing of 0.23 nm from origin (Figure S6) was observed in the diffraction pattern of moiré superstructure. It was observed that SAED patterns with d spacing 0.47 nm did not show any moiré fringes in the corresponding TEM images (Figure S7). On the other hand, d spacing of 0.21 nm were obtained from the sheets having moiré fringes. Further, it may be mentioned here that 2D film with moiré patterns is tilted while probing by TEM, a hexagonal moiré pattern may appear as parallel line pattern or vice-versa such as in h-BN[39] and HOPG[40] moiré superlattices. Since both hexagonal moiré patterns, which form multi-diffraction pattern and parallel line patterns with diffraction pattern as in Figure 3f are observed in our sample, the angular position of the sheets on the TEM grids determined the exact nature of moiré and diffraction pattern (Figure S8). Appearance of 0.47 nm d-spacing for a tilted moiré sample with observed d-spacing of 0.21 nm also supports our current observation.[23]

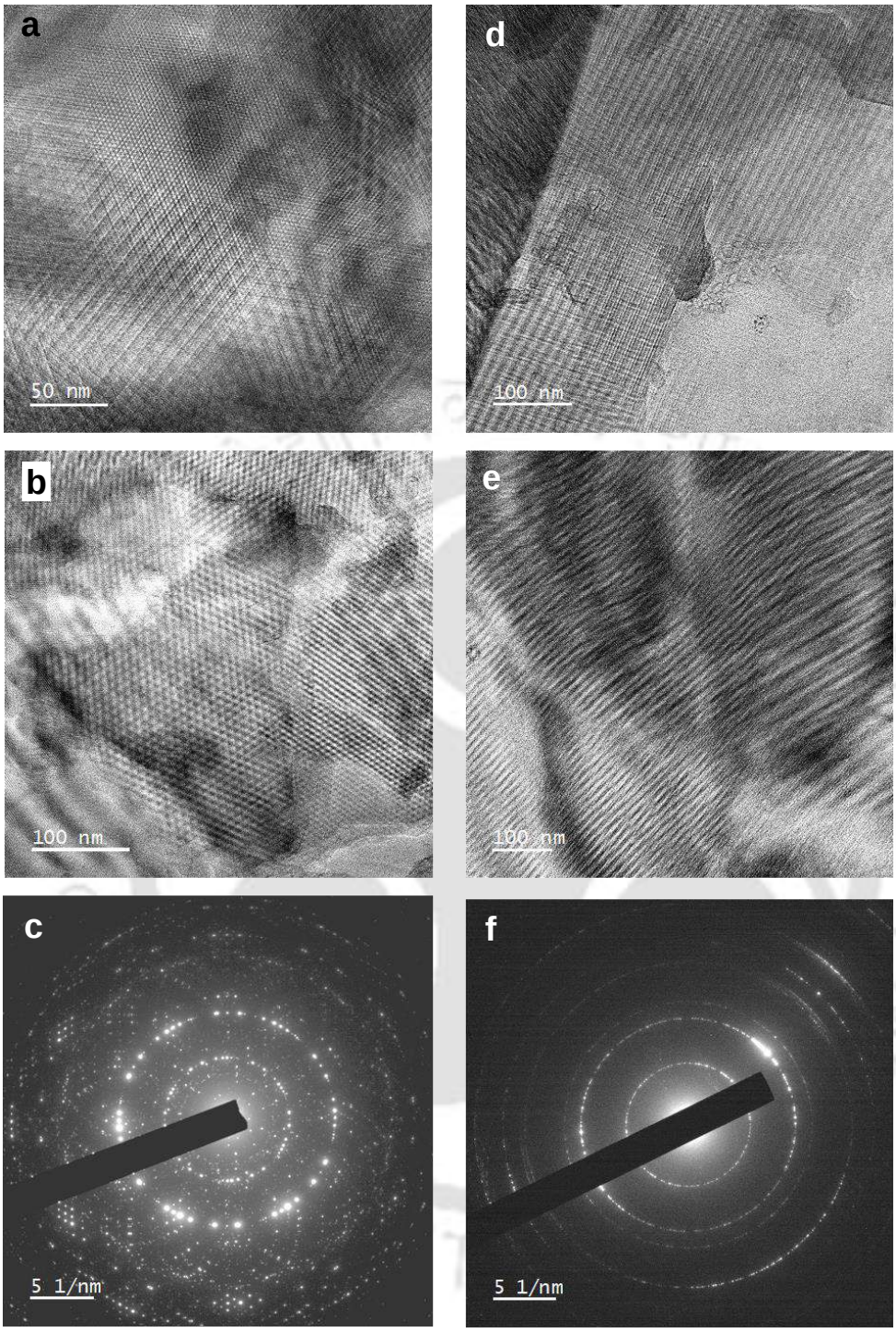

Figure 3. (**a)** and (**b**) Moiré patterns formed by the twisted stacking of single crystalline hexagonal 2-D nanosheets of trp. **(c)** SAED pattern corresponding to image in (**b)**. (**d)** and **(e)** parallel moiré pattern formed by the twisted stacking of single crystalline 2-D nanosheet of trp. **(f)** SAED pattern corresponding to image in (**e)**.

Diffraction Pattern from Moiré Superlattices

Schematically, the multi diffraction pattern obtained in Figure 3c is explained in Figure 4. In Figure 4a, the represented unit cell consists of the set of planes having d spacing of 0.23 nm and 0.47 nm as mentioned in the Figure S4. Since, d spacing of 0.21 nm was obtained for moiré sheets, we focused on the planes having d spacing 0.23 nm (Figure 4b) for understanding the diffraction pattern obtained in Figure 3c. The circles represent the diffraction spots that would be obtained for the respective hkl planes from a particular region of the crystal in the inverse space. The straight lines in Figure 4b-d are drawn to connect a set of diffraction planes as representations. As the reaction progressed, the crystalline nanosheets - for reasons explained in the next section - were stacked twisted angularly in the range of 25° to 35° (Figure S9). The initial step would be stacking of two crystalline nanosheets in the angular range mentioned above as observed in TEM images, which on further twisted stacking produced the diffraction pattern in Figure 3c and 3f. For example, as the two trp crystalline sheets are stacked at an angle of 28.9° for sheets marked as 1 and 2, respectively, two sets of hexagonal diffraction spots for the mentioned hkl planes in Figure 4b are obtained (Figure 4c). Further, simulated SAED patterns of twisted stacking of seven crystalline nanosheets with two consecutive nanosheets positioned at an angle in the range of 25°-35° are reproduced (Figure 4d) and super-positioned with an observed pattern in Figure 4e. The angles with which the adjacent nanosheets are twisted have been given in Table S2.

Although the twisted stacking of adjacent nanosheets are in the range 25º to 35º, the angle between alternate nanosheets could be sufficiently small resulting in high moiré periodicity. As can be seen in Figure 3b, moiré fringes are not uniform in the overall superlattices since the moiré superlattices were formed by the different sized nanosheets stacked on top of each other. For the example, the angle between sheets 1 and 2 is 28.9º and the angle between 2 and 3 is 25º, thus, resulting in an angle of 60- (25+28.9) = 6.1º between 1 and 3 (Figure S10). If the dimension of sheet 2 is less than those of 1 and 3, then there would be an overlap and thus, interaction between sheets 1 and 3 and moiré fringes with high periodicity would be observed. Similarly, an angle of ~ 3º between 1 and 5 and an angle of 4.3º between sheets 5 and 7 would produce moiré fringes. The moiré periodicities are calculated according to the equation

$$D = d/(2\mathrm{Sin}(\theta/2)) \qquad (1)$$

where d is the lattice constant taken as 0.46 nm, D is the distance between moiré fringes and θ is the twist angle. The corresponding moiré periodicities calculated for the angles 3, 4.3, 6.1 and 25º are 8.79, 6.13, 4.32 and 1.06 nm respectively.

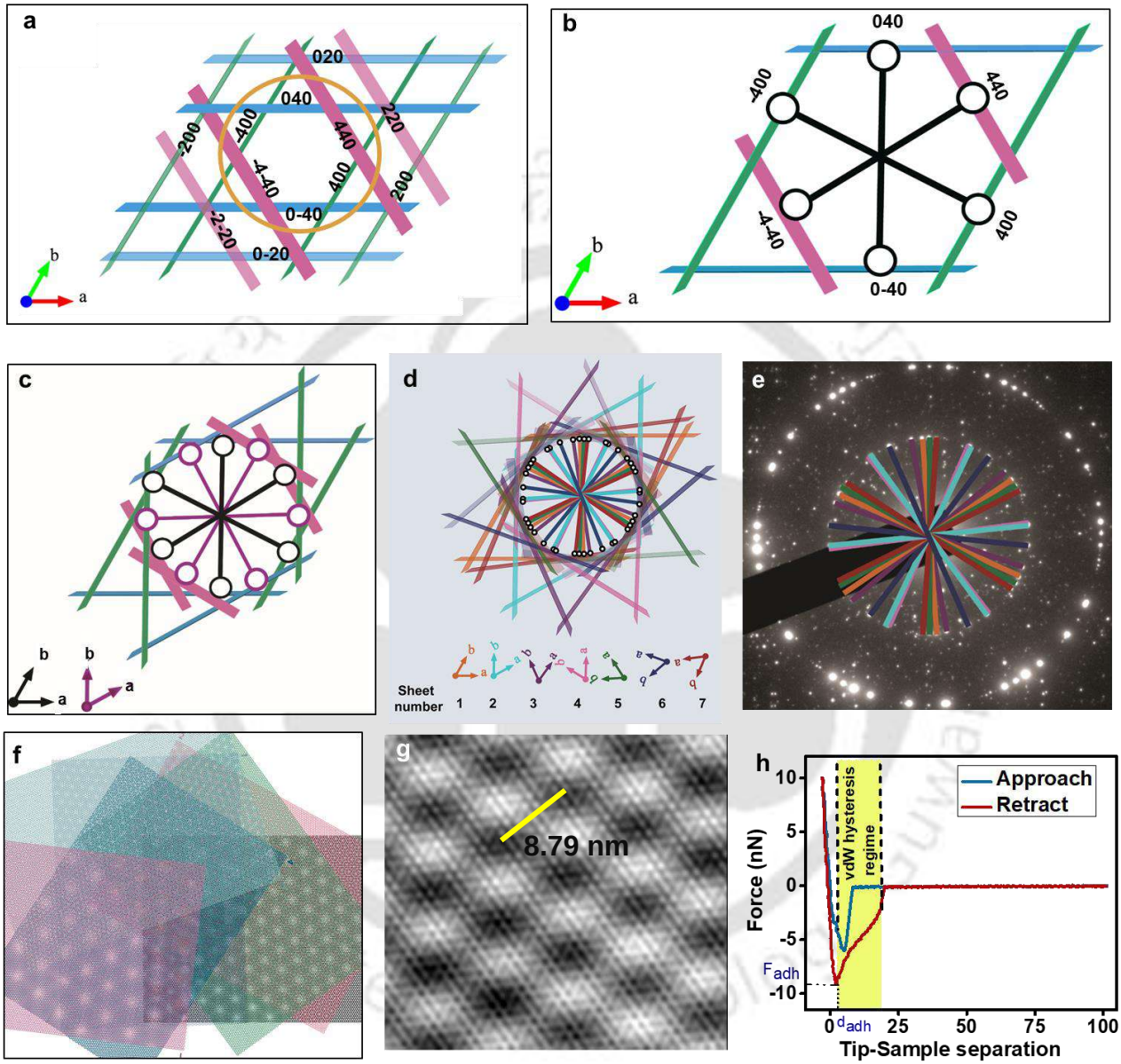

Figure 4. (a) Representation of trp crystal unit cell displaying the respective planes. **(b)** Enlarged view of the planes 400, 040, 440, -400, 0-40, -4-40. **(c)** Two superimposed unit cells when rotated at an angle of 28.9°. **(d)** Schematic representation of seven unit cells rotated at specific angles with respect to the first unit cell. The diffraction pattern generated from the layered unit cells resembles the experimental diffraction pattern in (**e**). **(f)** Schematic representation of the

moiré superlattice formed after twisted stacking of seven hexagonal sheet. **(g)** IFFT analysis of a small portion of the moiré sheet of Figure 3b. **(h)** A typical Force-Distance curve measured on a moiré nanosheet.

A schematic representation of the moiré pattern produced after twisted stacking of seven crystalline nanosheets is depicted in Figure 4f. In Figure 4g, inverse fast Fourier transform IFFT of a small portion of moiré superlattices of Figure 3b is presented, which results in moiré periodicities of 8.73, 1.51 and 1.06 nm that are comparable with the above calculated values. Further calculations of moiré periodicities obtained from the IFFT are presented in the SI. The smaller moiré periodicity would result from larger angles between adjacent sheets or alternate sheets.

Atomic force microscopic (AFM) images further supported the formation of the moiré patterns and force-distance (F-d) measurements on the sheets were pursued. A typical F-d curve measured on the moiré sheets is presented in Figure 4h where the tip-sample interaction resulting in vdW hysteresis regime[41] was observed. The height profile, phase and amplitude images along with 50 F-d curves are presented in Figure 5. The height profile of the moiré nanosheets is presented in Figure 5b and the average height of the sheets was 88.43 ± 5.76 nm. The adhesion force and the dissipation energy due to tip-sample interaction can be obtained after analysis of the F-d curves. The adhesion force is the minimum force required for the withdrawal of the tip after its contact with surface of the sample is established. Thus, the lowest point of the retract force curve gives the value of adhesion force (Figure 4h).[41] The adhesion force calculated from Figure 4h was 9.12 nN and dissipation energy was found to be 381.5 eV. The dissipation energy is the energy dissipated due to sample-tip interaction after indentation by the tip at the surface of the sample. If the approach and retract curves do not overlap, a hysteresis is observed and the dissipation energy can be calculated from the area enclosed between them.[41,42] During the tip-sample interaction, overlap of loading and unloading force curves in the repulsive region indicated the dominance of elastic properties while the large difference of the force curves in the attractive region suggested high dissipation of energy due to long range forces (Figure 4h). Since hydrophobic interaction between the aromatic groups and H-bond between the carboxylate and amine groups built up the moiré superstructure, a net dipole is expected to arise from the moiré nanosheets. Thus, the interaction between the neutral tip and the sample would be based on

Debye forces. The average dissipation energy calculated from 50 F-d curves (Figure 5c) was 540.5 ± 210.4 eV and the average adhesion force was 7.79 ± 3.29 nN as it depended on how strong the interaction between the tip and moiré nanosheets were. The dissipation energy values were typical of materials such as HOPG[42], DNA chip[43] and polymers[44].

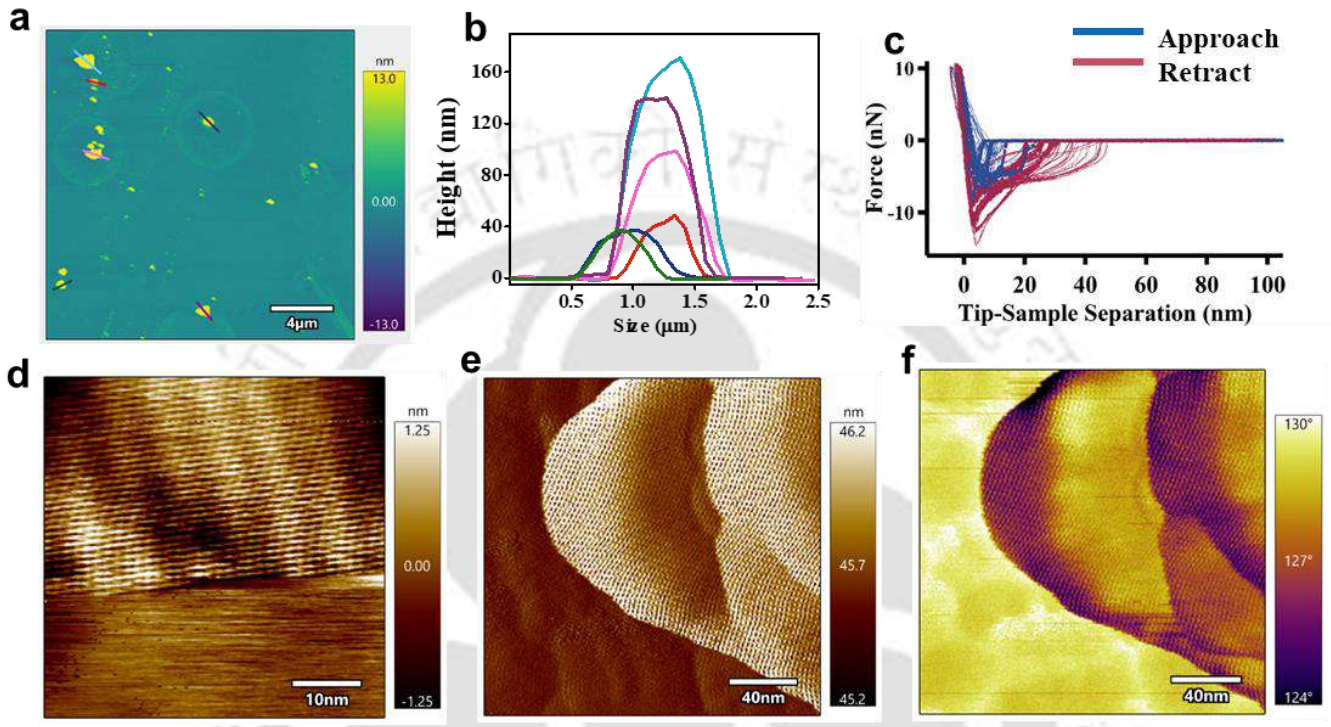

Figure 5. (a) AFM topographic image of trp moiré nanosheets. **(b)** Corresponding height profile of moiré sheets as obtained for the samples in (**a**). The various colors in the height profile in Figure 5b represents the respective moiré nanosheets in Figure 5a, which are marked with the same color corresponding to their height profile. **(c)** 50 Force-distance curves measured on several moiré nanosheets. (**d**) and **(e)** Amplitude images of moiré patterns obtained from trp nanosheets performed through tapping mode. **(f)** Corresponding phase image of (**e**).

Interestingly, the moiré superstructure was found to be stable under basic conditions. However, the non-moiré sheets were prone to roll into 1D structures when treated with 1.0 M NaOH solution. TEM results indicated that when a dispersion containing moiré and non-moiré sheets was treated with NaOH, moiré sheets remained unchanged while non-moiré sheets were damaged and subsequently transformed into 1D fibers (Figure 6). Further PL emission and excitation spectra of the dispersion were recorded before and after addition of base. After addition of base, the intensity of the emission maximum at 452 nm (λ_{ex} = 362 nm) decreased

(Figure 6a-(ii)) possibly indicating that the H-bond network in the crystal was affected. In addition to this, the peak at 500 nm attributed to moiré superlattices appeared distinctly when excited at 362 nm (Figure 6b). The excitation spectrum for λ_{em} = 500 nm resulted in an additional peak at 425 nm and UV-vis spectrum (Figure S12a) also comprised of absorbance peak at 410 nm. Upon exciting at 425 nm the emission peak with maxima at 520 nm was observed (Figure 6c). The dispersion was subjected to acid-base cycle where it was observed that the PL intensity at 452 nm was regained as the medium became acidic again (Figure 6d). The intensity of the intrinsic peak of trp at 360 nm increased and shifted as the medium became basic. Since the H-bond network was disrupted after addition of base, the inner filter effect originating from the superstructure was reduced and the intensity at 360 nm increased. The change in intensity of maxima at 360 nm, 452 nm and 520 nm with respect to the change in pH of the medium is presented in Figure 6d. This further supports the stability of the moiré superlattices of trp in basic and acidic medium with the PL intensity changing back to its original value after addition of 1.0 M HCl. It may be mentioned here that different peak maxima were observed ranging from 510 nm to 525 nm when excited at 425 nm (Figure S13). This might have originated due to different twisted angles of different stacked nanosheets.

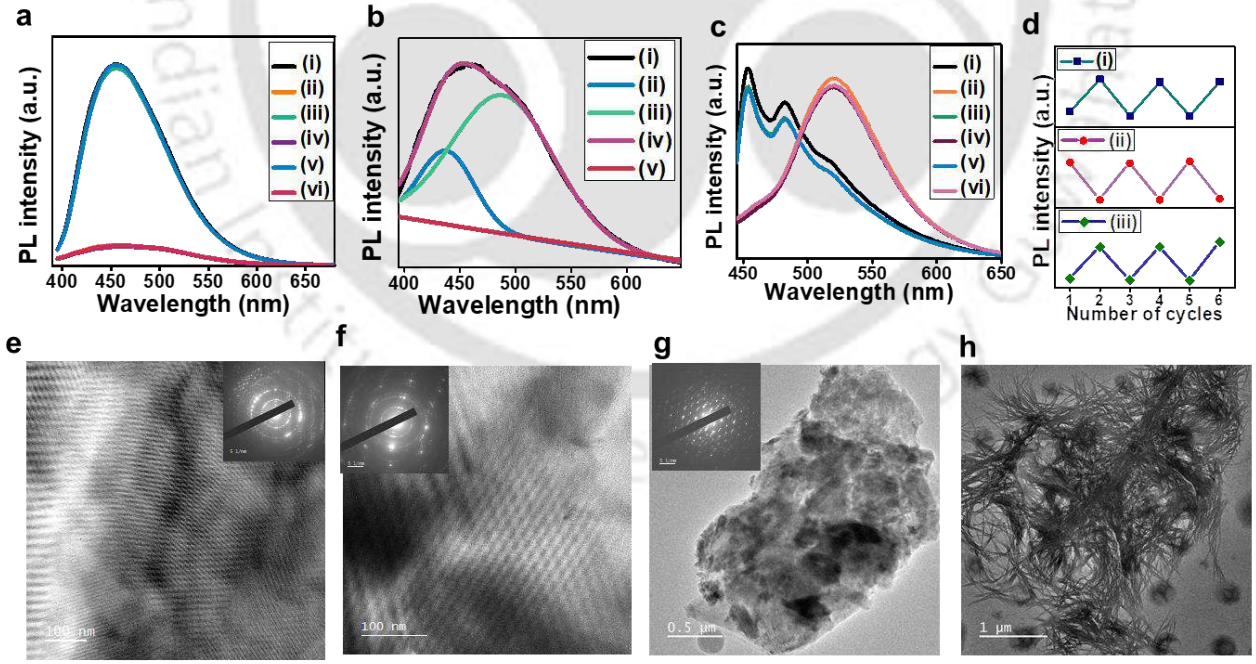

Figure 6. (a) PL spectrum (λ_{ex} = 362 nm) of tryptophan (trp) solution after **(i)** 24 h of vigorous stirring at 80 °C, which is subjected to a cycle of pH change where **(ii), (iii), (iv), (v)** and **(vi)**

represent alternative addition cycles of 40 µL 1M NaOH and 40 µL 1M HCl solutions, respectively, to the mixture. **(b)** PL peak after **(i)** addition of 40 µL of 1M NaOH that is deconvoluted into two peaks components having peak maxima at **(ii)** 450 nm and **(iii)** 500 nm where **(iv)** is fitted curve for the two components and **(v)** is the baseline. **(c)** PL spectra (λ_{ex} = 425 nm) of trp solution after **(i)** 24 h of vigorous stirring solution at 80 °C, which is subjected to a cycle of pH change where (**ii), (iii), (iv), (v)** and **(vi)** represent alternative addition cycles of 40 µL 1M NaOH and 40 µL 1M HCl solutions, respectively, to the mixture. **(d)** Intensity change for **(i)** 360 nm, **(ii)** 452 nm, and **(iii)** 420 nm peaks after the dispersion is subjected to base-acid cycle. TEM images of moiré superlattices **(e)** before and **(f)** after treating the dispersion with 40 µL 1M NaOH solution. TEM images of **(g)** non-moiré nanosheets converted to **(h)** 1D fibrous structures following treatment of the dispersion with 40 µL 1M NaOH solution. Inset: corresponding SAED pattern.

Chemical description of crystalline nanosheet and moiré formation

Since moiré fringes are formed by the twisted stacking of the crystalline nanosheet along the c axis, the interaction at the interface of the crystals must be different from within the crystal. Rotation of subsequent single crystals of height 'd' nm at angle ranging from 25º to 35º results in a spiral superstructure (Figure 7). During crystallization of trp, the growth along c axis involves alternate H-bonding and hydrophobic interactions between the layers of the molecules (Figure S14). If the crystallisation along the a and b axes continued unabated but that was terminated along the c axis after growth of a few nm, such crystalline nanosheets would be obtained. For D or L trp, the hydrophobic interaction involves ±60º interaction among the neighboring indole groups resulting in edge to face interaction.[37] For racemic DL-trp system, hydrophobic interaction involves face to face aromatic interaction between the indole groups providing rigidity to the structure.[33] For our system, twisting of crystalline nanosheets of pure L or D trp in the range of 25-35 degrees results in face to face interaction for half of the indole groups at the interface (marked with circles in Figure 7b) with remaining indole groups having edge to face interaction (unmarked). These interactions at the interface might have provided the additional stability to the superstructure. As the interaction of the molecules at the crystal interface is different from that of supramolecular interactions in the crystal, the interactions can be termed as

hypermolecular interaction. The new interactions at the interface might have generated a new energy state for which the emission at 500 nm was observed (Figure 1e and Figure 6b and 6c).

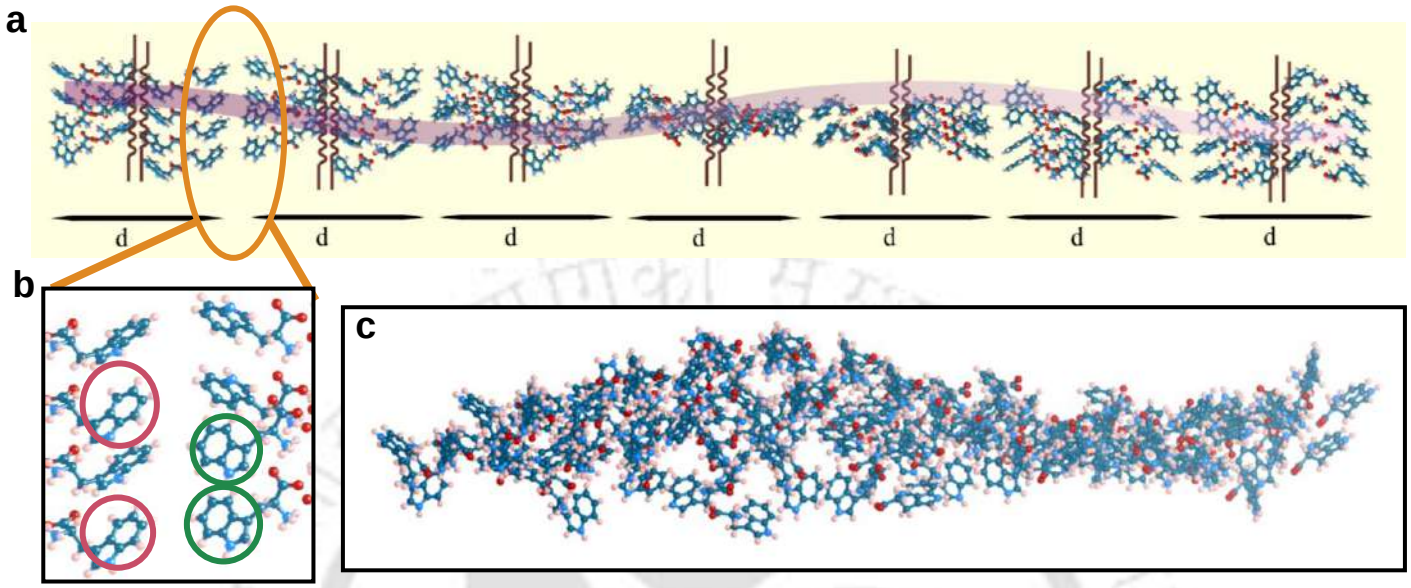

Figure 7. (a) Side view of molecular organization of the trp single crystalline 2-D nanosheets of thickness d into a twisted array to form moiré superlattice. **(b)** Magnified view of the interaction between two ends of trp single crystal nanosheets rotated at an angle of 28.9°. The red circles represent the two parallel units of crystal 1 having lateral interaction with another two units of crystal 2 encircled in green. **(c)** The super structure in (**a**) visualised from another direction exhibiting spiral nature.

The self-assembly of trp was confirmed by mass spectrometry and NMR spectroscopy. After 2 h of stirring at 80 ºC, mass spectra were acquired and after analysis, m/z values of 205.22, 409.18 and 613.17 were observed corresponding to $[C_{11}H_{12}N_2O_2+1H^+]$, $[(C_{11}H_{12}N_2O_2)_2 +1H^+]$ and $[(C_{11}H_{12}N_2O_2)_3 +1H^+]$, indicating the presence of monomer, dimer and trimer fragments of trp. (Figure S15). The results also indicated that the superlattices were made of trp molecules only. Analysis of time dependent NMR also indicated a chemical shift of the protons as the reaction proceeded (Figure S16 and Table S3). An upfield shift of the aromatic protons H_a, H_b, H_d and H_e indicated shielding due to π-π interaction. However, a downfield shift of H_c proton adjacent to aromatic ring N-H was observed. The shift was caused due to change in chemical surrounding of H_c proton after formation of H-bond between adjacent aromatic N-H and water. Similarly, downfield shift for protons H_f, H_g and H_h was observed for H-bond formation of the

neighbouring amine and carboxylate groups. With time, three new singlet peaks arose by 8 h as the reaction progresses in D_2O. The value of integrated area for the NMR peaks suggested that the area for peaks at 2.1, 4.2 and 8.3 ppm as compared to H_c had increased, indicating change in the chemical environment of H_c at crystal interface resulting in a large chemical shift (Table S4). It is known that change in the protein interface can cause a shift of about of 3 ppm[45] for protons, which is somewhat similar to change caused at the interface of two crystals of trp due to twisted stacking. The chemical shift values of all the protons are presented in Table S3.

Photo-activatable CO_2 sensing and storage

Additionally, the dispersions of the moiré superstructures were found suitable for sensing gaseous CO_2 through the changes in visible fluorescence. Thus, while the dispersion was purged with CO_2, an increase in the PL intensity at 452 nm was observed (Figure S17, Figure 8a). Again, if the system was purged with CO_2 while being irradiated with UV light (362 nm) the percentage increase in intensity at 452 nm was more compared to absence of UV light exposure (Figure 8c). Importantly, the results also indicated that with longer exposure time the intensity of the emission increased. Further, the rate of increase in PL intensity in the presence of CO_2 and following exposure to UV light was found to be 2.6 ± 0.9 times higher compared to that in the absence of UV light exposure. On the other hand, the release study of CO_2 indicated that when exposed to UV light, the release was slow while that for the system not exposed to UV light was faster (Figure 8d). Thus, the release rate for CO_2 from the system not irradiated with UV light was 2.5 ± 1.8 times higher compared to the system that was exposed to UV light for long. This indicated that when irradiated with 362 nm light, the moiré superlattices not only adsorbed CO_2 efficiently but also were able to store the same for longer times. The TEM images for the samples before and after CO_2 purging were acquired that indicated that the moiré superlattices remained unaffected (Figure S18). It has been established that CO_2 could be reversibly captured by aqueous solution of organic molecules through bicarbonate dimer formation via hydrogen bonded crystallisation.[46] For the current superlattices the CO_2 adsorption seems to have followed a similar mechanism where the surface amine and carboxyl groups participated in the H-bonding with CO_2.

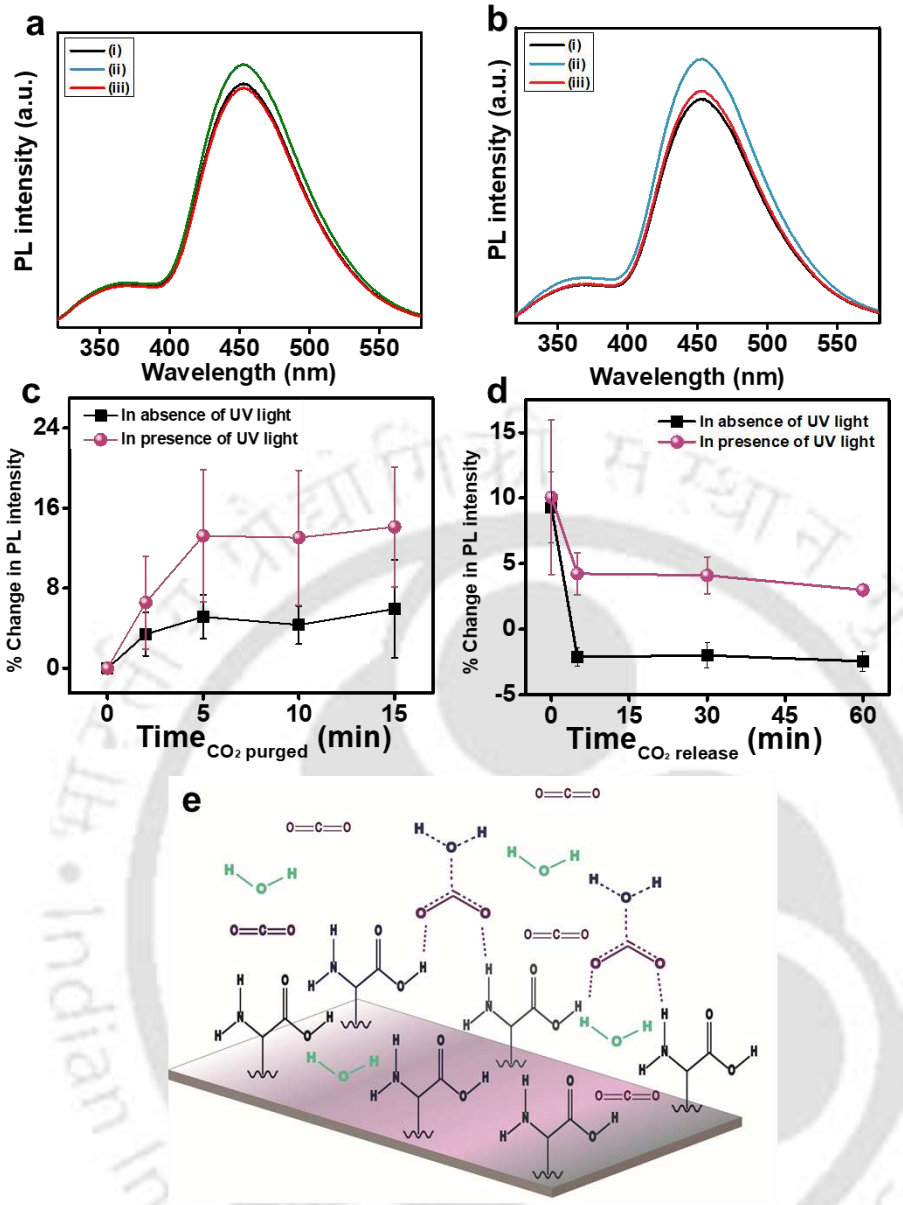

Figure 8. (a) PL spectra of the dispersion after **(i)** 24 h of reaction that was purged with CO_2 gas for **(ii)** 15 min and then kept in open for **(iii)** 60 min. **(b)** PL spectra of the dispersion after **(i)** 24 h of reaction that was purged with CO_2 gas for **(ii)** 15 min under the exposure of UV light and then kept in open for **(iii)** 60 min. **(c)** Change in PL intensity of 452 nm peak in the presence of CO_2 above the dispersion. **(d)** Rate of release of CO_2 from the system when kept open for 60 min. **(e)** Schematic representation of the adsorption of CO_2 through H-bond formation with the nanosheet.

The surface amine and carboxyl groups of the nanosheets were involved in inter molecular H-bonding or were solvated by surrounding water molecules. The attachment of the CO_2 molecules through hydrogen bonding at the edges of the lattices (Figure 8e) might have helped increase the PL intensity by rigidifying the edges exposed to the solvent molecules. The presence of UV-light might have supported facile hydrogen bond formation between the dissolved CO_2 molecules and the surface groups of the lattices. The dissolved CO_2 might have formed carbonic acid or bicarbonate ion in the medium that interacted with the surface groups of the nanosheets. When CO_2 was introduced in absence of UV light, the carbonic acid or bicarbonate ion might have bonded to the free carboxylate and amino groups through H-bonds, thus rigidifying the peripheral structure and as a consequence increasing the PL intensity of the dispersion. The energy required for the H-bond rupture at the surface to form new bonds with carbonic acid or bicarbonate ion was provided through excitation with UV light at 362 nm while the excess energy was released through solvent relaxation. Thus, upon excitation with UV light, a higher amount of dissolved CO_2 was able to interact with free terminal groups leading to the formation of a larger networked structure at the periphery. Similarly, the release rate for the UV exposed system was slower since the numbers of dissolved CO_2 (i.e., carbonic acid or bicarbonate ions) that bonded with surface of the nanosheets were higher as compared with the dispersion that was not exposed to UV light. The slow rate of diminishing PL intensity further supported the utilisation of UV exposure for better sensing and reversible storage of CO_2 for a longer period of time.

Conclusion

In summary, moiré superlattices of L or D trp were formed by vigorously stirring an aqueous solution of trp at 80 °C. Trp molecules self-assembled to form crystalline 2D nanosheets, which further twisted and stacked to form moiré superlattices. The layering of the sheets at angles ranging from 25° to 35° formed a spiral superlattice that produced moiré fringes involving alternate lattices positioned at low twist angles. A new emission due to the moiré superlattices was observed at ~500 nm. The superlattices were found to be stable under alkaline condition while the non-moiré sheets deformed into 1D fibers. The additional stability of moiré superlattices arose from the hypermolecular interactions at the rotated crystal interfaces. AFM results further supported vdW interaction amongst the lattices. Importantly, such a molecular

superlattices provided new way of reversible storage and sensing CO_2 in the presence of UV light with high sensitivity. The idea and results presented herein may bring about new chemistry of molecular assembly with wide application potential.

EXPERIMENTAL SECTION

Materials Used

L and D-tryptophan (trp, purity ≥ 98.0 % (HPLC)) were purchased from Sigma-Aldrich and used without further purification. Milli-Q grade water was used for all the experiments. D_2O was purchased from Sigma-Aldrich and used for NMR experiments.

Synthesis of Moiré Superlattices of trp

2 mL of trp (6 mg) solution was sonicated for 30 s to get a clear solution. 200 µL of the trp solution was added to 10 mL of water (resulting in 288 µM concentration) under constant stirring and heating at 80 ºC for 24 h. The dispersion after 24 h was then used for further experiments.

Optical Measurements

Time dependent UV-vis measurements were done using Perkin-Elmer Lambda 362+ where 3 mL of aliquot was collected at different times and absorbance was measured. Photoluminescence (PL) spectra were collected using HORIBA FluoroMax-4 spectrofluorometer where again 3 mL of aliquot was collected at different times to measure the PL spectrum.

Transmission electron microscopic (TEM) analysis and selected area electron diffraction (SAED) analysis

TEM and SAED data were collected after diluting the dispersion (400 µL of aliquot in 600 µL water) and drop casting on a carbon coated copper grid. TEM and SAED were performed using JEOL JEM 2100 F instrument.

Atomic force microscopic (AFM) analysis and measurement of Force-distance curve AFM images were acquired using Oxford Asylum Research MFP-3D model. Images were acquired in attractive tapping mode. Force-distance curves were measured in contact mode with tip of model AC240TS-R3 (k~2 Nm^{-1} and f = ~73 kHz).

Proton NMR and ESI-MS

Proton nuclear magnetic resonance (NMR) measurements were performed using 600 MHz Bruker ASCEND 600. The experiment was performed as described in 'synthesis of moiré superlattices' where D_2O (Sigma-Aldrich) was used in place of Milli-Q grade water. 600 µL of aliquot was taken at different times to perform the analysis. Electrospray ionization mass spectrometric (ESI-MS) analysis was performed using Agilent Accurate Mass (Q-TOF 6520) spectrometer in ESI positive mode where 1 mL of the aliquot was used for the analysis.

SAED Simulation and Structure Optimisation

The cif date file of L-trp was used for SAED simulation, which was done using ReciPro software. The unit cell, hkl planes and the structure were redrawn from cif file data using vesta. Twisting of the unit cells were performed using Avogadro software.

CO_2 sensing and storage measurements

3 mL of the dispersion obtained after 24 h of reaction was taken in a cuvette. PL emission of the dispersion was recorded first after which it was purged with CO_2 gas using a balloon. The PL emission was recorded after subsequent purging with CO_2. For UV exposed system, the dispersion was irradiated with UV light in the presence of CO_2 for different extent of time. After each exposure in sequence, the PL emission spectrum was recorded. For release study, the system was kept open for 60 min and PL emission was recorded at different intervals of time.

REFERENCES

1. Solomos, M. A.; Claire, F. J.; Kempa, T. J., 2D molecular crystal lattices: advances in their synthesis, characterization, and application. *J. Mater. Chem. A* **2019,** *7* (41), 23537-23562.
2. Corpinot, M. K.; Bučar, D.-K., A Practical Guide to the Design of Molecular Crystals. *Cryst. Growth Des.* **2019,** *19* (2), 1426-1453.
3. Commins, P.; Hara, H.; Naumov, P., Self-Healing Molecular Crystals. *Chem., Int. Ed.* **2016,** *55* (42), 13028-13032.
4. Horiuchi, S.; Tokura, Y., Organic ferroelectrics. *Nat. Mater.* **2008,** *7* (5), 357-366.

5. Ghosh, S.; Mishra, M. K., Elastic Molecular Crystals: From Serendipity to Design to Applications. *Cryst. Growth Des.* **2021,** *21* (4), 2566-2580.

6. Ahmed, E.; Karothu, D. P.; Warren, M.; Naumov, P., Shape-memory effects in molecular crystals. *Nat. Commun.* **2019,** *10* (1), 3723.

7. Hu, S.; Mishra, M. K.; Sun, C. C., Twistable Pharmaceutical Crystal Exhibiting Exceptional Plasticity and Tabletability. *Chem. Mater.* **2019,** *31* (10), 3818-3822.

8. Naumov, P.; Chizhik, S.; Panda, M. K.; Nath, N. K.; Boldyreva, E., Mechanically Responsive Molecular Crystals. *Chem. Rev.* **2015,** *115* (22), 12440-12490.

9. Krishna, G. R.; Devarapalli, R.; Lal, G.; Reddy, C. M., Mechanically Flexible Organic Crystals Achieved by Introducing Weak Interactions in Structure: Supramolecular Shape Synthons. *J. Am. Chem. Soc.* **2016,** *138* (41), 13561-13567.

10. Desiraju, G. R., Crystal Engineering: From Molecule to Crystal. *J. Am. Chem. Soc.* **2013,** *135* (27), 9952-9967.

11. Sasaki, N.; Kikkawa, J.; Ishii, Y.; Uchihashi, T.; Imamura, H.; Takeuchi, M.; Sugiyasu, K., Multistep, site-selective noncovalent synthesis of two-dimensional block supramolecular polymers. *Nat. Chem.* **2023,** *15* (7), 922-929.

12. Andrei, E. Y.; MacDonald, A. H., Graphene bilayers with a twist. *Nat. Mater.* **2020,** *19* (12), 1265-1275.

13. Brzhezinskaya, M.; Kononenko, O.; Matveev, V.; Zotov, A.; Khodos, I. I.; Levashov, V.; Volkov, V.; Bozhko, S. I.; Chekmazov, S. V.; Roshchupkin, D., Engineering of Numerous Moiré Superlattices in Twisted Multilayer Graphene for Twistronics and Straintronics Applications. *ACS Nano* **2021,** *15* (7), 12358-12366.

14. Devakul, T.; Crépel, V.; Zhang, Y.; Fu, L., Magic in twisted transition metal dichalcogenide bilayers. *Nat. Commun.* **2021,** *12* (1), 6730.

15. Yao, K.; Finney, N. R.; Zhang, J.; Moore, S. L.; Xian, L.; Tancogne-Dejean, N.; Liu, F.; Ardelean, J.; Xu, X.; Halbertal, D.; Watanabe, K.; Taniguchi, T.; Ochoa, H.; Asenjo-Garcia, A.; Zhu, X.; Basov, D. N.; Rubio, A.; Dean, C. R.; Hone, J.; Schuck, P. J.,

Enhanced tunable second harmonic generation from twistable interfaces and vertical superlattices in boron nitride homostructures. *Sci. Adv.* **2021,** *7* (10), eabe8691.

16. Fang, T.; Liu, T.; Jiang, Z.; Yang, R.; Servati, P.; Xia, G., Fabrication and the Interlayer Coupling Effect of Twisted Stacked Black Phosphorus for Optical Applications. *ACS Appl. Nano Mater.* **2019,** *2* (5), 3138-3145.

17. Shen, J.; Dong, Z.; Qi, M.; Zhang, Y.; Zhu, C.; Wu, Z.; Li, D., Observation of Moiré Patterns in Twisted Stacks of Bilayer Perovskite Oxide Nanomembranes with Various Lattice Symmetries. *ACS Appl. Mater. Interfaces* **2022,** *14* (44), 50386-50392.

18. Cao, Y.; Fatemi, V.; Fang, S.; Watanabe, K.; Taniguchi, T.; Kaxiras, E.; Jarillo-Herrero, P., Unconventional superconductivity in magic-angle graphene superlattices. *Nature* **2018,** *556* (7699), 43-50.

19. Alexeev, E. M.; Ruiz-Tijerina, D. A.; Danovich, M.; Hamer, M. J.; Terry, D. J.; Nayak, P. K.; Ahn, S.; Pak, S.; Lee, J.; Sohn, J. I.; Molas, M. R.; Koperski, M.; Watanabe, K.; Taniguchi, T.; Novoselov, K. S.; Gorbachev, R. V.; Shin, H. S.; Fal'ko, V. I.; Tartakovskii, A. I., Resonantly hybridized excitons in moiré superlattices in van der Waals heterostructures. *Nature* **2019,** *567* (7746), 81-86.

20. Cao, Y.; Fatemi, V.; Demir, A.; Fang, S.; Tomarken, S. L.; Luo, J. Y.; Sanchez-Yamagishi, J. D.; Watanabe, K.; Taniguchi, T.; Kaxiras, E.; Ashoori, R. C.; Jarillo-Herrero, P., Correlated insulator behaviour at half-filling in magic-angle graphene superlattices. *Nature* **2018,** *556* (7699), 80-84.

21. Pixley, J. H.; Andrei, E. Y., Ferromagnetism in magic-angle graphene. *Science* **2019,** *365* (6453), 543-543.

22. Das, P.; Chattopadhyay, A., Enhanced Chemical Stability in the Twisted Dodecagonal Stacking of Two-Dimensional Copper Nanocluster Assemblies. *J. Phys. Chem. Lett.* **2022,** *13* (37), 8793-8800.

23. Das, P.; Chattopadhyay, A., Moiré superlattices of two-dimensional copper nanocluster assemblies with tuneable twin emissions from hierarchical components leading to white light emission. *J. Mater. Chem. C* **2023,** *11* (35), 12029-12036.

24. Liu, L.; Sun, Y.; Cui, X.; Qi, K.; He, X.; Bao, Q.; Ma, W.; Lu, J.; Fang, H.; Zhang, P.; Zheng, L.; Yu, L.; Singh, D. J.; Xiong, Q.; Zhang, L.; Zheng, W., Bottom-up growth of homogeneous Moiré superlattices in bismuth oxychloride spiral nanosheets. *Nat. Commun.* **2019,** *10* (1), 4472.

25. Basu, S.; Chattopadhyay, A., Room-Temperature Delayed Fluorescence of Gold Nanoclusters in Zinc-Mediated Two-Dimensional Crystalline Assembly. *Langmuir* **2019,** *35* (15), 5264-5270.

26. Das, P.; Chattopadhyay, A., Delayed Dual Emission of Two-Dimensional Copper Nanocluster Assembly. *J. Phys. Chem. C* **2022,** *126* (2), 997-1005.

27. Bera, S.; Mondal, S.; Rencus-Lazar, S.; Gazit, E., Organization of Amino Acids into Layered Supramolecular Secondary Structures. *Acc. Chem. Res.* **2018,** *51* (9), 2187-2197.

28. Singh, P.; Brar, S. K.; Bajaj, M.; Narang, N.; Mithu, V. S.; Katare, O. P.; Wangoo, N.; Sharma, R. K., Self-assembly of aromatic α-amino acids into amyloid inspired nano/micro scaled architects. *Mater. Sci. Eng., C* **2017,** *72*, 590-600.

29. Guerin, S.; Stapleton, A.; Chovan, D.; Mouras, R.; Gleeson, M.; McKeown, C.; Noor, M. R.; Silien, C.; Rhen, F. M. F.; Kholkin, Andrei L.; Liu, N.; Soulimane, T.; Tofail, S. A. M.; Thompson, D., Control of piezoelectricity in amino acids by supramolecular packing. *Nat. Mater.* **2018,** *17* (2), 180-186.

30. Yang, F.; Li, J.; Long, Y.; Zhang, Z.; Wang, L.; Sui, J.; Dong, Y.; Wang, Y.; Taylor, R.; Ni, D.; Cai, W.; Wang, P.; Hacker, T.; Wang, X., Wafer-scale heterostructured piezoelectric bio-organic thin films. *Science* **2021,** *373* (6552), 337-342.

31. Meirzadeh, E.; Sapir, L.; Cohen, H.; Cohen, S. R.; Ehre, D.; Harries, D.; Lahav, M.; Lubomirsky, I., Nonclassical Crystal Growth as Explanation for the Riddle of Polarity in Centrosymmetric Glycine Crystals. *J. Am. Chem. Soc.* **2016,** *138* (44), 14756-14763.

32. Ji, W.; Xue, B.; Arnon, Z. A.; Yuan, H.; Bera, S.; Li, Q.; Zaguri, D.; Reynolds, N. P.; Li, H.; Chen, Y.; Gilead, S.; Rencus-Lazar, S.; Li, J.; Yang, R.; Cao, Y.; Gazit, E., Rigid Tightly Packed Amino Acid Crystals as Functional Supramolecular Materials. *ACS Nano* **2019,** *13* (12), 14477-14485.

33. Bera, S.; Xue, B.; Rehak, P.; Jacoby, G.; Ji, W.; Shimon, L. J. W.; Beck, R.; Král, P.; Cao, Y.; Gazit, E., Self-Assembly of Aromatic Amino Acid Enantiomers into Supramolecular Materials of High Rigidity. *ACS Nano* **2020,** *14* (2), 1694-1706.

34. Lakowicz J.R. *Principles of Fluorescence Spectroscopy*, 3rd ed.; Springer, **2006**.

35. Shaham-Niv, S.; Arnon, Z. A.; Sade, D.; Lichtenstein, A.; Shirshin, E. A.; Kolusheva, S.; Gazit, E., Intrinsic Fluorescence of Metabolite Amyloids Allows Label-Free Monitoring of Their Formation and Dynamics in Live Cells. *Angew. Chem., Int. Ed.* **2018,** *57* (38), 12444-12447.

36. Niyangoda, C.; Miti, T.; Breydo, L.; Uversky, V.; Muschol, M., Carbonyl-based blue autofluorescence of proteins and amino acids. *PLOS ONE* **2017,** *12* (5), e0176983

37. Gorbitz, C. H.; Tornroos, K. W.; Day, G. M., Single-crystal investigation of l-tryptophan with Z' = 16. *Acta Crystallogr., Sect. B: Struct. Sci.* **2012,** *68* (5), 549-557.

38. Seto, Y.; Ohtsuka, M., ReciPro: free and open-source multipurpose crystallographic software integrating a crystal model database and viewer, diffraction and microscopy simulators, and diffraction data analysis tools. *J. Appl. Crystallogr.* **2022,** *55* (2), 397-410.

39. Liao, Y.; Cao, W.; Connell, J. W.; Chen, Z.; Lin, Y., Evolution of Moiré Profiles from van der Waals Superstructures of Boron Nitride Nanosheets. *Sci. Rep.* **2016,** *6* (1), 26084.

40. Boi, F. S.; Shuai, G.; Wen, J.; Wang, S., Unusual Moiré superlattices in exfoliated μm-thin HOPG lamellae: An angular-diffraction study. *Diam. Relat. Mater.* **2020,** *108*, 107920.

41. Chiodini, S.; Kerfoot, J.; Venturi, G.; Mignuzzi, S.; Alexeev, E. M.; Teixeira Rosa, B.; Tongay, S.; Taniguchi, T.; Watanabe, K.; Ferrari, A. C.; Ambrosio, A., Moiré Modulation of Van Der Waals Potential in Twisted Hexagonal Boron Nitride. *ACS Nano* **2022,** *16* (5), 7589-7604.

42. Sun, H.; Oldfield, E., Tryptophan Chemical Shift in Peptides and Proteins: A Solid State Carbon-13 Nuclear Magnetic Resonance Spectroscopic and Quantum Chemical Investigation. *J. Am. Chem. Soc.* **2004,** *126* (14), 4726-4734.

43. Tamayo, J.; García, R., Relationship between phase shift and energy dissipation in tapping-mode scanning force microscopy. *Applied Physics Letters* **1998,** *73* (20), 2926-2928.

44. Phaner-Goutorbe, M.; Iazykov, M.; Villey, R.; Sicard, D.; Robach, Y., Energy dissipation effects on imaging of soft materials by dynamic atomic force microscopy: A DNA-chip study. *Mater. Sci. Eng., C* **2013,** *33* (4), 2311-2316.

45. Wang, D.; Liang, X.-B.; Liu, Y.-H.; Fujinami, S.; Nishi, T.; Nakajima, K., Characterization of Surface Viscoelasticity and Energy Dissipation in a Polymer Film by Atomic Force Microscopy. *Macromolecules* **2011,** *44* (21), 8693-8697.

46. Williams, N. J.; Seipp, C. A.; Brethomé, F. M.; Ma, Y.-Z.; Ivanov, A. S.; Bryantsev, V. S.; Kidder, M. K.; Martin, H. J.; Holguin, E.; Garrabrant, K. A.; Custelcean, R., CO2 Capture via Crystalline Hydrogen-Bonded Bicarbonate Dimers. *Chem* **2019,** *5* (3), 719-730.

Supporting Information

Rate constant for the reaction of tryptophan assembly:

As observed the photoluminescence (PL) intensity of tryptophan (trp) molecules decreased as the reaction progressed. As trp self-assembled the intrinsic fluorescence intensity of trp molecule decreased as the environment around the molecule in the assembly changed. PL intensity of a fluorophore depends on the concentration according to the following equation

$$I_f = kI_0\phi[1-(10^{-\varepsilon lc})] \quad (1)$$

where κ is a constant depending on the instrument, I_0 is the intensity of incident light, ϵ is the molar absorptivity, l is the path length, ϕ is the quantum yield and C is the concentration. At low concentration this equation would transform into following

$$I_f = \kappa I_0\phi[1-(1-\varepsilon lc)] \quad (2)$$

Or, $$I_f = AC \quad (3)$$

where $A = \kappa I_0\phi\varepsilon l$. Since low concentration (288 μM) of trp was taken for the reaction, the PL intensity would be directly proportional to the concentration, according to equation 3 and thus constant A could be calculated after dividing fluorescence intensity for 288 μM trp by its concentration. The plot of 1/(intensity) vs time for the reaction mentioned here resulted in a liner fit thus following 2nd order kinetics.

$$A/(I_f)_t = 1/C_t = 1/C_0 + kt \quad (4)$$

Or $$1/(I_f)_t = 1/(AC_t) = 1/(AC_0) + (k/A)t \quad (5)$$

Where C_t and $(I_f)_t$ are concentration and intensity of fluorescence at time t, k is the rate constant and C_0 is concentration at t = 0 h. Thus, the slope obtained (k/A) following equation 4 gives the rate constant of the reaction after multiplying it with constant A. For reactions in Figure 1(f) Figure S1a and Figure S1b the rate constants are 1.28×10^{-3}, 1.05×10^{-3} and 2.33×10^{-3} $\mu M^{-1} h^{-1}$, respectively. This gives an average rate constant of $(1.55 \pm 0.68) \times 10^{-3}$ $\mu M^{-1} h^{-1}$.

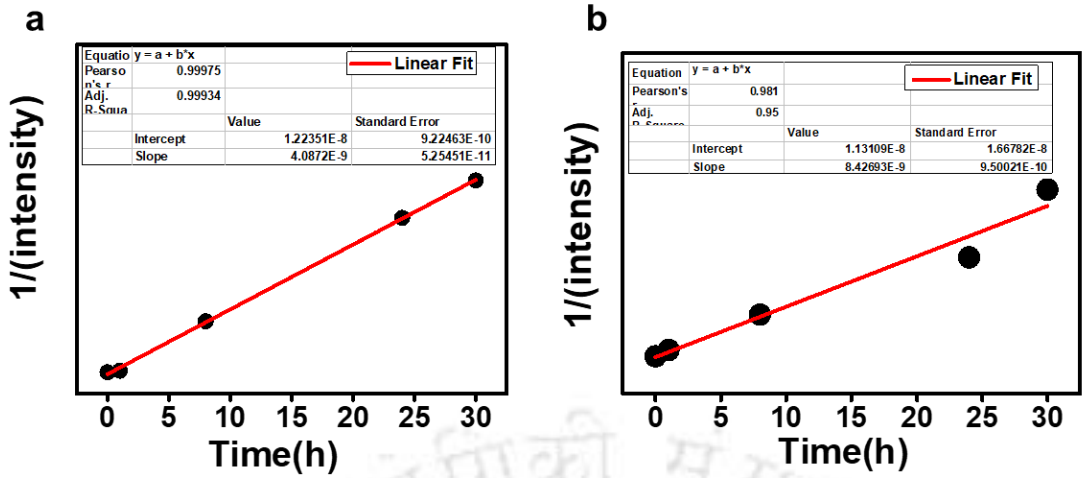

Figure S1. Rate constant determination. (a) and (b) 1/(intensity) vs time plot for the 360 nm fluorescence peak for two different experimental runs of reaction. (p.88)

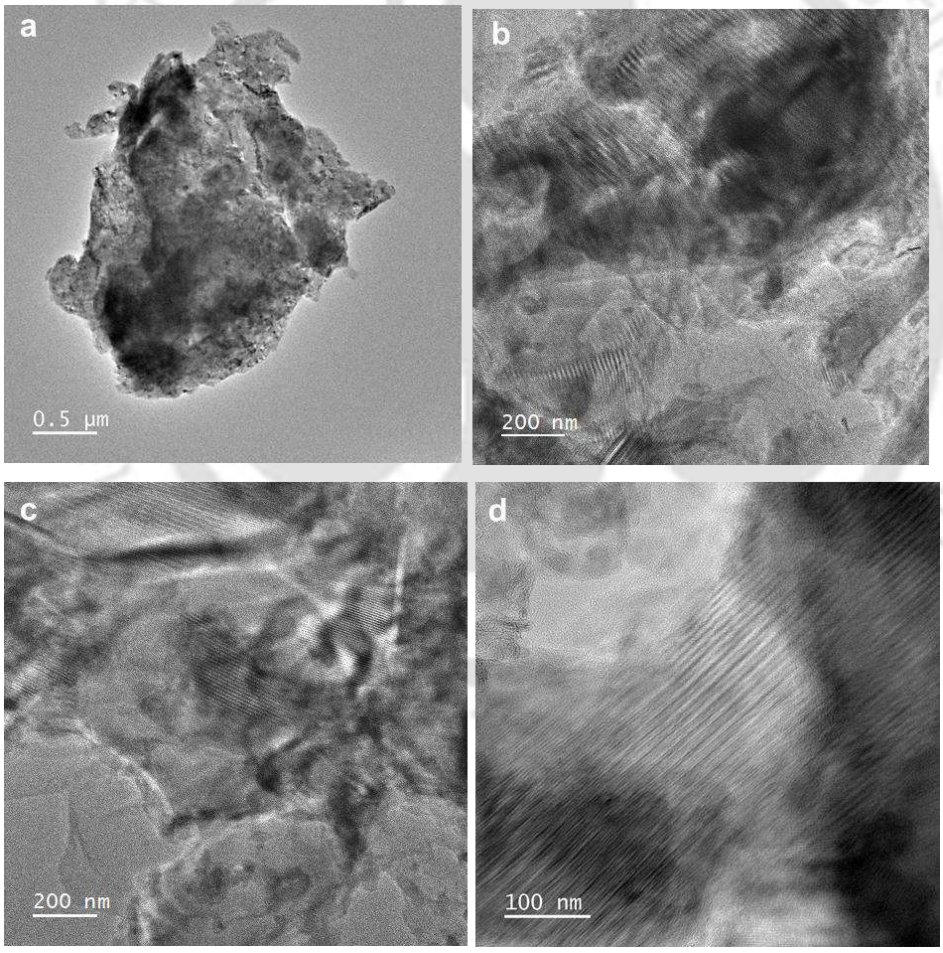

Figure S2. TEM images of the trp dispersion taken at **(a)** 5 min; **(b)** 1 h; **(c)** 8 h and **(d)** 30 h of reaction. (p.89)

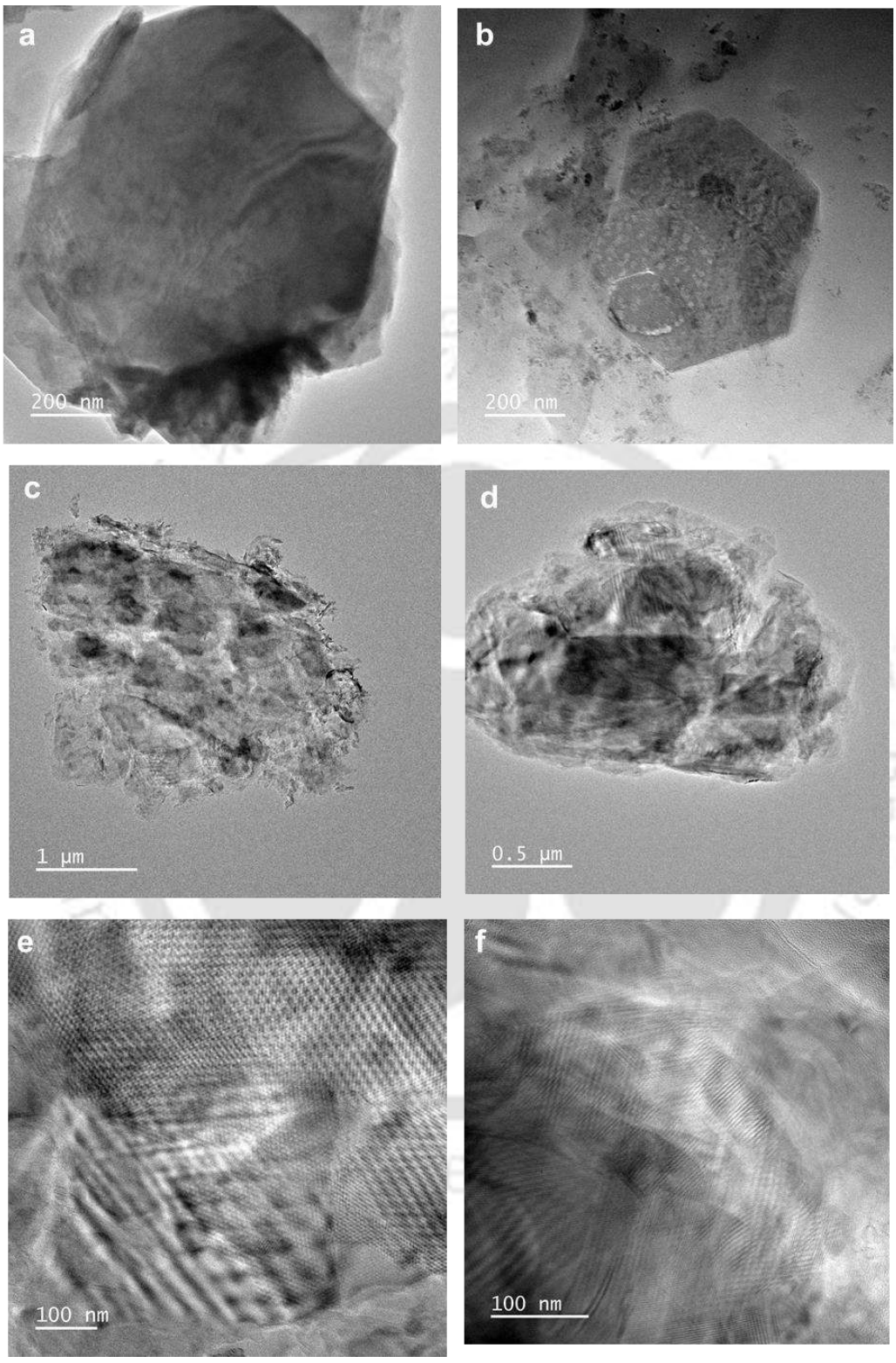

Figure S3. Transmission microscopic images (TEM) showing nanosheets observed from the dispersion of (**a) and (b)** single crystalline nanosheet of D-trp and L-trp respectively. (**c) and (d)**

moiré nanosheet of D-trp and L-trp respectively. (**e) and (f)** enlarged image of (**c)** and **(d)** respectively showing moiré superlattices. (p.89)

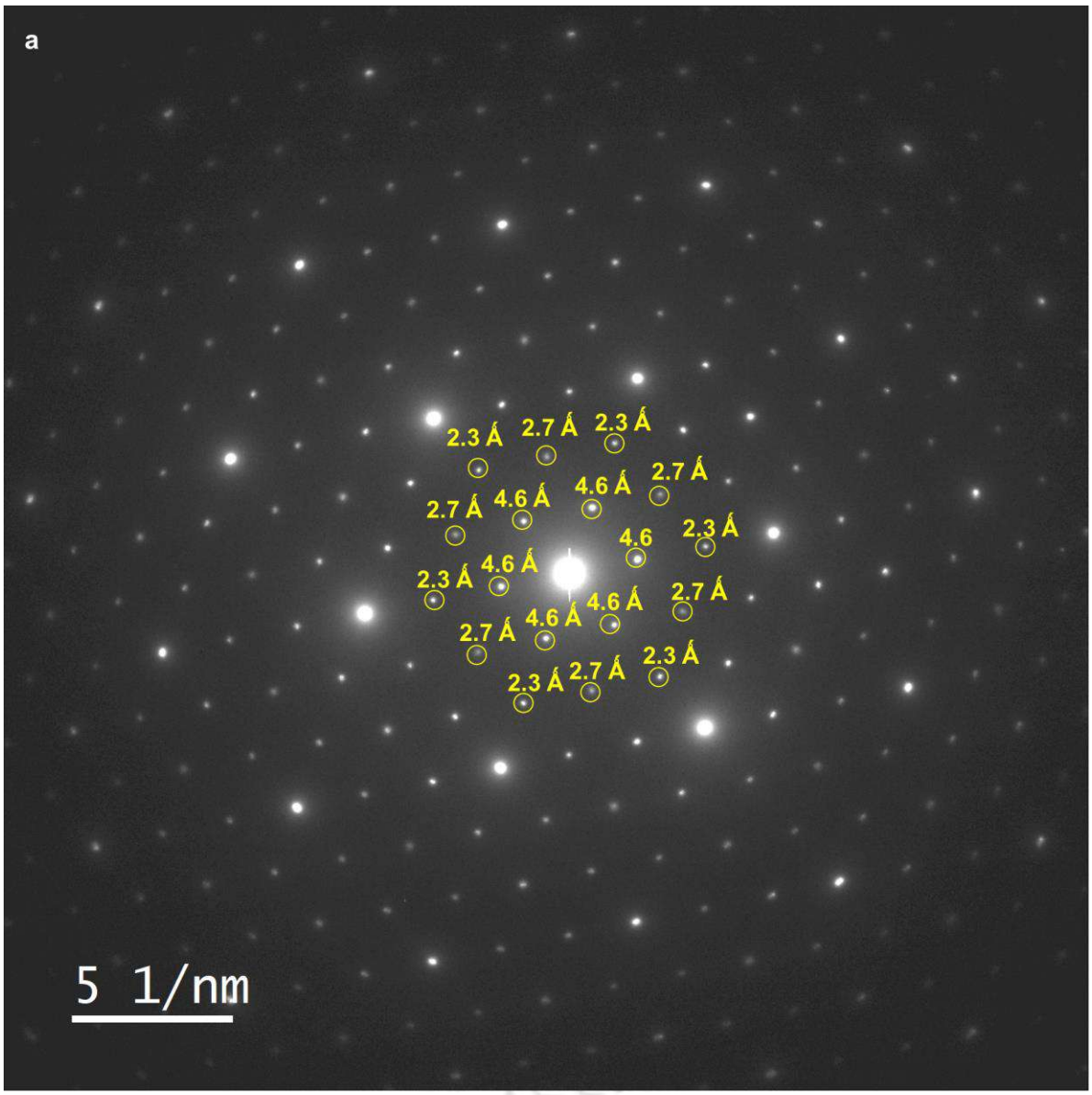

Figure S4. SAED pattern of the crystalline nanosheet from Figure 2B with d–spacing as calculated from the central spot. (p.89)

Table S1. Comparison of experimental and simulated d-spacing (p.89)

hkl planes	d-spacing (Å) obtained from SAED	Simulated d-spacing (Å) from cif file of trp
020	4.6	4.9
0-20	4.6	4.9
200	4.6	4.9
-200	4.6	4.9
220	4.6	4.9
-2-20	4.6	4.9
420	2.7	2.8
-4-20	2.7	2.8
240	2.7	2.8
-2-40	2.7	2.8
-220	2.7	2.8
2-20	2.7	2.8
040	2.3	2.4
0-40	2.3	2.4
400	2.3	2.4
-400	2.3	2.4
440	2.3	2.4
-4-40	2.3	2.4

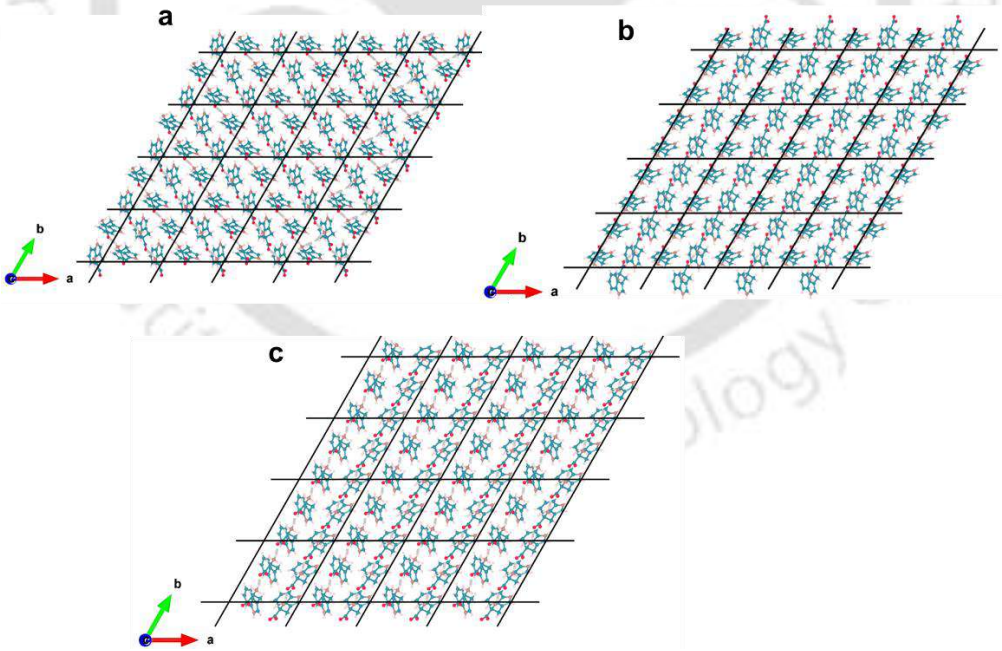

Figure S5. (a) 2nd layer of the supercell viewed along the c axis. **(b)** 3rd layer of the supercell viewed along the c axis. **(c)** 4th layer of the supercell viewed along the c axis. The first layer is presented in Figure 2e. (p.90)

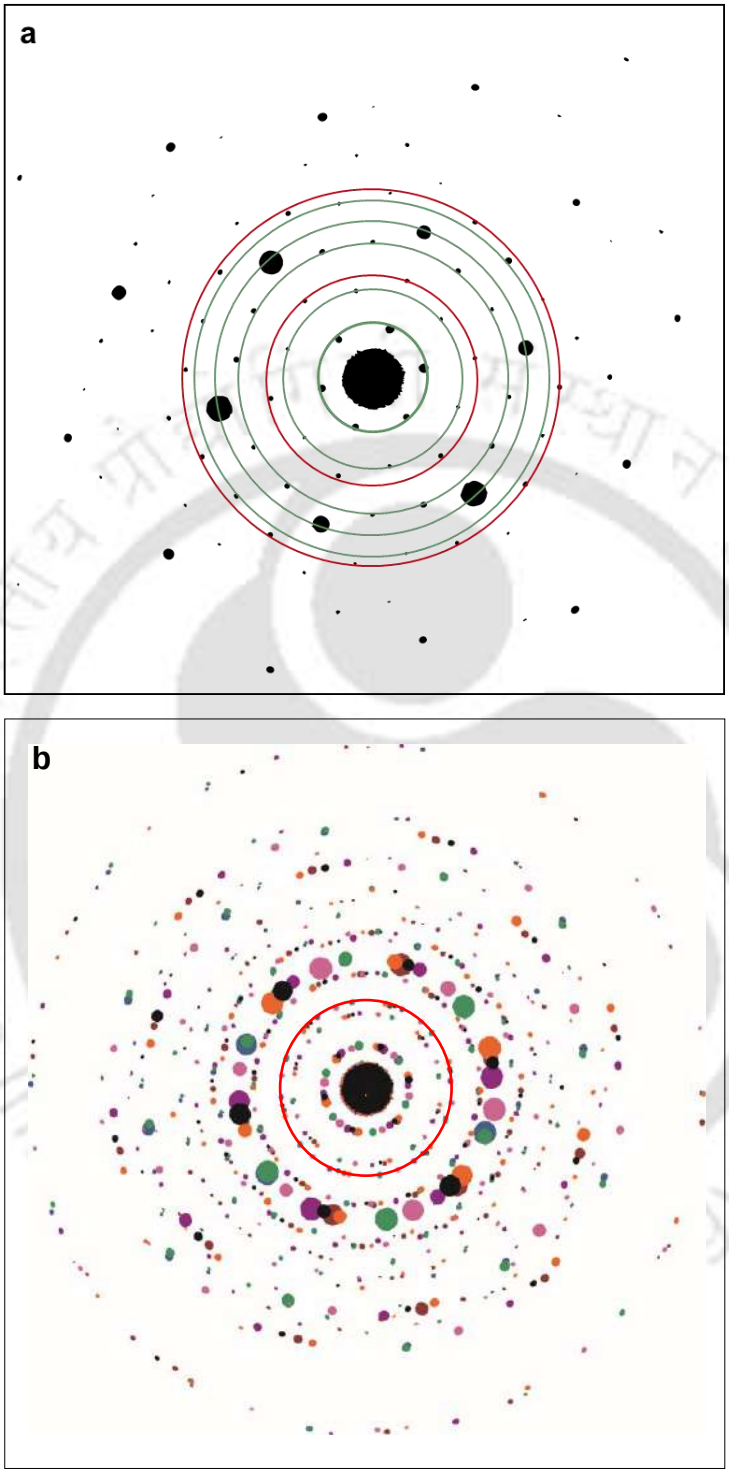

Figure S6. (a) Crystalline hexagonal SAED patterns where diffraction spots in the red circles were observed in the SAED pattern of moiré superlattices of Figure 3c and Figure 3f. **(b)**

Superposition of the hexagonal SAED pattern rotated according to the angles in Table S1 to reproduce the SAED pattern obtained for moiré superlattices. (p.91)

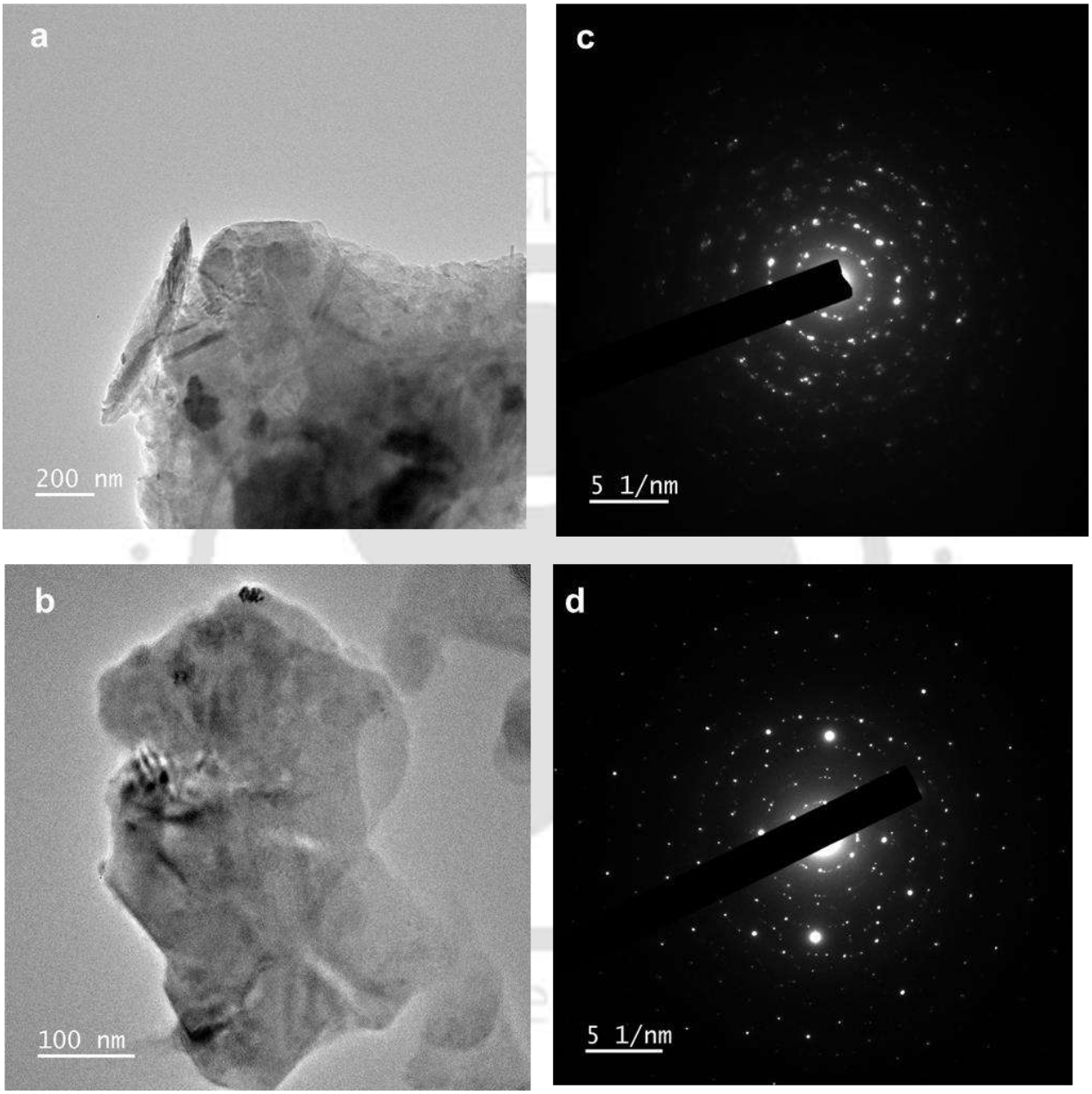

Figure S7. (a) and (b) Multi-layered sheet formed after twisted stacking of crystalline nanosheets showing no moiré patterns. (**c) and (d)** Corresponding SAED patterns of (**a) and (b)** respectively having d spacing 0.46 nm. (p.91)

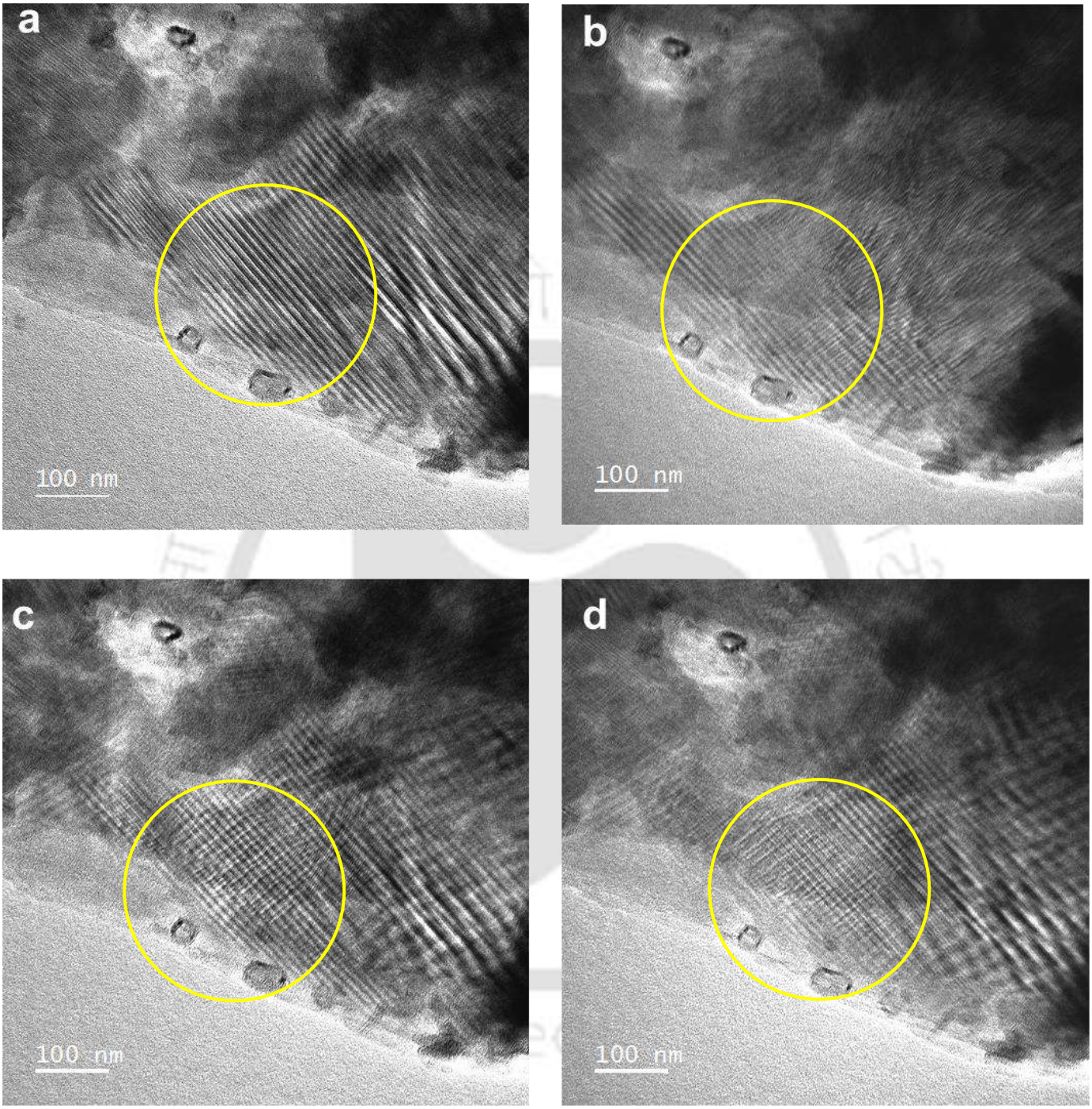

Figure S8. (a) TEM image of a typical moiré nanosheet with parallel line patterns. The same image recorded following tilting of the specimen along direction **(b)** x = 2º and y = 1º, **(c)** x = 5º and y = 8º, **(d)** x = 4º and y = 8º, respectively. The portions encircled in yellow exhibited the change in moiré patterns from parallel lines to cross patterns as the specimen was tilted accordingly. (p.91)

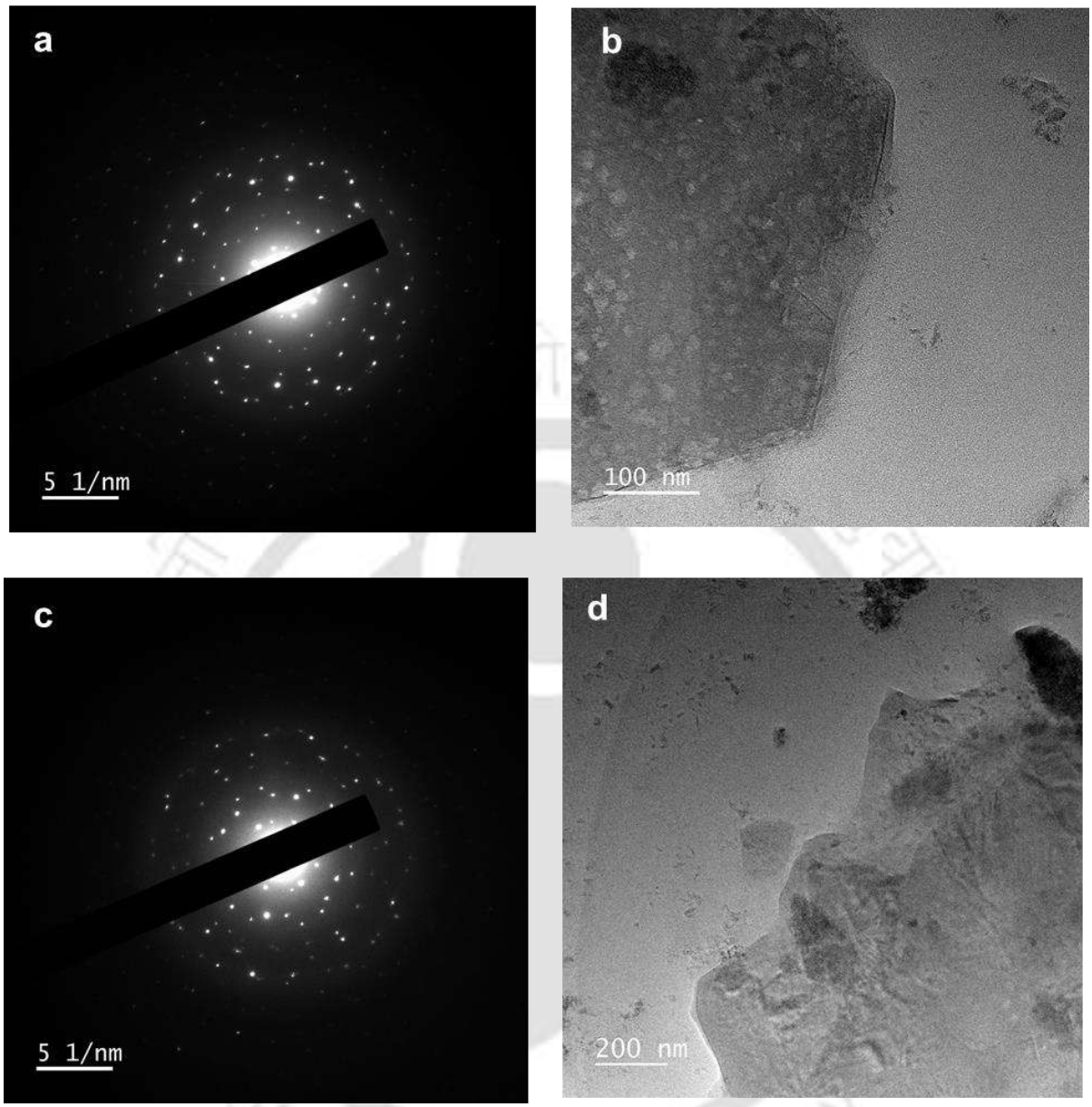

Figure S9. (a) SAED pattern where two hexagonal patterns superimposed at an angle 25º and **(b)** corresponding TEM images of D-trp nanosheets from where the SAED pattern were acquired. **(c)** SAED pattern where two hexagonal patterns superimposed at an angle 25.6º. **(d)** corresponding TEM images of L-trp nanosheets from where the SAED pattern were acquired. (p.93)

Table S2. The angles between the adjacent nanosheets after twisted stacking. (p.93)

sheet number	Rotation of nanosheet with respect to sheet 1	angle with respect to the previous sheet
1	0	-
2	28.9	28.9
3	53.9	25
4	87.6	33.7
5	122.9	35.3
6	159.3	36.4
7	187.2	27.9

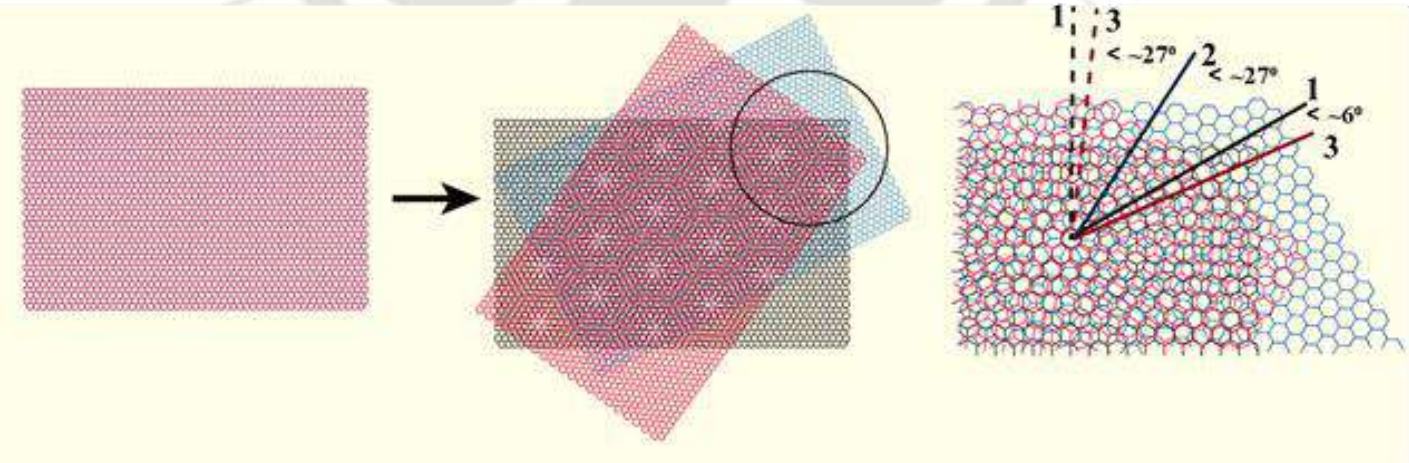

Figure S10. Schematic representation of moiré patterns formed by three stacked sheets where sheets 1 and 2 forms an angle of 27º and 2 and 3 forms angle 27º, thus resulting in an angle of 6º for sheets 1 and 3. (p.93)

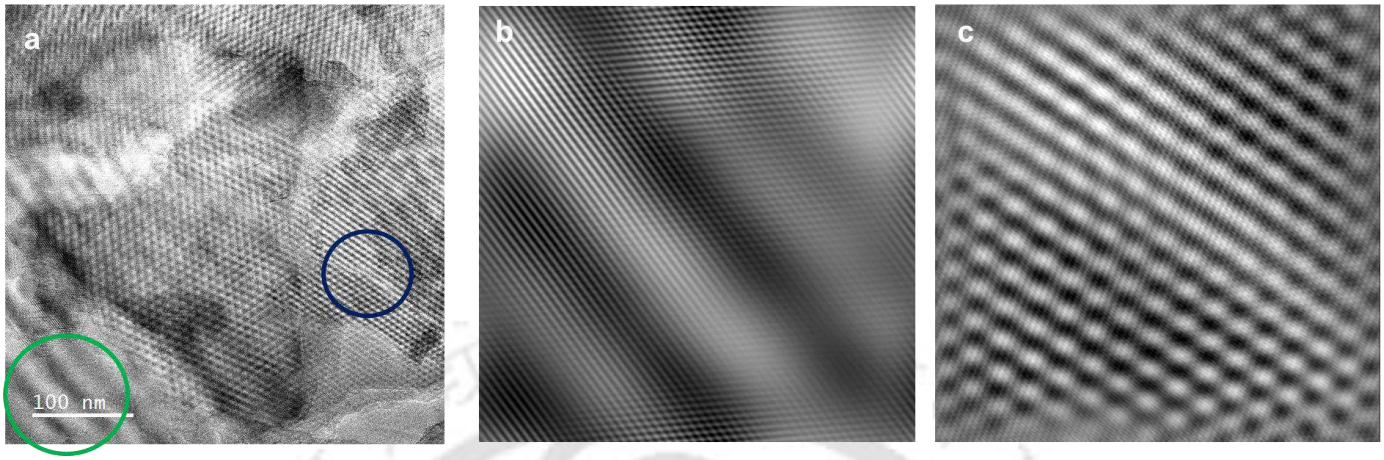

Figure S11. (a) TEM image of a moiré superlattices. **(b)** IFFT of region circled in green in **a** and **(c)** IFFT of region circled in blue in **a**. (p.95)

Determination of moiré periodicities

The moiré periodicities analyzed from Figure S11b are - 24 nm, which is followed by 2.13 nm and 1.92 nm and the moiré periodicities from Figure S11c are 6.61 nm, 2.36 nm and 1.06 nm. The corresponding angles for the above periodicities calculated from the equation

$$D = d/(2\mathrm{Sin}(\theta/2)) \qquad (6)$$

are 1.09º, 12.3º, 13.7º, 3.98, 11.1º and 25º respectively. In the above equation d is the lattice constant taken as 0.46 nm, D is the distance between moiré fringes and θ is the twist angle between two sheets. Further the angles obtained from the SAED between sheets 2 and 4 (1.3º), sheets 4 and 6 (11.7º), sheets 5 and 7 (4.3º) and 1 and 2 (25º) match well with the above calculated angles.

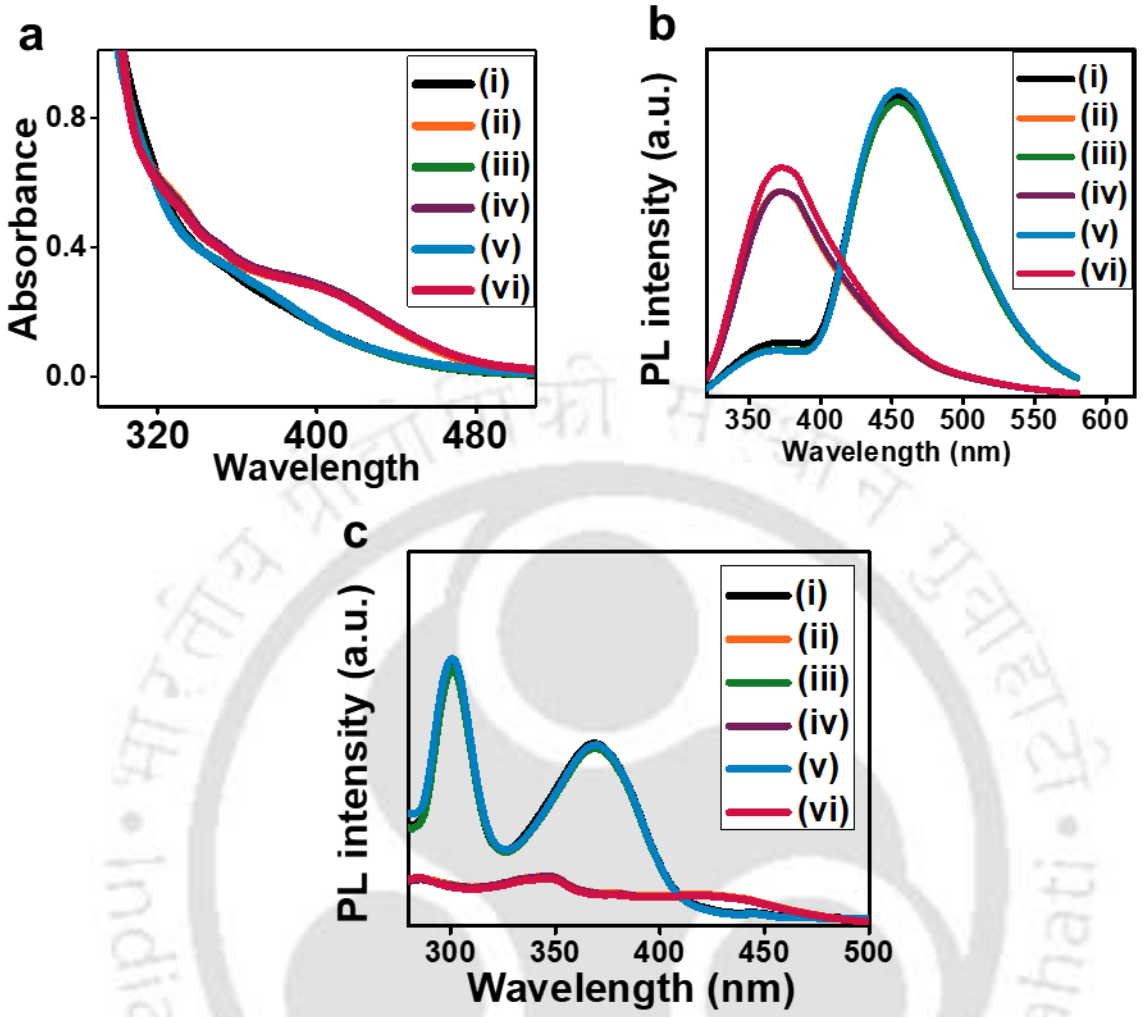

Figure S12. (a) Absorption spectra of trp solution after **(i)** 24 h of vigorous stirring at 80 °C (leading to the formation of trp moiré dispersion), which was subjected to a cycle of pH change where **(ii), (iii), (iv), (v)** and **(vi)** represent alternative addition cycles of 40 µL 1M NaOH and 40 µL 1M HCl solutions, respectively, to the mixture. **(B)** Photoluminiscence (PL) emission spectrum (λ_{ex} = 300 nm) of trp solution after **(i)** 24 h of vigorous stirring at 80 °(C) which is subjected to a cycle of pH change where **(ii), (iii), (iv), (v)** and **(vi)** represent alternative addition cycles of 40 µL 1M NaOH and 40 µL 1M HCl solutions, respectively, to the mixture. **(c)** PL excitation spectrum (λ_{em} = 452 nm) of trp solution after **(i)** 24 h of vigorous stirring at 80 °(C) which is subjected to a cycle of pH change where **(ii), (iii), (iv), (v)** and **(vi)** represent alternative addition cycles of 40 µL 1M NaOH and 40 µL 1M HCl solutions, respectively, to the mixture. (p.97)

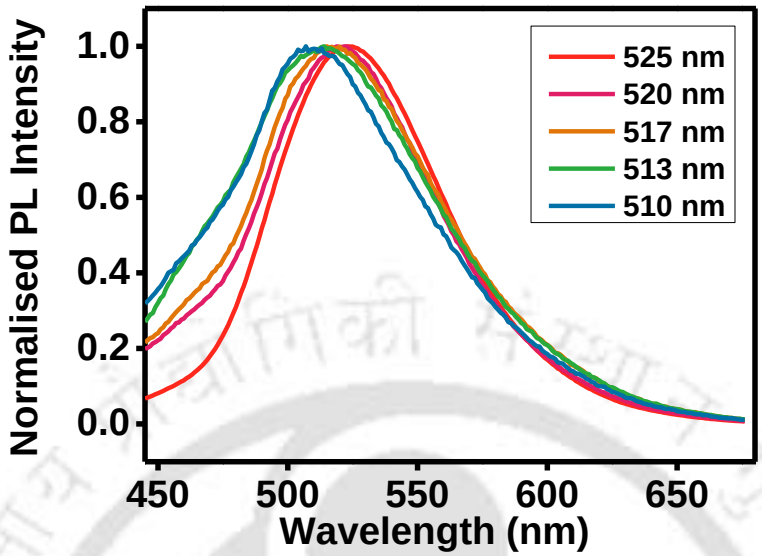

Figure S13. Normalised PL emission (λ_{ex} = 425 nm) spectra of different experimental runs of trp (moiré) reaction after addition of alkali having peak maxima ranging from 510 nm to 535 nm. (p.97)

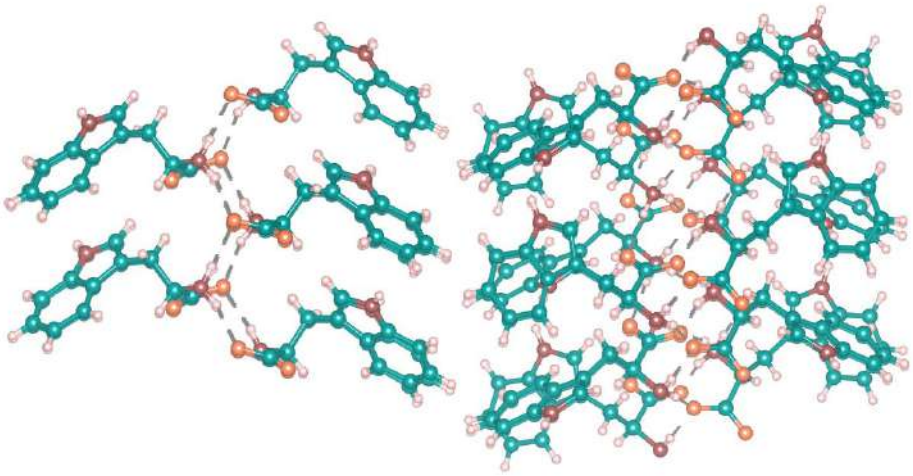

Figure S14. Self-assembly of trp where the molecule assembles through alternate hydrogen bonding and hydrophobic interaction to form 2D supramolecular crystalline nanosheet. (p.98)

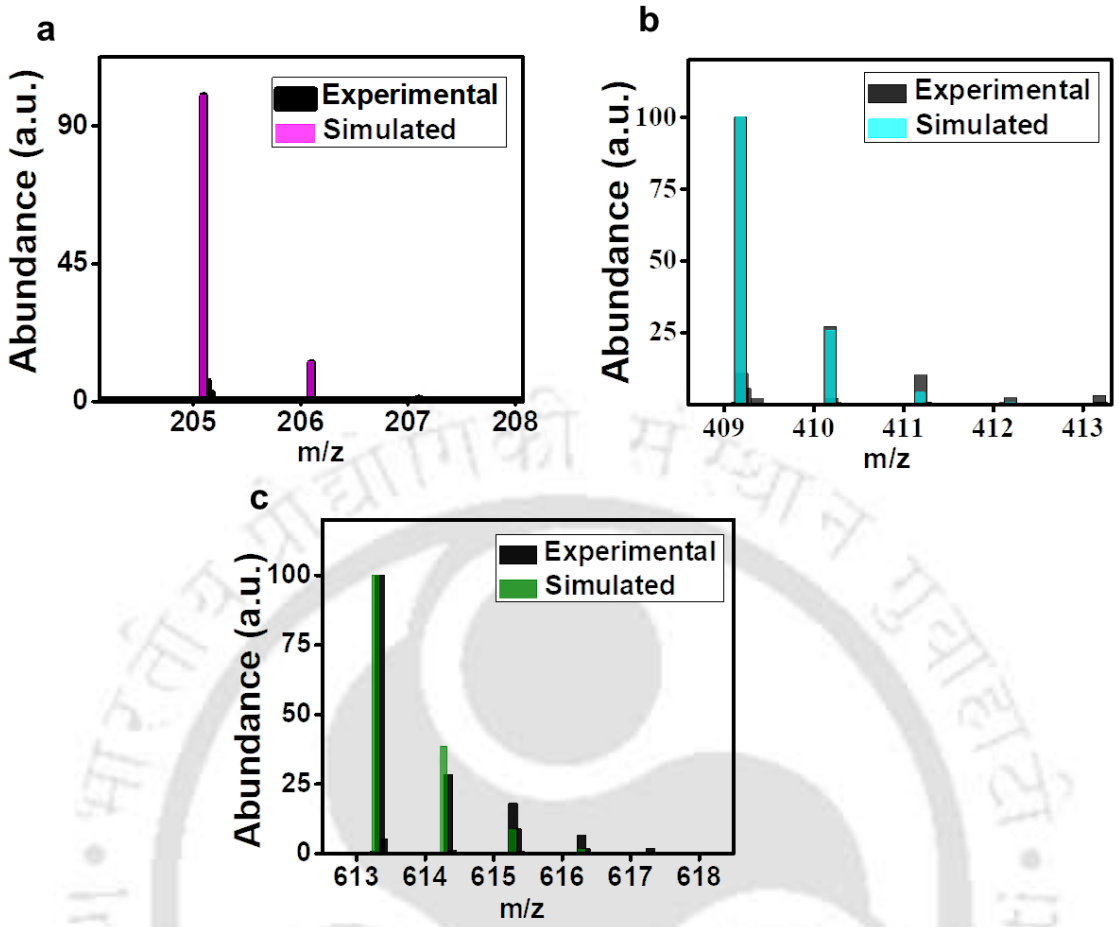

Figure S15. ESI-MS of dispersion obtained after 2 h of reaction showing spectrum of **(a)** $[C_{11}H_{12}N_2O_2+1H^+]$ at m/z = 205.22; **(b)** $[(C_{11}H_{12}N_2O_2)_2 +1H^+]$ at m/z = 409.18 and **(c)** $[(C_{11}H_{12}N_2O_2)_3 +1H^+]$ at m/z = 613.17. (p.99)

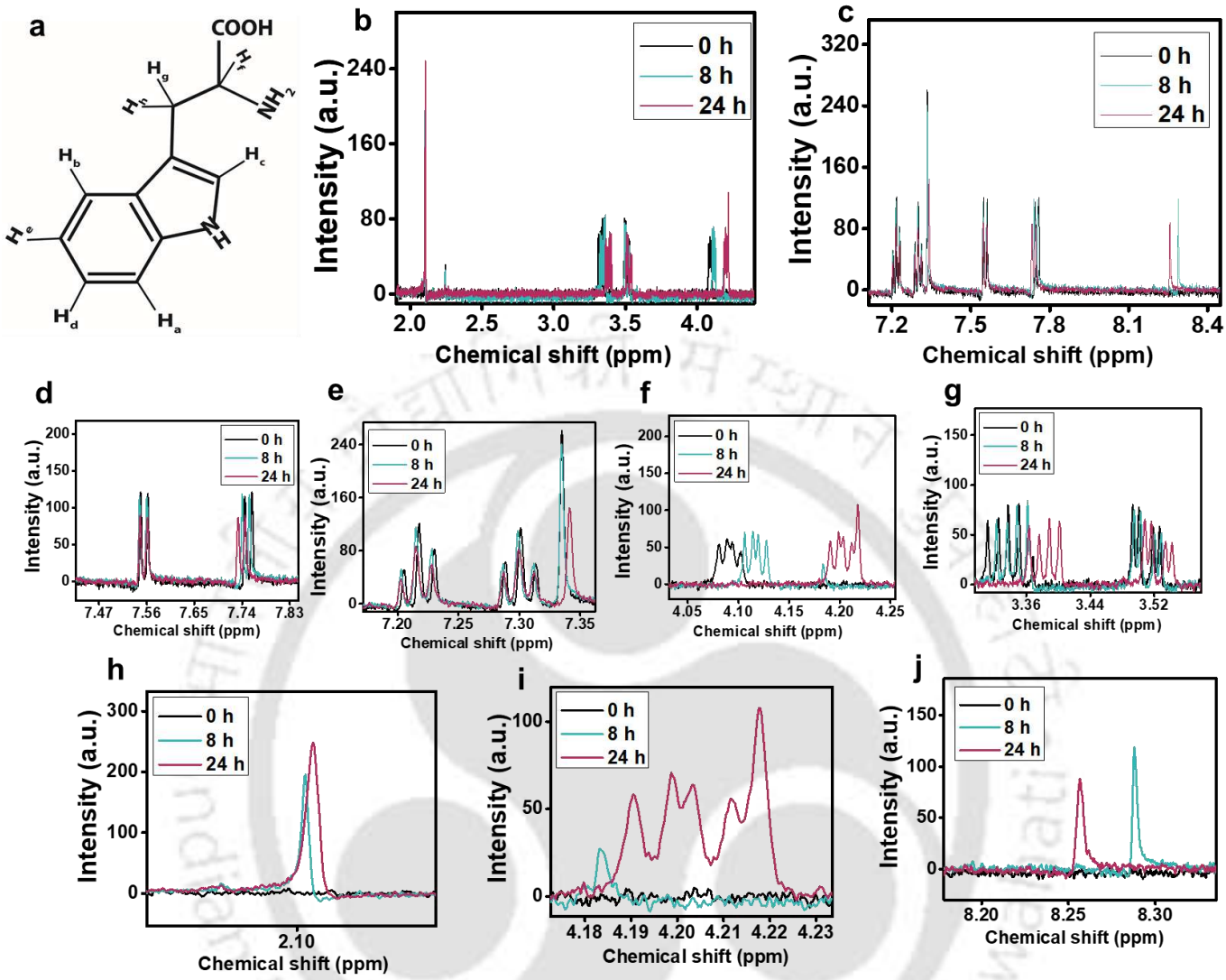

Figure S16. (a) Chemical structure of trp with different protons marked according to the chemical shift values**.** Chemical shift of trp at different time intervals ranging from **(b)** 2-5 ppm. **(c)** 7-8.5 ppm. NMR spectrum of proton **(d)** H_a and H_b **(e)** H_e, H_d and H_c **(f)** H_f **(g)** H_g and H_h. New NMR peak observed at **(h)** 2.1 ppm (**i)** 4.2 ppm (**j)** 8.2 ppm. (p.99)

Table S3. ^{1}H NMR peaks of trp solution in D_2O - leading to moiré superlattice formation - obtained at different times. (p.99, p.100)

Chemical shift(ppm)/ Time (h)	H_a	H_b	H_c	H_d	H_e	H_f	H_g and H_h
0	7.75	7.55	7.33	7.3	7.21	4.09	3.42
8	7.75	7.55	7.33	7.29	7.21	4.11	3.42
24	7.74	7.55	7.34	7.29	7.21	4.2	3.45

Table S4. Integration ratio of aromatic protons and new peaks (H_x) relative to H_g at different times. (p.100)

Integration ratio (Hx/Hg)/ Time (h)	**H_a**	**H_b**	**H_c**	**H_d**	**H_e**	**Peak at 2.1 ppm**	**Peak at 4.2 ppm**	**Peak at 8.2 ppm**
0	0.92	0.82	0.75	0.74	0.75	0	0	0
8	0.97	0.89	0.73	0.78	0.78	0.45	0.06	0.34
24	0.88	0.79	0.58	0.79	0.79	0.86	0.34	0.34

The moiré superlattices were formed by the twisted stacking of crystalline nanosheets at the crystal interfaces of hydrophobic region. The downfield and upfield shifts of the protons were caused due to self-assembly of trp. The integration ratio of the peaks with respect to H_g (which was taken as a standard for integration) suggested that with time there was a decrease in population of the aromatic protons. Among them the integration area of H_c decreased the most,

indicating the change in chemical environment of the proton as the moiré superlattices were continued to from. With time three new singlet peaks at 2.1, 4.2 and 8.3 ppm were observed along with the other ^{1}H NMR peaks of trp. A large chemical shift of H_c due to interaction at the crystal interface resulted in three new singlet peaks.

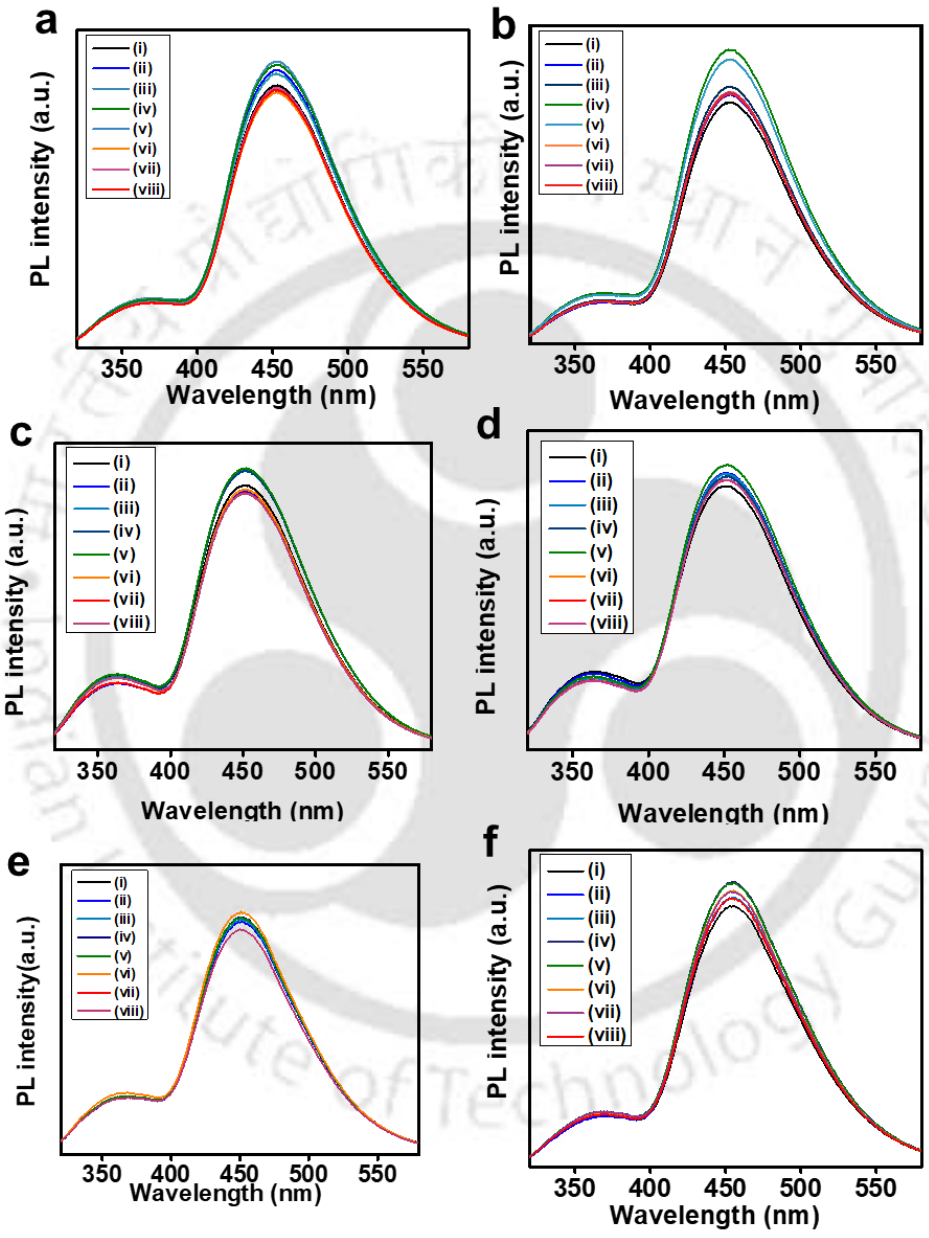

Figure S17. (a) PL spectra of the dispersion for experiment set 1 after **(i)** 24 h of reaction that was purged with CO_2 gas for **(ii)** 2 min, **(iii)** 5 min, **(iv)** 10 min and **(v)** 15 min, respectively and then kept in open for **(vi)** 5 min, **(vii)** 30 min **(viii)** 60 min respectively. **(b)** PL spectra of the

dispersion experiment set 1 after **(i)** 24 h of reaction that was purged with CO_2 gas for **(ii)** 2 min, **(iii)** 5 min, **(iv)** 10 min and **(v)** 15 min under the exposure of UV light and then kept in open for **(vi)** 5 min, **(vii)** 30 min **(viii)** 60 min respectively. **(c)** PL spectra of the dispersion for experiment set 2 after **(i)** 24 h of reaction that was purged with CO_2 gas for **(ii)** 2 min, **(iii)** 5 min, **(iv)** 10 min and **(v)** 15 min, respectively and then kept in open for **(vi)** 5 min, **(vii)** 30 min **(viii)** 60 min respectively. **(d)** PL spectra of the dispersion after **(i)** 24 h of reaction that was purged with CO_2 gas for **(ii)** 2 min, **(iii)** 5 min, **(iv)** 10 min and **(v)** 15 min under the exposure of UV light and then kept in open for **(vi)** 5 min, **(vii)** 30 min **(viii)** 60 min respectively. **(e)** PL spectra of the dispersion for experiment set 3 after **(i)** 24 h of reaction that was purged with CO_2 gas for **(ii)** 2 min, **(iii)** 5 min, **(iv)** 10 min and **(v)** 15 min, respectively and then kept in open for **(vi)** 5 min, **(vii)** 30 min **(viii)** 60 min respectively. **(f)** PL spectra of the dispersion experiment set 3 after **(i)** 24 h of reaction that was purged with CO_2 gas for **(ii)** 2 min, **(iii)** 5 min, **(iv)** 10 min and **(v)** 15 min under the exposure of UV light and then kept in open for **(vi)** 5 min, **(vii)** 30 min **(viii)** 60 min respectively. (p.100)

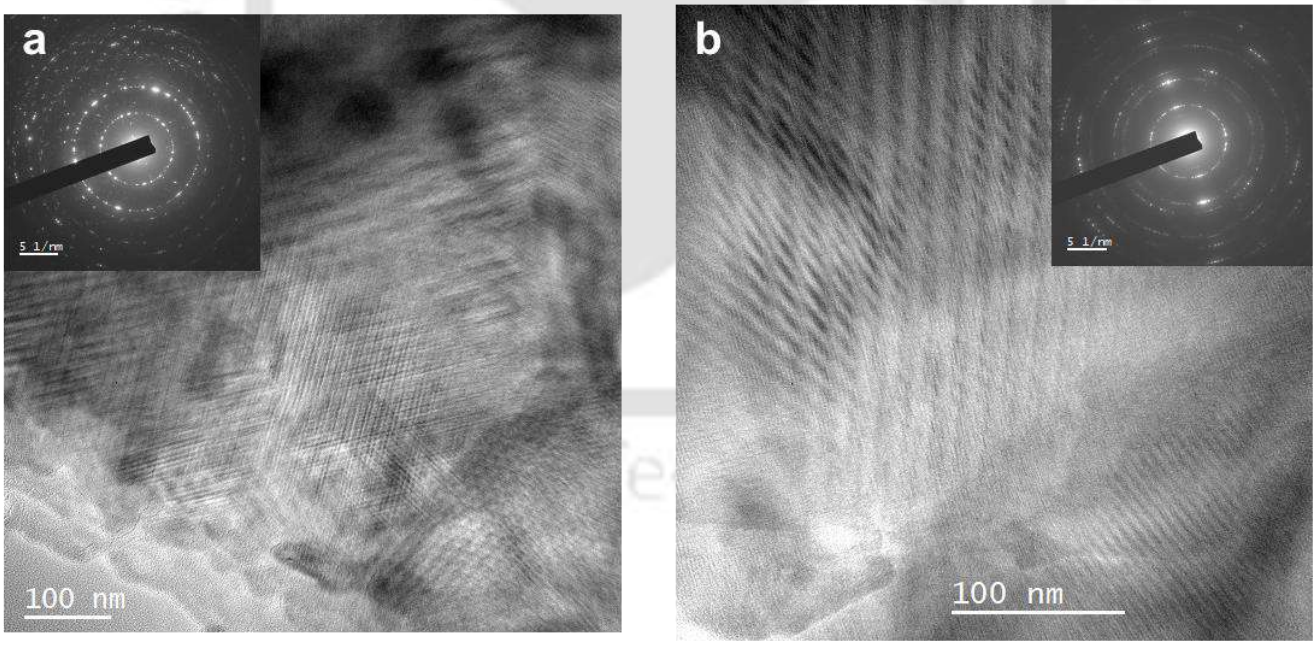

Figure S18. TEM images of moiré superlattices of trp **(a)** before and **(b)** after CO_2 exposure in presence of UV irradiation. Inset: Corresponding SAED pattern. (p.100)

Chapter 4: pH Controlled Twist-angle Dependent Interfacial Quantum Tunneling in Multilayer Molecular Moiré Superlattices of p-Phenylenediamine

Adv Quantum Technol. **2025**, 2400569

(https://advanced.onlinelibrary.wiley.com/doi/10.1002/qute.202400569)

Chapter 4

ABSTRACT

Molecule-based electronic circuits and device components may bring novel aspects in their functioning based on quantum phenomena that may not be attainable using conventional architecture. In order to implement such concepts development of well-defined assemblies that enable energy transfer, mass and charge transports across several length scales is necessary. Herein it is reported that multilayer molecular moiré superlattices may provide an initial direction for attaining the abovementioned objectives. For example, multilayered two-dimensional moiré superlattices of p-phenylenediamine showed easily identifiable twist angle-dependent electrical conductivity at each interface, as measured for the nanosheet using conductive atomic force microscopy. The absence of water molecules at the interfaces, as compared to the layered water molecules in the lattices, lowered the electron tunneling barrier and thus, increased the conductivity. Importantly, protonation and deprotonation of the superlattices in the dispersion resulted in high interfacial currents with about three orders of magnitude increase for the former. These results were further explained by density of states calculations along with carrier density and simulated scanning tunneling microscopy (STM) plots.

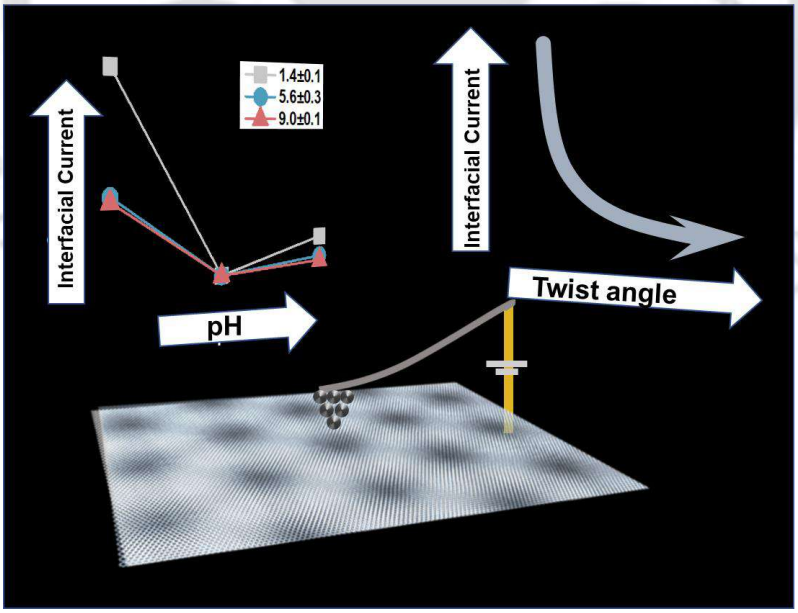

Scheme 1. Graphical representation showing pH-controlled twist-angle dependent conductivity in multilayer molecular moiré superlattices of p-phenylenediamine

Chapter 4

Introduction

Molecule-based electronics[1-3] may have the power to transform the fundamental concepts in fabrication and operation such as circuit design, information storage and retrieval, optical and electronic communications, sensing, artificial life and intelligence. For example, a network of molecules[4-7] with functional components connected by chemical bonds may be able to transmit and receive electromagnetic signals, store and retrieve information, and sense ions and molecules, based on principles of quantum mechanics[8,9]. One could conceive of molecular and supramolecular arrangements in both amorphous and crystalline forms in several dimensions with energy and mass transport providing the basis of functions.[3-4] The operability of such devices may be addressed using atomic and molecular components and their interactions, keeping in view the advantages of stereochemical and spatiotemporal arrangements. The past developments in molecular devices might help inspire discoveries that have the potential to lay the foundations of such advancements.

In molecular electronics, demonstrations of fabrications of rectifiers[10], transistors[11], resistive switches[12] and photoswitches[13] at nanometer-length scales usher confidence and guidance in futuristic developments of interconnected device components based on the principles of chemistry. Similarly, the advances in single supramolecular electronics[4] indicate that assemblies of molecules could be used to fabricate devices where multiple chemical bonds work in concert to improve the quality and functionality of the signals. In this regard, the role of non-covalent bonds may be pivotal in the functioning of the integrated circuits. Thus, ensembles of molecules may also be developed into customized functional devices by exploiting the chemical properties and interactions at the molecular level. These devices may not only have superior performances but also be operable in the liquid media as compared to their conventional counterparts.

One way of fabricating such superstructures could be based on layered ensembles of molecules forming crystalline mono lattices followed by their further arrangements into translational or angular stacking into moiré superlattices. The new chemical interactions at the lattice interfaces may give rise to extraordinary electrical and magnetic signals, forming the basis of functioning of the devices. Fabrication of multilayered molecular moiré superstructures[14] might have advantages of large molecule-electrode contact, customized properties according to molecular interactions and multiple electronic information storage based on the chemical interaction at each

interface. Multilayered materials such as multilayer giant magnetoresistance[15], graphene[16-17] or boron nitride[18] and nanodielectrics[19] provide advantages over monolayers in terms of material robustness, better charge carrying capacity, high charge storage, low leakage and tunable electrical properties due to interlayer electronic coupling. On the other hand, unconventional properties such as superconductivity[20-21], Mott-like insulator states[22] and moiré excitons[23] might arise due to formation of moiré superlattices owing to rotational misalignment of monolayers during stacking. However, the fabrication of graphene like moiré superlattices requires careful stacking of 2D monolayers obtained after exfoliation, which limits its bulk production. Whereas the chemical synthesis[14,24-26] of the molecular moiré superlattices can result in bulk production of multilayered moiré superlattices. The electrical properties in moiré superlattices can be studied through conductive atomic force microscopy[27-28] (c-AFM) that measures the vertical conductivity[29] of the moiré superlattices where the contact conductance between probe and sample is coupled with interlayer conductivity. Importantly, the interfacial conductivities could be decomposed from the overall conductivity by using Fourier transformation techniques. Typically, a monotonous decrease in the interlayer conductivity is observed as the twist angle increases.[30-32] Similarly, the charge transport in molecular moiré superlattices would depend on the combined effect of interlayer interactions[30-31] and electrons transfer through quantum mechanical tunneling[9] as observed for supramolecular electronics[4]. The tunneling barrier would depend upon the interaction within the lattices as well as those at the inter-lattice interfaces. These interactions could be controlled by factors such as pH of the syntheses medium. Such an approach in fabrication of electronic devices is yet to be developed.

Herein, we report the formation of chemically assembled multilayered molecular moiré superlattices of p-phenylenediamine (p-PD) that produced ten-fold increase in the interfacial current compared to its monolayer nanocrystal counterpart (Scheme 2). The formation of the moiré superlattices were confirmed by transmission emission microscopic (TEM) images and AFM measurements. The interlayer current was measured using AFM in conductive mode where a monotonous decrease in the interfacial current was observed as the twist angles in the multi-lattice moiré interfaces had increased. The conductivity observed at each interface was independent of other interfacial conductivity and was dependent on the hypermolecular (i.e., in between the twisted lattices) interactions at the respective interfaces. The intervening water

molecules in the 2D lattices led to high tunneling barrier as well as distance compared to those at the moiré interface, resulting in low conductivities of the lattices as opposed to their twisted interfaces. Furthermore, there was a significant increase in the interfacial current, that showed tunability as well stability, upon protonation and deprotonation of the moiré superlattices through change in the pH of the syntheses medium. These results were further supported by density of states calculations along with carrier density and simulated STM plots.

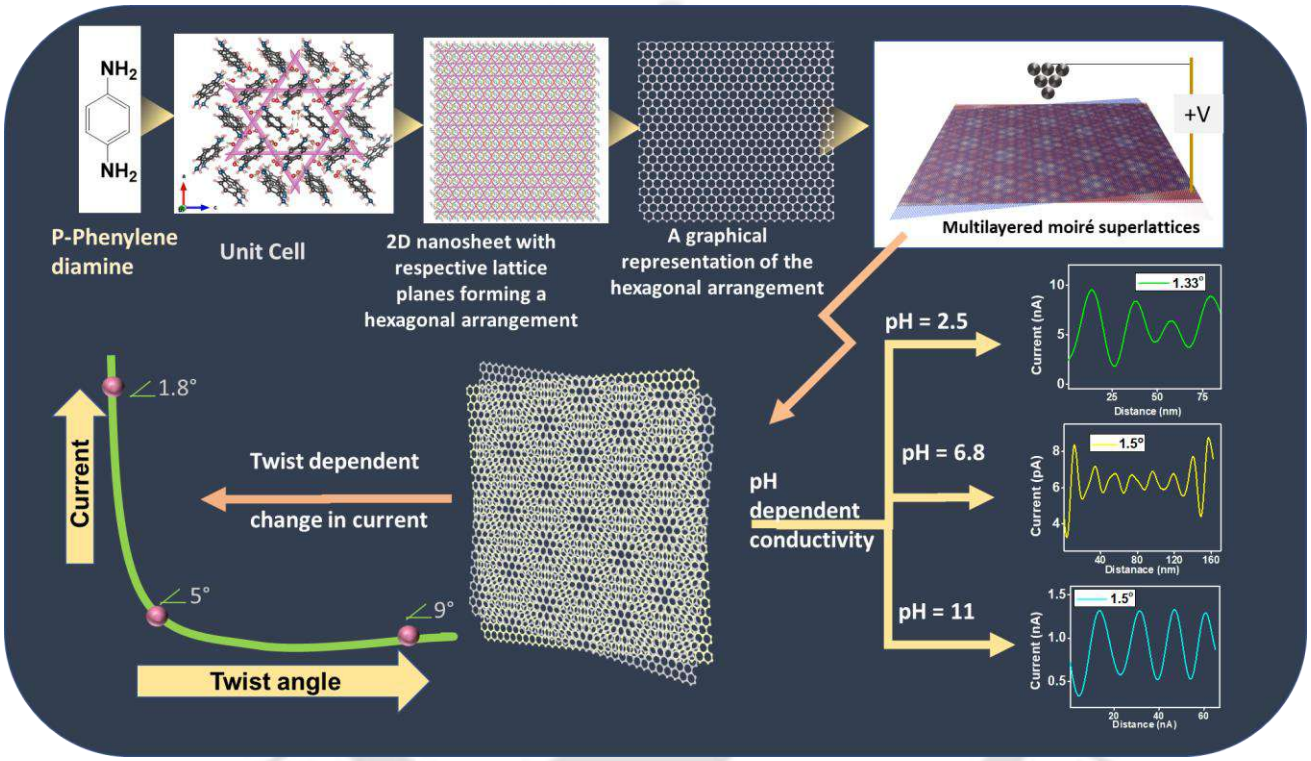

Scheme 2. Graphical representation of the formation of moiré superlattices of p-phenylenediamine showing variation in interfacial current with respect to twist angle that increases when the moiré superlattice is protonated or deprotonated.

Results and Discussion

Assembly of p-PD to form moiré superlattices

Moiré superlattices of p-phenylenediamine (p-PD) were synthesized following continuous stirring of the aqueous solution of the molecule (~450 µM) in a vial for 24 h at 80 ºC. TEM images confirmed the formation of moiré superlattices (Figure 1). TEM images taken at 2 h revealed that the dispersion was populated with 2D crystalline nanosheets (Figure 1A) having

hexagonal selected area electron diffraction (SAED) patterns with d-spacing of 0.46 nm (Figure 1B). The observed SAED patterns (Figure 1B, Figure S1A) were similar to the pattern simulated from the reported crystallographic file of p-PD using Recipro software[33] (Figure S1B). They indicated the formation of crystalline nanosheets that were formed by 2D assembly of the molecules held by intervening layers of water through hydrogen bonding (H-bonding) (Figure 1C-D, Figure S2), as reported previously[34]. At 24 h, the dispersion was populated with multilayered moiré nanosheets as was observed from the TEM images (Figure 1E-F, Figure S3). The moiré superlattices were formed by the twisted stacking of multiple crystalline 2D nanosheets (Figure S4) having twist angles on an average less than 10º (Figure S5B). Figure 1E-F represents two typical examples of the moiré nanosheets of p-PD and Figure 1G represents the SAED pattern obtained from Figure 1F where 11 2D lattices having hexagonal pattern were stacked at angles less than 15º with d-spacing of 0.21 nm as further explained in Supporting Information.

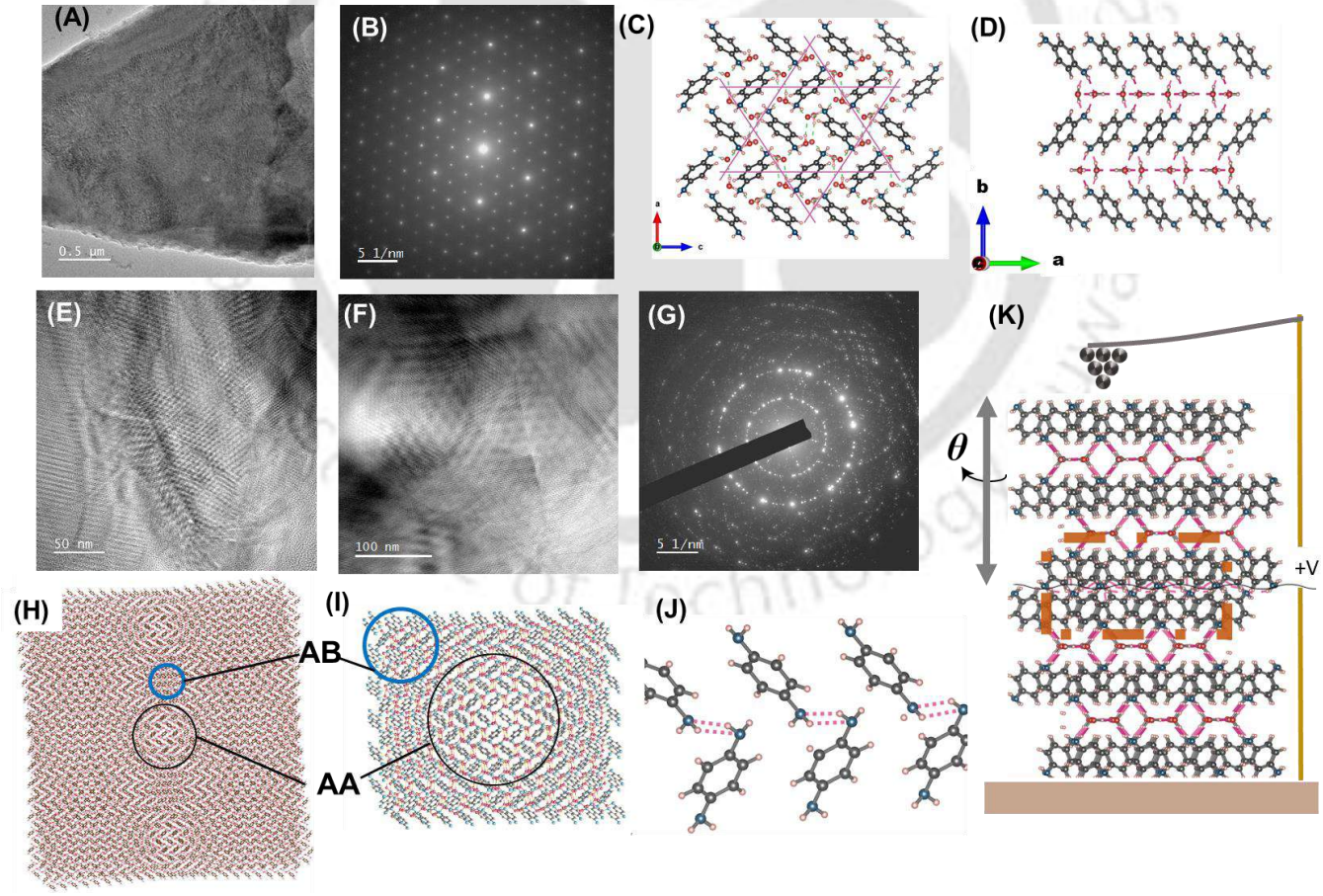

Figure 1. (A) TEM image of the 2D crystalline nanosheet at 2 h and **(B)** corresponding SAED pattern of (A). **(C)** Lattice crystal structure of p-PD along b axis showing the respective lattice plane. **(D)** Lattice crystal structure of p-PD along c axis **(E)-(F)** TEM images of the dispersion at 24 h showing formation of moiré superlattices and **(G)** SAED pattern corresponding to image in (F). **(H)** Molecular arrangement of p-PD in the moiré superlattices when viewed through b-axis. **(I)** Enlarged view of (H) showing AA and AB stacking. **(J)** H-bond between p-PD molecules in the interface at AA stacking arrangement. **(K)** Schematic of c-AFM measurements on molecular moiré superlattices of p-PD. The interface region is highlighted in bracketed bold color.

The time-dependent UV-Vis absorption and photoluminescence (PL) properties (Figure S6) of the dispersion further supported the self-assembly formation of p-PD. At 10 min, peaks ranging from 200 – 300 nm were observed in the UV-Vis spectrum that were inherent to p-PD molecules (Figure S6A). As the reaction progressed to 2 h (when the dispersion was populated with 2D crystalline nanosheets), a new peak at 500 nm appeared. When the dispersion was excited at 480 nm, a new emission peak at 600 nm was observed that was absent at 10 min (Figure S6B). The excitation spectrum recorded for λ_{em} = 600 nm resulted in a new peak at 480 nm (Figure S6C), which was in consonance with the UV-Vis spectrum at 2h. The results indicated formation of a new species through molecular interaction as the reaction progressed to 2h. At 5h, a prominent peak at 365 nm was observed in the UV-Vis spectrum along with a blue shift of 307 nm peak to 280 nm (Figure S6A). An increase in the absorbance of 500 nm peak was also observed. They indicated a further interaction between the molecules and the 2D nanosheets. As the reaction progressed to 24 h, when a large number of moiré nanosheets were present in the medium, increases in the absorbance for the peaks at 280 nm and 500 nm were observed along with red shift of the peak at 365 nm. When the dispersion was excited at 365 nm, a new peak at 500 nm - along with that at 600 nm - was observed (Figure S6D). Again, for the excitation spectra with λ_{em} = 500 nm (Figure S6E) and λ_{em} = 600 nm (Figure S6C), a new peak at 365 nm was observed, in concurrence with the UV-Vis spectrum at 24 h. The abovementioned optical properties at different time were also indicative of the formation of new species, probably the 2D crystalline nanosheets at initial hours (2 h) of the reaction and crystalline multi-lattice moiré nanosheets at later times (24 h).

Further, the interactions of p-PD molecules within the 2D nano lattice and in the moiré superlattice were further probed by proton nuclear magnetic resonance (^{1}H NMR) and mass spectra obtained from electro-spray ionization mass spectrometry (ESI-MS) and matrix-assisted laser desorption/ionization time-of-flight (MALDI-TOF). The reported crystalline arrangement proposes[34] an interaction of p-PD and water molecules as alternate layers through hydrogen bond (H-bond) (Figure S2, Figure 1D). The time-dependent NMR results (Figure S7) showed downfield shift of the aromatic ring C-H protons at 6.7 ppm, indicating change in chemical environment due to formation of H-bond networks as have been observed for other H-bonded molecules[14]. As mentioned earlier, the SAED pattern indicated the growth of the 2D nanosheet along a and c axes while the growth along the b axis was restricted (Figure S2B). Along b axis, there was an alternate layering of p-PD and water where the water molecules formed two H-bonds with p-PD molecules and other two with neighboring water molecules (Figure S2). This growth continued along a and c axes with alternate layering of the p-PD and water molecules along the b axis to have a thickness in nano dimensions forming a 2D lattice. These 2D lattices further twist-stacked to form the moiré superlattices (Figure 1H, Figure S8). This was further confirmed by mass spectra analysis of the fragments of the nanosheets obtained from MALDI-TOF and ESI-MS. The mass fragments, for example, corresponded to $(C_6H_8N_2)_6(H_2O)_2$ (m/z = 684.4), $(C_6H_8N_2)_6$ (m/z = 648.4) and $(C_6H_8N_2)_4$ (m/z = 432.4) that further confirmed the proposed structure of H-bonded p-PD and water molecules in the 2D lattice and H-bonded interaction of p-PD at the interface of moiré superlattices (Figure S9 and S10). It may be mentioned here that a few masses were also obtained corresponding to the polymer of p-PD that might have formed due to aerial oxidation of the molecule in the dispersion. But that didn't affect the formation of 2D nanosheets or moiré superlattices as confirmed from crystallographic data, mass and NMR spectral results. Thus, the interfacial interaction involved N-H$\cdots$N H-bonding of the surface NH_2 groups (Figure 1J) and for each twist angle, the number of H-bonds in AA region was different according to the rotational orientation of one lattice with respect to the other.

AFM measurements of moiré superlattices

The moiré superlattices so formed were then probed with conductive AFM (c-AFM) measurements (Figure 1K). The formation of moiré superlattices was also confirmed through

tapping mode AFM (Figure 2A). Force-distance (F-d) curves (Figure 2B, Figure S11A) were measured for the moiré superlattices by indentation of AFM tip on moiré sheets. The moiré nanosheets were formed through vdW interactions having an average vdW dissipation energy of 76.6 ± 26.1 eV. It gives a measure of the dissipated energy after tip-sample interaction and was calculated from the hysteresis of the approach and retract F-d curves. The average height of the moiré sheets was found to be 42.95 ± 12.6 nm as calculated from the height profile of the same (Figure S11B-C).

Conductive AFM measurements of moiré superlattices of p-PD

For the conductivity measurements of the moiré superlattices in contact mode (Figure 1K), a conductive tip was brought near the sample where it was scanned against a constant bias voltage (~2V). A constant load of ~100 nN was applied on the tip to minimize the contact resistance between tip and the sample surface. All the measurements reported herein, for the neutral, protonated and deprotonated samples, were performed after applying a constant load of ~ 100 nN on the tip. Since the moiré nanosheets were formed of multiple twisted 2D lattices, the overall current map was too dense to be well separated for the moiré fringes. Thus, fast Fourier transform (FFT) analysis was employed (as explained in suppoting information) to decipher the individual moiré patterns (Figure 2C and S11G-H) that corresponded to the sets of spots in the FFT.[35] A typical example is presented in Figure 2C, which is reconstructed from the FFT (Figure 2D) performed on the current map of the moiré superlattice (Figure S11F). The inverse FFT (IFFT) resulted in the reconstruction of the multi-lattice moiré superlattices and the current observed for the respective angles is plotted in Figure 2E-F. Figure 2F indicated a monotonous decrease in the interfacial current as the twist angle had increased. Further, there was 10 times increase in the overall current in the current map of moiré superlattices when compared to the 2D crystalline nanosheet (Figure S11I).

The observed increase in the conductance for the molecular multi-lattice moiré as compared to 2D nanolattice could be explained from the molecular arrangement within the lattice and twisted multi-lattice. As mentioned previously, the moiré nanosheets were formed through H-bonding where the interaction between p-PD molecules within the lattice was through H-bonded H_2O while at the interface, there was direct H-bond interaction of surface p-PD molecules of two different nanolattices. The charge transport mechanism would be similar to supramolecular

electronics formed through H-bonds, involving electron tunneling through H-bonds[4,9]. It has been reported that in molecular electronics, the electron transport is more efficient through H-bonds in comparison with σ bonds.[36]

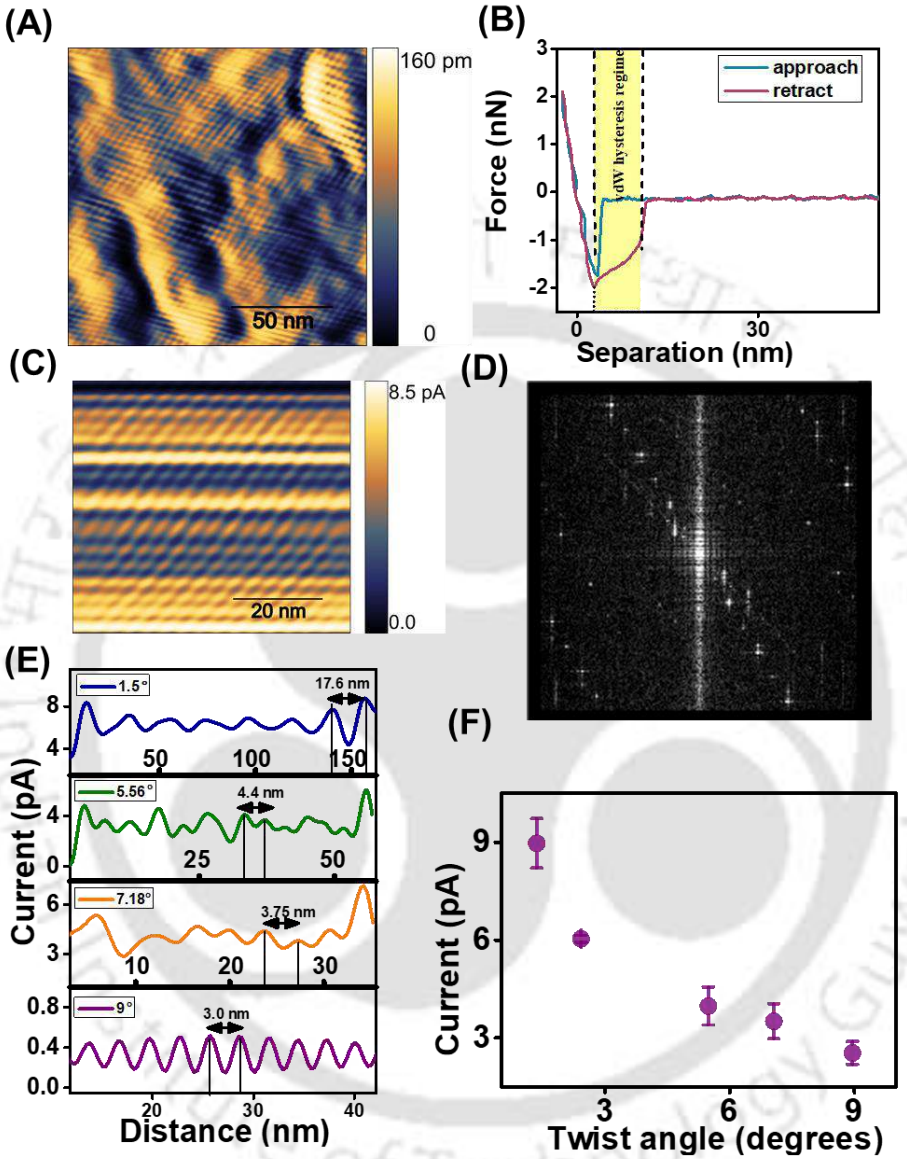

Figure 2. (A) AFM amplitude images of moiré superlattices of p-PD obtained through tapping mode. **(B)** A typical force–distance curve measured on a moiré superlattice. **(C)** Reconstruction of moiré superlattices from IFFT of current mapping of the moiré nanosheets performed using c-AFM. **(D)** Corresponding FFT of the current mapping from which the moiré superlattices in (C) is reconstructed. **(E)** Current profile obtained from moiré superlattices in (C) for respective twist angles. **(F)** Plot of current vs twist angle showing a monotonous decrease in current with increase in twist angle.

Additionally, the H-bond provides mechanical stability and an increased conductivity is observed if aromatic ring is present in the supramolecular backbone.[37] Here c-AFM was used to study the interfacial conductivity of the molecular moiré superlattices. The current mapping of the p-PD 2D nanosheet was done using c-AFM where low value of current (~1pA) was observed. When current mapping of moiré superlattices were performed, a sudden increase in the interfacial current (~10 pA) was observed. At the moiré superlattice interfaces, the p-PD molecules were directly H-bonded to each other through the constituent -NH_2 groups, where in AA region two H-bonds were formed for a pair of p-PD molecule (Figure 1J). This supported facile electron tunneling across the barrier. On the other hand, in the lattices, the σ bonds and H-bonds due to the intervening water molecular layers (Figure S2) increased the tunneling length and barrier to electron transport between two p-PD molecules, resulting in low conductivity Again, it has been reported that multiple H-bonds at supramolecular junctions result in high magnitude increase in the conductance suggesting a crucial role of the number of H-bonds present at junction for conductance across the same distance.[38] Thus, at low angles, twisted stacking provided the perfect orientation of the molecules to have maximum number of H-bonds. However, upon moving from AA region toward AB region, the large distance and geometrical constraints between the NH_2 groups decreased the number of H-bonds formed between them i.e., from two to one to none. Further, with larger twist angles, the moiré periods were smaller thus resulting in AA regions with smaller areas (Figure S12). As the number of H-bonds were maximum in AA region, the larger twist angles and distances of separation in such AA regions resulted in smaller numbers of H-bonds than those at the lower twist angles and hence the interfacial current had decreased significantly (Figure 2E-F). Thus, for a multi-lattice moiré superstructure, the overall current depended on the number of H-bonds at each interface that was depended on the twist angle.

Enhancement of conductivity upon protonation and deprotonation

Interestingly, for the protonated and deprotonated moiré superlattices, there were significant increases in the interfacial current. The moiré nanosheets were protonated and deprotonated in the dispersion by changing the pH of the medium. The TEM images and SAED patterns for the moiré superlattices following protonation as well as deprotonation were recorded (Figure S13). The observations of the retention of lattice parameters for the moiré patterns and the

corresponding SAED patterns following protonation as well as deprotonation suggested that the constituent crystal structure as well as the twisted superlattices remained unaffected with respect to pH change of the reaction medium. Further, the mass spectra obtained from ESI-MS analysis of the moiré superlattices following treatment with acid (Figure S15A-C) or base (Figure S15D-F) (protonation or deprotonation) revealed the same mass fragments; for example, $(C_6H_8N_2)_2(H_2O)_2$ (m/z = 250.15), $(C_6H_8N_2)_4(H_2O)_2$ (m/z = 466.7) and $(C_6H_8N_2)_4(H_2O)_5$ (m/z = 522.33), as were observed for neutral moiré superlattices. It was observed that the protonated moiré nanosheets at pH 2.5 were ~1000 times more conducting (Figure 3A-C) than the neutral moiré nanosheets. Whereas the deprotonated moiré superlattices at pH 11 had conductivity ~400 times more than the neutral nanosheets (Figure 3D-F). The contrast in the current for each angle could be seen from Figure 3G where for the same twist angle, the protonated moiré superlattices showed more conductivity than the deprotonated superlattices, which was followed by the neutral moiré superlattices.

The significant increase in the conductivity for the protonated moiré superlattices can be explained from the increase in the number of H-bonds at the interface (Figure 3H). As the moiré nanosheets were protonated or deprotonated, the TEM and AFM results suggested that the H-bond network within the lattice or at interface were not destroyed and the lattice parameters remained the same. This implied that the protonation or deprotonation would have occurred where the NH_2 groups didn't participate in H-bonds in the original superlattice structures due to high angular twist and distance between the two NH_2 groups, i.e., in the AB region. This also meant that H-bonds (and thus stability) of the moiré superlattices were unaffected by the protonation or deprotonation of the medium. Following protonation, the NH_2 groups at the interfaces formed additional H-bonds between the p-PD molecules from the opposite lattices (Figure 3H, Figure S16) in the AB region. Due to steric restraints, only one proton for two free NH_2 groups was involved in H-bonding as if mimicking a H-bond between NH_3^+ and NH_2. When moved further into the AB region, the spatial restraints restricted the H-bond formation. This would mean an increase in number of H-bonds at the interface only in the periphery of the AA regions, thus increasing the interfacial current. Similarly, when the moiré superlattices were deprotonated, the free NH_2 groups were converted to NH^-. Again, the NH^- would be in an orientation that could result in H-bond formation with NH_2 group of the other lattice as the

probability of H-bond formation increased with introduction of extra pair of electrons on N at the interface. Thus, for protonation and deprotonation, the chances of H-bond formation increased with introduction of a proton and an electron pair on the interfacial nitrogen. The charged ions were balanced by the counter ions such as Cl^- and Na^+. As the moiré superlattices were formed, the number of H-bonds decreased as we moved away from the periodic AA stacking (Figure S16). The protonation of free NH_2 groups probably occurred at the AB region keeping the H-bonded network unaffected.

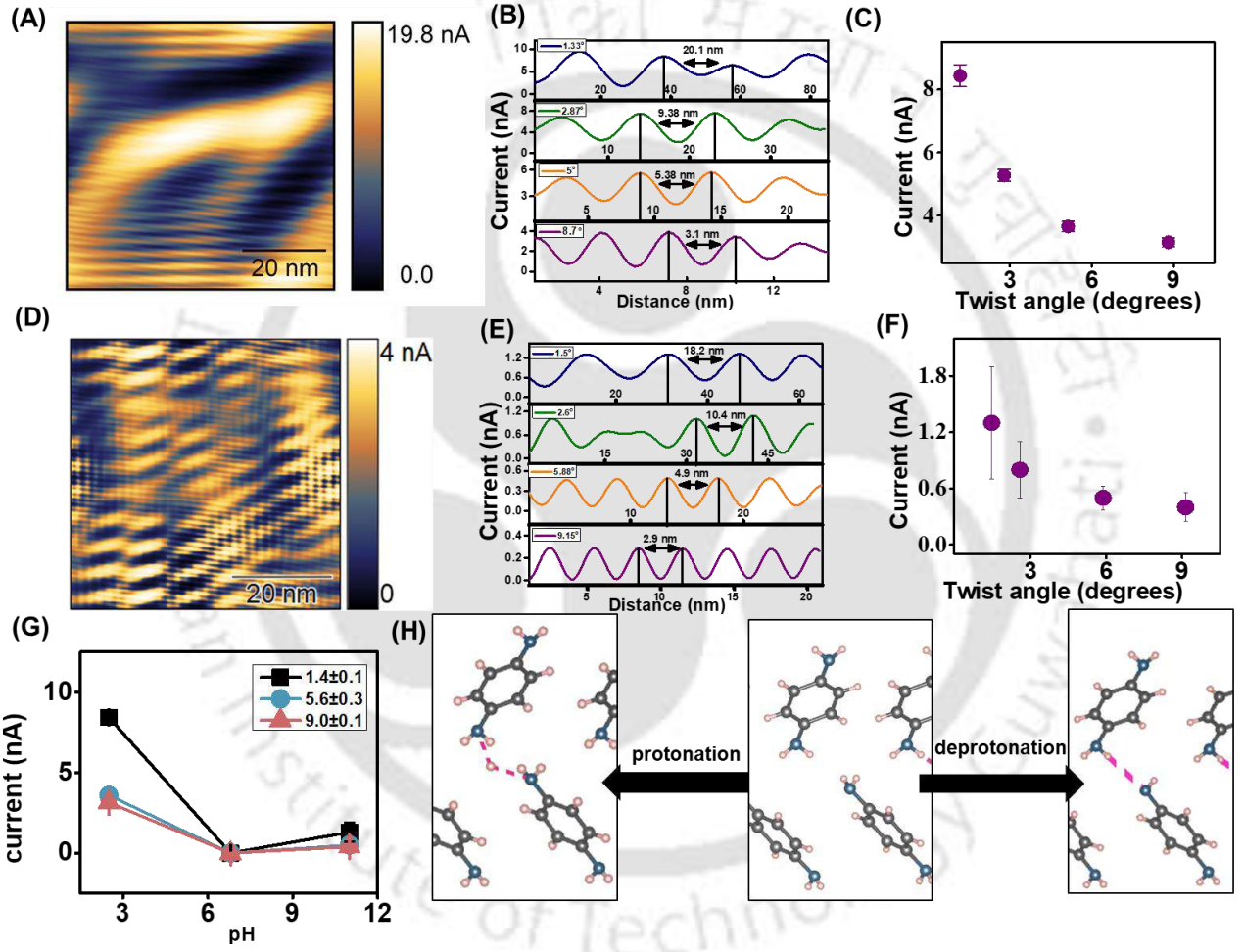

Figure 3. (A) Reconstruction of protonated moiré superlattices from IFFT of current mapping of the moiré nanosheets performed using c-AFM. **(B)** Current profile obtained from moiré superlattice in (A) for respective twist angles. **(C)** Plot of current vs twist angle showing a monotonous decrease in current with increase in twist angle. **(D)** Reconstruction of deprotonated moiré superlattices from IFFT of current mapping of the moiré nanosheets performed using c-AFM. **(E)** Current profile obtained from moiré superlattice in (D) for respective twist angles. **(F)**

Plot of current vs twist angle showing a monotonous decrease in current with increase in twist angle. **(G)** Comparison of current for deprotonated, protonated and neutral moiré superlattices for respective twist angles. **(H)** Schematic representation showing protonation and deprotonation of the neutral superlattice at the interface.

Simulations of structure and density of states

Further, simulations corresponding to the density of states (DOS) were carried out for the 2D nanocrystal of p-PD, twisted (moiré) interface and that for the protonated twisted (moiré) interface (Figure 4A). The DOS was plotted against E -E_{Fermi} where it was evident that higher number energy states were present near the fermi energy level for the twisted interface as compared to 2D nanocrystal. This indicated that in case of twisted interface there was a probability of higher number of electrons near fermi level, which increased the carrier concentration and charge mobility and thus had resulted in higher conductivity.

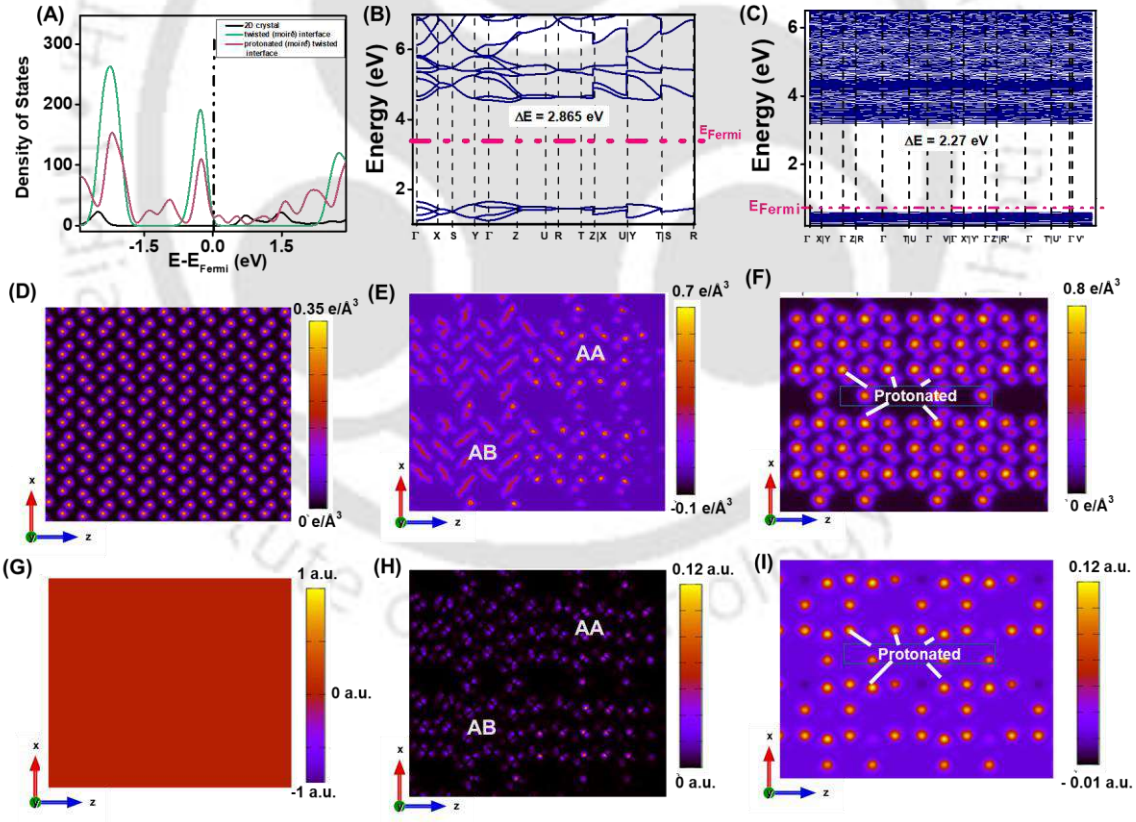

Figure 4. (A) Density of states plots for 2D nanocrystal, moiré interface and protonated moiré interface of p-PD. **(B)** and **(C)** Band structure plots of 2D nanocrystal and moiré interface,

respectively. **(D)**, **(E)** and **(F)** Carrier charge density plots for 2D nanocrystal, moiré interface and protonated moiré interface of p-PD, respectively. **(G), (H)** and **(I)** Simulated STM plots for 2D nanocrystal, moiré interface and protonated moiré interface of p-PD, respectively.

Again, from Figure 4A, it was observed that even higher DOS was present at the fermi energy level for the protonated twisted (moiré) interface. This further explains the high conductivity as observed for the protonated twisted interface when compared to the neutral moiré superlattices. The band structures of the 2D nanocrystal and the twisted (moiré) interface are presented in Figure 4B-C, which indicated reduction in band gap for the twisted (moiré) interface when compared to the 2D nanocrystal, thus facilitating the charge transfer between the twisted layers. Further the carrier charge density plot indicated that the carrier density was higher in the AA region of the moiré superlattice than the 2D nano crystal (Figure 4D-E). Figure 4F represents the charge density observed for the protonated twisted (moiré) interface where higher charge density was observed in the protonated region, thus facilitating charge transport for the protonated moiré superlattices. Additionally, STM plots are also presented, which clearly indicated the variation for twisted interface while for 2D nanocrystal, a constant value was observed (Figure 4G-H) while STM plot for protonated twisted interface showed higher value in the protonated region (Figure 4I).”

Conclusion

In conclusion, we have synthesized multilayered molecular moiré superlattices of p-PD where the combined effect of interlayer interaction and tunneling barrier was observed for the interfacial current. The molecular moiré superlattices were stable in the presence of acid or alkali in the dispersion medium. The interfacial current results revealed the deprotonated and protonated moiré superlattices had much higher conductivity than their neutral counterparts. These results were further supported by density of states calculations along with carrier density and simulated STM plots. These moiré superlattices could further be studied for their use as practical electronic devices as they offer larger electrode molecule surface area with a stable molecular arrangement within the superlattice. The superlattice interfaces offer specific electron conductivity that could be exploited for building complex circuits, information storage or sensing based on the principles of quantum mechanics at the molecular length scales.

Chapter 4

Experimental Section

Materials Used

p-Phenylenediamine (p-PD, 98% (HPLC)) was purchased from Sigma-Aldrich and used without further purification. Milli-Q grade water was used for all the experiments. D_2O was purchased from Sigma-Aldrich and used for NMR experiments.

Synthesis of Moiré Superlattices of p-PD

2 mL aqueous solution of p-PD (5 mg) was sonicated for 1-2 min to get a clear solution. 200 µL of the resulting solution was added to 10 mL of water (resulting in 454 µM concentration). The final mixture was then kept under constant stirring and heating at 80 ºC for 24 h. The dispersion after 24 h was then used for further experiments.

Synthesis of protonated and deprotonated moiré superlattices of p-PD

To synthesize protonated moiré superlattices, 40 µL of 1M HCl solution was added to 3mL of the dispersion resulting in pH = 2.5. Similarly, deprotonated moiré superlattices were synthesized 40 µL of 1M NaOH solution was added to 3mL of the dispersion resulting in pH = 2.5.

Optical Measurements

Time-dependent UV-vis measurements and photoluminescence (PL) spectra were recorded using Perkin-Elmer Lambda 365+ and HORIBA FluoroMax-4 spectrofluorometer, respectively, where 3 mL of aliquot was collected at different times for the measurement of absorbance and PL spectrum.

Transmission electron microscopic (TEM) analysis and selected area electron diffraction (SAED) analysis

TEM and SAED data were collected after diluting the dispersion (200 µL of aliquot in 1 mL water) and drop-casting on a carbon coated copper grid. TEM and SAED experiments were performed using JEOL JEM 2100 F instrument.

Atomic force microscopic (AFM) analysis and measurement of force-distance curve AFM images were acquired using Oxford Asylum Research MFP-3D model. Images were acquired in

attractive tapping mode. Force-distance curves were measured in contact mode with tip of model AC240TS-R3 (k~2 Nm^{-1} and f = ~73 kHz).

Conductive AFM (c-AFM) measurements and analysis

c-AFM measurements were pursued using Oxford Asylum Research MFP-3D model. Images were acquired using a tip of model ECONO SCM-PIT (k~ 3 Nm^{-1} and f = ~75 kHz). We have performed c-AFM measurements for about 10 different samples (at 3-4 different positions of the same sample) using several conductive AFM tips to rule out any uncertainty in measurements due to contact conditions. The error bar presented here were calculated from the c-AFM measurements for three different samples. A load of ~100 nN was applied on the tip to minimize the contact resistance between tip and the sample surface. This was achieved by slowly increasing the initial setpoint of 0.2 V to 0.5 V (~100 nN) for a c-AFM cantilever with force constant (k) around 2.5 N/m, as per the recommendation of the manufacturer. Thus, all the measurements reported herein, for the neutral, protonated and deprotonated samples, were performed after applying a constant force of ~ 100 nN on the tip.

Proton NMR, ESI-MS and MALDI-TOF

Proton nuclear magnetic resonance (NMR) measurements were performed using 600 MHz Bruker ASCEND 600. The experiment was performed as described in 'synthesis of moiré superlattices' where D_2O (Sigma-Aldrich) was used in place of Milli-Q grade water. 600 μL of aliquot was taken at different times to perform the analysis. Electrospray ionization mass spectrometric (ESI-MS) analysis was performed using Agilent Accurate Mass (Q-TOF 6520) spectrometer in ESI positive and negative modes where 2 mL of the aliquot was used for the analysis. Matrix-assisted laser desorption/ionization time-of-flight (MALDI-TOF) was performed using Bruker AUTOFLEX speed model. 2 μL of the matrix free sample was drop-cast on MALDI plate where it was allowed to dry and was subjected to mass analysis.

Simulations of SAED patterns and chemical structure of moiré superlattices

The reported crystallographic information file (cif) of p-PD was used for SAED simulation, which was done using ReciPro software. The unit cell, hkl planes and the structure were redrawn from cif file data using vesta. Twisting of the lattices were performed using Avogadro software and the interfacial interaction was redrawn using vesta.

Chapter 4

Simulations of structure and density of states

The structure relaxation, density of states calculations, carrier charge density and STM plot simulations were performed using Quantum ESPRESSO programme suite[39]. The structural model used for the calculations are presented in Figure S17. PBEsol's generalized gradient approach (GGA) was utilized to calculate the exchange-correlation function[40,41]. The core electrons were modelled using projector-augmented-wave (PAW) method[42]. The kinetic energy cut-off was set to 60 Ry. For the neutral and protonated twisted (moiré) interfaces the twist angle was set to 12°.

References

1. Yuan, M.; Qiu, Y.; Gao, H.; Feng, J.; Jiang, L.; Wu, Y., Molecular Electronics: From Nanostructure Assembly to Device Integration. *J. Am. Chem. Soc.* **2024,** *146* (12), 7885-7904.
2. Xiang, D.; Wang, X.; Jia, C.; Lee, T.; Guo, X., Molecular-Scale Electronics: From Concept to Function. *Chem. Rev.* **2016,** *116* (7), 4318-4440.
3. Li, T.; Bandari, V. K.; Schmidt, O. G., Molecular Electronics: Creating and Bridging Molecular Junctions and Promoting Its Commercialization. *Adv. Mater.* **2023,** *35* (22), 2209088.
4. Chen, H.; Fraser Stoddart, J., From molecular to supramolecular electronics. *Nat. Rev. Mater.* **2021,** *6* (9), 804-828.
5. Moulin, E.; Cid, J.-J.; Giuseppone, N., Advances in Supramolecular Electronics – From Randomly Self-assembled Nanostructures to Addressable Self-Organized Interconnects. *Adv. Mater.* **2013,** *25* (3), 477-487.
6. Li, X.; Ge, W.; Guo, S.; Bai, J.; Hong, W., Characterization and Application of Supramolecular Junctions. *Angew. Chem. Int. Ed.* **2023,** *62* (13), e202216819.
7. Meijer, E. W.; Schenning, A. P. H. J., Material marriage in electronics. *Nature* **2002,** *419* (6905), 353-354.
8. Huang, B.; Liu, X.; Yuan, Y.; Hong, Z.-W.; Zheng, J.-F.; Pei, L.-Q.; Shao, Y.; Li, J.-F.; Zhou, X.-S.; Chen, J.-Z.; Jin, S.; Mao, B.-W., Controlling and Observing Sharp-Valleyed Quantum Interference Effect in Single Molecular Junctions. *J. Am. Chem. Soc.* **2018,** *140* (50), 17685-17690.

9. Soni, S.; Ye, G.; Zheng, J.; Zhang, Y.; Asyuda, A.; Zharnikov, M.; Hong, W.; Chiechi, R. C., Understanding the Role of Parallel Pathways via In-Situ Switching of Quantum Interference in Molecular Tunneling Junctions. *Angew. Chem. Int. Ed.* **2020,** *59* (34), 14308-14312.

10. Aviram, A.; Ratner, M. A., Molecular rectifiers. *Chem. Phys. Lett.* **1974,** *29* (2), 277-283.

11. Song, H.; Kim, Y.; Jang, Y. H.; Jeong, H.; Reed, M. A.; Lee, T., Observation of molecular orbital gating. *Nature* **2009,** *462* (7276), 1039-1043.

12. Kiguchi, M.; Ohto, T.; Fujii, S.; Sugiyasu, K.; Nakajima, S.; Takeuchi, M.; Nakamura, H., Single Molecular Resistive Switch Obtained via Sliding Multiple Anchoring Points and Varying Effective Wire Length. *J. Am. Chem. Soc.* **2014,** *136* (20), 7327-7332.

13. Tebikachew, B. E.; Li, H. B.; Pirrotta, A.; Börjesson, K.; Solomon, G. C.; Hihath, J.; Moth-Poulsen, K., Effect of Ring Strain on the Charge Transport of a Robust Norbornadiene–Quadricyclane-Based Molecular Photoswitch. *J. Phys. Chem. C* **2017,** *121* (13), 7094-7100.

14. Dey, U.; Chattopadhyay, A., Two-dimensional molecular moiré superlattices of tryptophan with visible photoluminescence for photo-activatable CO2 sensing and storage. *J. Mater. Chem. C* **2024,** *12* (15), 5506-5516.

15. Ennen, I.; Kappe, D.; Rempel, T.; Glenske, C.; Hütten, A., Giant Magnetoresistance: Basic Concepts, Microstructure, Magnetic Interactions and Applications. *Sensors* **2016,** *16* (6), 904.

16. Bistritzer, R.; MacDonald, A. H., Transport between twisted graphene layers. *Phys. Rev. B* **2010,** *81* (24), 245412.

17. Min, H.; MacDonald, A. H., Chiral decomposition in the electronic structure of graphene multilayers. *Phys. Rev. B* **2008,** *77* (15), 155416.

18. Uchida, Y.; Nakandakari, S.; Kawahara, K.; Yamasaki, S.; Mitsuhara, M.; Ago, H., Controlled Growth of Large-Area Uniform Multilayer Hexagonal Boron Nitride as an Effective 2D Substrate. *ACS Nano* **2018,** *12* (6), 6236-6244

19. Feng, M.; Feng, Y.; Zhang, T.; Li, J.; Chen, Q.; Chi, Q.; Lei, Q., Recent Advances in Multilayer-Structure Dielectrics for Energy Storage Application. *Adv. Sci.* **2021,** *8* (23), 2102221.

20. Cao, Y.; Fatemi, V.; Fang, S.; Watanabe, K.; Taniguchi, T.; Kaxiras, E.; Jarillo-Herrero, P., Unconventional superconductivity in magic-angle graphene superlattices. *Nature* **2018,** *556* (7699), 43-50.

21. Park, J. M.; Cao, Y.; Xia, L.-Q.; Sun, S.; Watanabe, K.; Taniguchi, T.; Jarillo-Herrero, P., Robust superconductivity in magic-angle multilayer graphene family. *Nat. Mater.* **2022,** *21* (8), 877-883.

22. Cao, Y.; Fatemi, V.; Demir, A.; Fang, S.; Tomarken, S. L.; Luo, J. Y.; Sanchez-Yamagishi, J. D.; Watanabe, K.; Taniguchi, T.; Kaxiras, E.; Ashoori, R. C.; Jarillo-Herrero, P., Correlated insulator behaviour at half-filling in magic-angle graphene superlattices. *Nature* **2018,** *556* (7699), 80-84.

23. Alexeev, E. M.; Ruiz-Tijerina, D. A.; Danovich, M.; Hamer, M. J.; Terry, D. J.; Nayak, P. K.; Ahn, S.; Pak, S.; Lee, J.; Sohn, J. I.; Molas, M. R.; Koperski, M.; Watanabe, K.; Taniguchi, T.; Novoselov, K. S.; Gorbachev, R. V.; Shin, H. S.; Fal'ko, V. I.; Tartakovskii, A. I., Resonantly hybridized excitons in moiré superlattices in van der Waals heterostructures. *Nature* **2019,** *567* (7746), 81-86.

24. Das, P.; Chattopadhyay, A., Moiré superlattices of two-dimensional copper nanocluster assemblies with tuneable twin emissions from hierarchical components leading to white light emission. *J. Mater. Chem. C* **2023,** *11* (35), 12029-12036.

25. Liu, L.; Sun, Y.; Cui, X.; Qi, K.; He, X.; Bao, Q.; Ma, W.; Lu, J.; Fang, H.; Zhang, P.; Zheng, L.; Yu, L.; Singh, D. J.; Xiong, Q.; Zhang, L.; Zheng, W., Bottom-up growth of homogeneous Moiré superlattices in bismuth oxychloride spiral nanosheets. *Nat. Comm.* **2019,** *10* (1), 4472.

26. Hajra, A.; Chattopadhyay, A., Moiré Superlattices of Zn2+ Mediated 2D Assembly of Mn2+-Cysteine Complex Nanoparticles Alter Electron Spin Transitions in the X-Band. *Chem. Mater.* **2024**.

27. Zhang, S.; Gao, L.; Song, A.; Zheng, X.; Yao, Q.; Ma, T.; Di, Z.; Feng, X.-Q.; Li, Q., Tuning Local Electrical Conductivity via Fine Atomic Scale Structures of Two-Dimensional Interfaces. *Nano Lett.* **2018,** *18* (9), 6030-6036.

28. Summerfield, A.; Kozikov, A.; Cheng, T. S.; Davies, A.; Cho, Y.-J.; Khlobystov, A. N.; Mellor, C. J.; Foxon, C. T.; Watanabe, K.; Taniguchi, T.; Eaves, L.; Novoselov, K. S.; Novikov, S. V.; Beton, P. H., Moiré-Modulated Conductance of Hexagonal Boron Nitride Tunnel Barriers. *Nano Lett.* **2018,** *18* (7), 4241-4246.

29. Zhang, S.; Song, A.; Chen, L.; Jiang, C.; Chen, C.; Gao, L.; Hou, Y.; Liu, L.; Ma, T.; Wang, H.; Feng, X.-Q.; Li, Q., Abnormal conductivity in low-angle twisted bilayer graphene. *Sci. Adv.* **2020,** *6* (47), eabc5555.

30. Liao, M.; Wu, Z.-W.; Du, L.; Zhang, T.; Wei, Z.; Zhu, J.; Yu, H.; Tang, J.; Gu, L.; Xing, Y.; Yang, R.; Shi, D.; Yao, Y.; Zhang, G., Twist angle-dependent conductivities across MoS2/graphene heterojunctions. *Nat. Comm.* **2018,** *9* (1), 4068.

31. Yu, Z.; Song, A.; Sun, L.; Li, Y.; Gao, L.; Peng, H.; Ma, T.; Liu, Z.; Luo, J., Understanding Interlayer Contact Conductance in Twisted Bilayer Graphene. *Small* **2020,** *16* (15), 1902844.

32. Chari, T.; Ribeiro-Palau, R.; Dean, C. R.; Shepard, K., Resistivity of Rotated Graphite–Graphene Contacts. *Nano Lett.* **2016,** *16* (7), 4477-4482.

33. Seto, Y.; Ohtsuka, M., ReciPro: free and open-source multipurpose crystallographic software integrating a crystal model database and viewer, diffraction and microscopy simulators, and diffraction data analysis tools. *J. Appl. Crystallogr.* **2022,** *55* (2), 397-410.

34. Czapik, A.; Konowalska, H.; Gdaniec, M., p-Phenylenediamine and its dihydrate: two-dimensional isomorphism and mechanism of the dehydration process, and N—H...N and N—H...π interactions. *Acta Crystallogr. Sect. C* **2010,** *66* (3), o128-o132.

35. Li, Y.; Xue, M.; Fan, H.; Gao, C.-F.; Shi, Y.; Liu, Y.; Watanabe, K.; Tanguchi, T.; Zhao, Y.; Wu, F.; Wang, X.; Shi, Y.; Guo, W.; Zhang, Z.; Fei, Z.; Li, J., Symmetry Breaking and Anomalous Conductivity in a Double-Moiré Superlattice. *Nano Lett.* **2022,** *22* (15), 6215-6222.

36. Nishino, T.; Hayashi, N.; Bui, P. T., Direct Measurement of Electron Transfer through a Hydrogen Bond between Single Molecules. *J. Am. Chem. Soc.* **2013,** *135* (12), 4592-4595.

37. Bui, P. T.; Nishino, T., Electron transfer through coordination bond interaction between single molecules: conductance switching by a metal ion. *Phys. Chem. Chem. Phys.* **2014,** *16* (12), 5490-5494.

38. Wang, L.; Gong, Z.-L.; Li, S.-Y.; Hong, W.; Zhong, Y.-W.; Wang, D.; Wan, L.-J., Molecular Conductance through a Quadruple-Hydrogen-Bond-Bridged Supramolecular Junction. *Angew. Chem. Int. Ed.* **2016,** *55* (40), 12393-1239.

39. Giannozzi, P.; Baroni, S.; Bonini, N.; Calandra, M.; Car, R.; Cavazzoni, C.; Ceresoli, D.; Chiarotti, G. L.; Cococcioni, M.; Dabo, I.; Dal Corso, A.; de Gironcoli, S.; Fabris, S.; Fratesi, G.; Gebauer, R.; Gerstmann, U.; Gougoussis, C.; Kokalj, A.; Lazzeri, M.; Martin-Samos, L.; Marzari, N.; Mauri, F.; Mazzarello, R.; Paolini, S.; Pasquarello, A.; Paulatto, L.; Sbraccia, C.; Scandolo, S.; Sclauzero, G.; Seitsonen, A. P.; Smogunov, A.; Umari, P.; Wentzcovitch, R. M., QUANTUM ESPRESSO: a modular and open-source software project for quantum simulations of materials. *J. Phys.:Condens. Matter* **2009,** *21* (39), 395502.

40. Perdew JP, Yue W. Accurate and simple density functional for the electronic exchange energy: Generalized gradient approximation. *Phys. Rev. B: Condens. Matter Mater. Phys*. **1986**,*33*, 8800-8802.

41. Perdew, J. P.; Ruzsinszky, A.; Csonka, G. I.; Vydrov, O. A.; Scuseria, G. E.; Constantin, L. A.; Zhou, X.; Burke, K., Restoring the Density-Gradient Expansion for Exchange in Solids and Surfaces. *Phys. Rev. Lett.* **2008,** *100* (13), 136406.

42. Blöchl, P. E., Projector augmented-wave method. *Phys. Rev. B* **1994,** 50,17953-17979**.**

Chapter 4

Supporting Information

SAED diffraction of 2-D nanosheet

The selected area electron diffraction (SAED) pattern for the 2-D nanosheet of p-PD was acquired and a hexagonal pattern was observed with a d-spacing of 0.46 nm (Figure S1A). The SAED pattern was reconstructed using recipro[1] software from the crystallographic information file (cif) of p-PD (Figure S1B). Among the spots reconstructed from recipro, only the diffraction spots following the rule h+l = even was observed for the 2-D nanosheet, similar to the pattern observed for 2-D nanosheet of tryptophan[2].

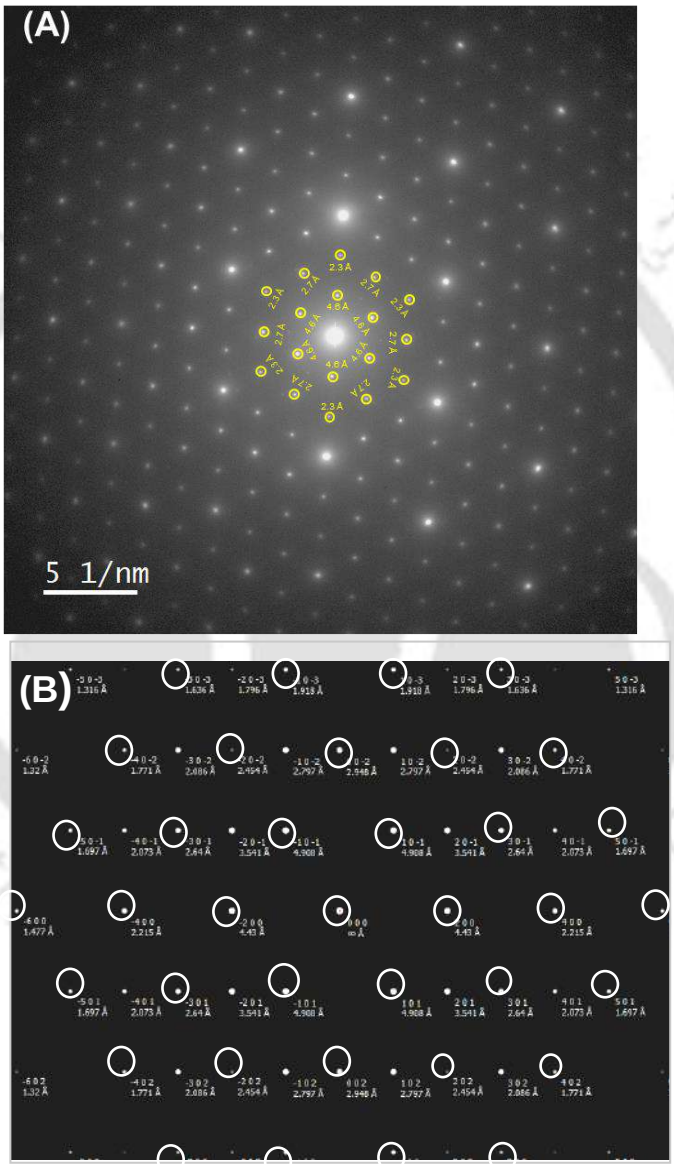

Figure S1. **(A)** SAED pattern of the crystalline nanosheet of p-PD with d–spacing as calculated from the central spot. **(B)** Simulated SAED pattern obtained from the crystallographic information file (cif) of the p-PD crystal that is redrawn using Recipro software where the observed diffraction spots are encircled in white. (p.134)

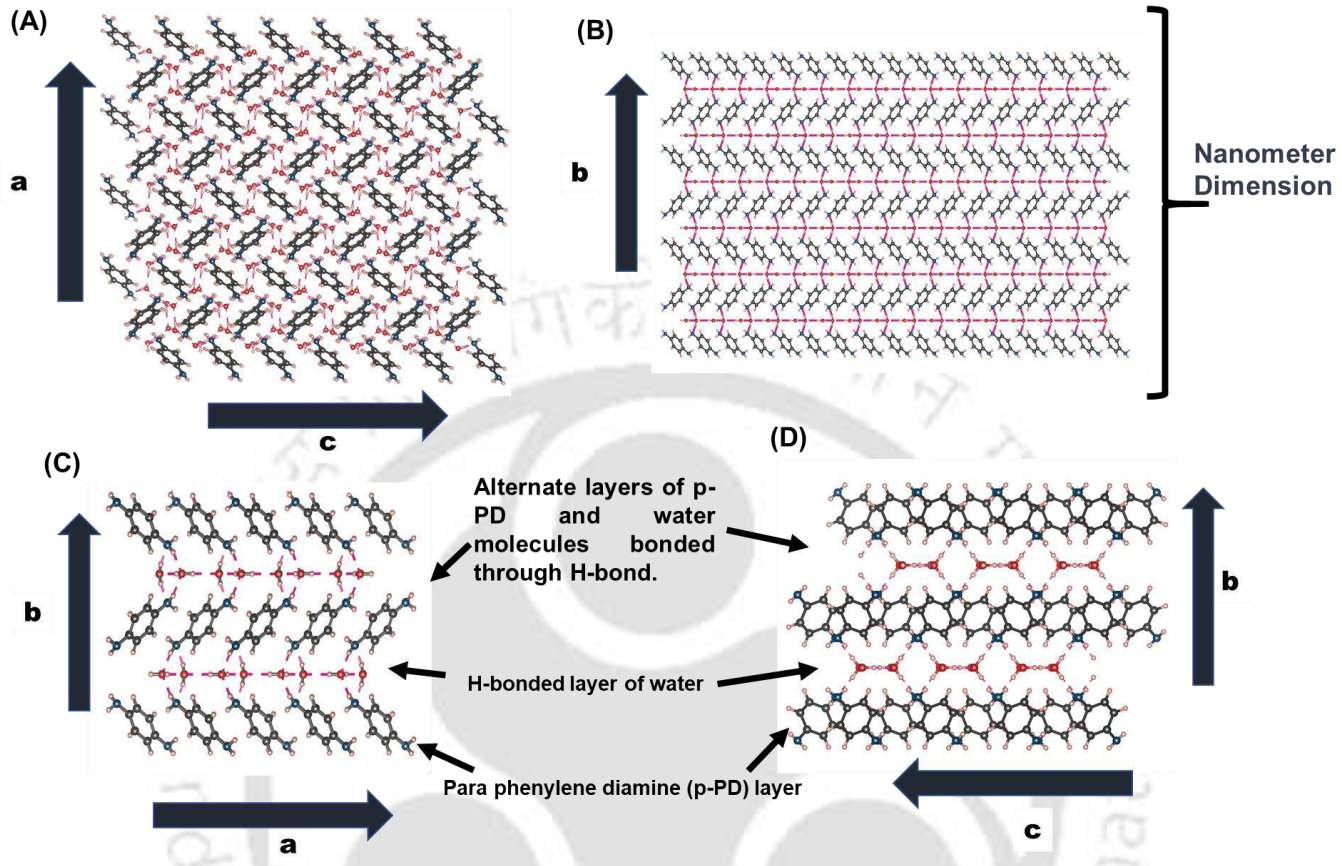

Figure S2. Schematic representation of the **(A)** growth of p-PD lattice along a and b axes for the formation of nanosheet where the **(B)** growth along b is restricted to nanometer length scale. **(C)** and **(D)** represent the enlarged view of the molecular arrangement along b axis showing hydrogen bonding between alternate layers of p-PD and water. (p.134),(p.136, p.138)

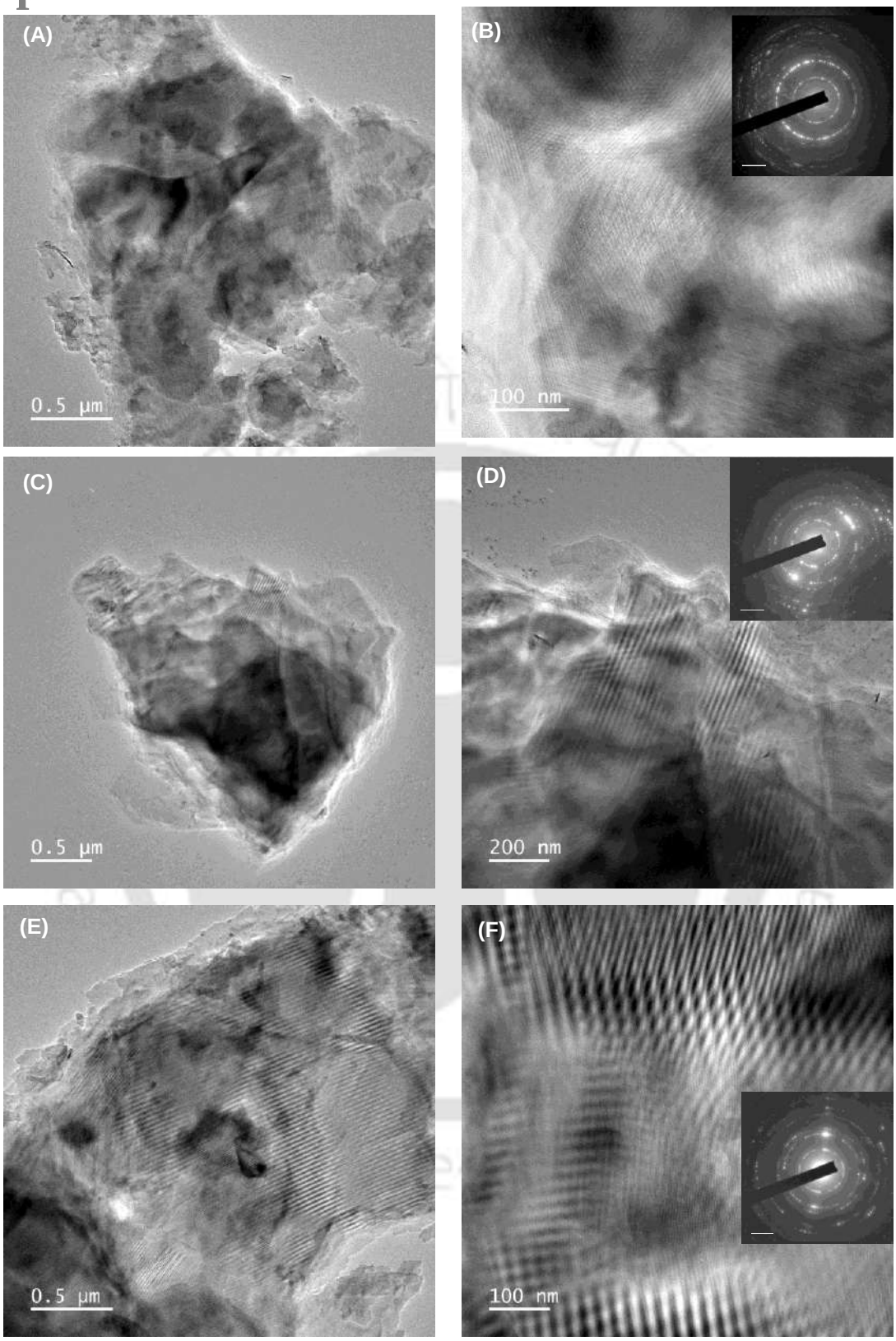

Figure S3. **(A)-(F)** Additional TEM images of moiré nanosheets of p-PD where **(B)**, **(D)** and **(F)** are the enlarged image of **(A)**, **(C)** and **(E)** respectively. **Inset**: Corresponding SAED patterns. (p.134)

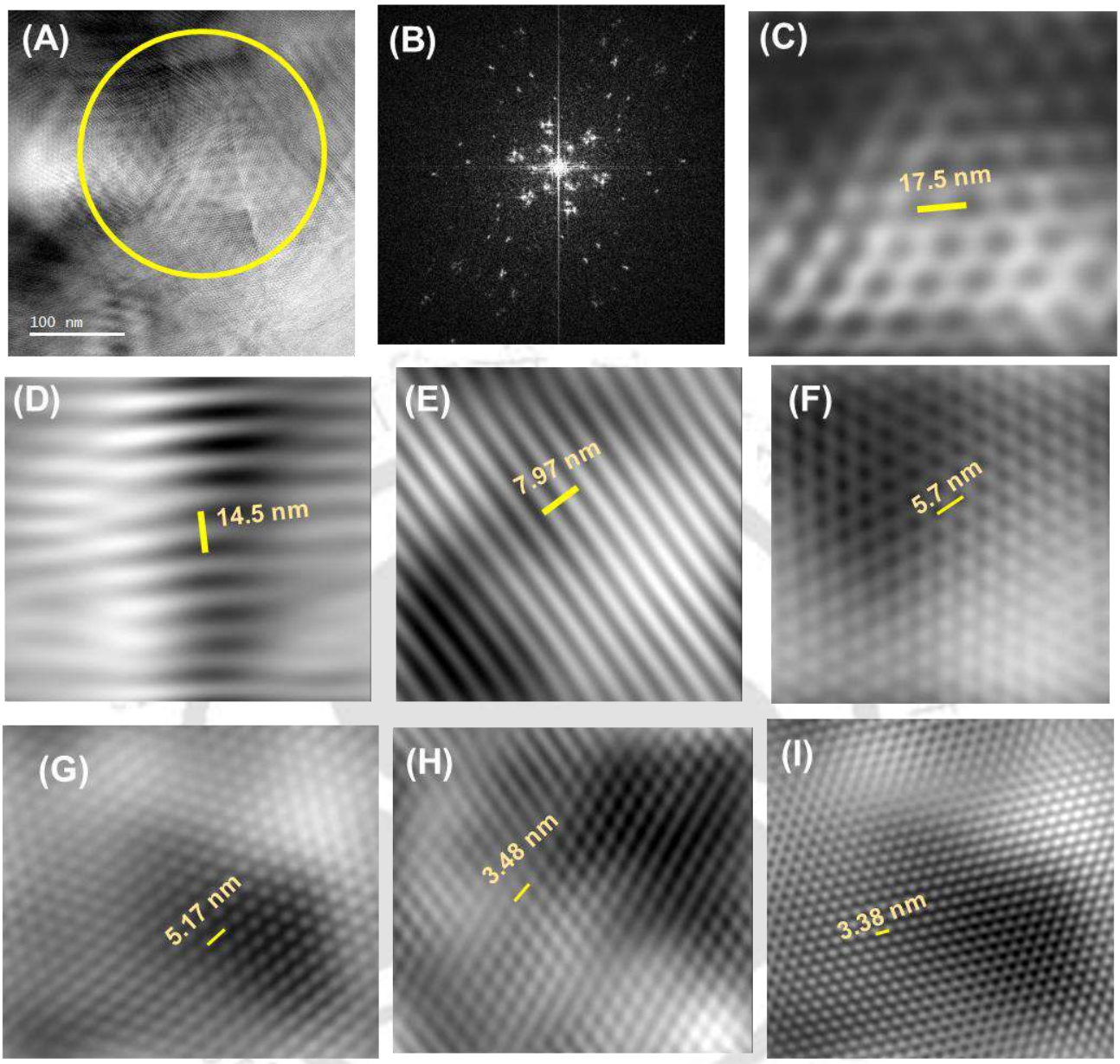

Figure S4. **(A)** TEM image of a moiré superlattices (same as in Figure 1F used here for further analysis). **(B)** FFT of the region encircled in yellow in (A). **(C)-(I)** Corresponding images as obtained after performing IFFT on the region circled in yellow in (A). (p.134)

SAED pattern and moiré periodicities

The moiré periodicities were obtained after performing Fourier transform on Figure S4A and the twist angles for the resulting periodicities were calculated using the following equation

$D = d/(2\mathrm{Sin}(\theta/2))$ …… S1

where d is the lattice constant taken as 0.46 nm, D is the moiré periodicity and θ is the twist angle between two sheets. The FFT of the moiré superlattice is presented in Figure S4B and the moiré periodicities obtained after performing IFFT are presented in Figure S4C-I. The angle between two consecutive sheets was on an average less than 10° as calculated from SAED pattern. These values were compared to twist angles calculated using equation S1 and presented in Figure S5A where it was observed that the experimental twist angles (Figure S5B) matched well with the calculated values. When multiple sheets, having a hexagonal diffraction pattern, are twisted-stacked, the resulting diffraction pattern would resemble Figure S5B-C where each hexagon (marked with different color in Figure S5C) are rotated at a particular angle with respect to the previous one. In the given example, 11 nanolattices (with hexagonal diffraction) were present and twisted at angles with respect to the immediate neighboring lattice as mentioned in Figure S5B.

The d-spacing value corresponding to the first circle of the SAED pattern of the moiré superlattices was 0.21 nm. It was observed that some of the spots corresponding to particular hkl planes were missing when compared with SAED pattern of the 2D lattice (Figure S5D). The planes marked with yellow circles were observed in the SAED pattern of moiré superlattices. Upon analyzing the hkl planes, it was observed that the planes following the set of rules: h+l = even and h and l = even appeared in the SAED pattern of the moiré superlattices. Thus, the planes that did not follow the above-mentioned rule were absent from the diffraction pattern of the moiré superlattices.

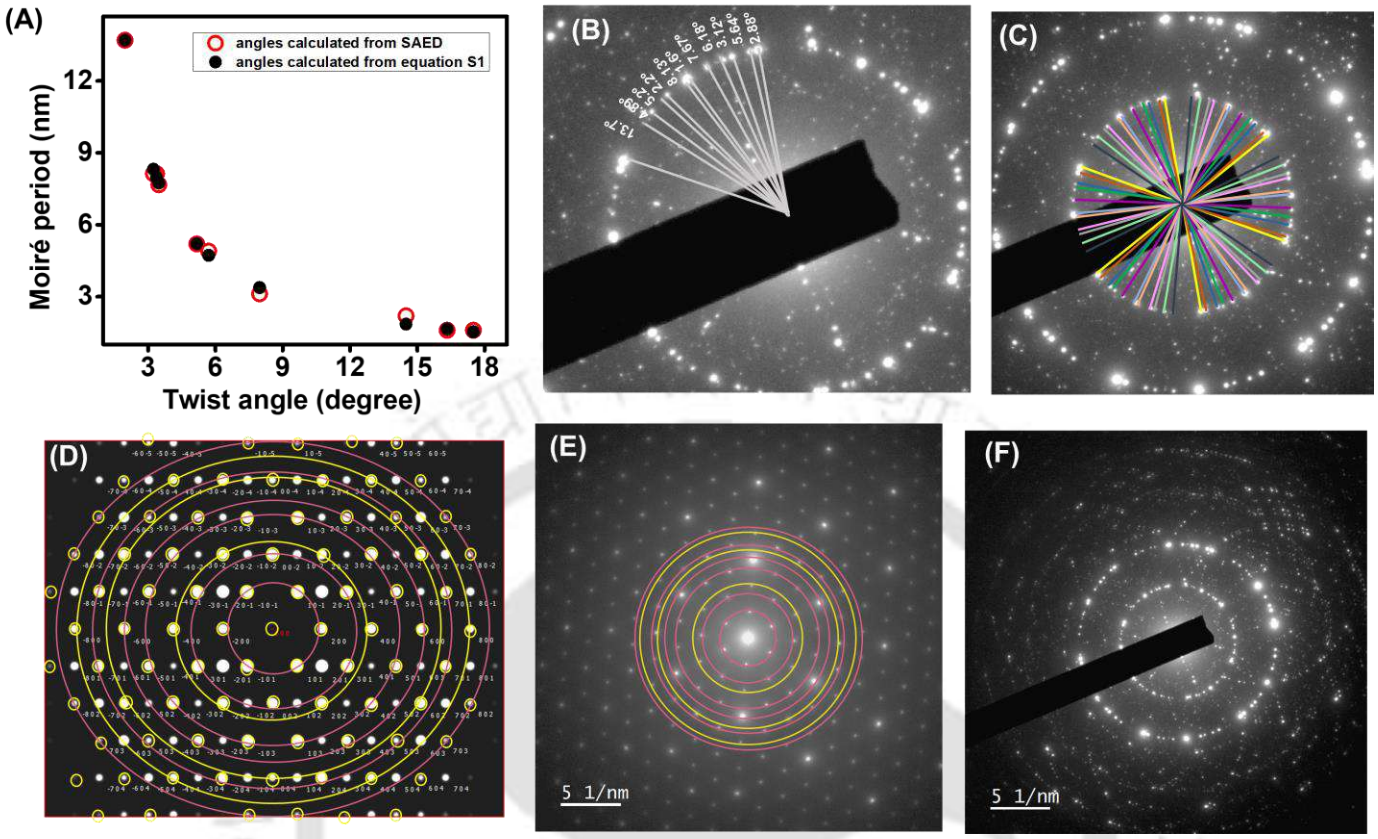

Figure S5. **(A)** Plot of moiré period vs twist angle where the comparison between the twist angles as obtained from the SAED pattern (marked with open red circles) and the twist angles as calculated using equation S1 (marked with closed black circles) after analyzing Figure S4 is shown. **(B)** Twist angles between two consecutive sheets as calculated from the SAED pattern. **(C)** A set of eleven hexagons are stacked twisted at particular angles where the respective colors represent a hexagon obtained for a particular sheet. **(D)** Simulated and **(E)** experimental SAED patterns of p-PD crystal where the observed planes in the **(F)** SAED of moiré superlattices are marked in yellow and those which were absent are marked in red. (p.134)

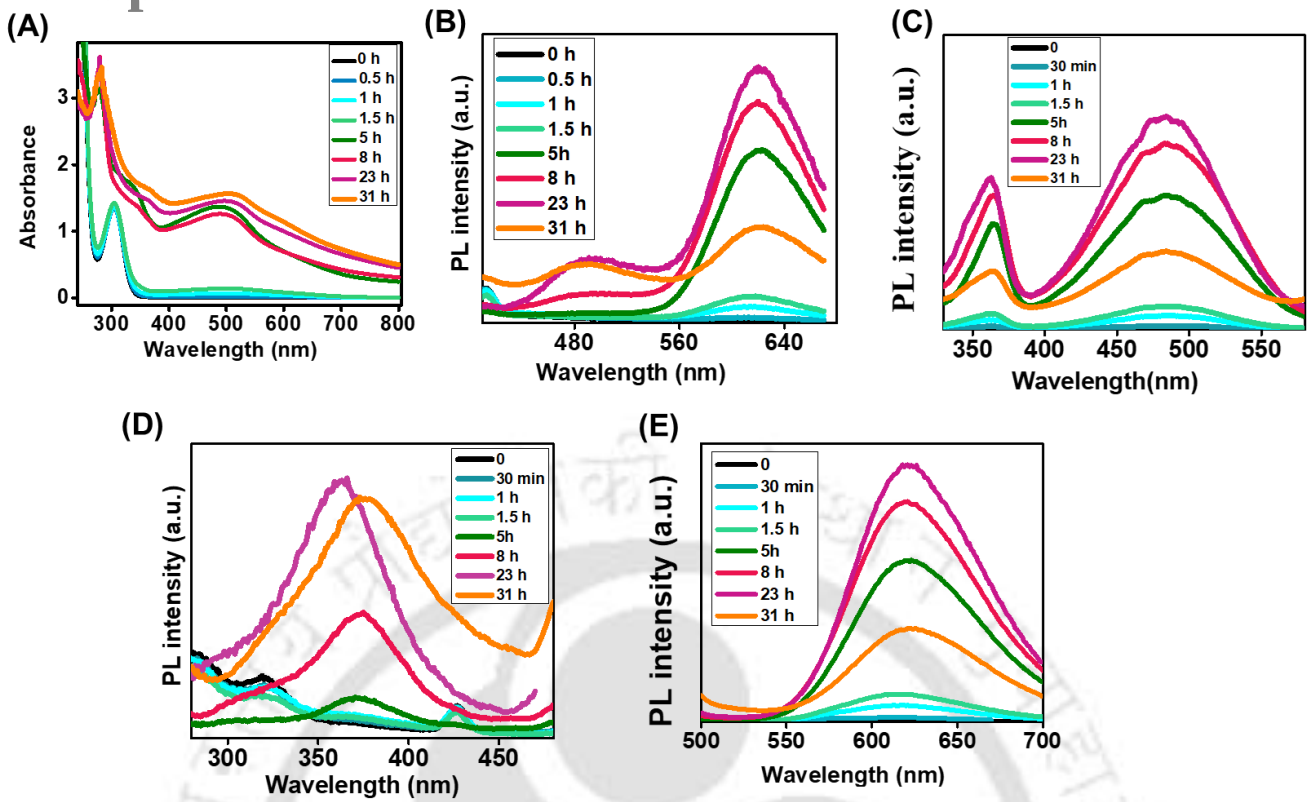

Figure S6. Time dependent **(A)** UV-Vis spectra, **(B)** emission spectra (λ_{ex} = 365 nm), **(C)** excitation spectra (λ_{em} = 600 nm), **(D)** excitation spectra (λ_{em} = 500 nm) and **(E)** emission spectra (λ_{ex} = 480 nm) recorded at respective reaction times – as mentioned in the legends - for an aqueous solution of p-PD. (p.135)

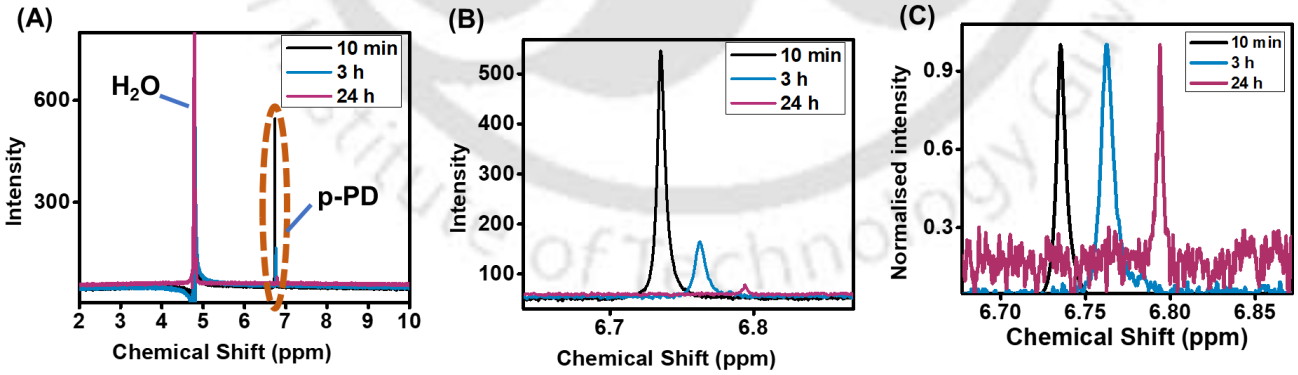

Figure S7. (A) NMR spectral chemical shift of p-PD at different time intervals ranging from 2-10 ppm showing two peaks at 4.79 ppm for H_2O and ~ 6.7 ppm for p-PD. **(B)** Chemical shift of p-PD showing downfield shift as the reaction progressed. **(C)** Normalized NMR spectra ranging from 6.6- 6.9 ppm.(p.136)

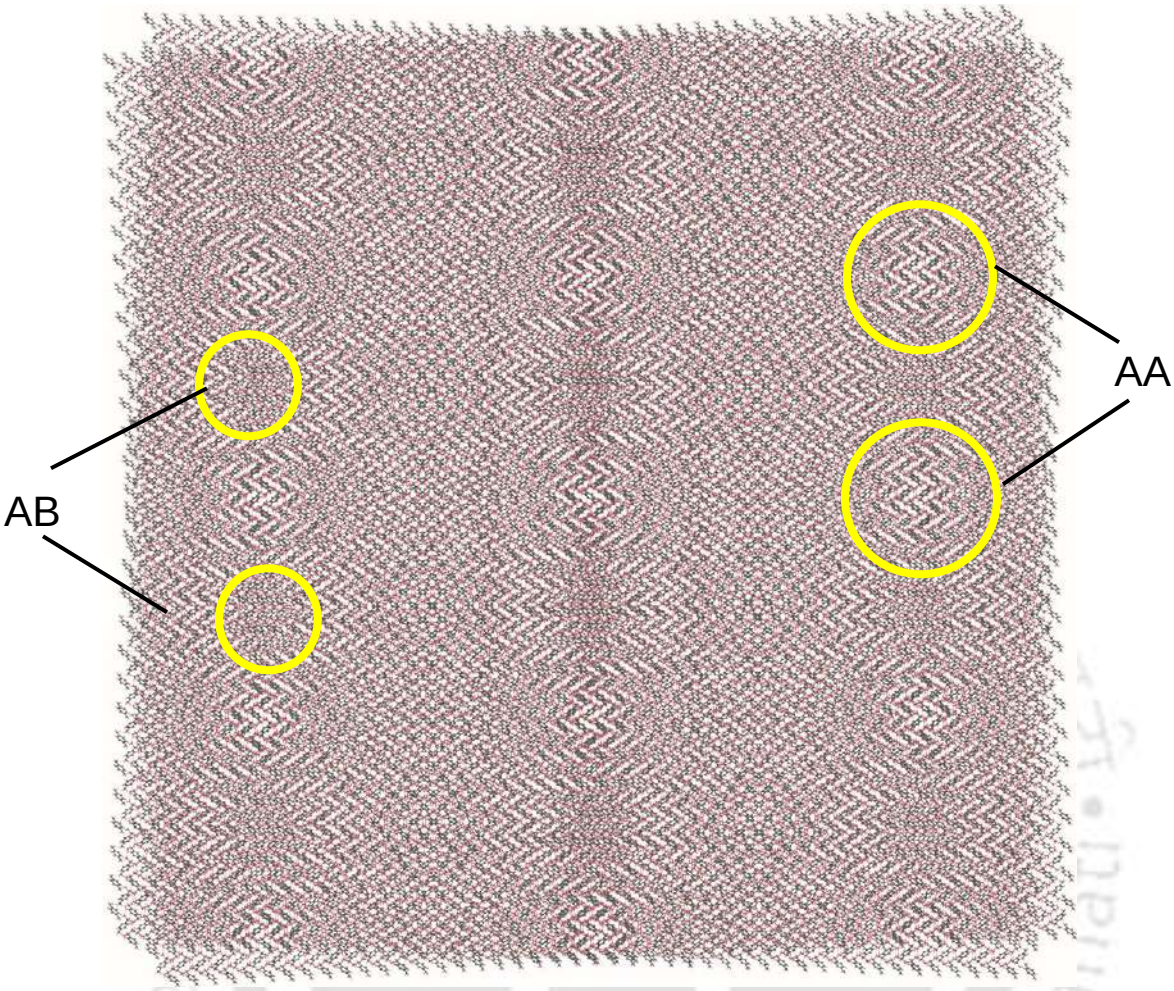

Figure S8. Molecular arrangement of p-PD in the moiré superlattices when viewed through b-axis showing AA and AB arrangement. (p.136)

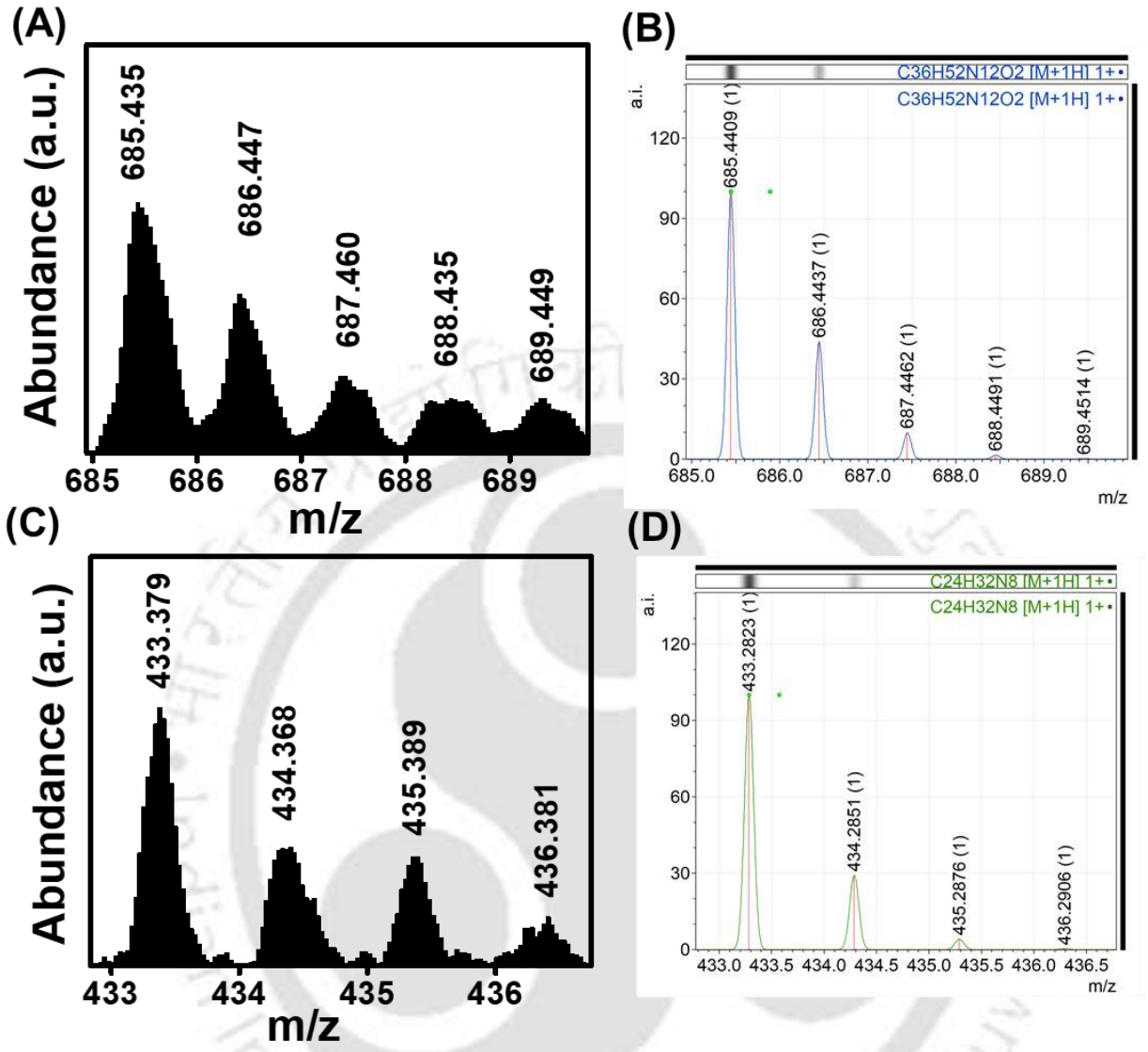

Figure S9. **(A)** MALDI-TOF mass spectrum of dispersion obtained after 18 h of reaction representing the product $[(C_6H_8N_2)_5(H_2O)_8 + 1H^+]$ having m/z = 685.43 and **(B)** the corresponding simulated mass spectrum. **(C)** MALDI-TOF mass spectrum of dispersion obtained after 18 h of reaction representing the product $(C_6H_8N_2)_4 + 1H^+$ having m/z = 433.37 and **(D)** the corresponding simulated mass spectrum. (p.136)

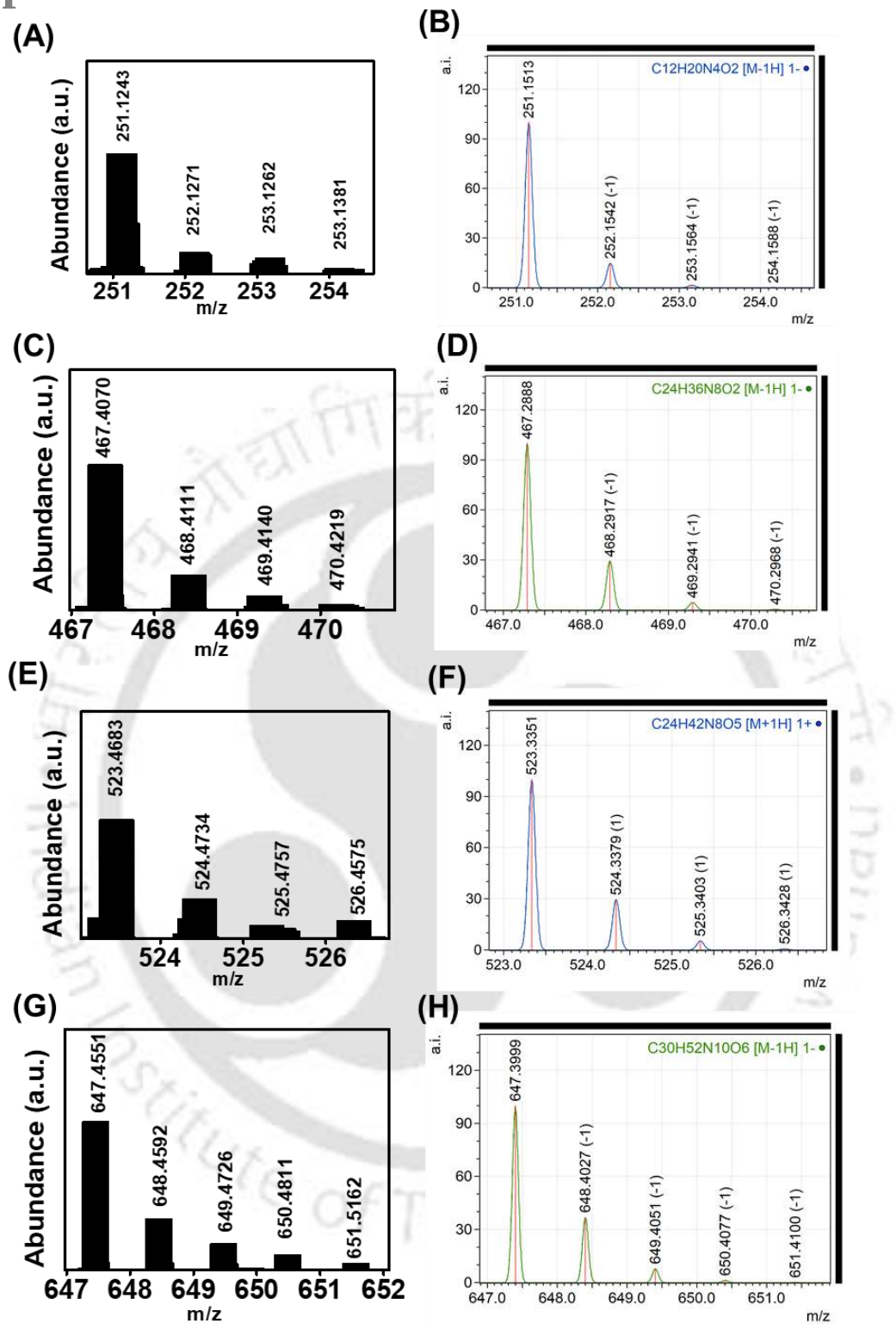

Figure S10. **(A)** ESI-MS of dispersion obtained after 18 h of reaction representing the product $[(C_6H_8N_2)_2(H_2O)_2 - 1H^+]$ having m/z = 251.12 and **(B)** the corresponding simulated mass spectrum. **(C)** ESI-MS of dispersion obtained after 18 h of reaction representing the product

$[(C_6H_8N_2)_4(H_2O)_2 -1H^+]$ having m/z = 467.40 and **(D)** the corresponding simulated mass spectrum. **(E)** ESI-MS of dispersion obtained after 18 h of reaction representing the product $[(C_6H_8N_2)_4(H_2O)_5 +1H^+]$ having m/z = 523.46 and **(F)** the corresponding simulated mass spectrum. **(G)** ESI-MS of dispersion obtained after 18 h of reaction representing the product $[(C_6H_8N_2)_6 -1H^+]$ having m/z = 647.45 and **(H)** the corresponding simulated mass spectrum. p.136

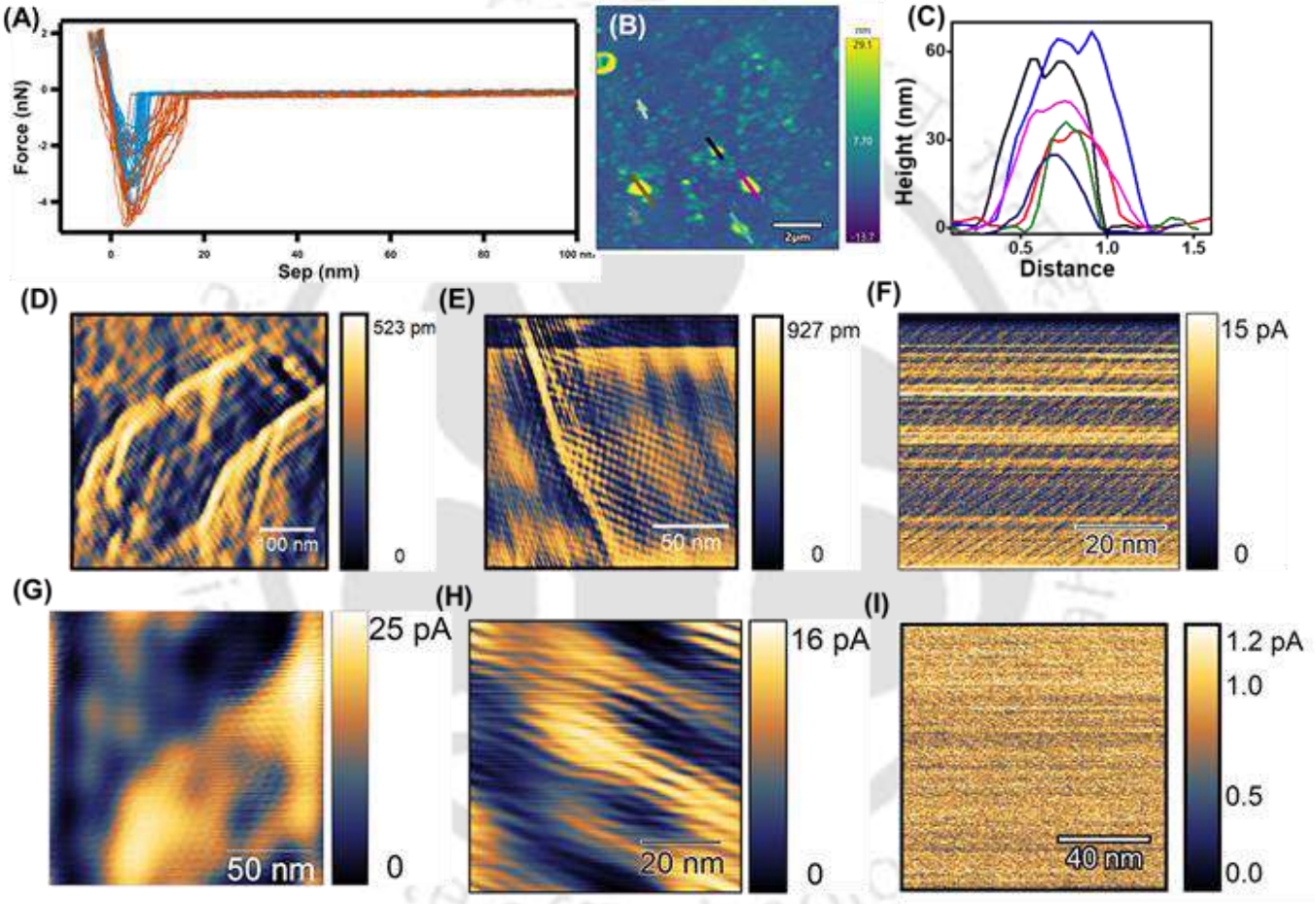

Figure S11. (A) Force–distance curves (30 in number) measured on several moiré nanosheets. **(B)** AFM topographic image of p-PD moiré nanosheet from which the **(C)** height profile of sheets were obtained. **(D)** and **(E)** Additional AFM images (done in tapping mode) showing moiré pattern reconstructed using Fourier transform analysis of the amplitude images. **(F)** The current mapping of the moiré superlattices from which the analyzed IFFT and FFT data are presented in Figure 2C and 2D in the article, respectively. **(G)-(H)** Additional current mapping

images of the neutral moiré superlattices as recorded using c-AFM. **(I)** A typical current mapping image of the 2D nanolattice as recorded using c-AFM. (p.137)

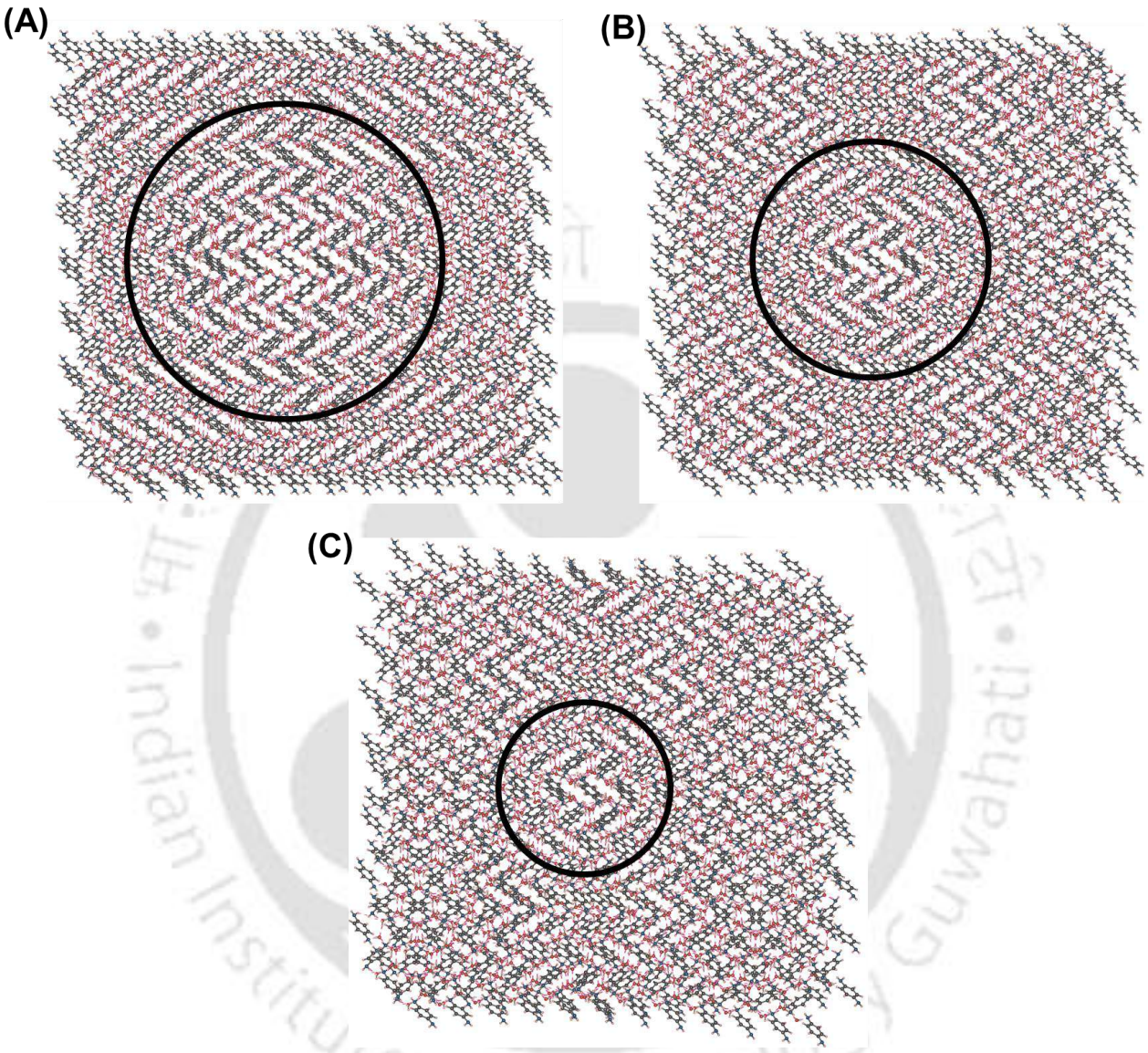

Figure S12. Moiré superlattices depicting AA region (marked by black circles) formed by the twisted stacking of 2D nanolattice of p-PD for twist angles **(A)** 3 degrees, **(B)** 6 degrees and **(C)** 9 degrees. (p.138)

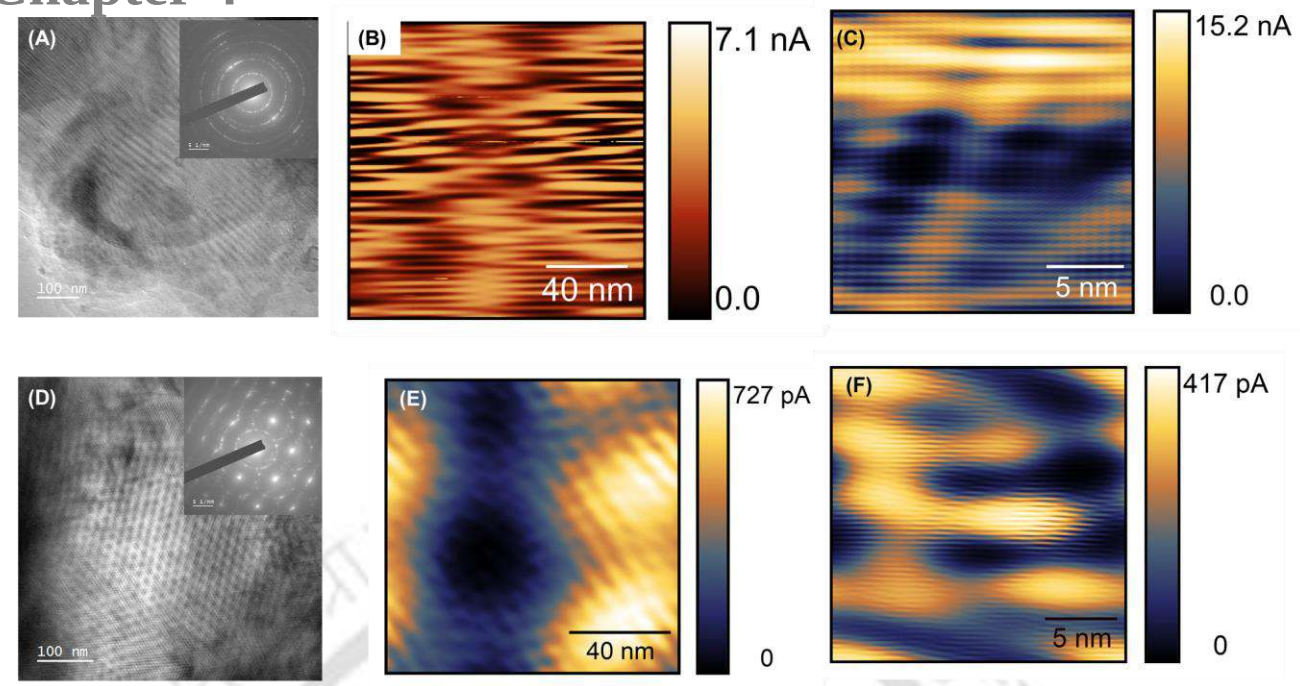

Figure S13. (A) TEM image showing the presence of moiré superlattices after changing the pH of the dispersion medium to 2.5 at 24 h reaction. **(B)** and **(C)** Additional AFM images of protonated moiré superlattices reconstructed from current mapping performed on the moiré nanosheets using Fourier transform. **(D)** TEM image showing the presence of moiré superlattices after changing the pH of the dispersion medium to 11 at 24 h reaction. **(E)** and **(F)** Additional AFM images of the deprotonated moiré superlattices reconstructed from current mapping performed on the moiré nanosheets using Fourier transform. **Insets in (A) and (D)**: Corresponding SAED patterns. (p.138)

Fast Fourier transformation and reconstruction of moiré pattern from current mapping

Conductive AFM measures the overall conductivity or resistance of the sample as the c-AFM tip scans the sample in XY direction. The current map that we observe is the total effective current across the measured dimensions of the sample. However, the current flow may differ according to the resistance of each layer of the system. Here, as mentioned in the article, the moiré superlattices consists of different layers having different charge transport capacity. The overall current that we observe in the current map of the moiré superlattice is the sum of the tunneling current flowing through the 2D nanocrystal and the twisted interfaces between two 2D nanocrystals. The 2D nanocrystal, due to the presence of intervening water molecules, has higher resistance whereas at the interface lower resistance was observed due to the direct interaction of the p-PD molecules. The conductivity at the interfaces also varies depending on

the twist angle. Overall the conductivity at each layer varies depending on the carrier density and tunneling barrier as explained in the article and should be equal to the total conductivity as observed in the current map of the sample (Figure S14A).

The moiré periodicities of a multilayered moiré superlattice can be deciphered from current mapping of the same using fast Fourier transform (FFT). In the FFT, a pair of spots corresponds to a particular moiré periodicity (or twist angle) having a corresponding conductivity (Figure S14B). The reconstruction of the moiré superlattices (Figure S14C) after Fourier transformation helps decipher each moiré periodicity showing current variations as observed in the AA and AB regions of that moiré pattern. A line drawn through the moiré period (Figure S14D-F), thus, results in a sinusoidal curve as observed in Figure 2E of article where the current variation is shown for the AA and AB regions. Again, for each moiré period, tunneling current varies according to the twist angle at the interface as observed from the graphs (Figure 2E of article). The current at each point of measurement is a sum total of currents flowing through the layers. However, the overall current cannot be deconvoluted into components for a point across the sample. On the other hand, once 2D mapping of the overall currents is obtained the component currents could be deconvoluted based on the moiré periodicity using FFT as mentioned above.

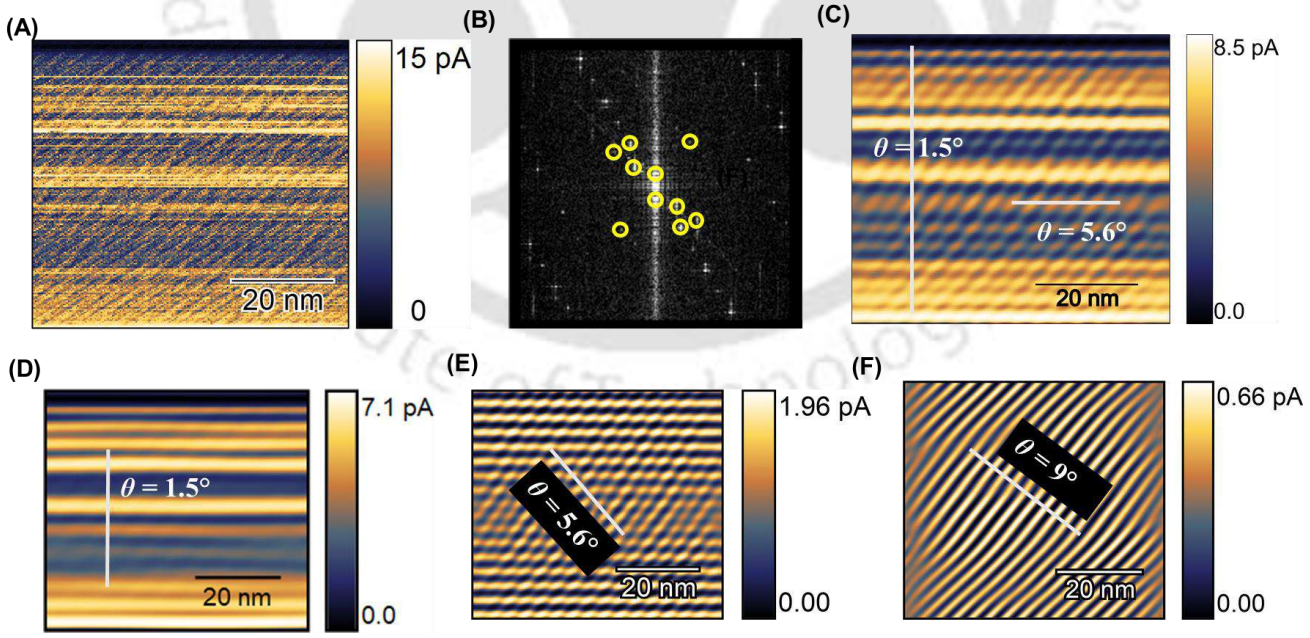

Figure S14. **(A)** Current mapping of the moiré superlattices (same as in Figure S11F used here for further analysis). **(B)** FFT of the current map in (A). **(C)** Corresponding images as obtained

after reconstructing the moiré superlattices after IFFT. **(D)-(F)** Reconstructed moiré superlattices after analysis of the FFT in figure (B) for θ = 1.5°, θ = 5.6° and θ = 9°.

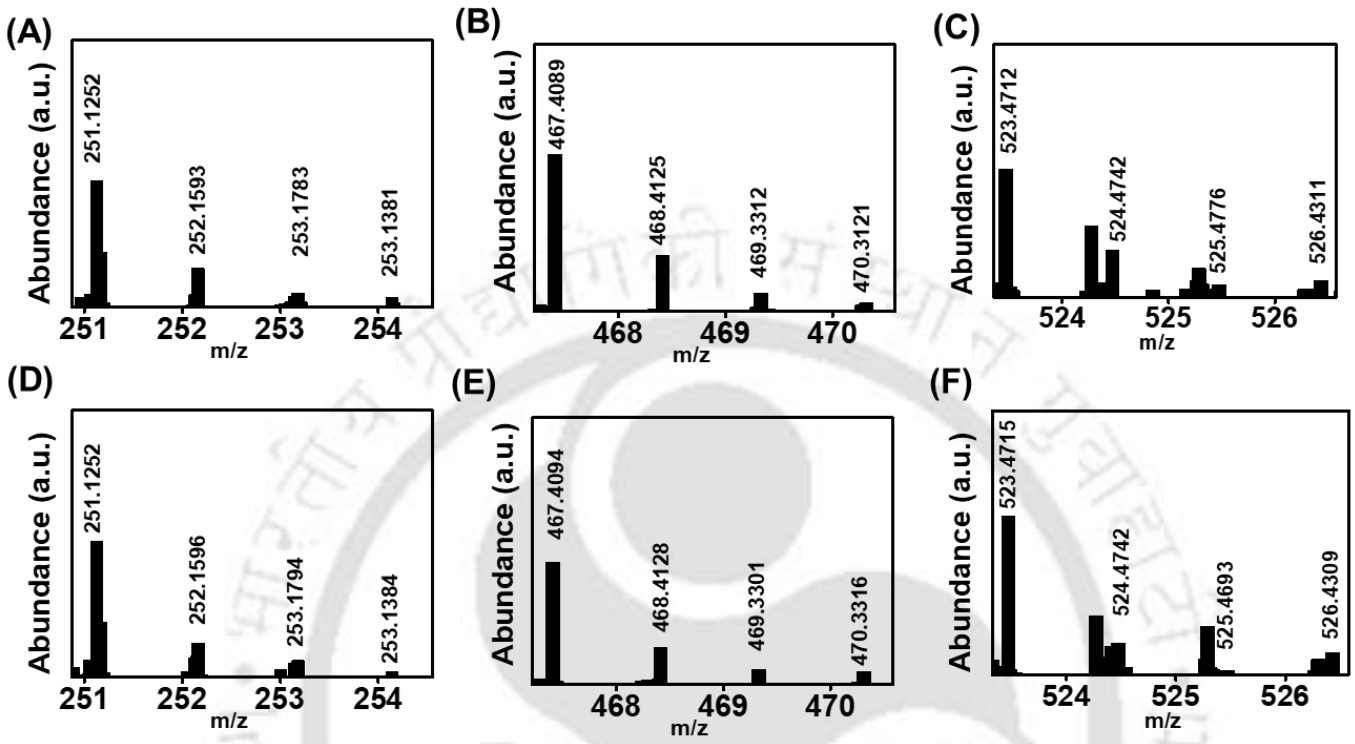

Figure S15. ESI-MS of dispersion obtained after addition of 40 µL 1M HCl solution to the dispersion containing moiré superlattices of p-PD representing the fragments having molecular formula **(A)** $(C_6H_8N_2)_2(H_2O)_2$, **(B)** $(C_6H_8N_2)_4(H_2O)_2$ and **(C)** $(C_6H_8N_2)_4(H_2O)_5$. ESI-MS of dispersion obtained after addition of 40 µL 1M NaOH solution to the dispersion containing moiré superlattices of p-PD representing the fragments having molecular formula **(D)** $(C_6H_8N_2)_2(H_2O)_2$**, (E)** $(C_6H_8N_2)_4(H_2O)_2$ and **(F)** $(C_6H_8N_2)_4(H_2O)_5$. (p.140)

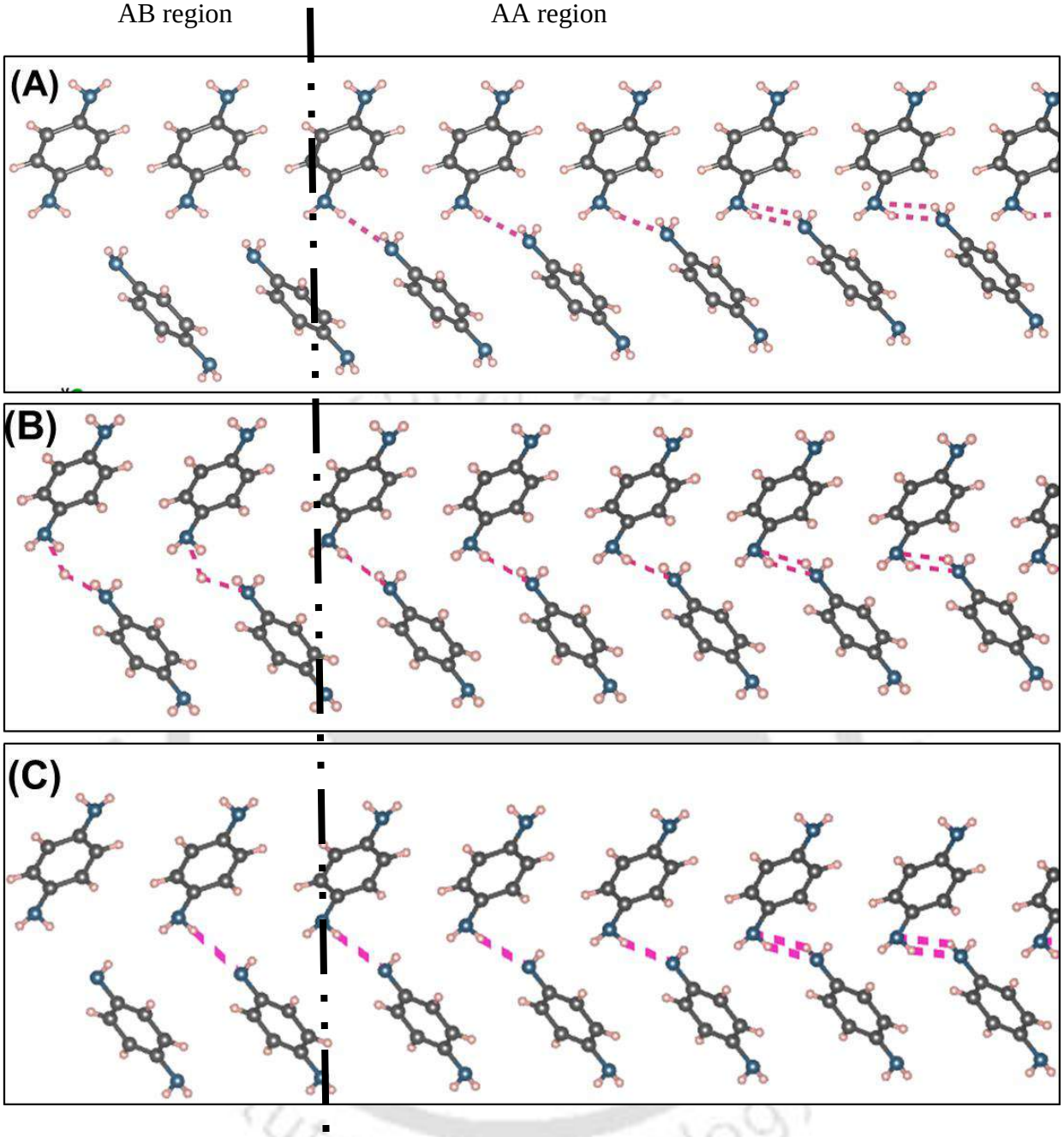

Figure S16. Description of H-bonding at the interfaces of **(A)** neutral superlattice, **(B)** protonated superlattice and **(C)** deprotonated superlattice. (p.140, p.141)

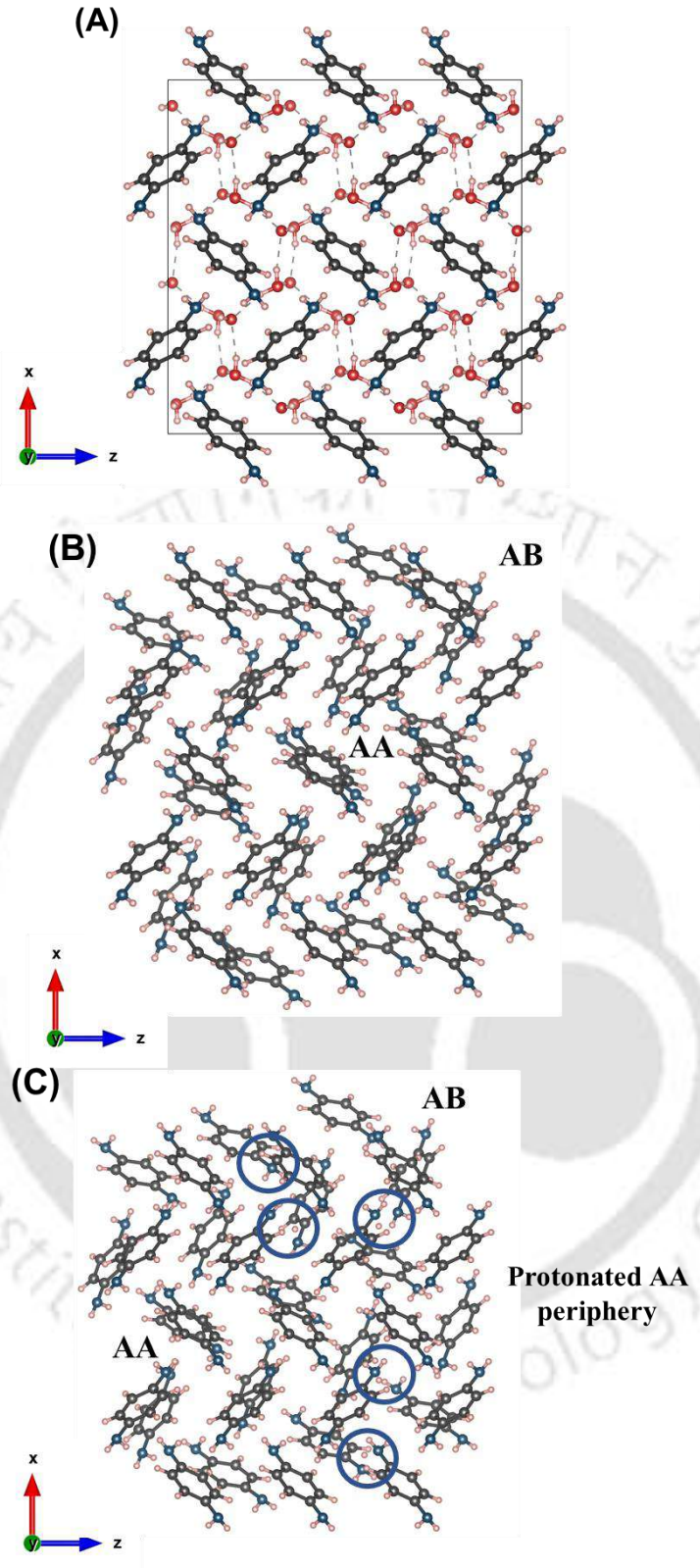

Figure S17. The calculation model for **(A)** 2D nanocrystal, **(B)** twisted (moiré) interface and **(C)** protonated twisted (moiré) interface. For the neutral and protonated twisted (moiré) interface the twist angle was set to 12°.

References

1. Seto, Y.; Ohtsuka, M., ReciPro: free and open-source multipurpose crystallographic software integrating a crystal model database and viewer, diffraction and microscopy simulators, and diffraction data analysis tools. *J. Appl. Crystallogr.* **2022,** *55* (2), 397-410.

2. Dey, U.; Chattopadhyay, A., Two-dimensional molecular moiré superlattices of tryptophan with visible photoluminescence for photo-activatable CO2 sensing and storage. *J. Mater. Chem. C* **2024,** *12* (15), 5506-5516.

Chapter 5: Chemical Reaction Based Precise Twist Angle Engineering of Molecular Moiré Superlattices for Spin Filtered Electron Transport

Chapter 5

Abstract

Programmed molecular assemblies have remarkably supported the growth of molecular intelligence, spintronics and quantum devices. An important challenge in spintronics is to fabricate chiral non-magnetic molecular assemblies as electron spin filter. Herein, we report the observation of chirality induced spin selectivity in spiral Zn-complexed molecular moiré superlattices of tryptophan. Importantly, complexation reaction of D/L-tryptophan precursor moiré superlattices with Zn^{2+} ions led the formation of new chiral superlattices with uniform periodicity based on precisely controlled twist angles. The presence of Zn in the superlattices not only increased the tunneling current but also resulted in nearly cent percent spin polarizability. Further, the observation of magnetic field strength dependent spin polarization in the electron transport across the moiré superlattices was rationalized based on change in the tunneling barrier as calculated from current-voltage curves. The increase in conductivity of the moiré superlattices was justified using density functional theory.

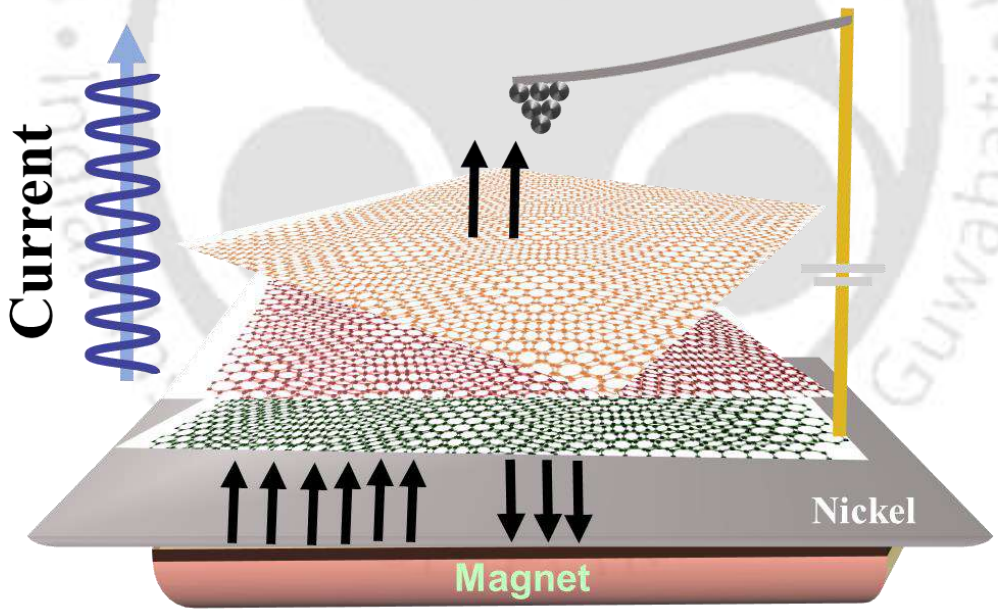

Scheme 1. Graphical representation showing spin selective electron transport through moiré superlattices of Zn-trp.

Chapter 5

Introduction

Molecule-based electronic devices may be able to address the challenges of resolution and complexity of circuits through the precise arrangements and versatile bonding of atoms, forming a network of interconnected components that work in concert. Thus, while single-molecule devices[1-2] offer high resolution, assembly of molecules[3-4] supplement complexity based on the hierarchy of organizations. In this regard, atoms and their bonding in three dimensions in single molecules decide the nature of mass transport and orientations of spins essential for building complex circuits.[5-6] On the other hand, intermolecular interactions in assembled molecules are key to the design of hierarchy and robustness of performance.[1-4] Further, polymers[7] and biomolecules such as DNA[8] and RNA[9] offer additional perspectives based on the nature of bonding and chirality. The recent progress in the synthesis of crystalline hierarchical structures through molecular engineering has opened up new opportunities for device fabrication. The advancements have the potential to revolutionize molecular electronics,[1-4] quantum information processing,[10] spintronics,[11] and quantum devices.[12-13]

An important class of matter that offers significant opportunities in this regard and is of current interests is the two-dimensional (2D) crystalline materials.[14-16] While atomic thin single layers offer strong electron confinements and enhanced mobilities,[17-18] their stacked formats enhance the application potential in electronic and quantum device fabrications.[19-21] Recent experiments suggest that angular stacking of 2D atomic or molecular crystals results in moiré superlattices with novel electronic properties that are strongly correlated with the twist angles.[22-24] Thus, multilayered molecular moiré superlattices have been used for CO_2 sensing and storage,[25] and pH and twist-angle dependent quantum tunneling across the layers,[26] They also exhibited altered electron spin resonance in hierarchically organized assembly.[27]

Physical methods of organizing stacked assemblies of 2D crystals, such as those of graphene, hexagonal boron nitride and metal chalcogenides, involve mechanical alignments of the layers with consistency and precision of the angles.[28-29] On the other hand, the chemical methods usually generate multilayered assembly lacking control over the angles of twists.[25-27,30-31] An important step towards this would be to successfully stack the nanolattices at a precise angle sequentially so that a uniform chiral structure is formed. Such structures may be useful in chirality induced spin selectivity[32-33] (CISS) in electron transport across superlattices with high

spin polarizability. Observation of CISS in chiral single molecules,[34] supramolecular assemblies,[35] quantum dots,[36] perovskites,[37] inorganic crystals,[38] and in 2D systems such as chiral molecules intercalated between transition metal dichalcogenides,[39] chiral metal organic framework,[40] and crystals of metal-coordinated chiral organic ligand[41] also supports the importance of spin-selective electron transport across the superlattices. Further, theoretical studies indicate that high spin polarizability (>50%) can be attained at large twist angles even just for two twist-stacked monolayers of $MoTe_2$.[42]

One way of achieving such well-defined chiral structure is possibly through chemical reactions of multilayered moiré superlattices with varying twist angles, leading to reorganization of the lattices into twisted stacking at uniform angles. Our recent results suggest that such a structural transformation may indeed be possible through reaction in the liquid medium. For example, treating moiré superlattices of tryptophan (trp) with alkali enhanced their photoluminescence intensity,[25] and acid-base reaction of p-phenylenediamine resulted in 2-3 orders of magnitude increase in the interfacial conductivity.[26] On the other hand, intercalated Zn^{2+} ions in Zn-phthalate moiré superlattices was removed using 8-hydroxyquinoline-5-sulfonic acid leading to 2D nanosheets, which could be again converted into moiré superlattices with addition of Zn^{2+} ions.[30]

Herein, we report achieving a precise control over the twist angle in molecular moiré superlattices of trp through complexation reaction with Zn^{2+} ions. A twist angle of 2.5 ± 1.0° between two successive lattices was formed following complexation. The chiral nature of the moiré superlattices allowed the magnetic field-dependent spin-selective electron transport through quantum tunneling. Importantly, the resultant superlattices displayed CISS with a very high spin polarizability of 98.0 ± 1.5% at 0.5 V under a magnetic field strength of 0.45 T. Analytical experiments supplemented by the simulated density of states (DOS) and charge density calculations helped rationalize the results.

Results and Discussions

Zn-complexed moiré superlattices of trp (Zn-trp moiré) were synthesized through reaction between the molecular moiré superlattices of trp and $ZnCl_2$ (refer Experimental Section). The emergence of a UV-vis absorption peak at 362 nm (Figure 1A, Figure S1A), and an emission peak at 452 nm (Figure 1B, Figure S1B), after 24 h of reaction, indicated the formation of moiré

superlattices of trp through H-bonding.[25,43-44] Following interaction with Zn^{2+} ions, a slight (~1 nm) blue shift at 290 nm (the peak of trp) suggested an interaction with the molecules, while the peak at 362 nm remained unchanged. In the photoluminescence (PL) spectra, a blue shift of about 4 nm with simultaneous decrease in intensity was observed, indicating that the H-bond network within the superlattice might have been partially broken due to complexation with Zn^{2+} ions.

The transmission electron microscopy (TEM) images and corresponding selected area electron diffraction (SAED) patterns (Figure 1C-D and Figure S2A-B) for samples collected after 24 h of reaction confirmed the formation of multilayered moiré superlattices (having lattice parameter 0.2 nm and multiple twist angles with a range of values 1-10˚ observed in the SAED) of D/L trp. However, similar studies following addition of Zn^{2+} ions (Figure 1E-F) revealed the formation of moiré superlattices with precisely controlled twist angle of 2.5 ± 1.0° between two consecutive nanolattices with a changed lattice parameter of 0.54 nm, as presented in the Supporting Information (Figure S3 and related texts).

Previous report[25] of the twisted stacking of multi-layered crystalline trp nanosheets suggested the formation of spiral moiré superlattices. Therefore, chiral properties of the assemblies were studied. Circular dichroism (CD) spectra (Figure 1G-H, Figure S4) substantiated the chiral nature of the precursor moiré superlattices and Zn-trp moiré where the chirality of the individual molecule after its assembly remained unaffected. A 50 nm blue shift and more intense negative ellipticity at 650 nm observed following addition of Zn^{2+} ions (refer Supporting Information) suggested a change in the spiral nature of the precursor L/ D-trp moiré superlattices. It may be mentioned here that Zn-trp moiré having precise twist angle with controlled stacking was formed only after reaction of the multilayered moiré superlattice of trp with Zn^{2+} ions (refer Supporting Information, Figure S5). The precursor superlattices were formed after twisted stacking of the crystalline 2D nanolattices of trp through hydrophobic and hydrophilic (H-bonding) interactions. The addition of Zn^{2+} ions partially affected the H-bond network with the formation of covalent bonds involving O and N of COOH and NH_2 groups that had previously participated in H-bonding that was further supported by ^1H NMR spectroscopic measurements (refer Supporting Information, Figure S6, Table S1 and related texts).

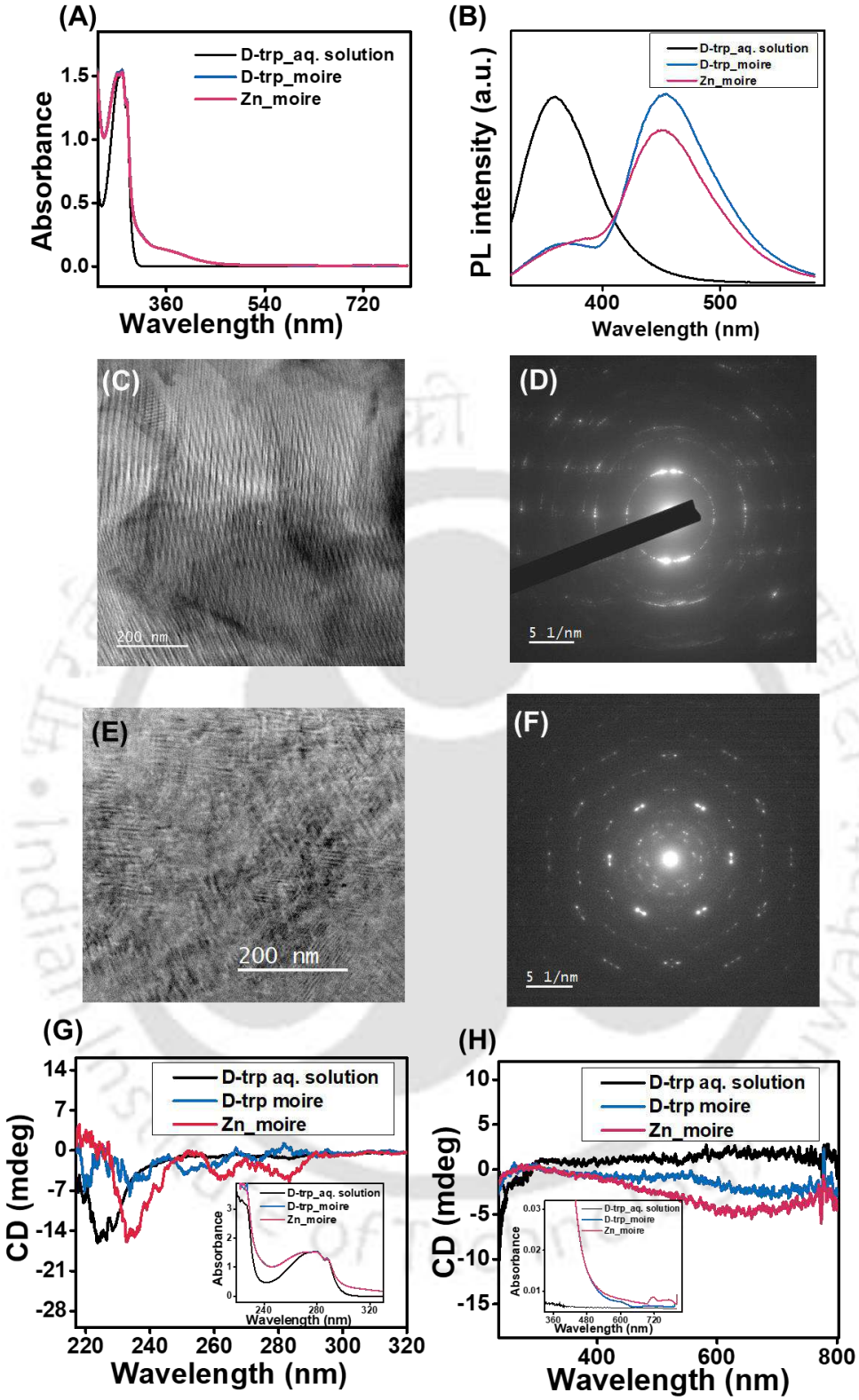

Figure 1. (A) UV-Vis spectrum and **(B)** PL spectrum ((λ_{ex} = 300 nm) of an aq. solution of D-trp, dispersion containing moiré superlattices of D-trp and Zn-complexed moiré superlattices of D-trp. **(C)** TEM image of a moiré superlattice of D-trp. **(D)** SAED pattern corresponding to the

image in (C). **(E)** TEM image of Zn-complexed moiré superlattice of D-trp. **(F)** SAED pattern corresponding to the image in (E). CD spectra **(G)** for the range 210 – 310 nm and **(H)** 310 – 800 nm of an aq. solution of D-trp, dispersion containing moiré superlattices of D-trp and Zn-complexed moiré superlattices of D-trp with insets displaying the UV-Vis spectra for the respective ranges.

Based on these observations, a structure was proposed that was optimized using Avogadro software where the Zn^{2+} ions formed bonds with O and N of molecule marked as 1 and with O of COOH group of molecules marked as 2 and 3 from the next layer of the precursor moiré superlattice (Figure 2). Thus, there was a reorientation of trp molecules within the superlattice to achieve the tetrahedral geometry. This resulted in the rotation of one layer of trp molecules with respect to the consecutive layer to a certain angle throughout the precursor superlattice that was favored for the tetrahedral geometry as can be observed in Figure 2 and Figure S7. The angle of rotation between two stacked lattices was about 3˚ in the optimized structure that is close to the 2.5˚ twist angle observed from the SAED pattern.

Further, the SAED patterns confirmed the crystalline nature of the Zn-trp moiré, with a newly ordered arrangement following Zn^{2+} ion insertion and reorientation within the structure, where the new lattice parameter 0.54 nm (lighter spots) was observed in addition to 0.3 nm (brighter spots) that was present in the original lattice of trp. While viewing the optimized structure through c axis, a hexagonal arrangement for the Zn atoms within the lattice was observed and the spacing between the lattice planes passing through them was 0.56 nm (Figure 2, Figure S7C), comparable to 0.54 nm observed in the SAED pattern. Further the rotation of the molecular layer resulting from Zn-complexation facilitated the movement of the molecules to help achieve the tetrahedral geometry and thus, twisted the layers to the particular angle of 2.5 ± 1.0°. A reordering was followed throughout the superlattice that might have also forced the original face-to-face aromatic interfacial interaction in moiré superlattices to undergo change.

It can be observed in Figure 2 that the number of twists was more than double in the Zn-trp moiré as compared to the precursor superlattice for almost same length (along the axis perpendicular to the stacked 2D lattices). So, a higher number of stacked-twisted layers were anticipated in the Zn-trp moiré; however, the diffraction spots (Figure 1F) suggested that following complexation the number of the twisted layers was restricted to 3-4 as compared to the

many layers (~7-13) of the precursor superlattices. This indicated a transition from uncontrolled to controlled stacking in Zn-trp moiré, which was also confirmed from the atomic force microscopy (AFM) height measurements (Figure S8), probably caused due to angle restraints after complexation. Thus, all the experimental results suggested that the superlattices were modified through complexation reaction with Zn^{2+}, resulting in rearrangements of molecules within the lattices and thus generating new diffraction planes (Figure 2).

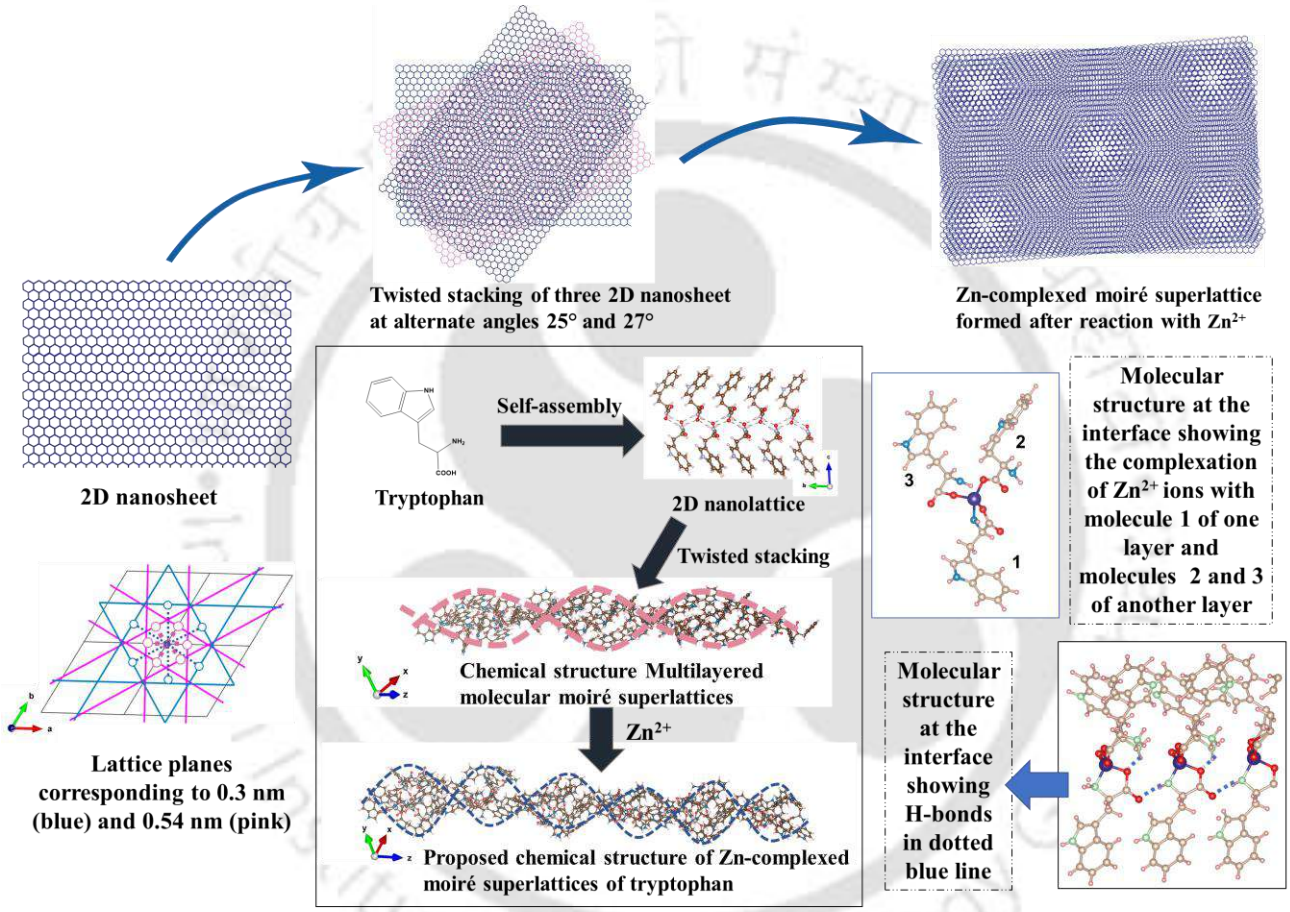

Figure 2. Schematic representation showing the self-assembly of tryptophan molecules into moiré superlattices that were further reacted with Zn^{2+} ions leading to the final superstructure. The optimized structures of a section of moiré superlattices of trp and Zn-trp moiré are presented here displaying a spiral configuration.

The spin-selective electron transport properties were studied using magnetic-conductive atomic force microscopy (mc-AFM) where Zn-trp moiré were deposited on a ferromagnet (nickel) that served as one electrode.[32,46] Current-voltage (I-V) curves of the moiré superlattices

(Figure 3, Figure S9) were recorded in contact mode while varying the magnetic field strengths. The current through a chiral system having its spin orientation parallel to the direction of electron's velocity was termed $I_{parallel}$, while that with antiparallel orientation was termed $I_{antiparallel}$.[45] The percent spin polarization was calculated from the I-V curves (Figures 3A, 3D and S10) using equation 1 and the maximum value obtained was nearly cent percent (Figure 3E).

$$\text{Spin polarization} = (I_{parallel} - I_{antiparallel})/ (I_{parallel} + I_{antiparallel}) \quad (1)$$

For both magnetization directions (north pole up or down), the I-V curves at different magnetic field strengths (Figure 3) indicated the occurrence of spin-filtered electron transport (Figure 3E-F) where the magnitude of the current was higher when the sample-containing electrode was magnetized with magnet's north pole pointing down (mag-down), as compared to when it was pointed up (mag-up).

The variation of percent spin polarization from -1 V to 1 V in the presence of a magnetic field of 0.45 T (Figure 3F) showed a maximum value of 98.0 ± 1.5 %. Beyond this range, the current exceeded the instrument measurement threshold of 20 nA. Additionally, the percent spin polarization at 0.5 V for different magnetic field strengths revealed a sigmoidal relationship (Figure 3G). Magnetizing the nickel substrate alters the distribution of electrons into two sub-bands, one with majority spin electrons occupying lower energy levels and another with minority spin electrons occupying higher energy levels, with the magnetization direction dictating the predominant spin.[33,47] As observed, the magnitude of current for Zn-trp moiré, was higher for mag down, probably due to the majority electrons of the magnetized nickel having the favored spin orientation for transport while north pole pointing up resulted in majority electrons having the opposite spin that was less favored for transport. It may be mentioned here that though the multilayered molecular moiré superlattices of trp were chiral in nature, they exhibited no spin-selective transport (Figure S11). However, the incorporation of Zn^{2+} ions into the superlattices resulted in increased current magnitudes with higher magnetic strengths, suggesting a significant role of the precise twist angles of the moiré superlattices in obtaining a high spin polarizability.

The experimental findings can be explained by transient spin polarization induced by charge polarization - observed in chiral systems following bias application, which leads to one end of the chiral system being associated with one type of spin, while the other end is linked to the

opposite spin type.[32,48] This results in the preference for transport of one type of spin through one end of the chiral system and the opposite spin through the other end depending on the chirality of the system. The spiral arrangement of trp-Zn-trp molecules in the superlattice likely created a chiral field that might have induced a spin polarization accompanying the charge polarization. The I-V curves suggested that the magnetization, with north pole pointing down, oriented the electrons' spin of the substrate such that it aligned with the spin orientation associated with the end of superlattice that was attached to the substrate and was preferred for transport. For north pole up, the nickel would be magnetized with majority electrons having the opposite spin, which would, however, have opposite alignment to the spin designated with the end of the superlattice attached with the substrate and would thus be less favorable for transport.

Further it was observed that the measured I-V curves were symmetric in nature as the applied voltage ranged from positive to negative values. The results bore similarity to typical chiral systems that displayed CISS.[32-33] When the sample was negatively biased, the enhanced current would result from the transport of the favored spin from the majority sub-band of the nickel substrate through the chiral superlattices. Whereas when positive bias was applied, the opposite spin would be transported in the opposite direction through the superlattices (i.e., from the tip to the minority sub-band of the nickel consisting the opposite spins). Thus, a symmetric I-V curves would be observed i.e., for both the positive and negative biases the transport of the favored spin alignment was observed where a higher magnitude of current was noticed when magnetized with north pole pointing down. It may be mentioned here that similar spin polarization (Figure S12) values were obtained for both Zn-complexed moiré superlattices of L or D-trp, where the electron transport was higher when the substrate was magnetized with north pole pointing down as both these moiré superlattices had the same chirality as was evident from their CD spectra.

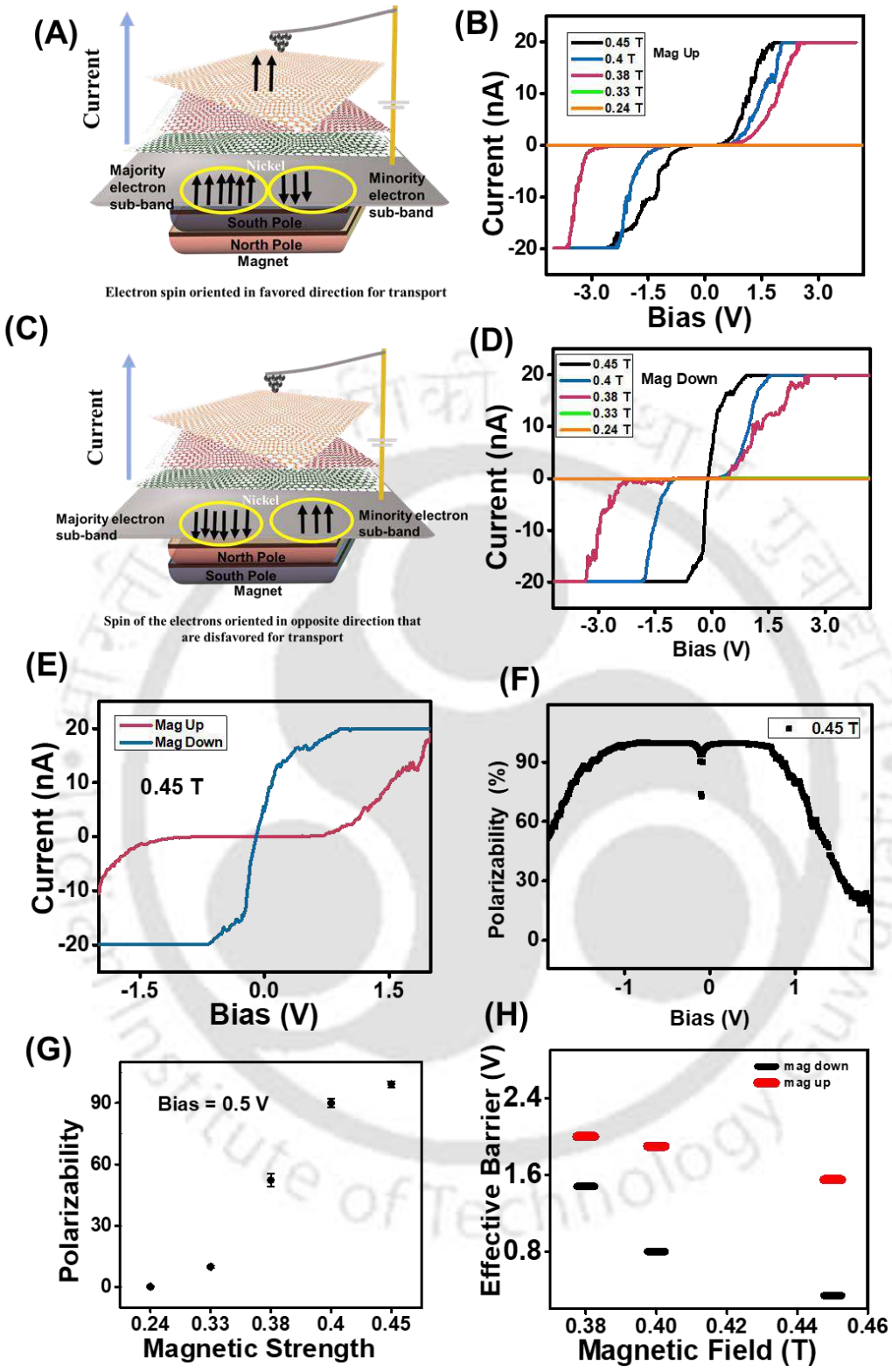

Figure 3. (A) Schematic representation of spin transport through Zn-trp moiré superlattices in the presence of magnetic field with the north pole of the magnet pointing up. **(B)** I-V curves for the corresponding orientation in Figure (A) for different strengths of magnetic field. **(C)**

Schematic representation of spin transport through Zn-trp moiré superlattices in the presence of magnetic field with the north pole of the magnet pointing down. **(D)** I-V curves for the corresponding orientation in Figure (C) for different strengths of magnetic field. **(E)** I-V curve obtained for mag-up and mag-down orientations for the magnetic field strength of 0.45 T **(F)** Plot of polarizability vs bias applied in presence of magnetic field 0.45 T. **(G)** Plot of percentage spin polarization at 0.5 V for magnetic fields ranging from 0.24 T- 0.45 T. **(H)** Tunneling barriers obtained from the dI/dV vs V plot (Figure S10) for magnetic field strengths of 0.38 T, 0.40 T and 0.45 T. The plot displays the increase in gap between tunneling barriers experienced by the two opposite spins.

Further the preference of one spin over another and the dependence on the external magnetic field strength for the electron transport could be justified by the tunneling barrier, calculated from dG (= dI/dV) vs V plot (Figure S10).[8] For the field strengths of 0.24 T and 0.33 T, the magnitudes of the current were comparatively less for both mag-up and mag-down and no sharp rise was observed for the differential conductance in the range -2 to 2 V. Thus, the values are not included in the barrier height vs applied voltage graph. When the magnetic field strength was increased, from 0.38 to 0.45 T, a decrease in the tunneling barrier starting with 1.48 V to 0.34 V was observed for mag-down whereas for mag-up, the decrease was from 2 V (for 0.38 T) to 1.55 V (for 0.45 T). This caused an increase in the tunneling probability as the strength of the magnetic field increased and thus, a rise in the current magnitude was observed. The results were similar to the negative magneto-resistance effect observed in organic materials like pentacene film and tetracene single crystal.[49]

Further it was observed that the decrease in barrier height for mag-down was more significant as compared to mag-up i.e., the tunneling barrier faced by the electrons when they were oriented in the preferred direction was low as compared to the high barrier that the unfavored electron spin had to overcome. This resulted in an increase in the gap between the tunneling barriers for the two opposite spins upon increasing the magnetic field (0.52 V for 0.38 T to 1.21 V for 0.45 T) and thus, leading to a facilitated electron transport of the preferred spin with a higher spin polarization value (Figure 3H). The observations helped conclude that increasing the magnetic field not only escalated the electron transport, but also facilitated spin-selective electron transport and the dependence plotted in Figure 3G was sigmoidal in nature.

The effect of magnetic field on the spin polarization and tunneling barrier was further confirmed when instead of ferromagnetic nickel, a diamagnetic copper substrate was used. A similar result was obtained where the electron transport was higher for mag-down orientation as compared to mag-up in presence of 0.45 T field strength. The spin polarization calculated using equation 1 was 55 ± 2.3 % for 0.45 T. It was less as compared to that for the nickel substrate; however, the results supported the preference of one spin over the other by the moiré superlattices for electron transport. This ascertained the role of the external magnetic field in the characteristics of the selective spin transport through the Zn-trp moiré (Figure S13).

Further, DOS calculations and charge density simulations were performed for the 2D nanocrystal of trp, twisted moiré interface of trp, and for the Zn-complexed twisted moiré interface. The DOS plots against $E - E_{Fermi}$ in Figure 4 indicated that the DOS near the fermi energy level for the twisted interface is higher as compared to that for the 2D nanocrystal. On the other hand, even higher DOS was present near the fermi level for Zn-complexed twisted moiré interface as compared to the unreacted twisted moiré interface. The results indicated that there would be a higher probability of electrons to be present near the fermi level for the Zn-trp moiré as compared to its 2D crystal and unreacted moiré superlattice counterparts and thus, would have higher conductivity and charge transport properties. The simulated carrier charge density was 10 times higher for Zn-trp moiré than its 2D crystal and unreacted moiré superlattice counterparts and thus, supported the experimentally observed higher conductivity for the Zn-trp moiré as compared with the unreacted moiré superlattices of trp.

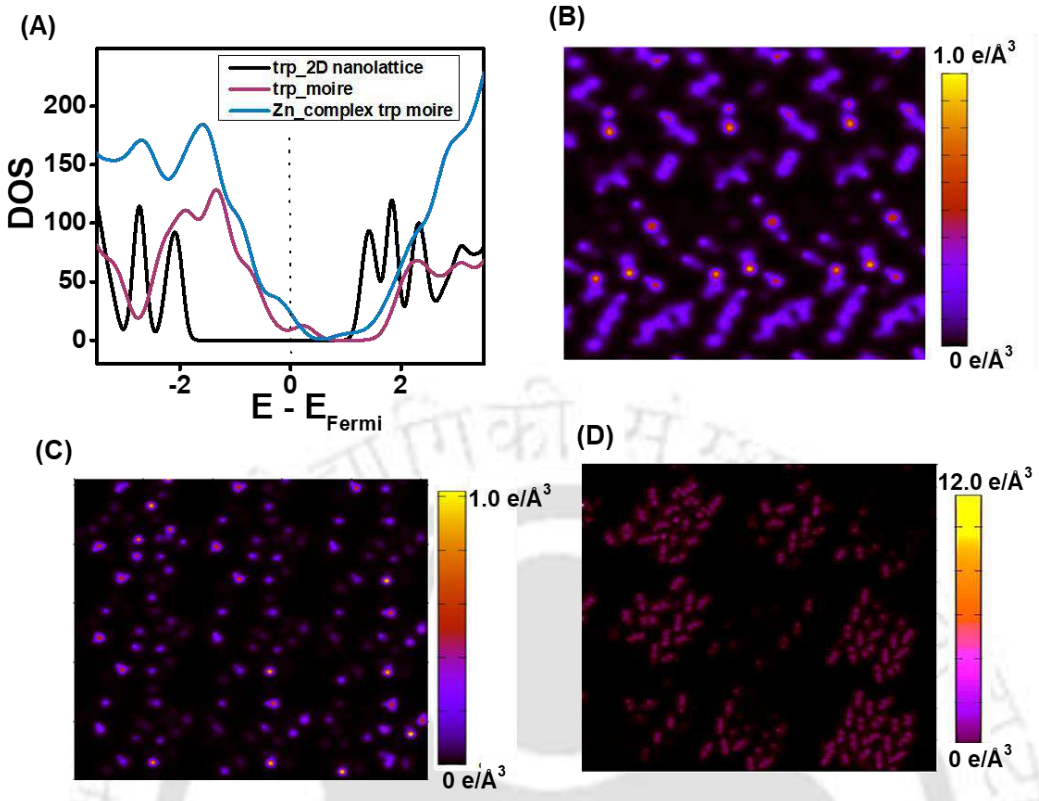

Figure 4. (A) Density of states plots for 2D nanocrystal, trp moiré interface and Zn-complexed moiré interface of trp. **(B)-(D)** Carrier charge density plots for 2D nanocrystal, trp moiré interface, and Zn-complexed moiré interface of trp, respectively.

Conclusion

In conclusion, we have synthesized Zn-complexed moiré superlattices of D/L-trp with a precise control over the twist angles that displayed a very high spin polarizability of 98.0 ± 1.5% at 0.5 V under a magnetic field strength of 0.45 T. The resulting moiré superlattices had a twist angle of 2.5 ± 1.0˚ between two successive lattices after a tetrahedron was formed through complexation of Zn^{2+} ions with trp at the interfaces. The CISS was observed in the chiral Zn-trp moiré and a high spin polarizability where a dependence on the magnetic field strength was observed for both L- and D-trp. The control over the twist angles in molecular moiré superlattices could provide uniformity in the physical and chemical properties especially for the multilayered superlattices and we believe that the selective spin transport properties displayed by these moiré superlattices could bring about new insights for the development of molecule-based spintronics devices, an important step toward quantum molecular devices.

Chapter 5

Experimental Section

Materials

D-tryptophan (trp, purity ≥ 98.0 % (HPLC)), L-trp (purity ≥ 98.0 % (HPLC)) and $ZnCl_2$ were purchased from Sigma-Aldrich and used without further purification. Milli-Q grade water was used for all the experiments. D_2O was purchased from Sigma-Aldrich and used for NMR experiments.

Synthesis of Moiré Superlattices of trp

6 mg of D/L-trp was added to 2 mL Milli-Q grade water and the resultant dispersion was sonicated for 30 s to obtain a clear solution. 200 μL from the resultant solution was pipetted out and added to 10 mL of water. The resulting 288 μM solution of D/L-trp was then stirred for 24 h under constant heating at 80 ºC. The dispersion after 24 h was then used for further experiments.

Synthesis of Zn-complexed Moiré Superlattices of trp (Zn-trp moiré)

To a 3mL dispersion containing moiré superlattices of D/L-trp, $ZnCl_2$ (7 mM) was added at room temperature. The resultant dispersion was then used for further experiments.

Optical Measurements

UV-vis measurements were recorded using Perkin-Elmer Lambda 365+ and photoluminescence (PL) spectra were recorded using a HORIBA FluoroMax-4 spectrofluorometer. The circular dichroism (CD) spectra were recorded using a JASCO J-1500 spectropolarimeter. 3 mL of an aq. solution of D/L-trp (288 μM), dispersion containing moiré superlattices before and after addition of $ZnCl_2$ were collected for the measurement of absorbance, PL and CD spectra.

Transmission electron microscopic (TEM) analysis and selected area electron diffraction (SAED) analysis

TEM and SAED data were collected after diluting the dispersions of moiré superlattices before and after addition of $ZnCl_2$ where the dispersion containing moiré superlattices of trp was diluted by adding 200 μL aliquot in 1 mL water, and similarly 40 μL aliquot of the dispersion containing $ZnCl_2$-added moiré superlattices was added to 1 mL of water. The diluted dispersions were drop-

cast on a carbon coated copper grid. TEM and SAED experiments were performed using a JEOL JEM 2100F instrument.

Proton NMR

Proton nuclear magnetic resonance (NMR) measurements were performed using 600 MHz Bruker ASCEND 600. The experiment was performed with the 'synthesis of moiré superlattices' where D_2O (Sigma-Aldrich) was used in place of Milli-Q grade water. 600 μL of aliquot was taken to perform the analysis.

Simulations of SAED patterns and chemical structure of moiré superlattices

The reported crystallographic information file[1] (cif) of L-trp was used for SAED simulation, which was done using ReciPro software[2]. The unit cell, hkl planes and the structure were redrawn from cif file data using vesta. Twisting of the lattices were performed using the Avogadro software and the interfacial interaction was redrawn using vesta.

Magnetic-conductive AFM (mc-AFM) measurements and measurement of I-V curve

The mc-AFM measurements were pursued using Oxford Asylum Research MFP-3D model. The sample was drop-cast on a nickel substrate, which was magnetized with the north pole of the magnet either pointing up or down. Conductive measurements were then made in contact mode. Images and current-voltage (I-V) curves were acquired using a tip of model ECONO SCM-PIT ($k\sim 3$ Nm^{-1} and $f = \sim 75$ kHz). The measurements were performed for different magnetic field strengths. All the analysis was performed using software Gwyddion and Asylum Research Igor pro.

Simulations of structure and density of states

The proposed structures for twisted moiré interface and Zn-complexed moiré interface were first optimized using Avogadro and were then used as models (Figure S14) for further simulations. The structural relaxation, density of states calculations and carrier charge density plot simulations were performed using Quantum ESPRESSO program suite[3]. PBEsol's generalized gradient approach (GGA) was utilized to calculate the exchange-correlation function.[4,5] The core electrons were modelled using projector-augmented-wave (PAW) method[6]. The kinetic energy cut-off was set to 60 Ry.

Chapter 5

References

1. Jensen, P. W. K.; Kristensen, L. B.; Lavigne, C.; Aspuru-Guzik, A., Toward Quantum Computing with Molecular Electronics. *J. Chem. Theory Comput.* **2022,** *18* (6), 3318-3326.
2. Moreno-Pineda, E., Quantum information processing with molecular magnets. *Phys. B Condens. Matter.* **2023,** *649*, 414486.
3. Cornia, A.; Seneor, P., The molecular way. *Nat. Mater.* **2017,** *16* (5), 505-506.
4. Fursina, A. A.; Sinitskii, A., Toward Molecular Spin Qubit Devices: Integration of Magnetic Molecules into Solid-State Devices. *ACS Appl. Electron. Mater.* **2023,** *5* (7), 3531-3545.
5. Kosloff, R., Quantum Molecular Devices. *ACS Phys. Chem. Au* **2024,** *4* (3), 226-231.
6. Yan, C.; Fang, C.; Gan, J.; Wang, J.; Zhao, X.; Wang, X.; Li, J.; Zhang, Y.; Liu, H.; Li, X.; Bai, J.; Liu, J.; Hong, W., From Molecular Electronics to Molecular Intelligence. *ACS Nano* **2024,** *18* (42), 28531-28556.
7. Xiang, D.; Wang, X.; Jia, C.; Lee, T.; Guo, X., Molecular-Scale Electronics: From Concept to Function. *Chem. Rev.* **2016,** *116* (7), 4318-4440.
8. Li, T.; Bandari, V. K.; Schmidt, O. G., Molecular Electronics: Creating and Bridging Molecular Junctions and Promoting Its Commercialization. *Adv. Mater.***2023,** *35* (22), 2209088.
9. Li, X.; Ge, W.; Guo, S.; Bai, J.; Hong, W., Characterization and Application of Supramolecular Junctions. *Angew. Chem. Int. Ed.* **2023,** *62* (13), e202216819.
10. Chen, H.; Fraser Stoddart, J., From molecular to supramolecular electronics. *Nat. Rev. Mater.* **2021,** *6* (9), 804-828.
11. Dey, U.; Chattopadhyay, A., pH Controlled Twist-Angle Dependent Interfacial Quantum Tunneling in Multilayer Molecular Moiré Superlattices of p-Phenylenediamine. *Adv. Quant. Technol.* **2025,** *n/a* (n/a), 2400569.
12. Fang, H.; Xiao, M., Tunnel Junctions with a Moiré Superlattice as a Barrier. *ACS Appl. Electron. Mater.* **2021,** *3* (6), 2543-2550.

13. Chiesa, A.; Privitera, A.; Macaluso, E.; Mannini, M.; Bittl, R.; Naaman, R.; Wasielewski, M. R.; Sessoli, R.; Carretta, S., Chirality-Induced Spin Selectivity: An Enabling Technology for Quantum Applications. *Adv. Mater.***2023,** *35* (28), 2300472.
14. Naaman, R.; Waldeck, D. H., Chiral-Induced Spin Selectivity Effect. *J. Phys. Chem. Lett.* **2012,** *3* (16), 2178-2187.
15. Bloom, B. P.; Paltiel, Y.; Naaman, R.; Waldeck, D. H., Chiral Induced Spin Selectivity. *Chem. Rev.* **2024,** *124* (4), 1950-1991.
16. Hajra, A.; Chattopadhyay, A., Chemically Reversible Translational Moiré Superlattice Formations in the Two-Dimensional Films of the Zinc Phthalate Complex. *J. Phys. Chem. Lett.* **2024,** *15* (39), 10046-10053.
17. Das, P.; Chattopadhyay, A., Moiré superlattices of two-dimensional copper nanocluster assemblies with tuneable twin emissions from hierarchical components leading to white light emission. *J. Mater. Chem.C* **2023,** *11* (35), 12029-12036.
18. Dey, U.; Chattopadhyay, A., Two-dimensional molecular moiré superlattices of tryptophan with visible photoluminescence for photo-activatable CO2 sensing and storage. *J. Mater. Chem.C* **2024,** *12* (15), 5506-5516.
19. Peluso, P.; Chankvetadze, B., Recognition in the Domain of Molecular Chirality: From Noncovalent Interactions to Separation of Enantiomers. *Chem. Rev.* **2022,** *122* (16), 13235-13400.
20. Cowan, J. A.; Furnstahl, R. J., Origin of Chirality in the Molecules of Life. *ACS Earth and Space Chem.* **2022,** *6* (11), 2575-2581.
21. Wang, G.; Qu, A.; Sun, M.; Xu, J.; Kuang, H., Chemical Mechanisms and Biological Effects of Chiral Nanomaterials. *Acc. Mater. Res.* **2024,** *5* (10), 1221-1236.
22. Aragonès, A. C.; Medina, E.; Ferrer-Huerta, M.; Gimeno, N.; Teixidó, M.; Palma, J. L.; Tao, N.; Ugalde, J. M.; Giralt, E.; Díez-Pérez, I.; Mujica, V., Measuring the Spin-Polarization Power of a Single Chiral Molecule. *Small* **2017,** *13* (2), 1602519.
23. Yang, C.; Li, Y.; Zhou, S.; Guo, Y.; Jia, C.; Liu, Z.; Houk, K. N.; Dubi, Y.; Guo, X., Real-time monitoring of reaction stereochemistry through single-molecule observations of chirality-induced spin selectivity. *Nat. Chem.* **2023,** *15* (7), 972-979.

24. Mondal, A. K.; Preuss, M. D.; Ślęczkowski, M. L.; Das, T. K.; Vantomme, G.; Meijer, E. W.; Naaman, R., Spin Filtering in Supramolecular Polymers Assembled from Achiral Monomers Mediated by Chiral Solvents. *J. Am. Chem. Soc.* **2021,** *143* (18), 7189-7195.
25. Li, X.; Ge, W.; Guo, S.; Bai, J.; Hong, W., Characterization and Application of Supramolecular Junctions. *Angew. Chem. Int. Ed.* **2023,** *62* (13), e202216819.
26. Sang, Y.; Zhu, Q.; Zhou, X.; Jiang, Y.; Zhang, L.; Liu, M., Ultrasound-Directed Symmetry Breaking and Spin Filtering of Supramolecular Assemblies from only Achiral Building Blocks. *Angew. Chem. Int. Ed.* **2023,** *62* (8), e202215867.
27. Bloom, B. P.; Kiran, V.; Varade, V.; Naaman, R.; Waldeck, D. H., Spin Selective Charge Transport through Cysteine Capped CdSe Quantum Dots. *Nano Lett.* **2016,** *16* (7), 4583-4589.
28. Bloom, B. P.; Graff, B. M.; Ghosh, S.; Beratan, D. N.; Waldeck, D. H., Chirality Control of Electron Transfer in Quantum Dot Assemblies. *J. Am. Chem. Soc.* **2017,** *139* (26), 9038-9043.
29. Tassinari, F.; Jayarathna, D. R.; Kantor-Uriel, N.; Davis, K. L.; Varade, V.; Achim, C.; Naaman, R., Chirality Dependent Charge Transfer Rate in Oligopeptides. *Adv. Mater.* **2018,** *30* (21), 1706423.
30. Mishra, S.; Mondal, A. K.; Pal, S.; Das, T. K.; Smolinsky, E. Z. B.; Siligardi, G.; Naaman, R., Length-Dependent Electron Spin Polarization in Oligopeptides and DNA. *J. Phys. Chem. C* **2020,** *124* (19), 10776-10782.
31. Mishra, S.; Poonia, V. S.; Fontanesi, C.; Naaman, R.; Fleming, A. M.; Burrows, C. J., Effect of Oxidative Damage on Charge and Spin Transport in DNA. *J. Am. Chem. Soc.* **2019,** *141* (1), 123-126.
32. Deng, L.; Bhat, I. H.; Guo, A.-M., Spin-selectivity effect of G-quadruplex DNA molecules. *J. Chem. Phys.* **2023,** *158* (24), 244116.
33. Xie, Z.; Markus, T. Z.; Cohen, S. R.; Vager, Z.; Gutierrez, R.; Naaman, R., Spin Specific Electron Conduction through DNA Oligomers. *Nano Lett.* **2011,** *11* (11), 4652-4655.
34. Wei, Q.; Ning, Z., Chiral Perovskite Spin-Optoelectronics and Spintronics: Toward Judicious Design and Application. *ACS Mater.s Lett.* **2021,** *3* (9), 1266-1275.
35. Shiota, K.; Inui, A.; Hosaka, Y.; Amano, R.; Ōnuki, Y.; Hedo, M.; Nakama, T.; Hirobe, D.; Ohe, J.-i.; Kishine, J.-i.; Yamamoto, H. M.; Shishido, H.; Togawa, Y., Chirality-

Induced Spin Polarization over Macroscopic Distances in Chiral Disilicide Crystals. *Phys. Rev. Lett.* **2021,** *127* (12), 126602.

36. Jia, L.; Wang, C.; Zhang, Y.; Yang, L.; Yan, Y., Efficient Spin Selectivity in Self-Assembled Superhelical Conducting Polymer Microfibers. *ACS Nano* **2020,** *14* (6), 6607-6615.
37. Qian, Q.; Ren, H.; Zhou, J.; Wan, Z.; Zhou, J.; Yan, X.; Cai, J.; Wang, P.; Li, B.; Sofer, Z.; Li, B.; Duan, X.; Pan, X.; Huang, Y.; Duan, X., Chiral molecular intercalation superlattices. *Nature* **2022,** *606* (7916), 902-908.
38. Huizi-Rayo, U.; Gutierrez, J.; Seco, J. M.; Mujica, V.; Diez-Perez, I.; Ugalde, J. M.; Tercjak, A.; Cepeda, J.; San Sebastian, E., An Ideal Spin Filter: Long-Range, High-Spin Selectivity in Chiral Helicoidal 3-Dimensional Metal Organic Frameworks. *Nano Lett.* **2020,** *20* (12), 8476-8482.
39. Mondal, A. K.; Brown, N.; Mishra, S.; Makam, P.; Wing, D.; Gilead, S.; Wiesenfeld, Y.; Leitus, G.; Shimon, L. J. W.; Carmieli, R.; Ehre, D.; Kamieniarz, G.; Fransson, J.; Hod, O.; Kronik, L.; Gazit, E.; Naaman, R., Long-Range Spin-Selective Transport in Chiral Metal–Organic Crystals with Temperature-Activated Magnetization. *ACS Nano* **2020,** *14* (12), 16624-16633.
40. Shaham-Niv, S.; Arnon, Z. A.; Sade, D.; Lichtenstein, A.; Shirshin, E. A.; Kolusheva, S.; Gazit, E., Intrinsic Fluorescence of Metabolite Amyloids Allows Label-Free Monitoring of Their Formation and Dynamics in Live Cells. *Angew. Chem., Int. Ed.* **2018,** *57* (38), 12444-12447.
41. Niyangoda, C.; Miti, T.; Breydo, L.; Uversky, V.; Muschol, M., Carbonyl-based blue autofluorescence of proteins and amino acids. *PLOS ONE* **2017,** *12* (5), e0176983.
42. Gorbitz, C. H.; Tornroos, K. W.; Day, G. M., Single-crystal investigation of l-tryptophan with Z' = 16. *Acta Crystallogr., Sect. B: Struct. Sci.* **2012,** *68* (5), 549-557.
43. Clever, C.; Wierzbinski, E.; Bloom, B. P.; Lu, Y.; Grimm, H. M.; Rao, S. R.; Horne, W. S.; Waldeck, D. H., Benchmarking Chiral Induced Spin Selectivity Measurements - Towards Meaningful Comparisons of Chiral Biomolecule Spin Polarizations. *Isr. J. Chem.* **2022,** *62* (11-12), e202200045.

44. Kawakami, R. K.; McCreary, K.; Li, Y., Fundamentals of Spintronics in Metal and Semiconductor Systems. In *Nanoelectronics and Photonics: From Atoms to Materials, Devices, and Architectures*, Korkin, A.; Rosei, F., Eds. Springer New York: New York, NY, 2008; pp 59-114.
45. Naaman, R.; Paltiel, Y.; Waldeck, D. H., Chiral Molecules and the Spin Selectivity Effect. *J. Phys. Chem. Lett.* **2020,** *11* (9), 3660-3666.
46. Nishioka, M.; Lee, Y.-B.; Goldman, A. M.; Xia, Y.; Frisbie, C. D., Negative magnetoresistance of organic field effect transistors. *Appl. Phys. Lett.* **2007,** *91* (9), 092117.

Chapter 5

Supporting Information

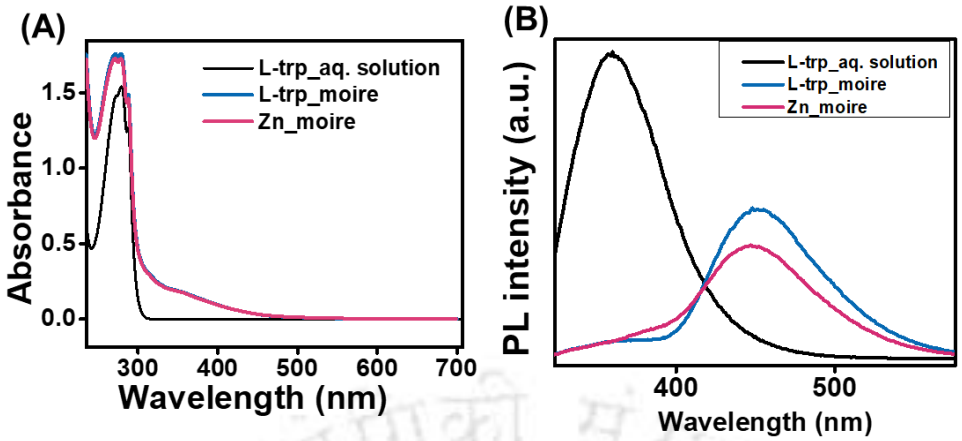

Figure S1. (A) UV-Vis spectrum and **(B)** PL spectrum ($(\lambda_{ex}$ = 300 nm) for an aq. solution of L-trp, and dispersions containing moiré superlattices of L-trp and Zn-complexed moiré superlattices of L-trp. (p.173)

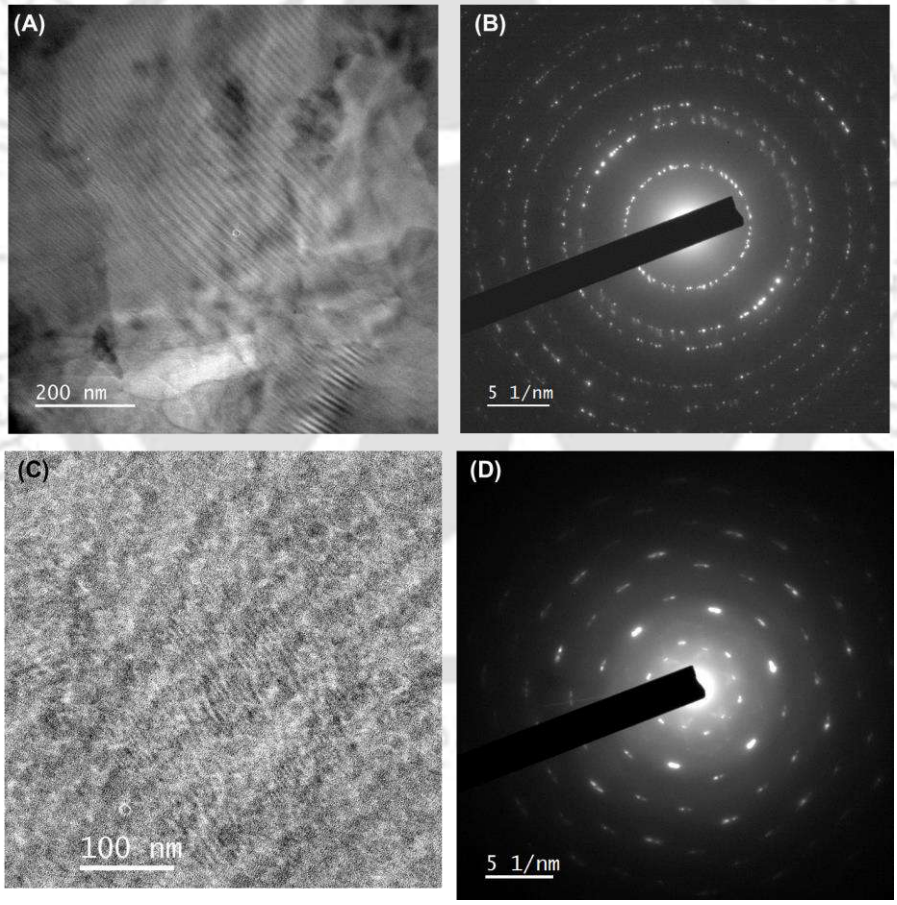

Figure S2. (A) TEM image of moiré superlattice of L-trp. **(B)** SAED pattern corresponding to the image in (A). **(C)** TEM image of Zn-complexed moiré superlattices of D-trp. **(D)** SAED pattern corresponding to the image in (C). **(p.174)**

Moiré periodicities and SAED pattern

The moiré periodicities were obtained after performing fast Fourier transformation (FFT) on Figure S3A, S3D, S3G and the twist angles for the resulting periodicities were calculated using the following equation

$$D = d/(2\mathrm{Sin}(\theta/2)). \quad \text{S1}$$

where d is the lattice constant taken as 0.54 nm, D is the moiré periodicity and θ is the twist angle between two sheets. The IFFT images of the moiré superlattices for Figure S3A is presented in Figure S3B-C, Figure S3D is presented in Figure S3E-F and for Figure S3G is presented in Figure S3H-I. The average moiré periodicities calculated from the IFFTs were 9.89 ± 1.12 nm and 5.18 ± 0.75. Using equation S1, the twist angle θ was calculated and the average twist angle calculated was equal to 2.94 ± 0.15˚ and 5.68 ± 0.58˚. The calculate twist angles were close to the experimental twist angles observed between two consecutive sheets due to the twisted stacking (2.5 ± 1.0° and 5.0 ± 1.0°) from SAED.

As compared to the SAED pattern (Figure 1D of main article) of multilayered moiré superlattices, which indicated the multiple twisted stacking of nanolattices with hexagonal diffraction pattern at varied range of angles, the SAED pattern for Zn-trp moiré in Figure 1F indicated diffraction spots for three superimposed layers with an angle 2.5° between two consecutive layers. The results suggested that following complexation with Zn^{2+} ions, the twisted stacking of these nanolattice layers was restricted to 2.5° angles.

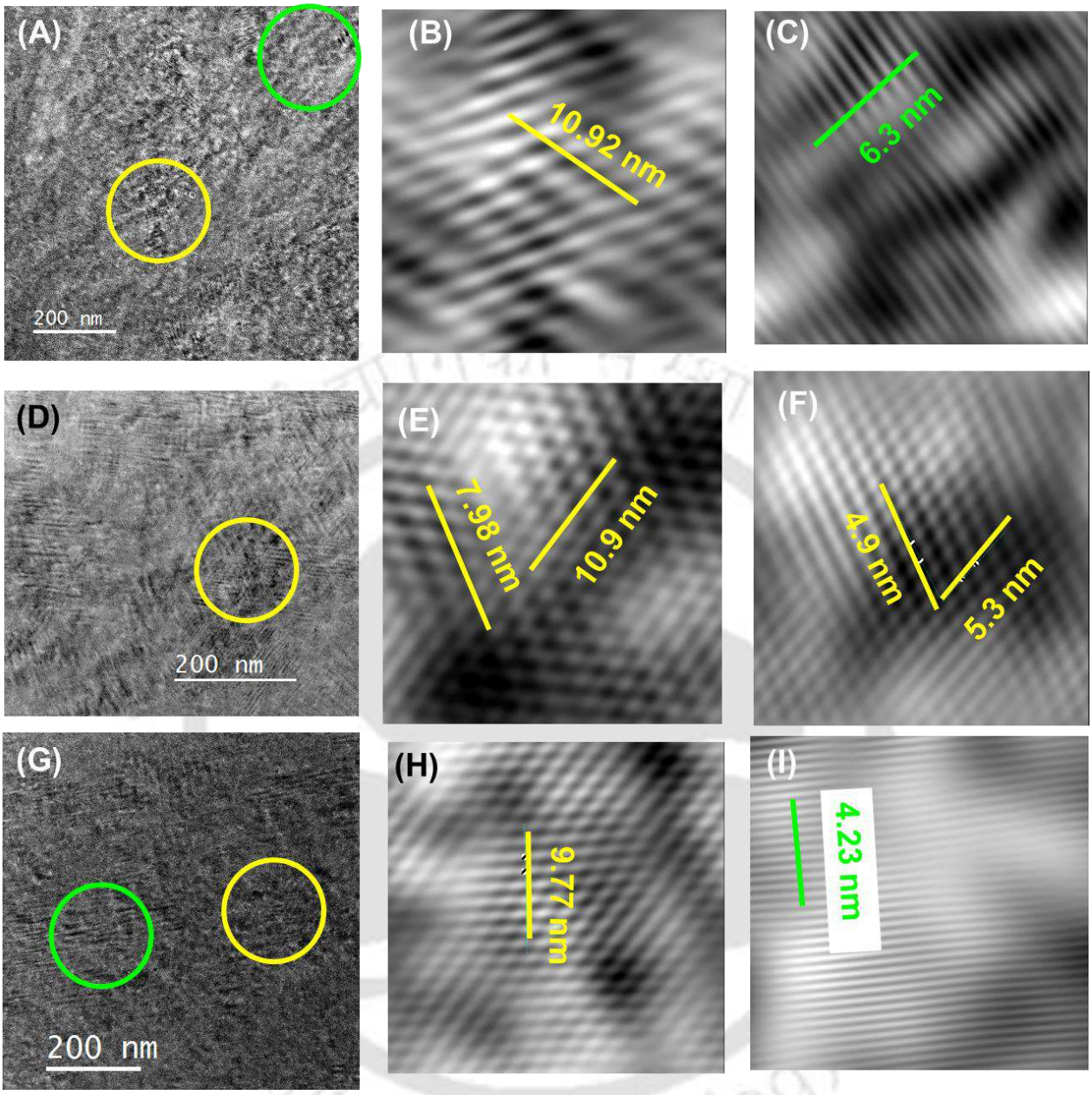

Figure S3. TEM image of different samples of Zn-complexed moiré superlattices of trp are presented in **(A), (D) and (G)**. **(B) and (C)** represents the IFFT of the marked regions in **(A). (E) and (F)** represents the IFFT of the marked regions in **(D). (H) and (I)** represents the IFFT of the marked regions in **(G). (p.174)**

The lattice parameters analyzed from the SAED pattern of the Zn-trp moiré had 0.3 nm (the closest bright spots from the center) and 0.54 nm (the closest lighter spots from the center) d-spacings (Figure S2D and Figure 1F of main article). When compared with the original 2D nanolattice, the lattice parameter 0.28 nm was present, which is close to 0.3 nm observed in the Zn-trp moiré but was absent in the unreacted moiré superlattice of trp. When moiré superlattices were formed after twisted stacking of the 2D nanolattices, the lattice planes having d-spacing 0.47, 0.28 were absent similar to the observation as reported earlier. However, the lattice planes corresponding to 0.3 nm recurred after reaction with Zn^{2+} ions and the small difference in the d-spacing might be due to the rearrangement of molecules within the lattice after complexation. Further, a new lattice parameter (0.54 nm) was observed after Zn^{2+} ions were incorporated in the superlattice while the ones (0.47 and 0.2 nm) corresponding to moiré superlattice of trp were not observed in the diffraction pattern. This indicated that new diffraction planes were generated upon Zn-complexation, possibly due to the ordered arrangement of Zn within the superlattice and hence suggested that the stackings of the nanolattices were modified but not completely destroyed after complexation. Further the number of stacked layers in the Zn-trp moiré, as analyzed from the diffraction spots of three SAED patterns was typically restricted to 3-4 layers whereas for the unreacted moiré superlattices of trp, numerous layers ranging from 7-13 layers were present in each superlattice.

CD experiments

The circular dichroism (CD) spectra were recorded for the dispersion containing D/L-trp moiré superlattices (Figure 1E-F of main article, Figure S1C-F) before and after addition of Zn^{2+} ions. For moiré superlattices of D-trp, new peaks were observed in the range 250-300 nm and a broad peak at 650 nm was observed in comparison to an aqueous solution of D-trp molecules (288 uM), thus substantiating their chiral nature. The characteristic CD peak of D-trp observed at 220 nm was shifted to 230 nm for the dispersion containing the moiré superlattices that might have resulted from the self-assembly of the molecules in the reaction medium. Addition of Zn^{2+} ions to the dispersion containing moiré superlattices of D-trp resulted in a more prominent CD spectral peak in the range of 500-700 nm with an observed blue shift of 50 nm. This further supported the interaction of Zn^{2+} ions with D-trp within the moiré superlattice and indicated the change in spiral nature of the superlattices. Further CD spectra for moiré superlattices of L-trp

and their Zn-complexed counterpart were recorded (Figure S1C and Figure S1E). For both L and D-trp moiré superlattices, negative ellipticity was observed at 650 nm that became more prominent after complexation with Zn^{2+}. The results indicated that similar spiral structures had been formed notwithstanding starting with L or D-trp to synthesize moiré superlattices. Importantly the chirality of the individual molecule of L or D-trp after its assembly into moiré superlattices remained unaffected.

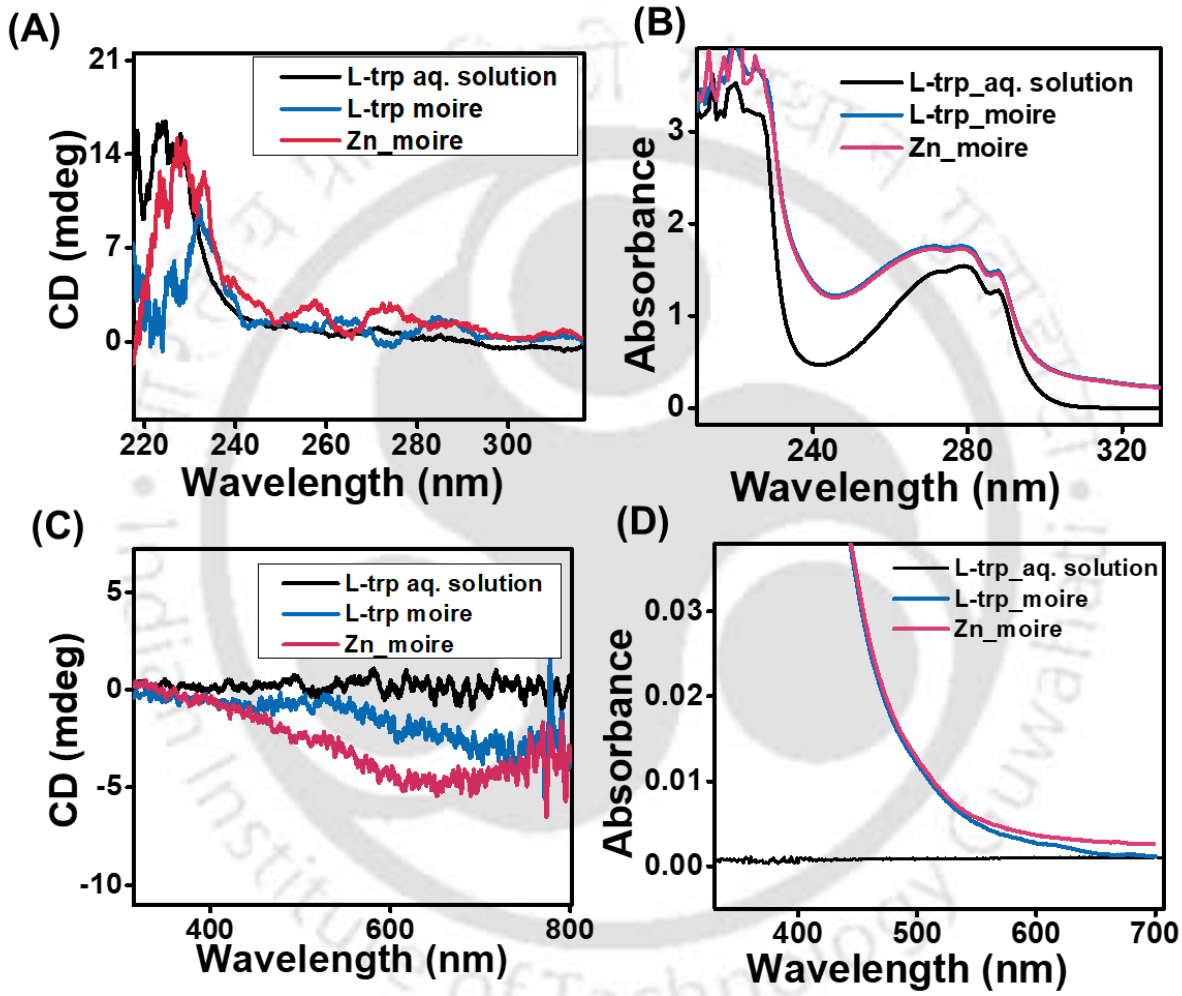

Figure S4. (A) CD spectra for the range 210 – 310 nm of an aq. solution of D-trp, and dispersions containing moiré superlattices of L-trp and Zn-complexed moiré superlattices of L-trp and **(B)** the corresponding UV-Vis spectra for the range. **(C)** CD spectra for the range 310 – 800 nm aq. solution of D-trp, and dispersion containing moiré superlattices of L-trp and Zn-complexed moiré superlattices of L-trp and **(D)** the corresponding UV-Vis spectra for the range. p.174

Control experiment

A mixture of 288 μM trp and 7 mM $ZnCl_2$ was taken in a vial and stirred continuously for 24 h while being heated at 80 ˚C as a control experiment to understand the reaction mechanism for the formation of the aforementioned moiré superlattices. A precipitate was formed after 24 h of reaction possibly due to formation of a Zn-trp complex, which was separated by centrifugation at 12000 rpm. The precipitate was redispersed in water and was excited at 300 nm where no emission peak was observed at 452 nm, indicating the absence of assembly through H-bonds. However, when the supernatant was excited at 300 nm, an emission peak at 452 nm was observed probably due to the self-assembly of the residual trp that didn't react with Zn^{2+} ions. TEM images for the supernatant was acquired (Figure S4) that displayed multilayered moiré superlattices having SAED pattern similar to the precursor trp moiré superlattices showing random twisted stacking. The PL and TEM images indicated that starting with a mixture of trp and $ZnCl_2$ would result in the formation of a multilayered molecular superlattices with variable twist angles. Thus, $ZnCl_2$ should be added, following the formation of the molecular moiré superlattices of trp after 24 h of reaction, to obtain precisely controlled moiré superlattices and starting with a mixture of Zn^{2+} ions and trp would result in the multilayered moiré superlattices with varied angles as observed in Figure 2 of main article.

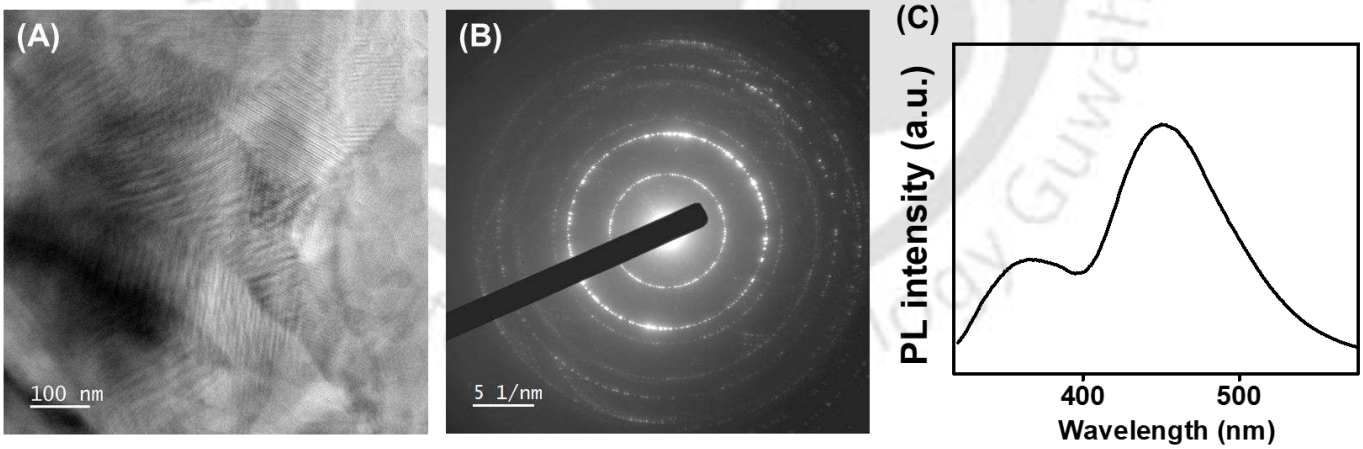

Figure S5. (A) TEM image of the supernatant obtained after centrifugation of the resultant dispersion for the control experiment formed after 24 h reaction. **(B)** SAED pattern corresponding to the image in (A). **(C)** PL spectrum ((λ_{ex} = 300 nm) of the supernatant obtained after centrifugation of the resultant dispersion for the control experiment formed after 24 h reaction. (p.174)

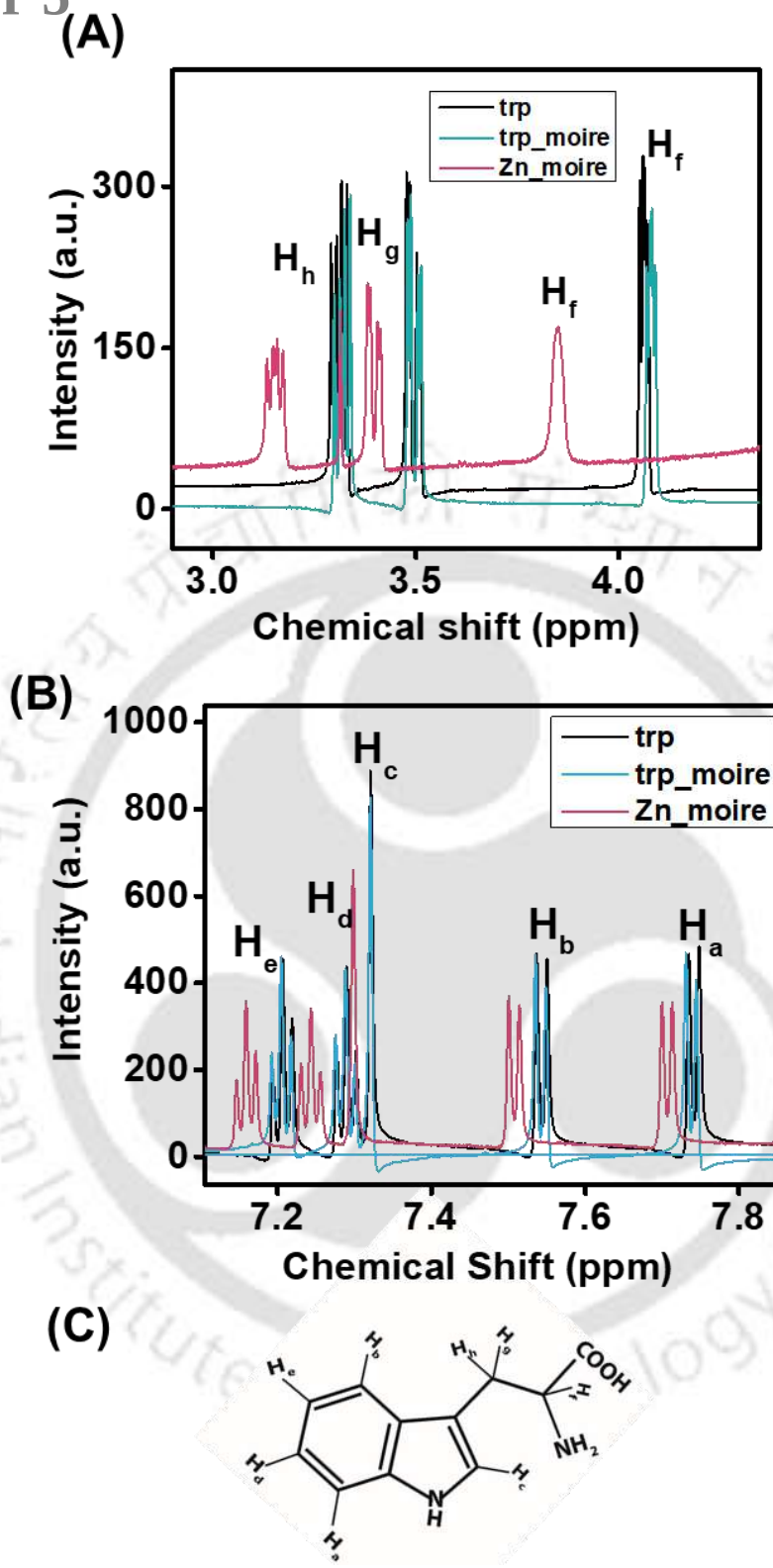

Figure S6. Chemical shift of trp, trp moiré and Zn-trp moiré ranging from **(A)** 2-5 ppm and **(B)** 7-8.5 ppm. **(C)** Chemical structure of trp where different protons are marked according to the chemical shift values. p.174

The complexation of Zn^{2+} ions with trp, followed by the change in the structure as proposed in the article was supported by ^{1}H NMR spectroscopic measurements (Figure S6, Table S1). It was observed that as trp molecules assembled to form the moiré nanosheets, a downfield shift of resonance had occurred due to the formation of 2D nanosheet and moiré superlattices that has also been reported earlier.[7] Following addition of Zn^{2+} ions to the dispersion containing moiré superlattices, an upfield shift was observed for all the protons near the Zn-O or Zn-N bonds. The presence of Zn resulted in the shielding of the protons due to high electron density and thus resulting in an upfield chemical shift.

Table S1. ^{1}H NMR peaks of an aq. trp solution, dispersions of moiré superlattice in D_2O before and addition of $ZnCl_2$. p.174

Chemical shift(ppm)/ Time (h)	H_a	H_b	H_c	H_d	H_e	H_f	H_g and H_h
Trp aq. solution	7.74	7.54	7.32	7.29	7.20	4.06	3.40
Trp moiré	7.73	7.54	7.32	7.28	7.20	4.08	3.41
Zn_trp moiré	7.70	7.50	7.30	7.29	7.15	3.84	3.28

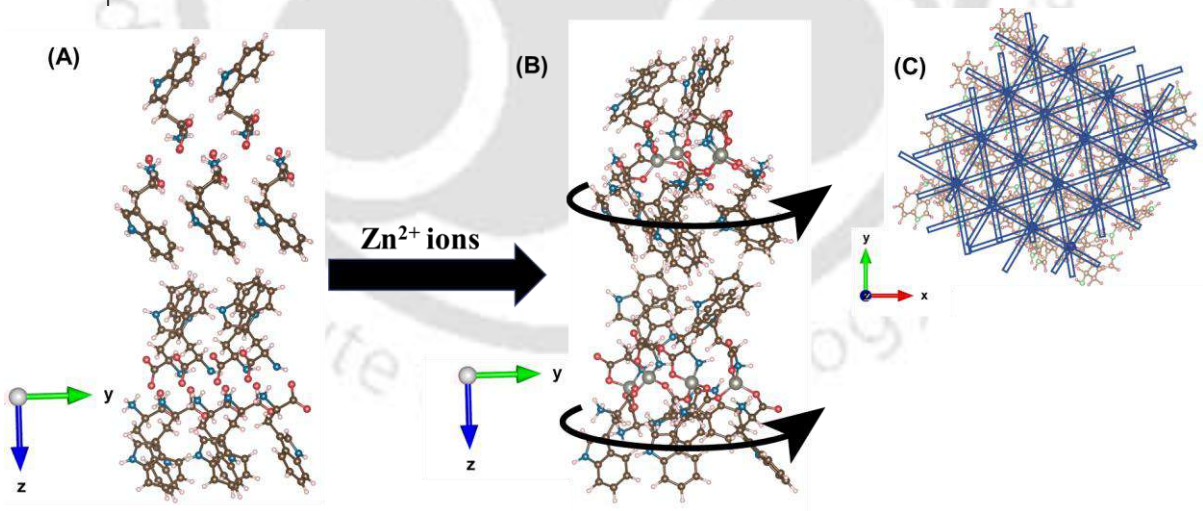

Figure S7. (A) Molecular representation of 2D nanolattice along the z axis. **(B)** Molecular representation corresponding to twisted stacking following complexation with Zn^{2+} ions along the z axis. **(C)** 2D nanolattice when viewed through z axis where the lattice planes passing through Zn atoms (with spacing 0.56 nm) is represented by the blue lines. (p.176)

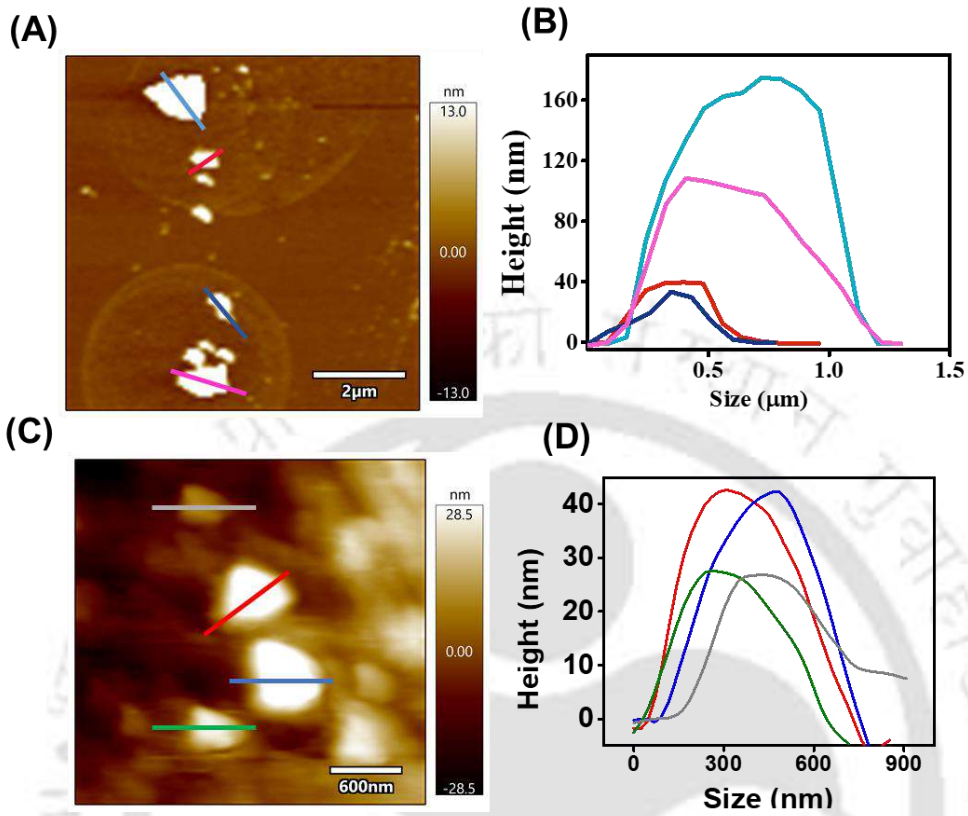

Figure S8. (A) AFM topographic image of the precursor trp moiré nanosheets. **(B)** Corresponding height profile (average height = 89.75 ± 47.58 nm) of moiré sheets as obtained for the samples in (**A**). **(C)** AFM topographic image of the Zn-trp moiré. **(D)** Corresponding height profile (average height = 34.5 ± 8.1 nm) of moiré superlattices as obtained for the samples in (**C**). (p.177)

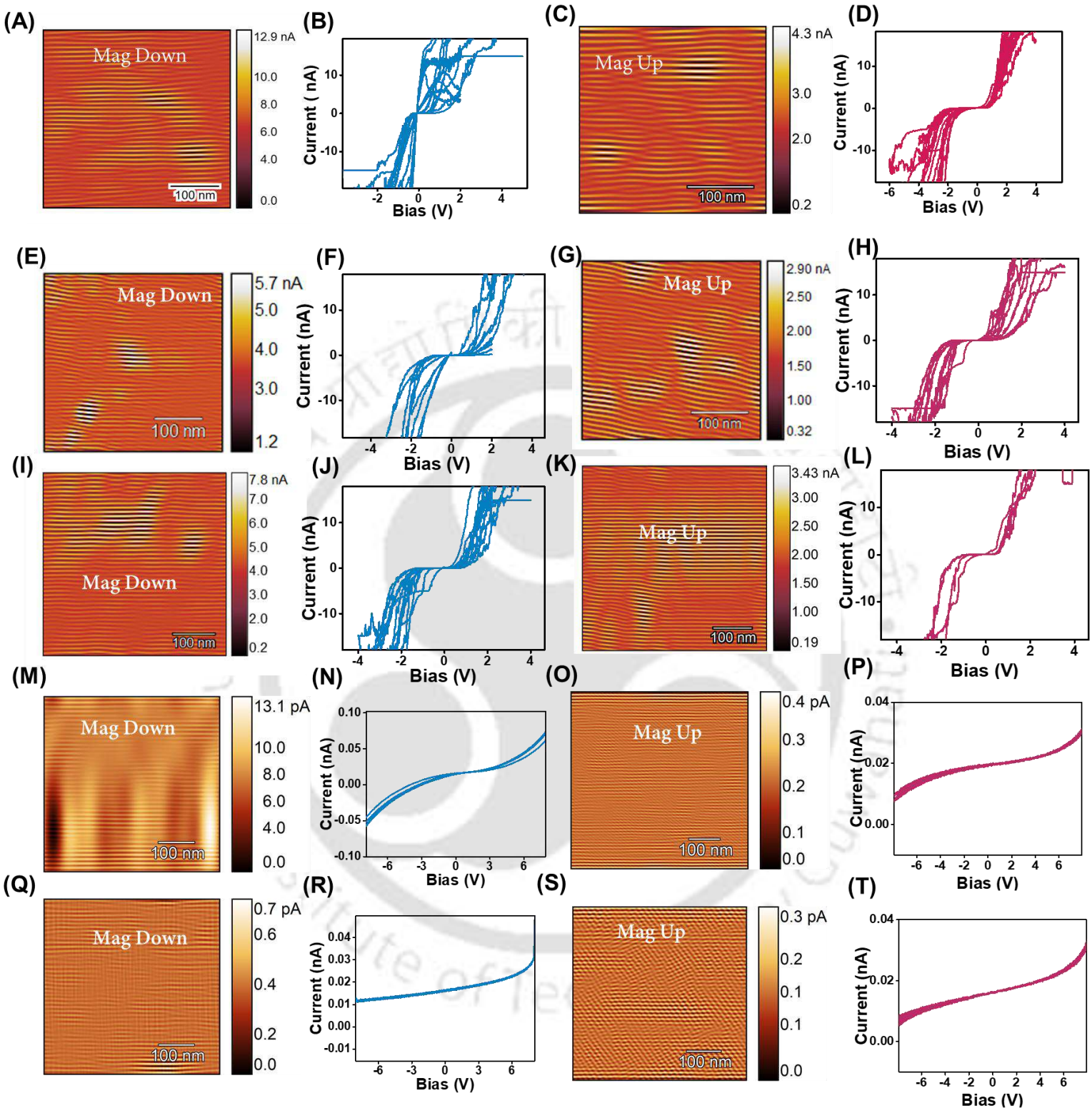

Figure S9. (A) The reconstructed current mapping using Fourier transform performed on Zn-trp moiré superlattices in the presence of magnetic field 0.45 T with north pole pointing down (mag-down). **(B)** I-V curves acquired on different Zn-trp moiré nanosheets in the presence of magnetic

field 0.45 T for mag-down. **(C)** The reconstructed current mapping using Fourier transform performed on Zn-trp moiré superlattices in the presence of magnetic field 0.45 T with north pole pointing up (mag-up). **(D)** I-V curves acquired on different Zn-trp moiré nanosheets in the presence of magnetic field 0.45 T. **(E)** The reconstructed current mapping using Fourier transform performed on Zn-trp moiré superlattices in the presence of magnetic field 0.4 T for mag-down. **(F)** I-V curves acquired on different Zn-trp moiré in presence of magnetic field 0.4 T for mag-down. **(G)** The reconstructed current mapping using Fourier transform performed on Zn-trp moiré superlattices in the presence of magnetic field 0.4 T with north pole pointing up (mag-up). **(H)** I-V curves acquired on different Zn-trp moiré in the presence of magnetic field 0.4 T. **(I)** The reconstructed current mapping using Fourier transform performed on Zn-trp moiré superlattices in the presence of magnetic field 0.38 T for mag-down. **(J)** I-V curves acquired on different Zn-trp moiré in presence of magnetic field 0.38 T for mag-down. **(K)** The reconstructed current mapping using Fourier transform performed on Zn-trp moiré superlattices in the presence of magnetic field 0.38 T with north pole pointing up (mag-up). **(L)** I-V curves acquired on different Zn-trp moiré in the presence of magnetic field 0.38 T. **(M)** The reconstructed current mapping using Fourier transform performed on Zn-trp moiré superlattices in the presence of magnetic field 0.33 T for mag-down. **(N)** I-V curves acquired on different Zn-trp moiré in presence of magnetic field 0.33 T for mag-down. **(O)** The reconstructed current mapping using Fourier transform performed on Zn-trp moiré superlattices in the presence of magnetic field 0.33 T with north pole pointing up (mag-up). **(P)** I-V curves acquired on different Zn-trp moiré in the presence of magnetic field 0.33 T. **(Q)** The reconstructed current mapping using Fourier transform performed on Zn-trp moiré superlattices in the presence of magnetic field 0.25 T for mag-down. **(R)** I-V curves acquired on different Zn-trp moiré in presence of magnetic field 0.25 T for mag-down. **(S)** The reconstructed current mapping using Fourier transform performed on Zn-trp moiré superlattices in the presence of magnetic field 0.25 T with north pole pointing up (mag-up). **(T)** I-V curves acquired on different Zn-trp moiré in the presence of magnetic field 0.25 T. (p.178)

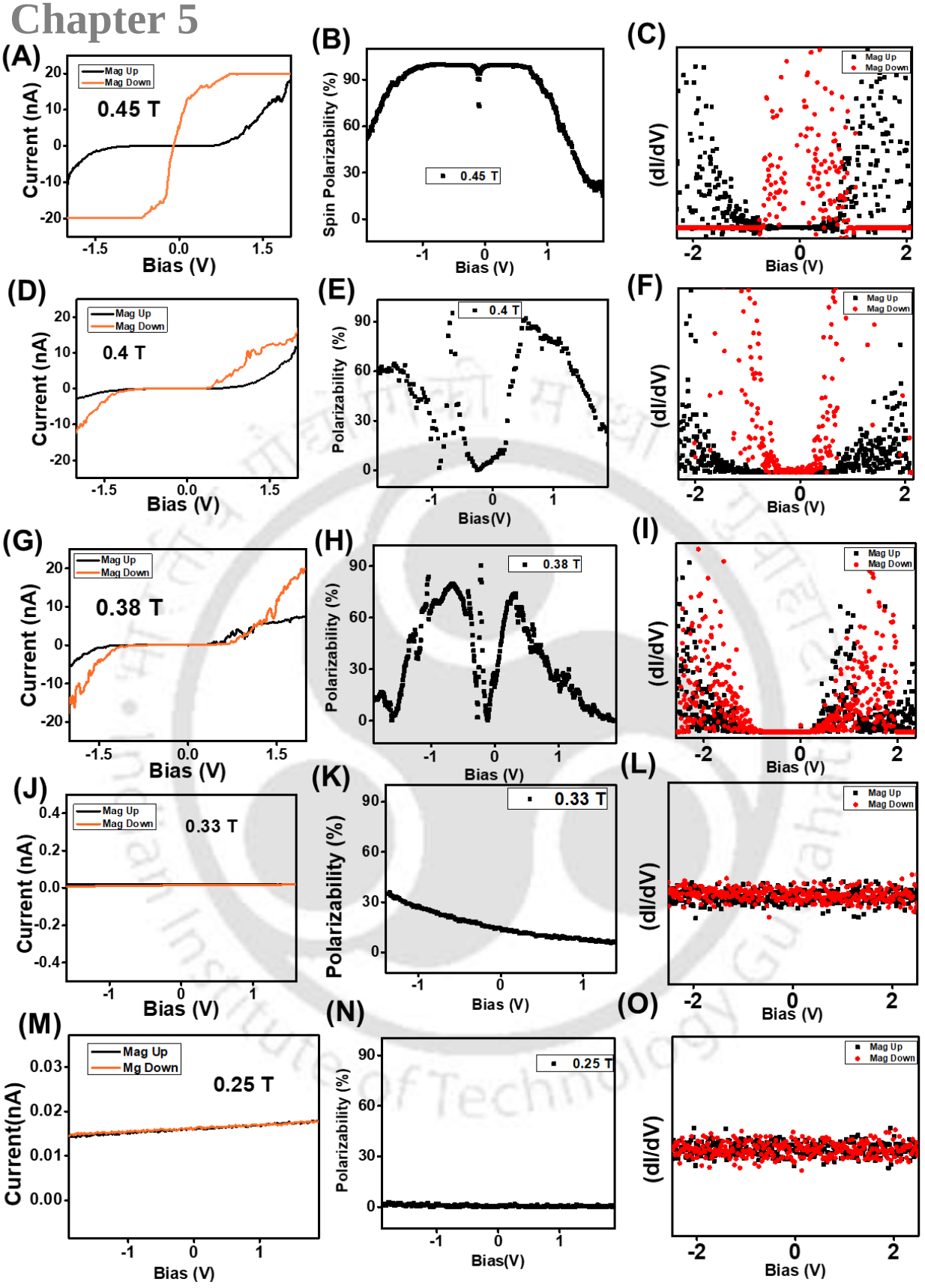

Figure S10. (A) I-V curve obtained for Zn-complexed moiré superlattices of D-trp in mag up and mag down orientations for magnetic field of 0.45 T. **(B)** Plot of polarizability vs bias voltage

applied and **(C)** dI/dV vs voltage plot for the magnetic field strength of 0.45 T. **(D))** I-V curve obtained for Zn-complexed moiré superlattices of D-trp in mag up and mag down orientations for magnetic field of 0.4 T **(E)** Plot of polarizability vs bias voltage applied and **(F)** dI/dV vs voltage plot for the magnetic field strength of 0.4 T. **(G))** I-V curve obtained for Zn-complexed moiré superlattices of D-trp in mag up and mag down orientations for magnetic field of 0.38 T **(H)** Plot of polarizability vs bias voltage applied and **(I)** dI/dV vs voltage plot for the magnetic field strength of 0.38 T. **(J))** I-V curve obtained for Zn-complexed moiré superlattices of D-trp in mag up and mag down orientations for magnetic field of 0.33 T **(K)** Plot of polarizability vs bias voltage applied and **(L)** dI/dV vs voltage plot for the magnetic field strength of 0.33 T. **(M))** I-V curve obtained for Zn-complexed moiré superlattices of D-trp in mag up and mag down orientations for magnetic field of 0.25 T **(N)** Plot of polarizability vs bias voltage applied and **(O)** dI/dV vs voltage plot for the magnetic field strength of 0.25 T. (p.178) , p.181

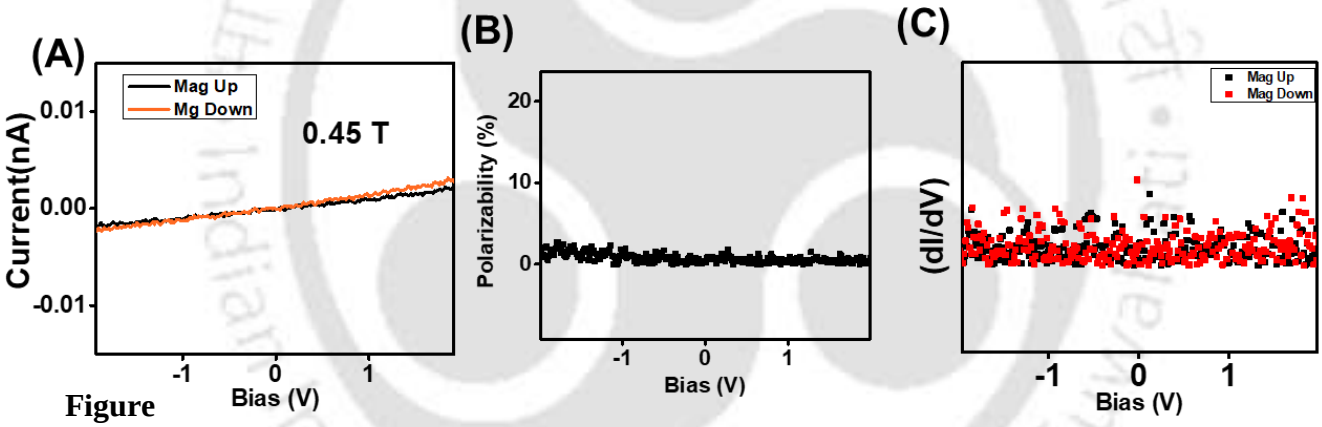

Figure S11. (A) I-V curve obtained for mag-up and mag-down orientations on the precursor trp moiré superlattices for the magnetic field of 0.45 T. **(B)** Plot of polarizability vs bias applied and **(C)** dI/dV vs voltage plot for the magnetic field strength of 0.45 T. (p.178)

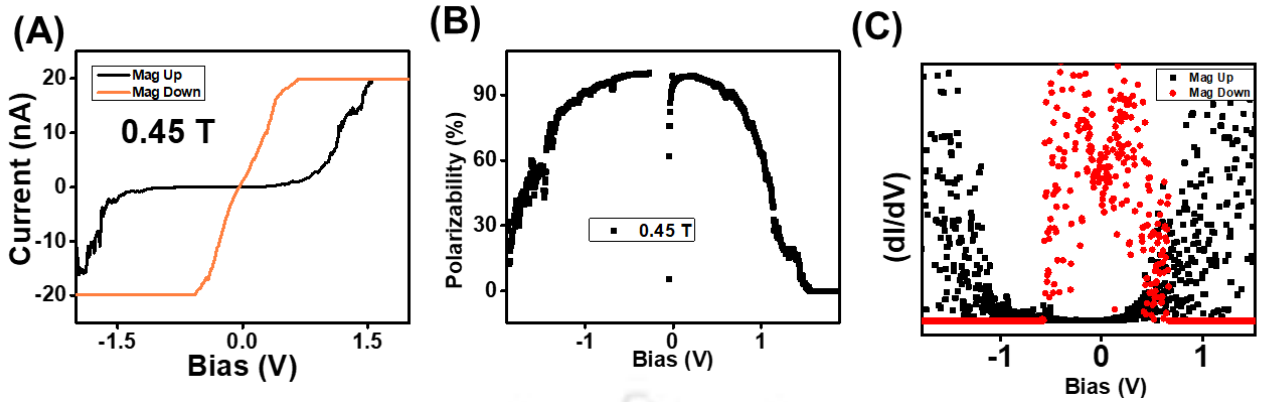

Figure S12. (A) I-V curve obtained for mag-up and mag-down orientations on the Zn-complexed L-trp moiré superlattices for the magnetic field of 0.45 T. **(B)** Plot of polarizability vs bias applied (98.7 % polarizability) and **(C)** dI/dV vs voltage plot for the magnetic field strength of 0.45 T. (p.179)

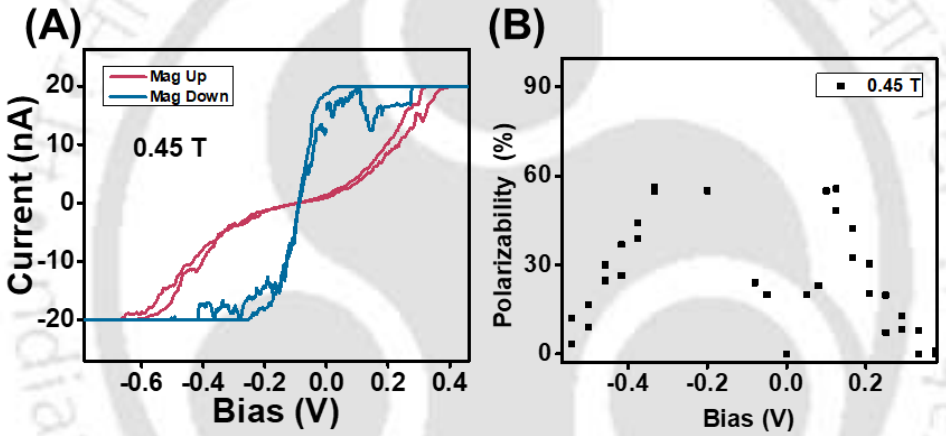

Figure S13. (A) I-V curve obtained on Zn-trp moiré for mag up and mag down orientations for the magnetic field of 0.45 T where copper tape was used as the substrate. **(B)** Plot of polarizability vs bias voltage applied for the magnetic field strength of 0.45 T calculated from (A). (p.182)

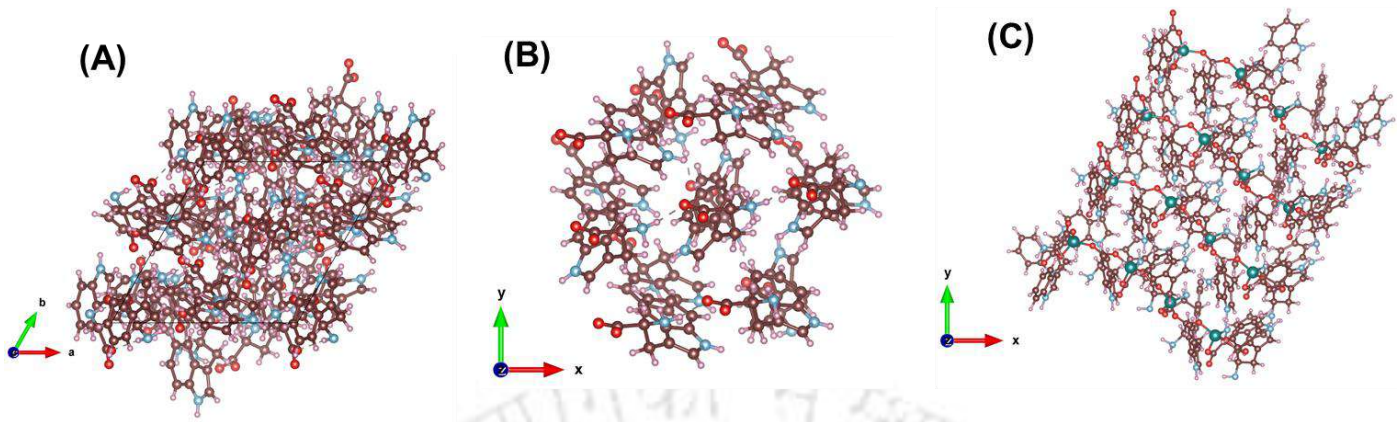

Figure S14. The structural model of **(A)** 2D nanocrystal, **(B)** twisted (moiré) interface and **(C)** Zn-complexed twisted (moiré) interface used for optimization, charge density plot simulation and density of states calculation.

References

1. Gorbitz, C. H.; Tornroos, K. W.; Day, G. M., Single-crystal investigation of l-tryptophan with Z' = 16. *Acta Crystallogr., Sect. B: Struct. Sci.* **2012,** *68* (5), 549-557.

2. Seto, Y.; Ohtsuka, M., ReciPro: free and open-source multipurpose crystallographic software integrating a crystal model database and viewer, diffraction and microscopy simulators, and diffraction data analysis tools. *J. Appl. Crystallogr.* **2022,** *55* (2), 397-410.

3. Giannozzi, P.; Baroni, S.; Bonini, N.; Calandra, M.; Car, R.; Cavazzoni, C.; Ceresoli, D.; Chiarotti, G. L.; Cococcioni, M.; Dabo, I., et al., *J. Phys.:Condens. Matter* **2009**, *21*, 395502.

4. Perdew, J. P.; Yue, W., *Phys. Rev. B: Condens. Matter Mater. Phys.* **1986**,*33*, 8800.

5. Perdew, J. P., Ruzsinszky, A., Csonka, G. I., Vydrov, O. A., Scuseria, G. E.; Constantin, L. A.; Zhou, X.; Burke, K., *Phys. Rev. Lett.* **2008**, *100*, 136406.

6. Blöchl, P. E., *Phys. Rev. B* **1994**, *50*, 17953-17979.

Chapter 6: Summary and Future prospects

Chapter 6

Summary and Future prospects

The works reported in the thesis focused on the bottom-up synthesis approaches and the properties of zero - and two-dimensional nanomaterials by using organic molecule or metal complex as building blocks. More precisely, the concept of molecular moiré superlattices, formed by the twisted stacking of the self-assembled crystalline 2D nanosheets of small organic molecules, has been introduced here. The chemical interactions at the interfaces were different from that those within the crystalline nanolattices, thus resulting in new properties not observed in the 2D nanolattice or the constituent molecules.

In the first work of this thesis, nanoparticles based on the assembly of metal complex of Gd-ascorbate were synthesized that displayed size-dependent optical and magnetic properties. The observations and conclusions from this work paved the way for synthesizing higher dimensional nanostructures. As mentioned in the introduction of this thesis, these metal-complex based nanoparticles can further be assembled into moiré superlattices using Zn^{2+} ions in the liquid media. But can these moiré superlattices be synthesized by assembly of small molecules? Can we further simplify the assembly of moiré superlattices in the liquid media? These questions inspired us to synthesize molecule-based moiré superlattices where a simple unit such as an organic molecule can be used as the building block. Thus, in the chapters 3-5, we studied the formation of 2D moiré superlattices of organic molecules in the liquid media where the synthesis was based on the principles of chemistry. Further, we explored their possible applications in the upcoming field of molecular quantum devices.

Again, it is well known that many small organic molecules form 1-D or 2-D structures through self-assembly, but assembly of these molecules into moiré superlattices are new. On the other hand, moiré superlattices of vdW materials like graphene and h-BN are well-known that can be fabricated using physical methods, but reports on chemical synthesis resulting in bulk production of molecular moiré superlattices are novel. This fills up a void for the bottom-up synthesis approaches for molecular moiré superlattices in the liquid media. This thesis addressed both these issues and reported the studies of the extraordinary properties observed due to molecular interaction at the twisted moiré interfaces.

In chapter 3, the moiré superlattices of tryptophan (trp) have been reported. These superlattices displayed photoluminescence in the visible region and were further applied for CO_2 sensing and storage. On the other hand, molecular moiré superlattices of p-phenylenediamine (p-PD) have

been reported in chapter 4 and in these superlattices an increased twist angle dependent conductivity was observed as compared to their 2D counterpart. The interfacial conductivity was further tuned by changing the pH of the synthesis medium where protonation and deprotonation of the neutral moiré superlattices increased the interfacial current to 1000 and 400 times, respectively.

So far, the molecular moiré superlattices were formed after twisted stacking at varying range of angles. Thus, in the chapter 5, we tried to control the twist angles, through incorporation of Zn^{2+} ions in the previously synthesized moiré superlattices of trp resulting in the Zn-complexed trp. A tetrahedron was formed due to the complexation of Zn with trp that resulted in the twist angle of $2.5 \pm 1.0^{\circ}$ between two adjacent lattices. The twisted stacking also resulted in the formation of chiral moiré superlattices. Further they were studied as spin filters where the chiral nature of the Zn-complexed moiré superlattices resulted in the spin selection in the charge transport with a maximum spin polarization of 98.0 ± 1.5 % at 0.5 V for 0.48 T.

The works presented in this thesis offer a new perspective for the interaction of the surface molecules of the 2D nanosheets at the interface of the moiré superlattices formed after twisted stacking. As the interfacial interactions results in new optical and electronic properties, these could be further explored for applications in circuit building, small molecule sensing and gas storage, and spintronics. These may even become useful in the emerging field of quantum molecular and molecular memory and processing devices. The molecular interactions at the twisted moiré interface provided chemical and physical stability and displayed tunable properties, an important aspect for device fabrication. For example, the photoluminescence property and stability of trp moiré superlattices, observed due to the face-to-face aromatic interactions, could further be studied for their utilization in sensing small molecules or harmful gases. The tunable conductivity of p-PD moiré superlattices could further be studied for device fabrication whereas the moiré superlattices of Zn-complexed trp moiré superlattices can be an important addition to molecular spintronics. These moiré superlattices could further be studied for their practical use as electronic devices as they offer electrode with larger molecule surface area having a stable molecular arrangement within the superlattice. The superlattice interfaces offer specific electron conductivity that could be exploited for building complex circuits, information storage or sensing based on the principles of quantum mechanics Their suitable size, cheaper fabrication and better performance can help in miniaturization of devices and circuits.

List of publications

1. **Dey, U.;** Chattopadhyay, A. The Potential of Gadolinium Ascorbate Nanoparticles as a Safer Contrast Agent. *J. Phys. Chem. B* **2023,** *127* (1), 346-358.
2. **Dey, U**.; Chattopadhyay, A. Two-dimensional molecular moiré superlattices of tryptophan with visible photoluminescence for photo-activatable CO_2 sensing and storage. *J. Mater. Chem. C* **2024,** *12*, 5506.
3. Bhakat, A.; **Dey, U.**; Chattopadhyay, A. Room-Temperature Persistent Phosphorescence of Aggregated Gold Nanoclusters under Molecular Crystal Confinements. *J. Phys. Chem. Lett.* **2024,** 15(32), 8151-8160.
4. Roy, S.; Debasmita, D.; **Dey, U.**; Ghosh, S. S.; Chattopadhyay, A. Unveiling the Cytotoxic Potential of Quercetin-Loaded Magnetic Bacterial Bots against Cervical Cancer. *ACS Appl. Mater. Interfaces* **2025,** 17(4), 5799-5812.
5. **Dey, U.**; Chattopadhyay, A. pH Controlled Twist-Angle Dependent Interfacial Quantum Tunneling in Multilayer Molecular Moiré Superlattices of p-Phenylenediamine. *Adv. Quantum Technol.* **2025,** 2400569.
6. **Dey, U.**; Chattopadhyay, A. Chemical Reaction Based Precise Twist Angle Engineering of Molecular Moiré Superlattices for Spin Filtered Electron Transport (Manuscript under preparation).

List of Patents

1. Arun Chattopadhyay, Arin Bhakat, **Ujjala Dey**. Method for Synthesizing moiré superlattices from crystals**.** *Indian Patent.* **2024**, Patent no. 557220.

Conferences attended

1. Northeast Research Conclave (NERC), IIT Guwahati, 2022
2. Research and Industrial conclave (RIC), IIT Guwahati, 2023
3. International conference on Electron Microscopy held by EMSI at IIT Bombay, 2024.

Annexure: Plagiarism check and AI writing overview

Chapter 1: Introduction

Ujjala DEY

Turnitin_ujjala_PhD thesis_chapter1_28042025

Turnitin_ujjala_PhD thesis_chapter5_28042025

Ujjala_PhD thesis_2025

Indian Institute of Technology Guwahati

Document Details

Submission ID
trn:oid:::1:3231626185

Submission Date
Apr 28, 2025, 5:54 PM GMT+5:30

Download Date
Apr 28, 2025, 6:02 PM GMT+5:30

File Name
thesis_UD_chapter_1.doc

File Size
17.4 MB

15 Pages

4,060 Words

25,441 Characters

0% detected as AI

The percentage indicates the combined amount of likely AI-generated text as well as likely AI-generated text that was also likely AI-paraphrased.

Caution: Review required.

It is essential to understand the limitations of AI detection before making decisions about a student's work. We encourage you to learn more about Turnitin's AI detection capabilities before using the tool.

Detection Groups

0 AI-generated only 0%
Likely AI-generated text from a large-language model.

0 AI-generated text that was AI-paraphrased 0%
Likely AI-generated text that was likely revised using an AI-paraphrase tool or word spinner.

Chapter 1: Introduction

Turnitin_ujjala_phD thesisChapter1_28042025

ORIGINALITY REPORT

8%	2%	7%	0%
SIMILARITY INDEX	INTERNET SOURCES	PUBLICATIONS	STUDENT PAPERS

PRIMARY SOURCES

1	Ujjala Dey, Arun Chattopadhyay. "Multilayer Molecular Moiré Superlattices of para Phenylene Diamine Exhibit Angle-dependent and pH Controlled High Interfacial Electrical Conductivity Through Tunneling", American Chemical Society (ACS), 2024 Publication	2%
2	Ujjala Dey, Arun Chattopadhyay. "Two-Dimensional Molecular Moiré Superlattices of Tryptophan with Visible Photoluminescence for Photo-activatable CO2 Sensing and Storage", Journal of Materials Chemistry C, 2024 Publication	1%
3	Suprem R. Das, Sajia Sadeque, Changwook Jeong, Ruiyi Chen, Muhammad A. Alam, David B. Janes. "Copercolating Networks: An Approach for Realizing High-Performance Transparent Conductors using Multicomponent Nanostructured Networks", Nanophotonics, 2016 Publication	1%
4	Ujjala Dey, Arun Chattopadhyay. "Tryptophan Molecular Moiré Superlattices with Visible Fluorescence", American Chemical Society (ACS), 2023 Publication	1%
5	core.ac.uk	

	Internet Source	1 %
6	chemrxiv.org Internet Source	1 %
7	www2.mdpi.com Internet Source	<1 %
8	d.docksci.com Internet Source	<1 %
9	pubmed.ncbi.nlm.nih.gov Internet Source	<1 %
10	www.mdpi.com Internet Source	<1 %
11	Qianxia Lin, Siyi Song, Jinfeng Pei, Leifang Zhang, Xiaoe Chen, Huoxi Jin. "Preparation and characterization of cysteine-rich collagen peptide and its antagonistic effect on microplastic induced damage to HK-2cells", Food Bioscience, 2024 Publication	<1 %
12	Sam Zhang. "Materials for Energy", CRC Press, 2020 Publication	<1 %
13	Syed Shahabuddin, Rama Gaur, Nandini Mukherjee. "Nanomaterials for Electrochemical Sensing", CRC Press, 2025 Publication	<1 %
14	pubs.acs.org Internet Source	<1 %
15	Udo Feldkamp, Christof M. Niemeyer. "Rational Design of DNA Nanoarchitectures", Angewandte Chemie International Edition, 2006 Publication	<1 %

16	Mavroidis, C, Gaurav Sharma, Ajay Ummat, and Atul Dubey. "Bio-Nanorobotics : State of the Art and Future Challenges", Electrical Engineering Handbook, 2006. Publication	<1 %

Exclude quotes	On	Exclude matches	Off
Exclude bibliography	On		

Chapter 5: Chemical Reaction Based Precise Twist Angle Engineering of Molecular Moiré Superlattices for Spin Filtered Electron Transport

Ujjala DEY

Turnitin_ujjala_PhD thesis_chapter5_28042025

Turnitin_ujjala_PhD thesis_chapter5_28042025
Ujjala_PhD thesis_2025
Indian Institute of Technology Guwahati

Document Details

Submission ID
trn:oid:::1:3231627520

Submission Date
Apr 28, 2025, 5:43 PM GMT+5:30

Download Date
Apr 28, 2025, 5:45 PM GMT+5:30

File Name
thesis_UD_Chapter_5.doc

File Size
2.2 MB

12 Pages
3,862 Words
21,434 Characters

0% detected as AI

The percentage indicates the combined amount of likely AI-generated text as well as likely AI-generated text that was also likely AI-paraphrased.

Caution: Review required.

It is essential to understand the limitations of AI detection before making decisions about a student's work. We encourage you to learn more about Turnitin's AI detection capabilities before using the tool.

Detection Groups

0 AI-generated only 0%
Likely AI-generated text from a large-language model.

0 AI-generated text that was AI-paraphrased 0%
Likely AI-generated text that was likely revised using an AI-paraphrase tool or word spinner.

Chapter 5: Chemical Reaction Based Precise Twist Angle Engineering of Molecular Moiré Superlattices for Spin Filtered Electron Transport

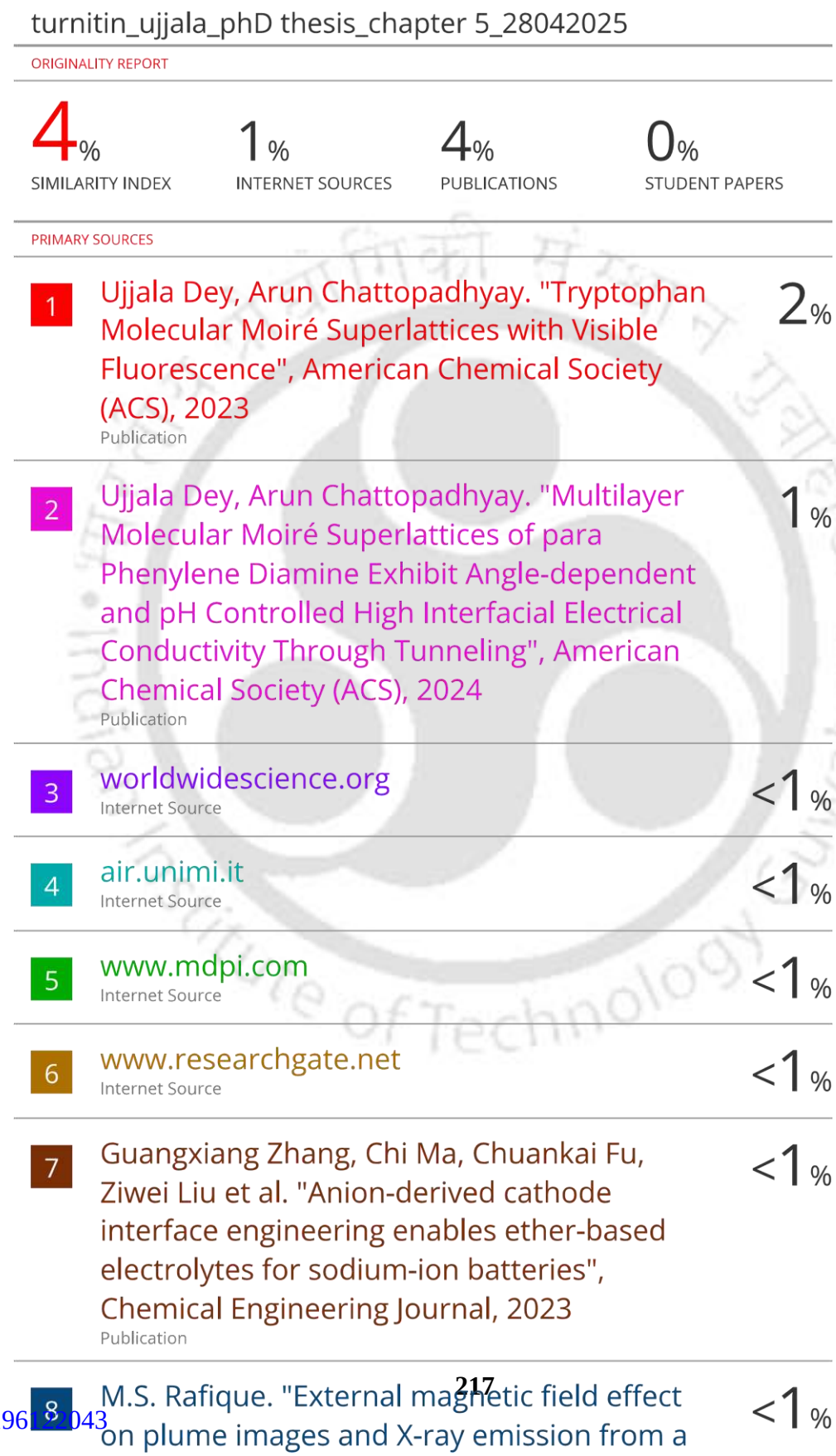

turnitin_ujjala_phD thesis_chapter 5_28042025

ORIGINALITY REPORT

4%	1%	4%	0%
SIMILARITY INDEX	INTERNET SOURCES	PUBLICATIONS	STUDENT PAPERS

PRIMARY SOURCES

1	Ujjala Dey, Arun Chattopadhyay. "Tryptophan Molecular Moiré Superlattices with Visible Fluorescence", American Chemical Society (ACS), 2023 Publication	2%
2	Ujjala Dey, Arun Chattopadhyay. "Multilayer Molecular Moiré Superlattices of para Phenylene Diamine Exhibit Angle-dependent and pH Controlled High Interfacial Electrical Conductivity Through Tunneling", American Chemical Society (ACS), 2024 Publication	1%
3	worldwidescience.org Internet Source	<1%
4	air.unimi.it Internet Source	<1%
5	www.mdpi.com Internet Source	<1%
6	www.researchgate.net Internet Source	<1%
7	Guangxiang Zhang, Chi Ma, Chuankai Fu, Ziwei Liu et al. "Anion-derived cathode interface engineering enables ether-based electrolytes for sodium-ion batteries", Chemical Engineering Journal, 2023 Publication	<1%
8	M.S. Rafique. "External magnetic field effect on plume images and X-ray emission from a	<1%

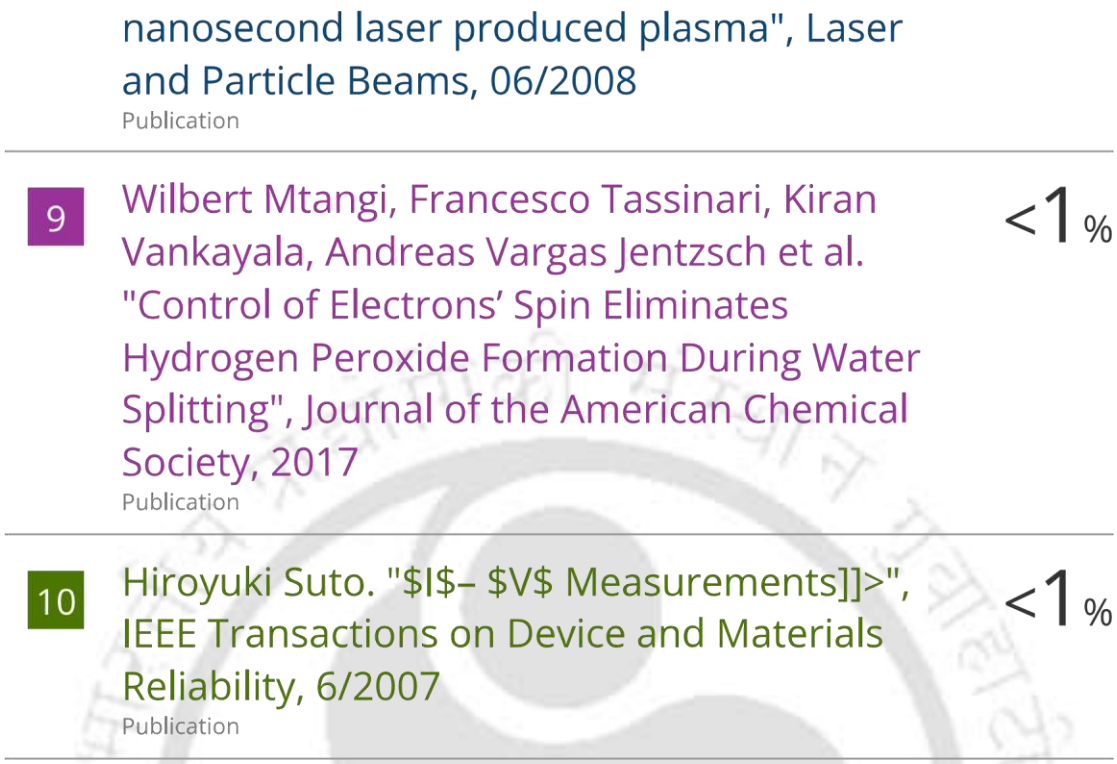

nanosecond laser produced plasma", Laser and Particle Beams, 06/2008
Publication

9 Wilbert Mtangi, Francesco Tassinari, Kiran Vankayala, Andreas Vargas Jentzsch et al. "Control of Electrons' Spin Eliminates Hydrogen Peroxide Formation During Water Splitting", Journal of the American Chemical Society, 2017 <1 %
Publication

10 Hiroyuki Suto. "I– V Measurements]]>", IEEE Transactions on Device and Materials Reliability, 6/2007 <1 %
Publication

Chapter 6: Summary and Future Prospects

Ujjala DEY

turnitin_ujjala_phD_chapter 6_28042025

Turnitin_ujjala_PhD thesis_chapter5_28042025

Ujjala_PhD thesis_2025

Indian Institute of Technology Guwahati

Document Details

Submission ID
trn:oid:::1:3231368652

Submission Date
Apr 28, 2025, 12:40 PM GMT+5:30

Download Date
Apr 28, 2025, 5:38 PM GMT+5:30

File Name
Thesis_UD_chapter_6.docx

File Size
[illegible]B

2 Pages

817 Words

4,710 Characters

turnitin Page 1 of 4 - Cover Page

0% detected as AI

The percentage indicates the combined amount of likely AI-generated text as well as likely AI-generated text that was also likely AI-paraphrased.

Caution: Review required.

It is essential to understand the limitations of AI detection before making decisions about a student's work. We encourage you to learn more about Turnitin's AI detection capabilities before using the tool.

Detection Groups

0 AI-generated only 0%
Likely AI-generated text from a large-language model.

0 AI-generated text that was AI-paraphrased 0%
Likely AI-generated text that was likely revised using an AI-paraphrase tool or word spinner.

turnitin_ujjala_phD_chapter 6_28042025

ORIGINALITY REPORT

0%	0%	0%	0%
SIMILARITY INDEX	INTERNET SOURCES	PUBLICATIONS	STUDENT PAPERS

PRIMARY SOURCES

Exclude quotes	On	Exclude matches	Off
Exclude bibliography	On		

Permissions

RightsLink

A Review of One-Dimensional Nanomaterials as Electrode Materials for Oxygen Reduction Reaction Electrocatalysis

Author: Shuaishuai Wang, Shengbin Luo, Gang Wang, et al
Publication: ChemElectroChem
Publisher: John Wiley and Sons
Date: Nov 11, 2022

Order Completed

Thank you for your order.

This Agreement between Ujjala Dey ("You") and John Wiley and Sons ("John Wiley and Sons") consists of your license details and the terms and conditions provided by John Wiley and Sons and Copyright Clearance Center.

Your confirmation email will contain your order number for future reference.

License Number	6016030721474
License date	Apr 25, 2025

Printable Details

Licensed Content

Licensed Content Publisher	John Wiley and Sons
Licensed Content Publication	ChemElectroChem
Licensed Content Title	A Review of One-Dimensional Nanomaterials as Electrode Materials for Oxygen Reduction Reaction Electrocatalysis
Licensed Content Author	Shuaishuai Wang, Shengbin Luo, Gang Wang, et al
Licensed Content Date	Nov 11, 2022
Licensed Content Volume	9
Licensed Content Issue	21
Licensed Content Pages	29

Order Details

Type of use	Dissertation/Thesis
Requestor type	University/Academic
Format	Print and electronic
Portion	Figure/table
Number of figures/ tables	1
Will you be translating?	No

About Your Work

Title of new work	Thesis
Institution name	IIT Guwahati
Expected presentation date	Jun 2025

Additional Data

Portions	Table of content or abstract figure
The Requesting Person / Organization to Appear on the License	Ujjala Dey

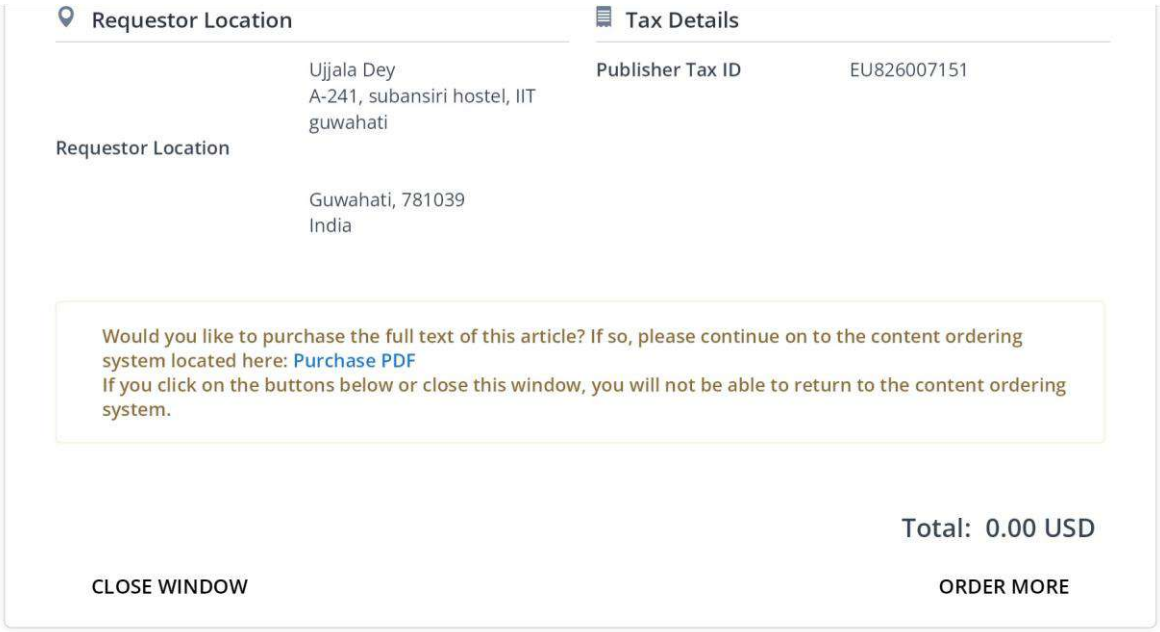

Requestor Location

Ujjala Dey
A-241, subansiri hostel, IIT guwahati

Requestor Location

Guwahati, 781039
India

Tax Details

Publisher Tax ID EU826007151

Would you like to purchase the full text of this article? If so, please continue on to the content ordering system located here: Purchase PDF
If you click on the buttons below or close this window, you will not be able to return to the content ordering system.

Total: 0.00 USD

CLOSE WINDOW ORDER MORE

Two-dimensional nanomaterials: A critical review of recent progress, properties, applications, and future directions

Author: Nadeem Baig
Publication: Composites Part A: Applied Science and Manufacturing
Publisher: Elsevier
Date: February 2023

Order Completed

Thank you for your order.

This Agreement between Ujjala Dey ("You") and Elsevier ("Elsevier") consists of your license details and the terms and conditions provided by Elsevier and Copyright Clearance Center.

Your confirmation email will contain your order number for future reference.

License Number	6016031010827
License date	Apr 25, 2025

Printable Details

Licensed Content

Licensed Content Publisher	Elsevier
Licensed Content Publication	Composites Part A: Applied Science and Manufacturing
Licensed Content Title	Two-dimensional nanomaterials: A critical review of recent progress, properties, applications, and future directions
Licensed Content Author	Nadeem Baig
Licensed Content Date	Feb 1, 2023
Licensed Content Volume	165
Licensed Content Issue	n/a
Licensed Content Pages	1

Order Details

Type of Use	reuse in a thesis/dissertation
Portion	figures/tables/illustrations
Number of figures/ tables/illustrations	1
Format	both print and electronic
Are you the author of this Elsevier article?	No
Will you be translating?	No

About Your Work

Title of new work	Thesis
Institution name	IIT Guwahati
Expected presentation date	Jun 2025

Additional Data

Portions	Graphical abstract
The Requesting Person / Organization to Appear on the License	Ujjala Dey

Requestor Location

Ujjala Dey
A-241, subansiri hostel, IIT guwahati

Requestor Location

Guwahati, 781039
India

Tax Details

Publisher Tax ID GB 494 6272 12

Total: 0.00 USD

CLOSE WINDOW ORDER MORE

Marketplace

This is a License Agreement between Ujjala Dey (“User”) and Copyright Clearance Center, Inc. (“CCC”) on behalf of the Rightsholder identified in the order details below. The license consists of the order details, the Marketplace Permissions General Terms and Conditions below, and any Rightsholder Terms and Conditions which are included below.

All payments must be made in full to CCC in accordance with the Marketplace Permissions General Terms and Conditions below.

Order Date	25-Apr-2025	**Type of Use**	Republish in a thesis/dissertation
Order License ID	1603607-1		
ISSN	2058-9689	**Publisher**	Royal Society of Chemistry
		Portion	Image/photo/illustration

LICENSED CONTENT

Publication Title	Molecular Systems Design & Engineering	**Rightsholder**	Royal Society of Chemistry
		Publication Type	e-Journal
Article Title	Self-limited self-assembly of nanoparticles into supraparticles: towards supramolecular colloidal materials by design	**Start Page**	155
		End Page	162
		Issue	2
		Volume	1
Author / Editor	Royal Society of Chemistry (Great Britain),, Institution of Chemical Engineers (Great Britain),		
Date	01/01/2016		
Language	English		
Country	United Kingdom of Great Britain and Northern Ireland		

REQUEST DETAILS

Portion Type	Image/photo/illustration	**Distribution**	Worldwide
Number of Images / Photos / Illustrations	1	**Translation**	Original language of publication
Format (select all that apply)	Print, Electronic	**Copies for the Disabled?**	No
		Minor Editing Privileges?	No
Who Will Republish the Content?	Academic institution	**Incidental Promotional Use?**	No
Duration of Use	Life of current edition	**Currency**	USD
Lifetime Unit Quantity	Up to 499		
Rights Requested	Main product		

NEW WORK DETAILS

Title	Thesis Work of Ujjala Dey	**Institution Name**	Indian Institute of Technology, Guwahati
Instructor Name	Prof. Arun Chattopadhyay		

Expected Presentation Date	2025-08-08

ADDITIONAL DETAILS

Order Reference Number	N/A	**The Requesting Person / Organization to Appear on the License**	Ujjala Dey

REQUESTED CONTENT DETAILS

Title, Description or Numeric Reference of the Portion(s)	Abstract Figure or Table content grahic	**Title of the Article / Chapter the Portion Is From**	Self-limited self-assembly of nanoparticles into supraparticles: towards supramolecular colloidal materials by design
Editor of Portion(s)	Piccinini, Esteban; Pallarola, Diego; Battaglini, Fernando; Azzaroni, Omar	**Author of Portion(s)**	Piccinini, Esteban; Pallarola, Diego; Battaglini, Fernando; Azzaroni, Omar
Volume / Edition	1		
Page or Page Range of Portion	155-162	**Issue, if Republishing an Article From a Serial**	2
		Publication Date of Portion	2016-08-02

RightsLink

UD

ACS Publications
Most Trusted. Most Cited. Most Read.

Stacking Order Engineering of Two-Dimensional Materials and Device Applications

Author: Carter Fox, Yulu Mao, Xiang Zhang, et al

Publication: Chemical Reviews

Publisher: American Chemical Society

Date: Feb 1, 2024

PERMISSION/LICENSE IS GRANTED FOR YOUR ORDER AT NO CHARGE

This type of permission/license, instead of the standard Terms and Conditions, is sent to you because no fee is being charged for your order. Please note the following:

- Permission is granted for your request in both print and electronic formats, and translations.
- If figures and/or tables were requested, they may be adapted or used in part.
- Please print this page for your records and send a copy of it to your publisher/graduate school.
- Appropriate credit for the requested material should be given as follows: "Reprinted (adapted) with permission from {COMPLETE REFERENCE CITATION}. Copyright {YEAR} American Chemical Society." Insert appropriate information in place of the capitalized words.
- One-time permission is granted only for the use specified in your RightsLink request. No additional uses are granted (such as derivative works or other editions). For any uses, please submit a new request.

If credit is given to another source for the material you requested from RightsLink, permission must be obtained from that source.

BACK CLOSE WINDOW

RightsLink

UD

SPRINGER NATURE

Advance in two-dimensional twisted moiré materials: Fabrication, properties, and applications

Author: Han Yang et al
Publication: Nano Research
Publisher: Springer Nature
Date: Nov 15, 2022

Order Completed

Thank you for your order.

This Agreement between Ujjala Dey ("You") and Springer Nature ("Springer Nature") consists of your license details and the terms and conditions provided by Springer Nature and Copyright Clearance Center.

Your confirmation email will contain your order number for future reference.

License Number	6016060381306
License date	Apr 25, 2025

Printable Details

Licensed Content

Licensed Content Publisher	Springer Nature
Licensed Content Publication	Nano Research
Licensed Content Title	Advance in two-dimensional twisted moiré materials: Fabrication, properties, and applications
Licensed Content Author	Han Yang et al
Licensed Content Date	Nov 15, 2022

Order Details

Type of Use	Thesis/Dissertation
Requestor Type	academic/university or research institute
Format	print and electronic
Portion	figures/tables/illustrations
Number of figures/ tables/illustrations	1
Will you be translating?	no
Circulation/ distribution	1 - 29
Author of this Springer Nature content	no

About Your Work

Title of new work	Thesis
Institution name	IIT Guwahati
Expected presentation date	Jun 2025

Additional Data

Portions	table of content graphic or abstract figure
The Requesting Person / Organization to Appear on the License	Ujjala Dey

Requestor Location

Requestor Location	Ujjala Dey A-241, subansiri hostel, IIT guwahati Guwahati, 781039 India

Tax Details

Billing Information

Billing Type	Invoice
Billing address	Ujjala Dey A-241, subansiri hostel, IIT guwahati Guwahati, India 781039

Total: 0.00 USD

CLOSE WINDOW ORDER MORE

License Details

This Agreement between Ujjala Dey ("You") and John Wiley and Sons ("John Wiley and Sons") consists of your license details and the terms and conditions provided by John Wiley and Sons and Copyright Clearance Center.

Print Copy

License Number	6015950734469
License date	Apr 25, 2025
Licensed Content Publisher	John Wiley and Sons
Licensed Content Publication	Angew. Chem. Int. Ed.
Licensed Content Title	From Chemical Topology to Molecular Machines (Nobel Lecture)
Licensed Content Author	Jean-Pierre Sauvage
Licensed Content Date	Jun 20, 2017
Licensed Content Volume	56
Licensed Content Issue	37
Licensed Content Pages	14
Type of Use	Dissertation/Thesis
Requestor type	University/Academic
Format	Print and electronic
Portion	Figure/table
Number of figures/tables	3
Will you be translating?	No
Title of new work	Thesis
Institution name	IIT Guwahati
Expected presentation date	Jun 2025
Portions	Figure 9, figure 10 and Figure 12
The Requesting Person / Organization to Appear on the License	Ujjala Dey
Requestor Location	Ujjala Dey A-241, subansiri hostel, IIT guwahati Guwahati, 781039 India
Publisher Tax ID	EU826007151
Total	0.00 USD

Comments? We would like to hear from you. E-mail us at customercare@copyright.com

RightsLink

Mechanically Interlocked Molecules (MIMs)—Molecular Shuttles, Switches, and Machines (Nobel Lecture)

Author: J. Fraser Stoddart
Publication: Angewandte Chemie International Edition
Publisher: John Wiley and Sons
Date: Aug 16, 2017

Order Completed

Thank you for your order.

This Agreement between Ujjala Dey ("You") and John Wiley and Sons ("John Wiley and Sons") consists of your license details and the terms and conditions provided by John Wiley and Sons and Copyright Clearance Center.

Your confirmation email will contain your order number for future reference.

License Number	6015971134288
License date	Apr 25, 2025

Printable Details

Licensed Content

Licensed Content Publisher	John Wiley and Sons
Licensed Content Publication	Angewandte Chemie International Edition
Licensed Content Title	Mechanically Interlocked Molecules (MIMs)—Molecular Shuttles, Switches, and Machines (Nobel Lecture)
Licensed Content Author	J. Fraser Stoddart
Licensed Content Date	Aug 16, 2017
Licensed Content Volume	56
Licensed Content Issue	37
Licensed Content Pages	32

Order Details

Type of use	Dissertation/Thesis
Requestor type	University/Academic
Format	Print and electronic
Portion	Figure/table
Number of figures/ tables	3
Will you be translating?	No

About Your Work

Title of new work	Thesis
Institution name	IIT Guwahati
Expected presentation date	Jun 2025

Additional Data

Portions	Abstract Figure, Figure number 15 and Figure 16
The Requesting Person / Organization to Appear on the License	Ujjala Dey

Requestor Location

Ujjala Dey
A-241, subansiri hostel, IIT guwahati

Requestor Location

Guwahati, 781039
India

Tax Details

Publisher Tax ID EU826007151

Would you like to purchase the full text of this article? If so, please continue on to the content ordering system located here: Purchase PDF
If you click on the buttons below or close this window, you will not be able to return to the content ordering system.

Total: 0.00 USD

CLOSE WINDOW ORDER MORE

RightsLink

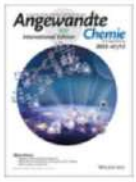

The Art of Building Small: From Molecular Switches to Motors (Nobel Lecture)

Author: Ben L. Feringa

Publication: Angewandte Chemie International Edition

Publisher: John Wiley and Sons

Date: Jul 27, 2017

Order Completed

Thank you for your order.

This Agreement between Ujjala Dey ("You") and John Wiley and Sons ("John Wiley and Sons") consists of your license details and the terms and conditions provided by John Wiley and Sons and Copyright Clearance Center.

Your confirmation email will contain your order number for future reference.

License Number	6015980067534
License date	Apr 25, 2025

Printable Details

Licensed Content

Licensed Content Publisher	John Wiley and Sons
Licensed Content Publication	Angewandte Chemie International Edition
Licensed Content Title	The Art of Building Small: From Molecular Switches to Motors (Nobel Lecture)
Licensed Content Author	Ben L. Feringa
Licensed Content Date	Jul 27, 2017
Licensed Content Volume	56
Licensed Content Issue	37
Licensed Content Pages	19

Order Details

Type of use	Dissertation/Thesis
Requestor type	University/Academic
Format	Print and electronic
Portion	Figure/table
Number of figures/ tables	1
Will you be translating?	No

About Your Work

Title of new work	Thesis
Institution name	IIT Guwahati
Expected presentation date	Jun 2025

Additional Data

Portions	figure 10
The Requesting Person / Organization to Appear on the License	Ujjala Dey

Requestor Location

Ujjala Dey
A-241, subansiri hostel, IIT guwahati

Requestor Location

Guwahati, 781039
India

Tax Details

Publisher Tax ID EU826007151

Would you like to purchase the full text of this article? If so, please continue on to the content ordering system located here: Purchase PDF
If you click on the buttons below or close this window, you will not be able to return to the content ordering system.

Total: 0.00 USD

CLOSE WINDOW ORDER MORE

RightsLink

UD

SPRINGER NATURE

From molecular to supramolecular electronics

Author: Hongliang Chen et al
Publication: Nature Reviews Materials
Publisher: Springer Nature
Date: Apr 1, 2021

Order Completed

Thank you for your order.

This Agreement between Ujjala Dey ("You") and Springer Nature ("Springer Nature") consists of your license details and the terms and conditions provided by Springer Nature and Copyright Clearance Center.

Your confirmation email will contain your order number for future reference.

License Number	6017611380399
License date	Apr 28, 2025

Printable Details

Licensed Content

Licensed Content Publisher	Springer Nature
Licensed Content Publication	Nature Reviews Materials
Licensed Content Title	From molecular to supramolecular electronics
Licensed Content Author	Hongliang Chen et al
Licensed Content Date	Apr 1, 2021

Order Details

Type of Use	Thesis/Dissertation
Requestor Type	academic/university or research institute
Format	print and electronic
Portion	figures/tables/illustrations
Number of figures/tables/illustrations	1
Would you like a high resolution image with your order?	no
Will you be translating?	no
Circulation/distribution	1 - 29
Author of this Springer Nature content	no

About Your Work

Title of new work	Thesis
Institution name	IIT Guwahati
Expected presentation date	Jun 2025

Additional Data

Portions	Figure 1
The Requesting Person / Organization to Appear on the License	Ujjala Dey

Requestor Location

Ujjala Dey
A-241, subansiri hostel, IIT guwahati

Requestor Location

Guwahati, 781039
India

Tax Details

Billing Information

Billing Type Invoice

Ujjala Dey
A-241, subansiri hostel, IIT guwahati

Billing address

Guwahati, India 781039

Total: 0.00 USD

CLOSE WINDOW ORDER MORE

RightsLink

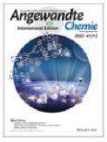

Characterization and Application of Supramolecular Junctions

Author: Xiaohui Li, Wenhui Ge, Shuhan Guo, et al
Publication: Angewandte Chemie International Edition
Publisher: John Wiley and Sons
Date: Jan 18, 2023

Order Completed

Thank you for your order.

This Agreement between Ujjala Dey ("You") and John Wiley and Sons ("John Wiley and Sons") consists of your license details and the terms and conditions provided by John Wiley and Sons and Copyright Clearance Center.

Your confirmation email will contain your order number for future reference.

Printable Details

License Number	6017620232984
License date	Apr 28, 2025

Licensed Content

Licensed Content Publisher	John Wiley and Sons
Licensed Content Publication	Angewandte Chemie International Edition
Licensed Content Title	Characterization and Application of Supramolecular Junctions
Licensed Content Author	Xiaohui Li, Wenhui Ge, Shuhan Guo, et al
Licensed Content Date	Jan 18, 2023
Licensed Content Volume	62
Licensed Content Issue	13
Licensed Content Pages	22

Order Details

Type of use	Dissertation/Thesis
Requestor type	University/Academic
Format	Print and electronic
Portion	Figure/table
Number of figures/tables	1
Will you be translating?	No

About Your Work

Title of new work	Thesis
Institution name	IIT Guwahati
Expected presentation date	Jun 2025

Additional Data

Portions	Figure 1
The Requesting Person / Organization to Appear on the License	Ujjala Dey

Requestor Location

Requestor Location	Ujjala Dey A-241, subansiri hostel, IIT guwahati Guwahati, 781039 India

Tax Details

Publisher Tax ID	EU826007151

Would you like to purchase the full text of this article? If so, please continue on to the content ordering system located here: Purchase PDF

If you click on the buttons below or close this window, you will not be able to return to the content ordering system.

Total: 0.00 USD

CLOSE WINDOW ORDER MORE

RightsLink

UD

SPRINGER NATURE

The molecular way

Author: Andrea Cornia et al
Publication: Nature Materials
Publisher: Springer Nature
Date: Apr 25, 2017

Order Completed

Thank you for your order.

This Agreement between Ujjala Dey ("You") and Springer Nature ("Springer Nature") consists of your license details and the terms and conditions provided by Springer Nature and Copyright Clearance Center.

Your confirmation email will contain your order number for future reference.

License Number	6017610965732
License date	Apr 28, 2025

Printable Details

Licensed Content

Licensed Content Publisher	Springer Nature
Licensed Content Publication	Nature Materials
Licensed Content Title	The molecular way
Licensed Content Author	Andrea Cornia et al
Licensed Content Date	Apr 25, 2017

Order Details

Type of Use	Thesis/Dissertation
Requestor Type	academic/university or research institute
Format	print and electronic
Portion	figures/tables/illustrations
Number of figures/tables/illustrations	1
Would you like a high resolution image with your order?	no
Will you be translating?	no
Circulation/distribution	1 - 29
Author of this Springer Nature content	no

About Your Work

Title of new work	Thesis
Institution name	IIT Guwahati
Expected presentation date	Jun 2025

Additional Data

Portions	Figure 1
The Requesting Person / Organization to Appear on the License	Ujjala Dey

Requestor Location

Requestor Location	Ujjala Dey A-241, subansiri hostel, IIT guwahati Guwahati, 781039 India

Billing Information

Billing Type	Invoice
Billing address	Ujjala Dey A-241, subansiri hostel, IIT guwahati Guwahati, India 781039

Tax Details

Total: 0.00 USD

CLOSE WINDOW ORDER MORE

RightsLink

UD

From Molecular Electronics to Molecular Intelligence

ACS Publications
Most Trusted. Most Cited. Most Read.

Author: Chenshuai Yan, Chao Fang, Jinyu Gan, et al
Publication: ACS Nano
Publisher: American Chemical Society
Date: Oct 1, 2024

PERMISSION/LICENSE IS GRANTED FOR YOUR ORDER AT NO CHARGE

This type of permission/license, instead of the standard Terms and Conditions, is sent to you because no fee is being charged for your order. Please note the following:

- Permission is granted for your request in both print and electronic formats, and translations.
- If figures and/or tables were requested, they may be adapted or used in part.
- Please print this page for your records and send a copy of it to your publisher/graduate school.
- Appropriate credit for the requested material should be given as follows: "Reprinted (adapted) with permission from {COMPLETE REFERENCE CITATION}. Copyright {YEAR} American Chemical Society." Insert appropriate information in place of the capitalized words.
- One-time permission is granted only for the use specified in your RightsLink request. No additional uses are granted (such as derivative works or other editions). For any uses, please submit a new request.

If credit is given to another source for the material you requested from RightsLink, permission must be obtained from that source.

BACK CLOSE WINDOW

RightsLink

UD

The Potential of Gadolinium Ascorbate Nanoparticles as a Safer Contrast Agent

ACS Publications
Most Trusted. Most Cited. Most Read.

Author: Ujjala Dey, Arun Chattopadhyay
Publication: The Journal of Physical Chemistry B
Publisher: American Chemical Society
Date: Jan 1, 2023

PERMISSION/LICENSE IS GRANTED FOR YOUR ORDER AT NO CHARGE

This type of permission/license, instead of the standard Terms and Conditions, is sent to you because no fee is being charged for your order. Please note the following:

- Permission is granted for your request in both print and electronic formats, and translations.
- If figures and/or tables were requested, they may be adapted or used in part.
- Please print this page for your records and send a copy of it to your publisher/graduate school.
- Appropriate credit for the requested material should be given as follows: "Reprinted (adapted) with permission from {COMPLETE REFERENCE CITATION}. Copyright {YEAR} American Chemical Society." Insert appropriate information in place of the capitalized words.
- One-time permission is granted only for the use specified in your RightsLink request. No additional uses are granted (such as derivative works or other editions). For any uses, please submit a new request.

If credit is given to another source for the material you requested from RightsLink, permission must be obtained from that source.

BACK CLOSE WINDOW

RightsLink

pH Controlled Twist-Angle Dependent Interfacial Quantum Tunneling in Multilayer Molecular Moiré Superlattices of p-Phenylenediamine

Author: Ujjala Dey, Arun Chattopadhyay
Publication: ADVANCED QUANTUM TECHNOLOGIES
Publisher: John Wiley and Sons
Date: Feb 14, 2025

Order Completed

Thank you for your order.

This Agreement between Ujjala Dey ("You") and John Wiley and Sons ("John Wiley and Sons") consists of your license details and the terms and conditions provided by John Wiley and Sons and Copyright Clearance Center.

Your confirmation email will contain your order number for future reference.

License Number	6017630510959
License date	Apr 28, 2025

Printable Details

Licensed Content

Licensed Content Publisher	John Wiley and Sons
Licensed Content Publication	ADVANCED QUANTUM TECHNOLOGIES
Licensed Content Title	pH Controlled Twist-Angle Dependent Interfacial Quantum Tunneling in Multilayer Molecular Moiré Superlattices of p-Phenylenediamine
Licensed Content Author	Ujjala Dey, Arun Chattopadhyay
Licensed Content Date	Feb 14, 2025
Licensed Content Volume	0
Licensed Content Issue	0
Licensed Content Pages	9

Order Details

Type of use	Dissertation/Thesis
Requestor type	Author of this Wiley article
Format	Print and electronic
Portion	Full article
Will you be translating?	No

About Your Work

Title of new work	Thesis
Institution name	IIT Guwahati
Expected presentation date	Jun 2025

Additional Data

The Requesting Person / Organization to Appear on the License	Ujjala Dey

Requestor Location

Requestor Location	Ujjala Dey A-241, subansiri hostel, IIT guwahati Guwahati, 781039 India

Tax Details

Publisher Tax ID	EU826007151